frontiers | Research Topics

Physical and chemical processes within the planetary boundary layer and their impacts on air pollution

Edited by
Yucong Miao, Gen Zhang, Xiaolan Li and Chaoyang Xue

Published in
Frontiers in Environmental Science

ISSN 1664-8714
ISBN 978-2-8325-2635-4
DOI 10.3389/978-2-8325-2635-4

About Frontiers

Frontiers is more than just an open access publisher of scholarly articles: it is a pioneering approach to the world of academia, radically improving the way scholarly research is managed. The grand vision of Frontiers is a world where all people have an equal opportunity to seek, share and generate knowledge. Frontiers provides immediate and permanent online open access to all its publications, but this alone is not enough to realize our grand goals.

Frontiers journal series

The Frontiers journal series is a multi-tier and interdisciplinary set of open-access, online journals, promising a paradigm shift from the current review, selection and dissemination processes in academic publishing. All Frontiers journals are driven by researchers for researchers; therefore, they constitute a service to the scholarly community. At the same time, the *Frontiers journal series* operates on a revolutionary invention, the tiered publishing system, initially addressing specific communities of scholars, and gradually climbing up to broader public understanding, thus serving the interests of the lay society, too.

Dedication to quality

Each Frontiers article is a landmark of the highest quality, thanks to genuinely collaborative interactions between authors and review editors, who include some of the world's best academicians. Research must be certified by peers before entering a stream of knowledge that may eventually reach the public - and shape society; therefore, Frontiers only applies the most rigorous and unbiased reviews. Frontiers revolutionizes research publishing by freely delivering the most outstanding research, evaluated with no bias from both the academic and social point of view. By applying the most advanced information technologies, Frontiers is catapulting scholarly publishing into a new generation.

What are Frontiers Research Topics?

Frontiers Research Topics are very popular trademarks of the *Frontiers journals series*: they are collections of at least ten articles, all centered on a particular subject. With their unique mix of varied contributions from Original Research to Review Articles, Frontiers Research Topics unify the most influential researchers, the latest key findings and historical advances in a hot research area.

Find out more on how to host your own Frontiers Research Topic or contribute to one as an author by contacting the Frontiers editorial office: frontiersin.org/about/contact

Physical and chemical processes within the planetary boundary layer and their impacts on air pollution

Topic editors

Yucong Miao — Chinese Academy of Meteorological Sciences, China
Gen Zhang — Chinese Academy of Meteorological Sciences, China
Xiaolan Li — Institute of Atmospheric Environment, CMA, China
Chaoyang Xue — Max Planck Institute for Chemistry, Germany

Citation

Miao, Y., Zhang, G., Li, X., Xue, C., eds. (2023). *Physical and chemical processes within the planetary boundary layer and their impacts on air pollution*. Lausanne: Frontiers Media SA. doi: 10.3389/978-2-8325-2635-4

Table of contents

frontiers | Frontiers in Environmental Science

TYPE Editorial
PUBLISHED 23 May 2023
DOI 10.3389/fenvs.2023.1221546

OPEN ACCESS

EDITED AND REVIEWED BY
Tirthankar Banerjee,
Banaras Hindu University, India

*CORRESPONDENCE
Yucong Miao,
miaoyucong@yeah.net

RECEIVED 12 May 2023
ACCEPTED 16 May 2023
PUBLISHED 23 May 2023

CITATION
Miao Y, Zhang G, Li X and Xue C (2023), Editorial: Physical and chemical processes within the planetary boundary layer and their impacts on air pollution. *Front. Environ. Sci.* 11:1221546. doi: 10.3389/fenvs.2023.1221546

Editorial: Physical and chemical processes within the planetary boundary layer and their impacts on air pollution

Yucong Miao[1]*, Gen Zhang[1], Xiaolan Li[2] and Chaoyang Xue[3,4]

[1]State Key Laboratory of Severe Weather and Key Laboratory of Atmospheric Chemistry of CMA, Chinese Academy of Meteorological Sciences, Beijing, China, [2]Institute of Atmospheric Environment, China Meteorological Administration, Shenyang, China, [3]Laboratoire de Physique et Chimie de l'Environnement et de l'Espace (LPC2E), CNRS–Université Orléans–CNES, Orléans, France, [4]Max Planck Institute for Chemistry, Mainz, Germany

KEYWORDS

turbulence, transport, dispersion, boundary layer height, chemical reactions

Editorial on the Research Topic
Physical and chemical processes within the planetary boundary layer and their impacts on air pollution

1 Introduction

Air pollution is a critical environmental problem that arises from diverse natural and anthropogenic emissions and poses significant threats to public health (Bu et al., 2021), ecosystems (Hu et al.), and climate change (Bellouin et al., 2020). Despite some progress in reducing emissions and improving air quality in certain regions, many parts of the world still experience dangerous levels of pollution (Sicard et al., 2023).

The planetary boundary layer (PBL) forms the lowest layer of the troposphere and is a key player in the complex dynamics of air pollution through various physical and chemical processes (Stull, 1988). A comprehensive understanding of these processes is critical to devising effective strategies to mitigate air pollution. This entails the optimization of emission reduction measures, as well as the development of accurate air quality forecasting models. Such knowledge can inform sound public policy decisions aimed at reducing air pollution levels and safeguarding public health.

2 Physical processes

The PBL is a highly intricate and multi-scale system, involving a variety of physical processes (Serafin et al., 2018; Miao et al., 2022), such as turbulence, convection, radiation, and advection. The exchange of heat, moisture, and momentum between the surface and the atmosphere is largely governed by the thermal stratification of the PBL and its underlying surface characteristics (Stull, 1988). This exchange strongly influences the transport and dispersion of air pollutants, including aerosols and trace gases, from the surface to the upper troposphere.

TABLE 1 Main findings from the published research papers within the Research Topic on "*Physical and Chemical Processes within the Planetary Boundary Layer and Their Impacts on Air Pollution*."

PBL processes	Main findings
Physical processes	Xiong et al. developed a new numerical method to isolate the direct and semi-direct effects of aerosols and compare their effects with the indirect effect and found that the effects of aerosols through clouds, especially the indirect effect, play the dominant role in their feedback processes on PBL structure and air quality under cloudy conditions.
	Wei et al. summarized the current state of low-level jet (LLJ)-pollutant interactions from the perspectives of observations, models, and mechanisms, and proposed to conduct high-resolution spatiotemporal observations of pollutants and turbulence to better understand their interactions.
	Li et al. combined the Kolmogorov-Zurbenko filter method and the multiple linear stepwise regression method to study the influence of meteorological parameters on ozone concentration in Zibo and found that the overall meteorological influence was variable.
Chemical processes	Guo et al. conducted an online measurement of VOCs in the urban area of the city of Lhasa for the first time in May 2019 and observed a total of 49 VOCs.
	Wang et al. conducted a field observation lasting approximately 5 months, from 25 October 2021 to 22 March 2022, and found that most of the $PM_{2.5}$ pollution events occurred under conditions of low wind speed, temperature inversion, and high humidity, which favored the accumulation and secondary transformation of pollutants.
	Du et al. numerically found that the O_3-sensitive regimes in the city of Chengdu were in a transition zone, while the other neighboring cities were in the NOx-limited zone.
	Hao et al. studied the interfacial partition constant of 2-chloroacetophenone by measuring the mass uptake vapor on various environmental water films of different thicknesses and found that the adsorption partitioning ability of 2-chloroacetophenone at the air/water interface was negatively correlated with the surface tension.
	Hu et al. applied a remote sensing-based method to assess the impact of O_3 on the net primary productivity (NPP) of China's terrestrial ecosystems by combining MODIS NPP and the latest ground-based observations of O_3 concentration.
	Ai et al. evaluated existing diesel pollution control policies in Beijing and proposed emission control measures taking into account air quality improvement, emission reduction needs, diesel consumption characteristics, and existing emission reduction problems.
	Wang et al. found that cloud cover can influence O_3 pollution in Beijing, Hangzhou, and Guangzhou.

Turbulence is the dominant feature of the PBL and is responsible for mixing and transporting heat, moisture, and pollutants (Wei et al.). Convection, on the other hand, is responsible for the vertical transport of heat and moisture (Margairaz et al., 2020). Radiation plays a significant role in determining the energy balance of the PBL (Lee, 2018) and its interaction with aerosols (Xiong et al.). Meanwhile, advection involves the transport of air masses horizontally (Miao et al., 2022), and certain synoptic conditions and PBL dynamics can result in the long-range transport of pollutants (Colarco et al., 2004; Xiao et al., 2020).

The height and stability of the PBL determine the concentration of pollutants at the surface (Miao and Liu, 2019) and regulate their vertical distribution (Bourgeois et al., 2018; Banerjee et al., 2022). Therefore, understanding the dynamics and physical processes of the PBL is crucial in predicting air pollutant concentrations and developing effective air pollution mitigation strategies. For example, the interaction between aerosols and the PBL (Wang et al., 2022) is a critical factor in air pollution formation and dispersion. High concentrations of aerosols can enhance the stability of the PBL, resulting in decreased PBL height and exacerbating pollution levels (Petäjä et al., 2016). Additionally, aerosols can affect cloud adjustments and microphysical processes, leading to changes in the PBL height and the concentration of pollutants (Xiong et al.).

3 Chemical processes

Chemical processes within the PBL are the critical drivers in affecting the composition and concentration of atmospheric pollutants (Wang et al., 2017). Reactions between pollutants (Ma et al., 2012), including nitrogen oxides (NO_x) and volatile organic compounds (VOCs), with the involvement of sunlight and other atmospheric compounds such as oxygen, can lead to the formation of secondary pollutants such as photo oxidants and aerosols. One of the most crucial processes is the photochemical production of ozone (O_3) (Wang et al.), which occurs during the VOCs degradation process with the presence of NO_x and sunlight (Du et al.). Additionally, the transformation of primary gaseous pollutants, including nitrogen monoxide (NO) and sulfur dioxide (SO_2), into secondary particle pollutants (Wang et al.) such as nitric acid (HNO_3) and sulfate aerosols (SO_4) is another critical process. The other category triggering this transformation is atmospheric oxidants, including hydroxyl radicals (OH), O_3, and nitrate radicals (NO_3), and heterogeneous reactions, which are generated through various photochemical reactions (Brown and Stutz, 2012; Wang et al., 2017; Ye et al., 2022).

Meteorological conditions such as air temperature, humidity, and wind speed influence these chemical processes (Li et al.; Wang et al.). For example, higher temperatures and stronger solar radiation accelerate the photochemical reactions, leading to a higher production rate of O_3 and other secondary pollutants, and finally causing photochemical pollution. In contrast, increased wind speed and turbulence can enhance the mixing and dispersion of pollutants within the PBL, leading to lower concentrations of these compounds distributed near the surface.

Thereby, understanding the mechanisms behind these PBL chemical processes and their links with meteorological conditions is crucial for predicting and mitigating air pollution.

4 Summary

In short, the physical and chemical processes occurring within the PBL have profound effects on air pollution (Table 1), and it is essential to comprehend these processes thoroughly. To achieve this goal, it is necessary to conduct extensive research, including field measurements (e.g., Guo et al.), laboratory experiments (e.g., Hao et al.), and model simulations (e.g., Ai et al.). Such research will enable us to develop a comprehensive understanding of the sources, transformations, and transport of atmospheric pollutants, benefitting the development of future air pollution mitigation strategies and further reducing adverse effects on human and ecosystem health.

Author contributions

YM and GZ wrote the editorial with inputs from XL and CX. All authors contributed to the article and approved the submitted version.

Funding

This work was supported by the National Natural Science Foundation of China (42275198) and China Scholarship Council (202205330018).

Conflict of interest

The authors declare that the research was conducted in the absence of any commercial or financial relationships that could be construed as a potential conflict of interest.

Publisher's note

References

Banerjee, T., Anchule, A., Sorek-Hamer, M., and Latif, M. T. (2022). Vertical stratification of aerosols over South Asian cities. *Environ. Pollut.* 309, 119776.

Bellouin, N., Quaas, J., Gryspeerdt, E., Kinne, S., Stier, P., Watson-Parris, D., et al. (2020). Bounding global aerosol radiative forcing of climate change. *Rev. Geophys.* 58, 660. doi:10.1029/2019RG000660

Bourgeois, Q., Ekman, A. M. L., and Renard, J.-B. (2018). How much of the global aerosol optical depth is found in the boundary layer and free troposphere? *Atmos. Chem. Phys.* 18, 7709–7720.

Brown, S. S., and Stutz, J. (2012). Nighttime radical observations and chemistry. *Chem. Soc. Rev.* 41 (19), 6405–6447. doi:10.1039/c2cs35181a

Bu, X., Xie, Z., Liu, J., Wei, L., Wang, X., Chen, M., et al. (2021). Global PM2.5-attributable health burden from 1990 to 2017: Estimates from the Global Burden of disease study 2017. *Environ. Res.* 197, 111123. doi:10.1016/J.ENVRES.2021.111123

Colarco, P. R., Schoeberl, M. R., and Doddridge, B. G. (2004). Transport of smoke from Canadian forest fires to the surface near Washington, DC: Injection height, entrainment, and optical properties. *J. Geophys. Res. Atmos.* 109 (D6). doi:10.1029/2003JD004248

Lee, X. (2018). *Fundamentals of boundary-layer meteorology*. Berlin, Germany: Springer International Publishing. doi:10.1007/978-3-319-60853-2

Ma, J., Xu, X., Zhao, C., and Yan, P. (2012). A review of atmospheric chemistry research in China: Photochemical smog, haze pollution, and gas-aerosol interactions. *Adv. Atmos. Sci.* 29, 1006–1026. doi:10.1007/s00376-012-1188-7

Margairaz, F., Pardyjak, E. R., and Calaf, M. (2020). Surface thermal heterogeneities and the atmospheric boundary layer: The relevance of dispersive fluxes. *Boundary-Layer Meteorol.* 175, 369–395. doi:10.1007/S10546-020-00509-W/FIGURES/12

Miao, Y., and Liu, S. (2019). Linkages between aerosol pollution and planetary boundary layer structure in China. *Sci. Total Environ.* 650. doi:10.1016/j.scitotenv.2018.09.032

Miao, Y., Zhang, X., Che, H., and Liu, S. (2022). Influence of multi-scale meteorological processes on PM2.5 pollution in wuhan, central China. *Front. Environ. Sci.* 10, 1–7. doi:10.3389/fenvs.2022.918076

Petäjä, T., Järvi, L., Kerminen, V. M., and Ding, A. J. (2016). Enhanced air pollution via aerosol-boundary layer feedback in China. *Sci. Rep.* 6 (1), 18998.

Serafin, S., Adler, B., Cuxart, J., De Wekker, S., Gohm, A., Grisogono, B., et al. (2018). Exchange processes in the atmospheric boundary layer over mountainous terrain. *Atmosphere* 9, 102. doi:10.3390/atmos9030102

Sicard, P., Agathokleous, E., Anenberg, S. C., De Marco, A., Paoletti, E., and Calatayud, V. (2023). Trends in urban air pollution over the last two decades: A global perspective. *Sci. Total Environ.* 858, 160064. doi:10.1016/J.SCITOTENV.2022.160064

Stull, R. B. (1988). in *An introduction to boundary layer meteorology*. Editor R. B. Stull (Dordrecht: Springer Netherlands). doi:10.1007/978-94-009-3027-8

Wang, T., Xue, L., Brimblecombe, P., Lam, Y. F., Li, L., and Zhang, L. (2017). Ozone pollution in China: A review of concentrations, meteorological influences, chemical precursors, and effects. *Sci. Total Environ.* 575, 1582–1596. doi:10.1016/j.scitotenv.2016.10.081

Wang, Z., Xue, L., and Liu, J. (2022). Roles of atmospheric aerosols in extreme meteorological events: A systematic review. *Curr. Pollut. Rep.* 8, 177–188. doi:10.1007/s40726-022-00216-9

Xiao, Z., Miao, Y., Du, X., Tang, W., Yu, Y., Zhang, X., et al. (2020). Impacts of regional transport and boundary layer structure on the PM2.5 pollution in wuhan, central China. *Atmos. Environ.* 230, 117508.

Ye, C., Lu, K., Song, H., Mu, Y., Chen, J., and Zhang, Y. (2022). A critical review of sulfate aerosol formation mechanisms during winter polluted periods. *J. Environ. Sci.* 123, 387–399. doi:10.1016/j.jes.2022.07.011

frontiers | Frontiers in Environmental Science

TYPE Original Research
PUBLISHED 23 August 2022
DOI 10.3389/fenvs.2022.941100

OPEN ACCESS

EDITED BY
Gen Zhang,
Chinese Academy of Meteorological Sciences, China

REVIEWED BY
Xingru Li,
Capital Normal University, China
Pengfei Liu,
Research Center for Eco-environmental Sciences (CAS), China

*CORRESPONDENCE
Weili Lin,
linwl@muc.edu.cn

SPECIALTY SECTION
This article was submitted to Atmosphere and Climate, a section of the journal Frontiers in Environmental Science

RECEIVED 11 May 2022
ACCEPTED 20 July 2022
PUBLISHED 23 August 2022

CITATION
Guo S, Wang Y, Zhang T, Ma Z, Ye C, Lin W, Yang Zong DJ and Yang Zong BM (2022), Volatile organic compounds in urban Lhasa: variations, sources, and potential risks.
Front. Environ. Sci. 10:941100.
doi: 10.3389/fenvs.2022.941100

Volatile organic compounds in urban Lhasa: variations, sources, and potential risks

Shuzheng Guo[1], Yaru Wang[2], Tiantian Zhang[1], Zhiqiang Ma[3], Chunxiang Ye[2], Weili Lin[1]*, De Ji Yang Zong[4] and Bai Ma Yang Zong[4]

[1]Key Laboratory of Ecology and Environment in Minority Areas (Minzu University of China), National Ethnic Affairs Commission, Beijing, China, [2]College of Environmental Science and Technology, Peking University, Beijing, China, [3]Beijing Shangdianzi Regional Atmosphere Watch Station, Beijing, China, [4]Tibet Meteorological Bureau, Lhasa, China

Lhasa is a typical high-altitude city with strong solar radiation and high background ozone levels. With the rapid development and urbanization, the emission of volatile organic compounds (VOCs) in Tibet has been increasing annually. However, VOCs activity and the impact on air quality and human health have scarcely been investigated. We conducted online measurement of VOCs in urban Lhasa during May 2019. The mean mixing ratio (with one standard deviation) of the total VOCs was 21.5 $\pm$ 18.6 ppb. Of the total VOCs, alkanes, alkenes, and aromatic hydrocarbons accounted for 57.7%, 20.9%, and 21.4%, respectively. On the basis of VOC atmospheric reactivity, the ozone formation potential (*OFP*) and hydroxyl radical loss rate (L_{OH}) were 91.7 ppb and 3.1 s^{-1}, respectively. Alkenes accounted for the largest proportion of the *OFP* and L_{OH}, followed by aromatic hydrocarbons. The results of correlation analysis on the benzene series (BTEX), and the similarity of the diurnal changes in CO, NOy, BTEX, and TVOC mixing ratios indicated that Lhasa city strongly affected by motor vehicle emissions. Source apportionments using positive matrix factorization (PMF) model further confirmed that traffic related emissions, including gasoline automobiles, diesel vehicles, and public transportation vehicles fueled with liquid natural gas contributed the most in total VOCs concentration (44.5%–50.2%), L_{OH} (41.6%–46.8%) and *OFP* (47.4%–52.3%). Biomass combustion, mainly from the traditional biomass fuel in the plateau, was the second contributor to ambient VOCs (41.3%), L_{OH} (26.4%), and *OFP* (29.7%), and existed a less variation in diurnal changes with a feature of regional background. Plants contributed only about 1.5% to the VOCs concentration but a relatively high (approximately 14.6%) L_{OH}. The noncarcinogenic risk of BTEX did not exceed the hazard quotient value, but the carcinogenic risk of benzene was 4.47 $\times$ 10^{-6}, indicating a potential risk.

KEYWORDS

Tibet Plateau, benzene series, atmospheric reactivity, ozone formation potential, health risk, VOCs

1 Highlights

- Variations in volatile organic compounds were explored in a highland urban city
- Air quality in urban Lhasa city was strongly affected by motor vehicle emissions
- Benzene has a potential carcinogenic risk in urban Lhasa now

2 Introduction

Volatile organic compounds (VOCs) in the atmosphere are crucial precursors of ozone (O_3) and secondary organic aerosols (SOAs) (Tang et al., 2006; Santos et al., 2021). VOCs play a critical role in tropospheric atmospheric chemistry, affecting the atmospheric oxidation balance, greenhouse effect, and secondary aerosol formation (Constable et al., 2001; Klinger et al., 2002). They also have a definite impact on human health (Zhao et al., 2019; Lyu et al., 2020). In China, emissions of anthropogenic VOCs have been increasing annually (Li et al., 2019), especially in economically developed and densely populated areas such as the North China Plain (Liu et al., 2005; Song et al., 2007; Wang et al., 2012; Li et al., 2020), Yangtze River Delta (Huang et al., 2011a; Huang et al., 2015; Dai et al., 2017), and Pearl River Delta (Liu et al., 2007; Guo et al., 2011; Han et al., 2019). However, few studies are carried out on atmospheric pollutants, especially VOCs, in the Tibetan Plateau, where the air is always considered as clean background since it is far away from polluted areas. Limited data have revealed that VOC concentrations in the Tibetan rural regions were higher than those in the Arctic and Antarctic regions but lower than those in many remote rural areas of Asia (Xue et al., 2013; Li et al., 2017). An early study suggested that VOCs in Lhasa mainly originate from biomass combustion and plant emissions (Yu et al., 2001). In recent years, anthropogenic VOC emissions from fossil fuel combustion (motor vehicles and coal burning) and industry have become increasingly prevalent (Ran et al., 2014; Bai et al., 2018; Chen et al., 2018; Yin et al., 2019). In 2019, 265,000 motor vehicles have been reported to be owned by the 555,000 registered residents of Lhasa city, and approximately 65% of the residents lived in the urban area of less than 150 km^2 (data from Lhasa Statistics Bureau), indicating a high density of vehicles in the city. As the urban area of Lhasa city has continued to develop and expand, the number of motor vehicles, including vehicles from other provinces, and the emissions and ambient levels of gaseous pollutants (e.g., NOx, CO, and SO_2) have increased significantly (Wei et al., 2011; Ran et al., 2014). The Tibetan Plateau has strong solar radiation (Chen et al., 2015), high background ozone levels (Lin et al., 2015), and high atmospheric oxidation capacity (Lin et al., 2008), which facilitates the formation of airborne particulates from the organic precursors, such as polycyclic aromatic hydrocarbons (Qi et al., 2003; Liu et al., 2013), but also increases a potential risk of photochemical smog from the increasing photochemical precursors in highland cities with dense populations (Ran et al., 2014). The potential risks of air quality deterioration and photochemical pollution have not yet evaluated by measurement. Therefore, performing observational studies on VOCs to determine their concentrations, composition and variation characteristics, photochemical properties in the atmosphere, and potential risks to human health in urban Lhasa, a typical highland city, is vital. In this paper, we presented the variations of VOCs, which were continuously and firstly measured by on-line techniques, and then discussed their sources implication and potential risks.

3 Measurement and analysis methods

3.1 Online measurement

From May 1 through 31 May 2019, VOCs were measured in the yard of the Meteorological Bureau of the Tibet Autonomous Region in Lhasa city (91.13°E, 29.65°N, 3,667 m above sea level). The sample inlet was on the rooftop of a four-storey building. The measurement site was adjacent to the Linkuo North Road in the northern part of the city. The site was surrounded by office and residential areas, and the famous Potala Palace was located 2 km to the west, as illustrated in Figure 1.

In this study, an online gas chromatograph analyzer (Syntech Spectras GC955, Groningen, Netherlands) was used to measure the ambient VOC concentrations. The ambient air sample entered the analyzer after particulate filtering and Nafion tube drying. The sampling flow rate was 0.5 $L{\cdot}min^{-1}$. C_6–C_{12} and C_2–C_5 compounds, with high and low boiling points, respectively, were measured separately. C_6–C_{12} compounds were preconcentrated and enriched on a Tenax GR tube at room temperature, heated, and quickly desorbed. The compounds then entered a DB-1 chromatographic column with a carrier gas for separation and were finally detected by a photoionization detector (PID). C_2–C_5 compounds were cooled and preconcentrated at a low temperature (5°C) on a Carbonsieve SIII tube. After heating and desorption, they were separated using a porous layer open tubular chromatographic column and were finally monitored using a PID and a flame ionization detector (FID). 40-min cycles were set during the measurement. VOC standard gases (55 VOC mixtures, ~1.0 ppm, Linde Spectra Environmental Gases, Germany), namely 28 alkanes, 11 alkenes, and 16 aromatics, were used in qualitative and quantitative analyses. Zero and span (~5 ppb) calibrations were performed in the early and late stages of field observation. High purity N_2 (99.999%) was used as zero and dilution gas. According to the order of peak areas and the retention times of the standard spectrogram, the individual VOCs compounds were determined and quantified. During

FIGURE 1
Measurement site's location and nearby topography in Lhasa. Measurement was conducted in the central urban area.

the measurement, there were 49 species of VOCs identified and quantified. In general, the precision for VOCs was below 15%. The linear correlation coefficients of calibration curves were mostly greater than 0.99 for individual VOCs compounds as tested in the lab.

Surface CO mixing ratios were measured using a gas filter correlation infrared absorption analyzer (48i trace level, Thermo Fisher, Uinted States). Reactive nitrogen species (NOy) were detected using a chemiluminescence analyzer (Model 42i-Y, Thermo Scientific, Uinted States) equipped with an external molybdenum converter heated to approximately 375°C. Meteorological data were obtained from the Tibet Meteorological Bureau.

3.2 Data analysis methods

3.2.1 Calculation of mixing layer depth

The National Centers for Environmental Prediction and National Center for Atmospheric Research reanalysis meteorological data set (https://ready.arl.noaa.gov/archives.php) was input into National Oceanic and Atmospheric Administration Hysplit (http://ready.arl.noaa.gov/HYSPLIT.php) software to calculate mixing layer depths (MLDs) during the measurement period.

3.2.2 Calculation of ozone formation potential

The maximum incremental reactivity (*MIR*) method was used to calculate the *OFP* of each VOC component to evaluate the contribution of VOCs to O_3 generation. The *OFP* calculation formula is as follows:

$$OFP_i = MIR_i \times [VOC]_i \quad (1)$$

where *MIR* is the maximum incremental reactivity, and the value of *MIR* is obtained from the California Code of Regulations, 2010 (Carter, 2010); $[VOC]_i$ is the concentration of each VOC component in ppb.

3.2.3 Calculation of loss rate of hydroxyl radical

The OH radical loss rate (L_{OH}) of VOC components was calculated using the following formula:

$$L_{OHi} = k_i^{OH} \times [VOC]_i \quad (2)$$

where k^{OH} is the reaction rate constant of VOCs and hydroxyl radicals, and the data originate from reference (Atkinson and Arey, 2003).

3.2.4 Positive matrix factorization analysis

Positive matrix factorization (PMF) model was first proposed to factor analysis in 1994 (Paatero and Tapper, 1994) and it has been widely used recently as a tool to resolve VOCs source-receptor relationship and to evaluate the different sources contributions. PMF is a receptor model which quantifies contributions from various sources by mathematical statistics according to the different chemical composition or source fingerprint. In this paper, the EPA PMF 5.0 software with a multiple linear engine version 2 (ME-2) platform (Norris et al., 2014) is used for source analysis. Based on Eq. 3, PMF calculates

the following parameters: 1) the number of VOCs source factors p, 2) the chemical composition of each source factor f, 3) contribution g of each source factor to the sample, and 4) residual e_{ij} of each species to each sample. The constraint of PMF is that the contribution g and source factor f in the equation should be non-negative to have physical significance.

$$X_{ij} = \sum_{k=1}^{p} g_{ik} f_{kj} + e_{ij} \quad (3)$$

where, the data matrix X_{ij} represents the concentration of VOCs, i represents the observed sample, j represents the species.

The target of PMF is to minimize the functional residual Q in the Eq. 4, where n and m are the number of samples and the number of species respectively, and u_{ij} is the uncertainty of X_{ij}.

$$Q = \sum_{i=1}^{n} \sum_{j=1}^{m} \left[\frac{\sum_{k=1}^{p} g_{ik} f_{kj} + e_{ij} - \sum_{k=1}^{p} g_{ik} f_{kj}}{u_{ij}} \right] \quad (4)$$

The input file consists of two matrices, observed species concentration (X_{ij}) and uncertainty (u_{ij}).

Uncertainty calculation formula is:

$$Unc = \begin{cases} \sqrt{(Error\ Fraction \times Conc.)^2 + (0.5 \times MDL_j)} & Conc. > \text{MDL} \\ \frac{5}{6} \times Conc. & Conc. \le MDL \\ 4 \times media\ conc. & Missing\ data \end{cases} \quad (5)$$

$$Q_{expected}. = n \times m - p \times (n + m)$$

Based on the extensively used principles, missing rates greater than 25% or concentrations lower than MDL are excluded (Han et al., 2021). Finally, 21 species were selected and input into the PMF model calculation. Three to nine factors were estimated to obtain the best resolution based on the $Q_{true}/Q_{expected}$ and Q_{true}/Q_{robust} value (Li et al., 2020). In this study, six factors were determined with regard to the Q_{true}/Q_{robust} = 1.06 and $Q_{true}/Q_{expected}$ = 1.09. Around 95% of the scaled residuals were between −3 and 3. Fpeak with the value of −1 to 1 at intervals of 0.1 was determined to investigate the free rotation (Song et al., 2018). The results showed that Fpeak values had no significant difference, indicating a good fit of the modeled results.

3.2.5 Health risk assessment

To quantitatively describe the relationship between the human exposure dose and adverse health reaction, according to the carcinogenicity of substances, health risk assessments are generally of two types: carcinogenic and noncarcinogenic risk assessments (Xia et al., 2014; Cheng et al., 2019). In this study, the assessment indexes were calculated using Eqs. 6–9.

$$EC = C \times \frac{ET \times EF \times ED}{AT} \quad (6)$$

$$Risk = IUR \times EC \quad (7)$$

$$HQ = EC/RfC \quad (8)$$

$$HI = \sum_{i=1}^{n} HQ_i \quad (9)$$

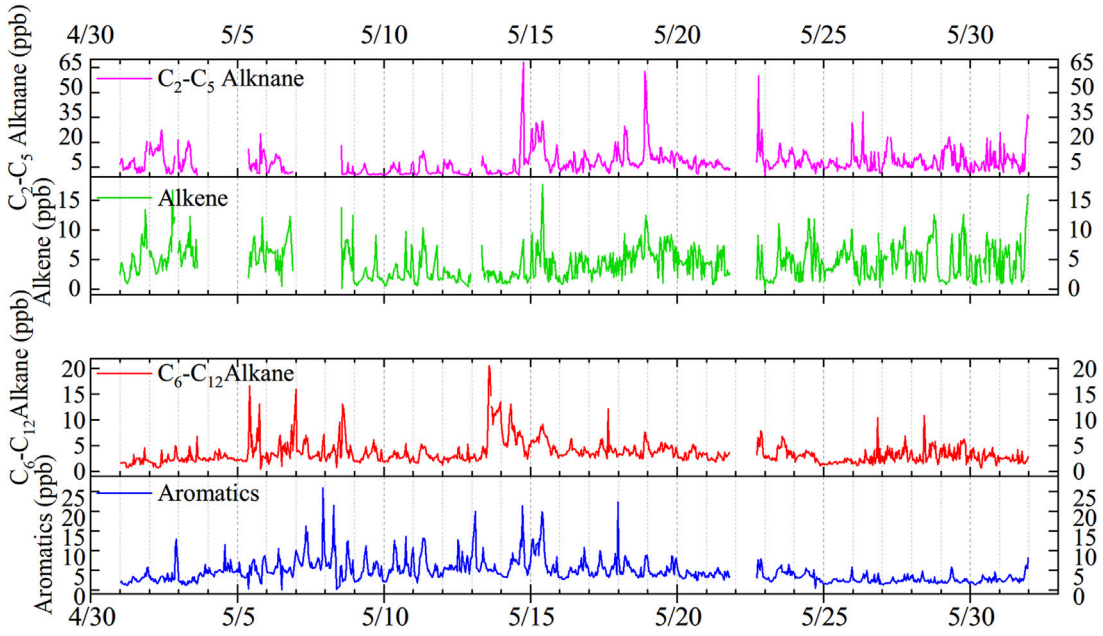

FIGURE 2
Time series variations in alkenes, C2–C5 alkanes, C6–C12 alkanes, and aromatics mixing ratios in the 2019 study.

TABLE 1 Concentrations and ratios of the classification of VOCs in May in urban Lhasa.

Species	Mean (ppb)	Std (ppb)	Median (ppb)	Proportion (%)
Alkanes	12.4	11.2	9.8	57.7
Alkenes	4.5	2.8	4.1	20.9
Aromatics	4.6	3.5	3.9	21.4
TVOCs	21.5	18.6	17.8	100

where *EC* is the exposure concentration in μg/m^3, *C* is the environmental concentration of pollutants in μg/m^3, *ET* is the exposure time, *EF* is the exposure frequency, *ED* is the exposure duration (in years), *AT* is the average time, *RfC* is the inhaled carcinogenic risk concentration in mg/m^3, *IUR* is the US Environmental Protection Agency (EPA) inhalation unit risk in μg/m^3, *Risk* is the value of carcinogenic risk, *HQ* is the noncarcinogenic risk hazard quotient (*HQ*), and *HI* is the noncarcinogenic risk index. *EF* was obtained from the US EPA Integrated Risk Information System (IRIS, 365 d/y; http://www.epa.gov/iris), and *ET*, *ED*, and *AT* were 3.68 h/day, 74.8 years, and 74.8 × 365 × 24 h, respectively (Cheng et al., 2019).

4 Results and discussion

4.1 Time series variation in VOC mixing ratios

As illustrated in Figure 2, during the entire observation period, the volume mixing ratios of C_2–C_5 alkanes, alkenes, C_6–C_{12} alkanes, and aromatics were 2.1–67.4, 0.39–16.8, 1.2–22.3, and 0.95–20.6 ppb, respectively. Regarding C_2–C_5 alkanes, higher spikes were found from May 14–19, 2019, whereas C_6–C_{12} alkanes demonstrated higher concentrations on May 5–9 and 13–16, 2019 (maximum value: 22.3 ppb, daily average value: 7.4 ppb). Aromatics fluctuated more from May 7–18, 2019, with a greater number of peaks (maximum value: 20.6 ppb, daily average value: 8.7 ppb). Alkenes demonstrated fluctuations for the whole measurement period. The daily mean concentrations of C_2–C_5 alkanes only exhibited a significant correlation (R = 0.44, p < 0.05) with alkenes, and the daily mean concentrations of C_6–C_{12} alkanes only had a significant correlation (R = 0.65, p < 0.05) with aromatics. This indicated a difference in sources and sinks between C_2–C_5 and C_6–C_{12} VOC compounds.

4.2 Statistics and comparison of VOC mixing ratios

4.2.1 Concentration level of volatile organic compounds

As detailed in Table 1, the hourly mean mixing ratio with ±1 σ of total VOCs in our measurement was 21.5 ± 18.6 ppb (median: 17.8 ppb), which was lower than the annual average VOC mixing ratio of 37.4 ppb (sum of alkanes, alkenes and aromatics) obtained in Lhasa city during 2019 through Summa canister offline sampling (Yu et al., 2022). Leaving their difference in sampling time and frequency aside, it indicated that there have months with high VOCs at Lhasa than that in May when we measured. The concentration was also lower than those reported in large cities such as Beijing, Tianjin, Nanjing, and Los Angeles (see Table 2) but higher than those reported in clean rural sites such as Gonggar Mountain. The alkane volume mixing ratio was 12.4 ± 11.2 ppb, accounting for 57.7% of the total VOCs, whereas the ratios of aromatics and alkenes were 4.6 ± 3.5 and 4.5 ± 2.8 ppb, accounting for 21.4% and 20.9% of the total VOCs, respectively. The relative contribution of the four types of VOCs here was similar to other cities, inferring comparable emission inventory structure of VOCs. Much

TABLE 2 Comparison of atmospheric VOCs in Lhasa with other observation sites.

Site	Period	Site type	No. of species	Conc./ppb	Method	Reference
Lhasa	2019.05	Urban	49	21.5 ± 18.6	Online/GC	This study
Menyuan	2013.9.13–10.14	Background	38	11.03	Offline/GCMS	Bai et al. (2016)
Lanzhou	2013	Urban	53	38.29	Online/GC	Jia et al. (2016)
Dushanzi	2015.09-2016.04	Urban	57	17.05 ± 13.61	Offline/GCMS	Zhang et al., (2019)
Tianjin	2019	Urban	56	48.9 μg m^{-3}	Online/GC	Gao et al., (2021)
Beijing	2016	Urban	99	101.5 ± 65.2 μg m^{-3}	Online/GCMS	Liu et al., (2021)
Nanjing	2013.12-2014.02	Urban	56	27 ± 14	Online/GC	An et al., (2017)
Los Angeles	2010.05	Urban	26	41.3	Online/PTRMS	Warneke et al., (2012)
Southwest of the U.S.	2017.4-2017.9	National Park	56	0.1~21	Offline/GCMS	Benedict et al., (2020)
East Rongbuk Glacier	2009	Background	108	8.56~36.77	Offline/GC×GC	Wang et al., (2009)
Gongga Mountain	2008.1-2011.12	Background	40	8.75 ± 5.76	Offline/GCMS	Zhang et al., (2014)

TABLE 3 Top 10 species ranked in terms of proportions of concentration, *OFP*, and L_{OH}.

Species	Conc. (ppb)	Ratio (%) in conc.	Species	*OFP* (ppb)	Ratio (%) in *OFP*	Species	L_{OH} (s^{-1})	Ratio (%) in L_{OH}
Ethane	2.86	13.3	Isobutene	14.47	15.8	Isoprene	0.52	16.6
Isobutene	2.34	10.9	m/p-Xylene	9.60	10.5	1-Hexene	0.41	13.0
Isobutane	1.97	9.2	Toluene	9.26	10.1	Propene	0.31	9.8
n-Butane	1.72	8.0	o-Xylene	8.21	9.0	n-Undecane	0.29	9.3
Bezene	1.65	7.7	Propene	8.07	8.8	cis-2-Butene	0.23	7.4
n-Undecane	1.36	6.3	Hexene	6.08	6.6	m/p-Xylene	0.18	5.8
Toluene	1.21	5.6	cis-2-Butene	4.82	5.3	n-Decane	0.15	4.7
2,2-Dimethylbutane	0.99	4.6	Isoprene	3.76	4.1	o-Xylene	0.12	3.9
Propene	0.79	3.7	Isobutane	2.94	3.2	Styrene	0.12	3.7
n-Hexane	0.70	3.3	n-Undecane	2.70	2.9	Toluene	0.12	3.7
Total	15.6	72.5	Total	69.9	76.3	Total	2.4	78.0

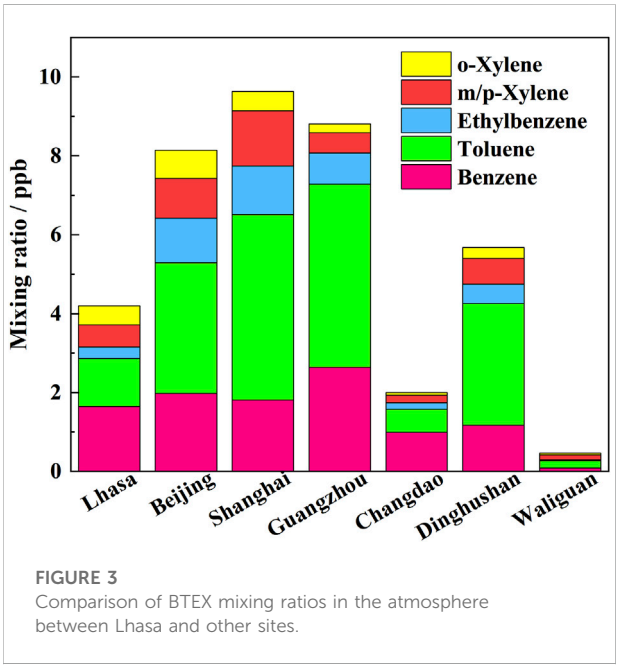

FIGURE 3
Comparison of BTEX mixing ratios in the atmosphere between Lhasa and other sites.

lower VOCs might be related to the relatively lower emission strength in the city of Lhasa. According to mixing ratios, the top 10 VOC components were ethane, isobutene, isobutane, n-butane, benzene, toluene, n-undecane, 2,2-dimethylbutane, propylene, and n-hexane, respectively (Table 3).

4.2.2 Characteristics of BTEX mixing ratios

BTEX is a general term for benzene, toluene, ethylbenzene, and three xylene isomers (m-xylene, p-xylene, and o-xylene); it represents a key group among VOCs. BTEX mainly originates from solvent use, fossil fuel and biomass combustion, and it plays a pivotal role in atmospheric photochemical smog and particulate pollution (Zhang et al., 2016; Yao et al., 2017).

Supplementary Figure S1 depicts the time series variations in benzene, toluene, ethylbenzene, m/p-xylene, and o-xylene mixing ratios from May 1 to 31 May 2019. BTEX mixing ratios exhibited day-to-day fluctuations of 1.8–20.2 ppb. The average benzene, toluene, ethylbenzene, m/p-xylene, and o-xylene mixing ratios with ±1 σ were 1.65 ± 0.8, 1.21 ± 1.02, 0.29 ± 0.25, 0.56 ± 0.58, 0.49 ± 0.48 ppb, respectively, and BTEX accounted for 19.5% of the total VOCs.

Figure 3 provides a comparison of BTEX mixing ratios in Lhasa with the ratios recorded in other cities. The BTEX mixing ratios in Lhasa were much lower than those in Beijing (January 2014) (Li et al., 2015), Shanghai (January 2007–March 2010) (Cai et al., 2010), Guangzhou (November–December 2009) (Zhang et al., 2013), and the Dinghushan rural site in the Pearl River Delta (April 2005) (Tang et al., 2007). However, it is worth noting that the benzene to BTEX ratio was higher in Lhasa (39%) than that in Beijing (24%), Shanghai (19%), and Guangzhou (30%). The BTEX mixing ratio in Lhasa was higher than that at the rural site in Changdao, Shandong province (March–April 2011) (Yuan et al., 2013) and Waliguan, Tibet Plateau (April–May 2003) (Xue et al., 2013).

4.3 Diurnal variations

Figure 4 shows the average diurnal variations in the mixing ratios of various classes of VOCs, atmospheric

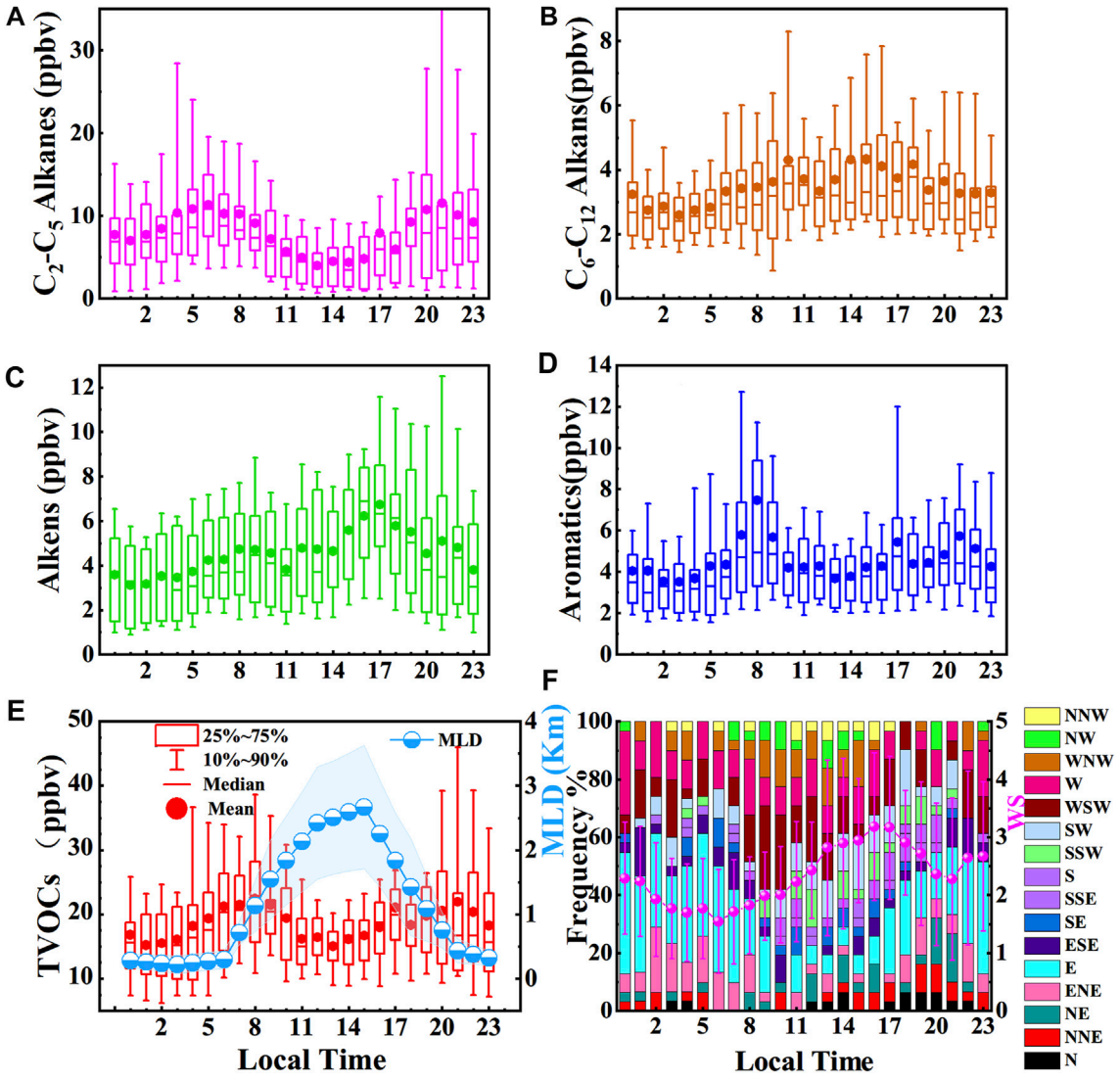

FIGURE 4
Daily variations in **(A)** C2–C5 alkanes, **(B)** C6–C12 alkanes, **(C)** alkenes, **(D)** aromatics, **(E)** TVOCs mixing ratios and mixing layer depths (MLD), and **(F)** wind direction frequency and wind speed (shade and error bar indicate 1 σ).

MLD, wind direction frequency, and wind speed. Easterly winds were predominant at nighttime (19:00–6:00), whereas westerly winds were more prevalent during daytime. Strong winds were observed in the afternoon and reached a peak at 16:00–17:00.

The peak value of C_2–C_5 alkanes was found at 6:00 when the wind speed was the lowest for the day. The concentrations then gradually decreased; a trough value appeared at 14:00, and another peak value appeared at 21:00. The mean value at 6:00 (11.3 ppb) was close to the median value (10.8 ppb), whereas the mean value (11.5 ppb) at 21:00 was much higher than the median value (8.2 ppb), which indicated the heavier influence of local emissions at night peak time. The concentration (6.9 ppb) of C_2–C_5 alkanes in daytime was lower than that at night (9.3 ppb).

Alkenes exhibited two peaks at approximately 9:00 in the morning (4.7 ppb) and 17:00 at night (6.7 ppb), and the morning peak appeared at a time similar to that of the aromatics. Distinct from C_2–C_5 alkanes, the mean value of alkenes in the daytime (4.7 ppb) was slightly higher than that at night (4.0 ppb). This shall be attributed to a stronger emission of them in daytime than nighttime, since there are stronger dilutions and sinks in daytime than nighttime.

Diurnal variation was found for the aromatics: an obvious peak value (7.5 ppb) occurred at 8:00 in the morning, followed by a

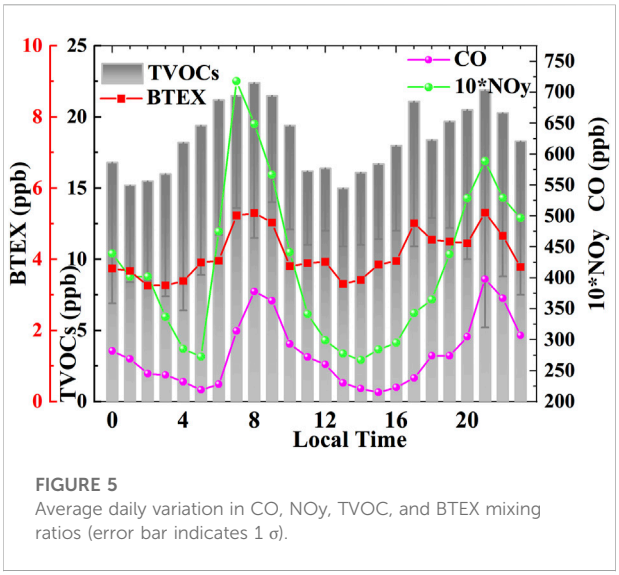

FIGURE 5
Average daily variation in CO, NOy, TVOC, and BTEX mixing ratios (error bar indicates 1 σ).

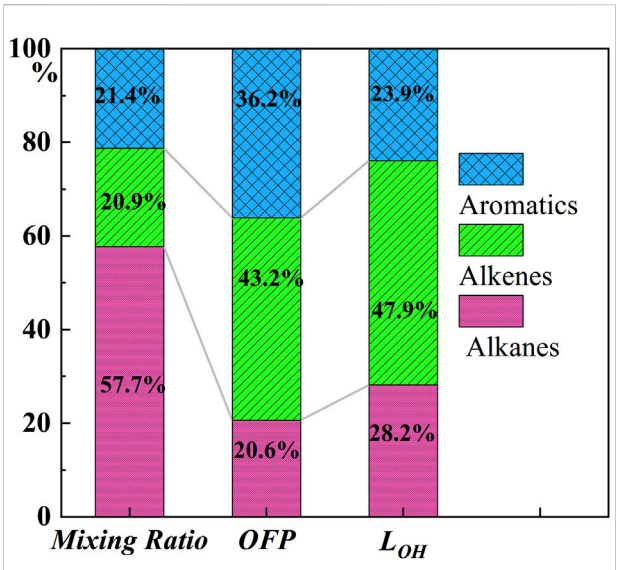

FIGURE 6
Relative contributions of mixing ratios, OFP, and LOH activities of alkanes, alkenes, and aromatics.

gradual decrease, reaching a trough (3.7 ppb) at 13:00–14:00 and then increasing up to a second peak (5.5 ppb) at 17:00. The daytime concentration of aromatics (4.8 ppb) was also slightly higher than that (4.3 ppb) at night. The morning peak of C_2–C_5 alkanes appeared earlier and lasted longer, whereas the morning peak of aromatic hydrocarbons appeared sharply later on.

Generally, the diurnal variations were lower in C_6–C_{12} alkanes and alkenes than in aromatics and C_2–C_5 alkanes, in terms of their amplitudes in diurnal variations. For total VOCs (TVOCs), diurnal variation was found: two peak values of 22.4 ppb at 8:00 and 21.9 ppb at 21:00, and two trough values of 15.2 ppb at 2:00 and 15.0 ppb were found at 13:00. During the day, the mixing ratios of TVOCs decreased and reached their lowest values at approximately 13:00. The higher MLD and wind speed in daytime would promote the convective and advective dilution of the pollutants. Therefore, the timing of diurnal variation of distinct VOC species differed slightly as a result of the differences in emission sources, in addition to varied species activity, and sink. Notably, freight vehicles have been restricted on roads in urban Lhasa from 5:00 to 21:00 every day, which may have affected the diurnal variations in some species of VOCs, for example the night peaks of them. This requires further exploration.

Figure 5 depicts the average diurnal variations in CO, NOy, BTEX, and TVOCs mixing ratios. The diurnal change of BTEX exhibited a pattern consistent with that of TVOCs; a significant correlation (R = 0.86, p < 0.01, Supplementary Table S1) was observed. Except for a high peak at approximately 17:00 for BTEX and TVOCs, a similar variation pattern was observed for the BTEX (TVOCs), CO, and NOy mixing ratios. CO mainly originates from incomplete combustion (Shao et al., 2020) and is a tracer of combustion emissions. The CO, NOy, and BTEX (TVOCs) mixing ratios reached peaks during the morning rush hour period at 8:00, which was likely due to vehicle exhaust emissions. During the evening rush hours, a peak for BTEX (TVOCs) was also observed at approximately 17:00, but no peaks for CO and NOy were noticeable. Another distinct nighttime peak appeared at 21:00 for CO, NOy, and BTEX (TVOCs), which may be primarily due to high vehicle emissions associated with the habits of local people and the end of the driving restrictions on freight vehicles (Huang et al., 2011b). The similarity of the CO, NOy, BTEX, and TVOC mixing ratios during the 2:00–4:00 and 13:00–14:00 periods indicated that the pollutants could not easily accumulate in the Lhasa valley at night in May because the geographical scale of urban Lhasa is small and the air above is easily diluted and replaced by fresh and clean surrounding air.

In addition to source emissions, meteorological factors also have an impact on the diurnal change of pollutants. Pearson correlations of meteorological parameters with the hourly mean NOy, CO, and various classes of VOCs mixing ratios are showed in Supplementary Table S2. In addition to C_6–C_{12} alkanes, other pollutant concentrations, including TVOCs, were significantly and negatively correlated with changes in wind speed, which indicated a feature of local emission. MLD seemed to have a complex influence on different pollutants. MLD showed significant and negative correlations with NOy, C_2–C_5 alkanes and TVOCs, significant and positive correlations with alkenes and C_6–C_{12} alkanes, but insignificant with CO, BTEX, and aromatics. Air temperature were significantly and positively correlated with changes in BTEX, aromatics, and NOy, but insignificant with other pollutants.

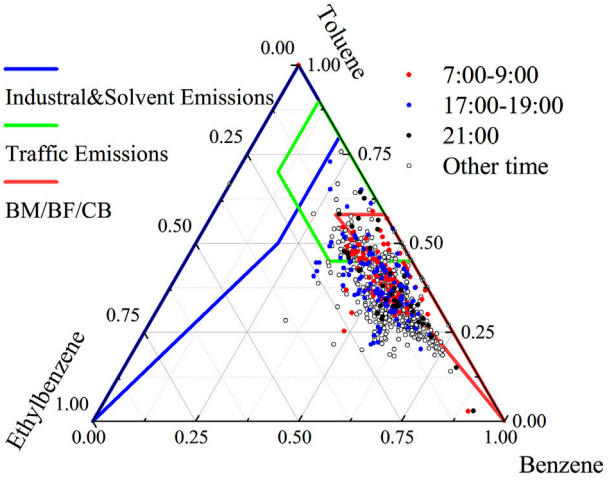

FIGURE 7
Ternary diagram of the normalized benzene, toluene, and ethylbenzene mixing ratios. The wireframes include > 90% of the scatter collected for the three lumped source categories of industrial and solvent emissions, traffic emissions, biomass/biofuel/coal burning (BM/BF/CB).

4.4 *OFP* and OH loss rate of VOC components

The atmospheric lifetimes and reactivity of different species of VOCs varied greatly. Therefore, the concentration alone does not fully reflect the roles of these factors in the processes of atmospheric chemistry; this shortcoming can be overcome to some extent by considering the properties of chemical reactivity, such as *OFP* and OH loss rate (Bufalini et al., 1976).

The total *OFP* of the observed species was 91.7 ppb during the entire observation period, and the *OFP* of alkanes, alkenes, and aromatic hydrocarbons was 18.9, 39.6, and 33.2 ppb with contributions of 20.6%, 43.2%, and 36.2%, respectively. The total L_{OH} was 3.1 s^{-1} for all observed species, with values of 0.9, 1.5, and 0.7 s^{-1} and contributions of 28.2%, 47.9%, and 23.9% for alkanes, alkenes, and aromatic hydrocarbons, respectively. As illustrated in Figure 6, alkanes were the most abundant components (57.7%) in the total VOCs but had the lowest contributions to OFP (20.6%) and L_{OH} (28.2%), whereas alkenes had the highest contributions to *OFP* (43.2%) and L_{OH} (47.9%), which indicated higher activity and hydroxyl radical reaction rate for alkenes than for alkanes in Lhasa. Aromatics contributed 36.2% to the *OFP* and 23.9% to L_{OH}. The top 10 VOC species were ranked in terms of concentration, *OFP*, and L_{OH}, respectively, and are shown in Table 3. Although ethane and benzene had high concentration proportions, their *OFP* and L_{OH} were not ranked in the top 10 due to their relatively weak reactivity. In terms of the control of ozone generation, the priorities for controlling VOC species are isobutylene, m/p-xylene, toluene, o-xylene, propene, hexene, cis-2-butene, isoprene, isobutane, and n-undecane, which accounted for 76.3% of *OFP*.

4.5 Source apportionments through BTEX correlation ratios and positive matrix factorization analysis

4.5.1 BTEX components ternary analysis

The main emission sources of benzene are combustion processes, including biomass, biofuel, or coal burning (BM/BF/CB). The proportion of benzene in BM/BF/CB sources is higher than that of toluene, whereas the proportion of benzene in motor vehicle emissions is generally lower than that of toluene (Barletta et al., 2005). In this study, a ternary diagram of benzene, toluene, and ethylbenzene mixing ratios was used to determine the predominant emission sources (Zhang et al., 2016), and the results are presented in Figure 7. In the diagram, the benzene, toluene, and ethylbenzene mixing ratios are normalized. The distribution of benzene, toluene, and ethylbenzene mostly occurred in the biomass burning and transportation emission areas, and the BM/BF/CB areas accounted for a larger proportion of the emissions than the areas with industrial and solvent and traffic emissions. However, most the scattering dots did not fall within the wireframes, which indicated different emission spectrums on the plateau from that in the area with low altitudes. Studies on aerosols and other air pollutants in Lhasa have demonstrated the considerable impact of biomass burning related to religious activities and regional transport (Cui et al., 2018; Duo et al., 2018). As displayed in Figure 8, during rush hours (7:00–9:00 and 17:00) and nighttime peak periods (21:00), which were expected to be associated with higher traffic-related emissions, the emission levels did not differ with those of other time periods. Because the patterns of benzene, toluene, and ethylbenzene distribution between BM/BF/CB and traffic emissions should differ, traffic emissions were expected to have been a dominant influence on ambient VOCs in Lhasa since disorderly incense and biomass burning activities have been greatly restrained in protecting the environment in recent years.

4.5.2 BTEX components correlation

The ratio of distinct VOC species can be used to determine the predominant pollution sources on the basis of the difference in the characteristic species of VOCs in the corresponding sources. The toluene-to-benzene (T/B) ratio has often been used to identify the sources of pollutants (Niu et al., 2012; Y. Zhang et al., 2013). The T/B ratio of ≤2 indicates that the main sources are vehicle exhaust emissions or biomass burning. A T/B ratio of >2 indicates that the pollutants were emitted from other sources, and a T/B ratio of 4.25–10.00 strongly implies the influence of industrial emission sources (Barletta et al., 2008; Niu et al., 2012; Kumar et al., 2018). A study on pollution sources revealed that the T/B ratio for biomass combustion was

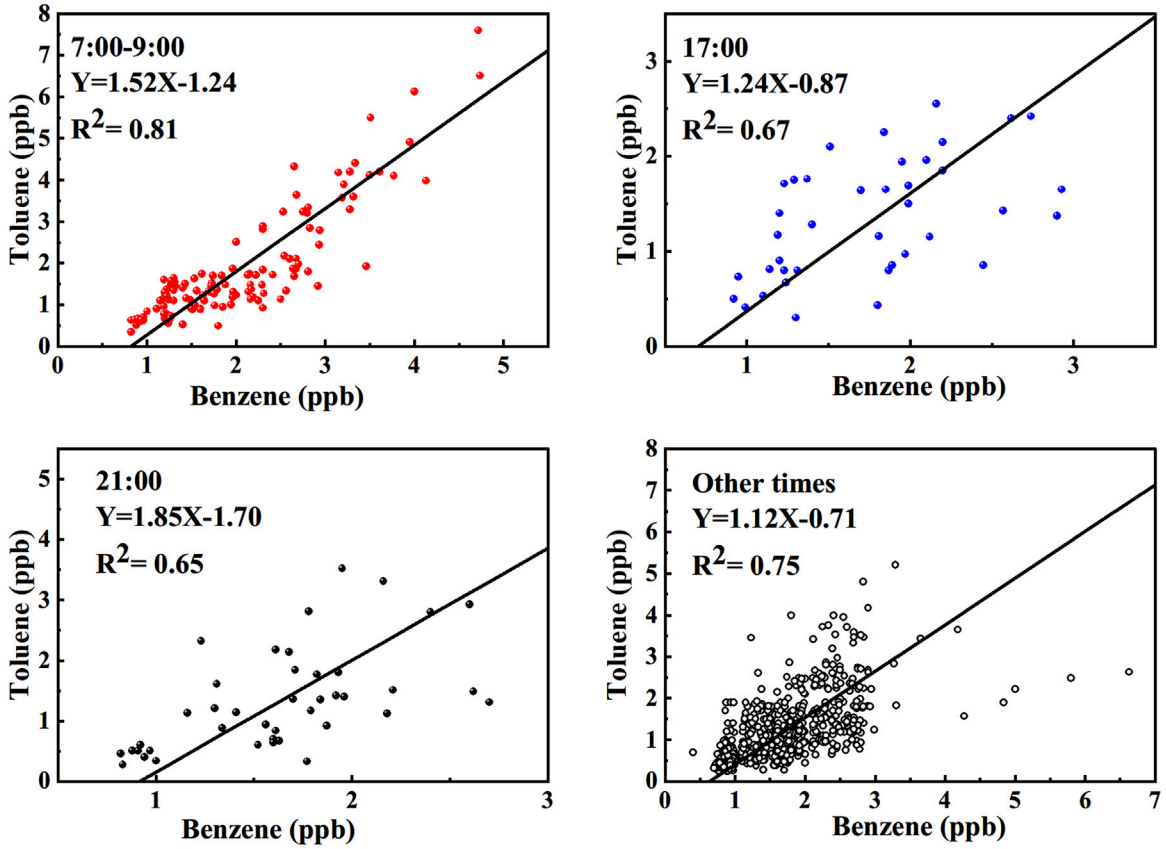

FIGURE 8
Correlations between benzene and toluene at distinct time periods ($p < 0.05$).

approximately 0.5 or even lower, whereas that for motor vehicle emissions was nearly 1.7 (Barletta et al., 2005).

The correlations between toluene and benzene mixing ratios in distinct periods are depicted in Figure 8. All the correlations were significant ($R^2 > 0.6$ and $p < 0.05$), indicating that the pollutants were emitted from the same or similar sources. The slopes (T/B ratio) of the fitting curves were 1.52 at 7:00–9:00 and 1.85 at 21:00, both of which are higher than the T/B ratio values of 1.24 at 17:00 and 1.12 during other periods. The emissions from motor vehicles were associated with higher T/B ratios than biomass combustion (Zhang et al., 2013); thus, the results reflected more traffic-related emissions during the periods of 7:00–9:00 and 21:00.

4.5.3 Air mass age analysis

M/p-xylene and ethylbenzene usually have a common source, but the reaction rate of m/p-xylene with hydroxyl radicals is nearly three times higher than that of ethylbenzene, and the ratio of m/p-xylene to ethylbenzene (X/E) gradually decreases as the photochemical reaction proceeds; hence, the X/E can be used as an indicator of the degree of air mass aging (Huang et al., 2015; Han et al., 2020).

Figure 9 displays the average diurnal variations in benzene, toluene, m/p-xylene, and ethylbenzene mixing ratios, as well as in T/B and X/E ratios. Benzene, toluene, ethylbenzene, and m/p-xylene mixing ratios had peak values and high T/B and X/E ratios were found from 7:00 to 9:00 in the morning, which coincided with the morning rush hours. Similar patterns were observed during other times of peak traffic at approximately 17:00 and 21:00. Trough values were observed at 13:00–14:00, as well as low T/B and X/E ratios. The peak and trough values of toluene and m/p-xylene mixing ratios were more obvious than those of benzene and ethylbenzene mixing ratios because toluene and m/p-xylene have higher photochemical reactivity. The average diurnal variation in T/B ratios was 0.5–0.9, which is close to the values obtained at the rural site of Shangdianzi (Han et al., 2020). The low T/B ratio indicates the crucial influence of biomass combustion. The average diurnal variation in the X/E ratio was 0.8–2.0, which was higher than the ratios obtained at Shangdianzi and Beijing (Han et al., 2020).

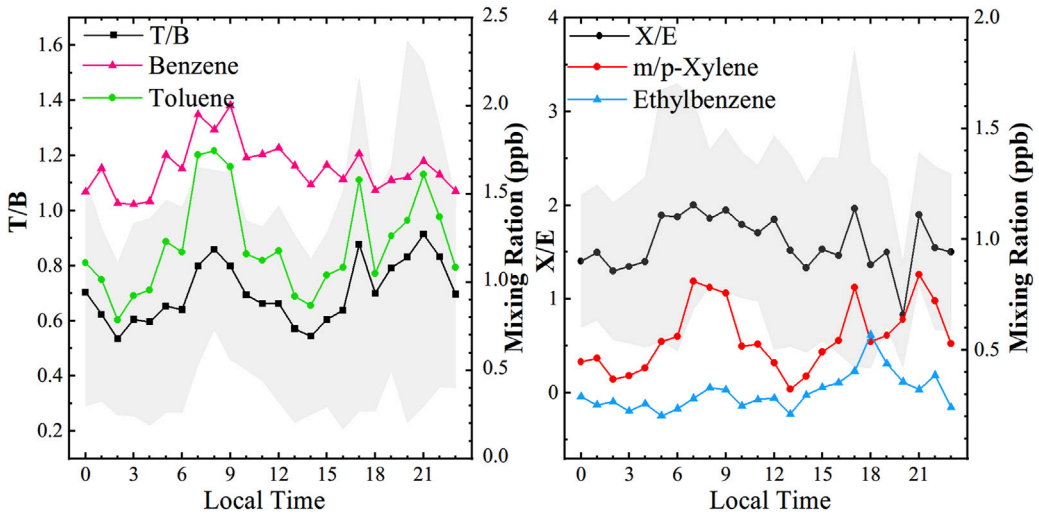

FIGURE 9
Average diurnal variations in benzene, toluene, m/p-xylene, and ethylbenzene mixing ratios and T/B and X/E ratios.

4.5.4 Volatile organic compounds source apportionment by positive matrix factorization

The result of VOCs source apportionment by PMF model analysis was shown in Figure 10 (left panel), in which six factors' resolutions with a stable Q value were identified as the dominant source of VOCs in urban Lhasa city. The average diurnal variations in each source concentration were shown in Figure 10 (right panel).

The first factor was characterized by the strong presence of ethane, ethene, n-butane, butene, 2-methylpentan, 3-methylpentan, aromatics like toluene, benzene, xylene. These species are mainly from traffic emissions and gasoline evaporation (Li et al., 2020). Therefore, this source is identified as gasoline automobile emissions. As can be seen in Figure 10 (right panel), the average diurnal variation in gasoline automobile emissions presented peaks at 7:00–9:00, 17:00 and 21:00, which peaks reflected the influences of traffic rush hours.

Factor 2 was distinguished by a high percentage of alkanes with high carbon number, such as n-decane and n-undecane, which were abundant in diesel vehicle exhaust (Zhang et al., 2021). Ethane, ethene, propene and benzene, ethyl benzene and xylene were also rich in this factor with high percentages. These species are associated with diesel vehicular emissions. Thus, Factor 2 was featured as diesel vehicle exhaust. Due to restrictions in freight vehicles in the daytime, the VOCs emissions contribution from diesel vehicles might be lower during the day than at night. In addition, lower MLD also increased the level of the corresponding VOCs mixing ratio at night (Figure 10, right).

Factor 3 was characterized by high levels of aromatics (xylene, styrene, ethylbenzene, and benzene). Toluene, ethylbenzene, xylene, and 1,3,5-trimethylbenzene are used as organic solvents in various industries and can be regarded as indicator species for solvent volatilization. Alkanes like methylpentane, methylheptane, n-decane, n-undecane, are also widely used as nonpolar solvents (Yuan et al., 2010; Song et al., 2018). Therefore, source 3 was identified as solvents usage. Because solvent usage often occurred in daytime and the solvents have a more volatility under higher temperature, VOCs concentrations from solvents usage contribution were higher during the day than at night. The change of BTEX and aromatics mixing ratios were significantly and positively correlated with air temperature in Supplementary Table S2 also supported this conclusion.

Factor 4 was distinguished by high percentages of ethane, ethene, butane and butene which could be emitted from incomplete combustion of biomass (Ling et al., 2011; Li et al., 2020). In addition, benzene accounts for a high load with a contribution of 44%. The concentration of benzene was higher than toluene in this factor, which is consistent with the characteristics of biomass combustion. There was high level of VOCs from biomass burning in the morning (Figure 10, right), which may partly be related to the more activities in incense burning in the forenoon. There had a distinct feature with a flat curve and with relatively high concentrations for its diurnal change in this factor, which indicates that biomass burning in Lhasa is still common since biomass fuel is the main traditional fuel in the plateau. The less variation in diurnal changes might

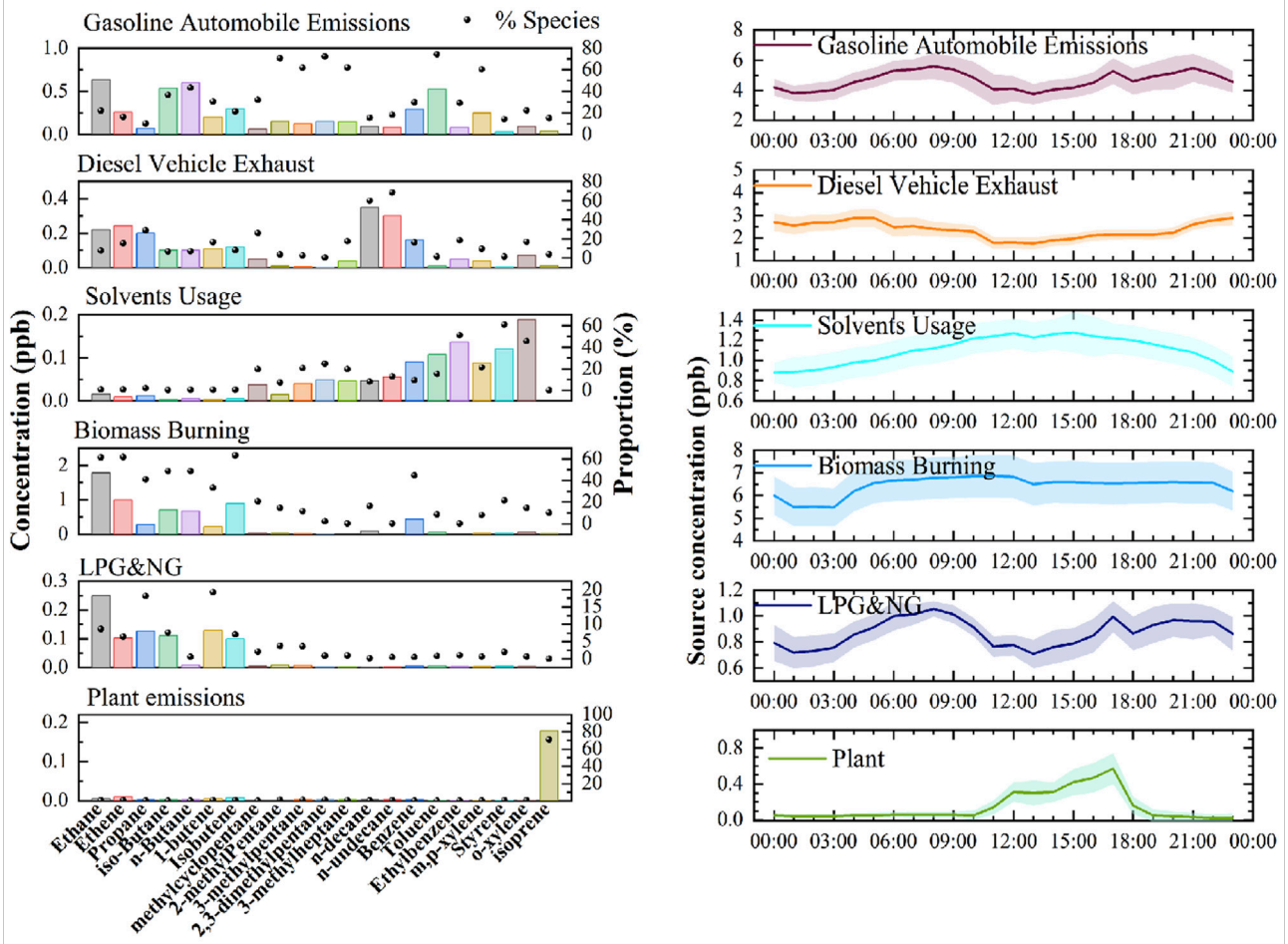

FIGURE 10
The resolved factor profiles (left) by PMF analysis and the corresponding diurnal variations in each source's mixing ratio (right).

also tell us that the influence of biomass burning there is of regional characteristics.

Factor 5 was distinguished by high percentages of C_2-C_4 alkanes, propane, i-butane, and n-butane are regarded as the major compounds of liquid petroleum gas (LPG) and natural gas (NG) (Shao et al., 2016; Han et al., 2021). LPG and NG both play important roles in domestic catering and traffic. Thus, source 5 is assigned to LPG & NG usage. The diurnal variation of this source was similar to motor vehicles, except no obvious peak at 21:00. Public transportation in Lhasa has promoted the fuel conversion from oil to natural gas since 2014. Since this diurnal variation showed a similar pattern with factor 1, it reflected more contribution from traffic emissions than others.

The source profile of factor 6 was dominated by isoprene, which contributed 71% to the total isoprene. Isoprene is a typical tracer for plant emission, but traffic emissions and combustion also emit a small amount of isoprene (Borbon et al., 2001). Plants emit more isoprene during the day with solar radiation and higher temperature than at night. Therefore, the diurnal variation in plant emission showed typical feature with high values in the daytime and low at night (Song et al., 2018; Li et al., 2020). Our result in factor 6 was consistent with this natural law. Accordingly, factor 6 was identified as plant emission.

Figure 11 showed the contribution of each source to the concentration, L_{OH} and *OFP*. Traffic emissions contributed 44.5%, including gasoline automobile emissions (30.3%), diesel vehicle exhausts (14.2%), to TVOCs; 41.6% to L_{OH} and 47.4% to *OFP*. In addition, LPG&NG related emissions contributed 5.7% to TVOCs, including cooking fuel emissions, gas station volatilization, natural gas bus and taxi emissions, and so on. Biomass burning contributed 41.3% to TVOCs, 26.4% to L_{OH} and 29.7% to *OFP*. Overall, air quality in urban Lhasa city was strongly affected by motor vehicle emissions now, exceeding the biggest contribution of biomass burning from the result of Yu et al. (2022). Plant emissions contributed only 1.5% to TVOCs, but relatively high proportions to L_{OH} (14.6%) and *OFP* (4.8%),

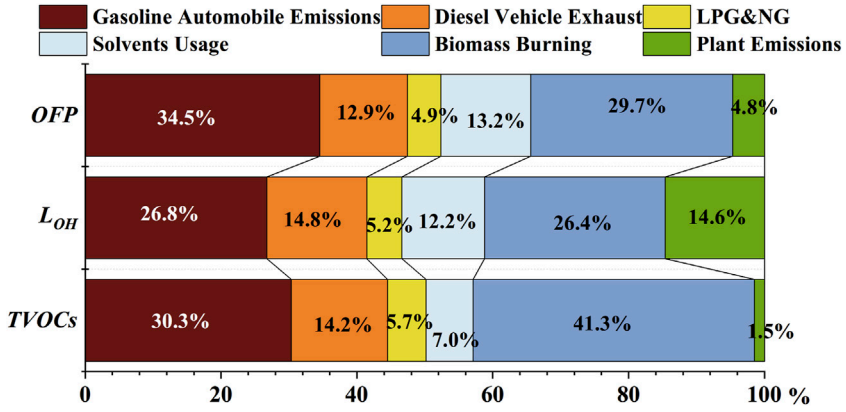

FIGURE 11
The contribution of each source to TVOCs, L_{OH} and *OFP*.

TABLE 4 Health risks of BTEX in Lhasa.

Species	*EC* (μg/m^3)	*RfC* (mg/m^3)	*IUR* (m^3/μg)	*HQ*	*Risk*
Benzene	0.57	0.03	7.80×10^{-6}	1.91×10^{-2}	4.47×10^{-6}
Toluene	0.49	5.00	-	9.88×10^{-5}	-
Ethylbenzene	0.14	1.00	-	1.38×10^{-4}	-
m/p-Xylene	0.26	0.10	-	2.63×10^{-3}	
o-Xyelene	0.23	0.10	-	2.29×10^{-3}	
BTEX	-	-	-	HI (0.02)	4.47×10^{-6}

EC is the exposure concentration, *RfC* is the inhaled carcinogenic risk concentration, *IUR* is the inhalation unit risk.

due to the high reactivity of isoprene. The contribution of plant emissions was similar with the other studies (Yu et al., 2001; Yu et al., 2022).

5 Risk assessment on BTEX

Benzene is the most toxic compound among them and has been listed as a class I carcinogen for human beings by the International Agency for Research on Cancer. Other BTEX compounds have also been identified as harmful air pollutants (Yang et al., 2017; Zhang et al., 2017; Abd Hamid et al., 2020). In 1983, the US National Academy of Sciences proposed a four-step approach to health risk assessment, which consists of hazard identification, dose–response assessment, exposure assessment, and risk characterization (National Research Council Committee on the Institutional Means for Assessment of Risks to Public Health, 1983); this is now an internationally accepted approach. Many of the VOCs recorded in this study have their own toxicity risks (Shu et al., 2019; Lyu et al., 2020), and benzene also has a carcinogenic risk.

The US EPA suggests that the acceptable carcinogenic risk for adults is 1×10^{-6} (US EPA, 2009). For noncarcinogenic risk assessment, an HQ of greater than 1 for a contaminant implies a noncarcinogenic risk, and an HQ of less than or equal to 1 implies a small or negligible risk.

The EC, inhalation RfC, inhalation unit risk concentration (IUR), noncarcinogenic risk HQ, noncarcinogenic risk HI, and risk value of BTEX in Lhasa are detailed in Table 4. The HQ of benzene was the highest, followed by those of m/p-xylene and o-xylene. The total HI of BTEX was 0.02 during the observation period, which was lower than the value of 1 determined by the US EPA and lower than the noncarcinogenic risk index of Xianghe (Yang et al., 2019). The benzene risk value was 4.47×10^{-6}, much lower than Xianghe in moderate pollution days and heavy pollution days, however higher than Xianghe in clean days. The US EPA recommended value is 1×10^{-6}, indicating the potential health hazard of benzene in the atmosphere of Lhasa city.

6 Conclusion

In this study, online measurement of VOCs in urban Lhasa city was conducted in May 2019 for the first time, and a total of 49 VOCs were observed. The mean mixing ratio of the VOCs was 21.5 ± 18.6 ppb, of which alkanes accounted for 12.4 ± 11.2 ppb (57.7% of the total VOCs), aromatic hydrocarbons accounted for 4.6 ± 3.5 ppb (21.4%), and alkenes accounted for 4.5 ± 2.8 ppb (20.9%). VOC mixing ratios showed a noticeable diurnal variation, with two obvious peaks; one during the morning rush hours (7:00–9:00) and another at approximately 21:00. Another minor peak was observed at 17:00. A trough value appeared at 13:00–14:00 under conditions of high MLD and strong winds. TVOCs, BTEX, NO_y and CO mixing ratios exhibited similar diurnal variations, with two peak values appearing at 7:00–9:00 and 21:00, each indicating a distinct spike in traffic emissions.

The total *OFP* was 91.7 ppb, among which alkanes, alkenes, and aromatic hydrocarbons accounted for 20.6%, 43.2%, and 36.2%, respectively. The total ·OH loss rate was 3.1 s^{-1}, of which alkanes, alkenes, and aromatic hydrocarbons contributed 28.2%, 47.9%, and 23.9%, respectively. From the viewpoint of ozone generation control, the priorities for controlling VOC species were isobutylene, m/p-xylene, toluene, o-xylene, propene, hexene, cis-2-butene, isoprene, isobutane, and n-undecane, which accounted for 76.3% of the *OFP*.

The PMF analysis resolved six source factors, including gasoline automobile emissions, diesel vehicle exhaust, LPG & NG usage, solvent usage, biomass combustion, and plant emission. Their contributions to TVOCs were 30.3%, 14.2%, 5.7%, 7.0%, 41.3% and 1.5%, respectively. Their contributions to L_{OH} were 26.8%, 14.8%, 5.2%, 12.2%, 26.4% and 14.6%, respectively. Their contributions to *OFP* were 34.5%, 12.9%, 4.9%, 13.2%, 29.7% and 4.8%, respectively. Overall, air quality in urban Lhasa city was strongly affected by motor vehicle emissions now.

The total noncarcinogenic risk HI of BTEX was 0.02, which was far below the hazard threshold of 1 recognized by the US EPA. The carcinogenic risk of benzene was 4.47×10^{-6}, which was higher than the accepted carcinogenic risk threshold of 1×10^{-6}, indicating a potential risk that should be further considered.

Data availability statement

The raw data supporting the conclusions of this article will be made available by the authors, without undue reservation.

Author contributions

CY and WL designed the research. YW and TZ performed the experiments. DY and BY contributes analysis on meteorological results. SG analyzed the VOCs data and wrote the manuscript. All authors contributed to manuscript revision and read and approved the submitted version.

Funding

This study was funded by the National Natural Science Foundation of China (grant nos. 21876214, 91744206).

Acknowledgments

We thank the support of the project of field campaigns of the atmospheric chemistry over the Tibetan Plateau: measurement, processing, and the impacts on climate and air quality (referred as @Tibet field campaigns).

Conflict of interest

The authors declare that the research was conducted in the absence of any commercial or financial relationships that could be construed as a potential conflict of interest.

Publisher's note

Supplementary material

The Supplementary Material for this article can be found online at: https://www.frontiersin.org/articles/10.3389/fenvs.2022.941100/full#supplementary-material

References

Abd Hamid, H. H., Latif, M. T., Uning, R., Nadzir, M. S., Khan, M. F., Ta, G. C., et al. (2020). Observations of BTEX in the ambient air of Kuala Lumpur by passive sampling. *Environ. Monit. Assess.* 192 (6), 342. doi:10.1007/s10661-020-08311-4

An, J., Wang, J., Zhang, Y., and Zhu, B. (2017). Source apportionment of volatile organic compounds in an urban environment at the Yangtze River Delta, China. *Arch. Environ. Contam. Toxicol.* 72 (3), 335–348. doi:10.1007/s00244-017-0371-3

Atkinson, R., and Arey, J. (2003). Atmospheric degradation of volatile organic compounds. *Chem. Rev.* 103 (12), 4605–4638. doi:10.1021/cr0206420

Bai, Y., Bai, Z. P., and Li, W. (2016). Characteristics and sources analysis of atmospheric volatile organic compounds in the Tibetan Plateau. *Acta Sci. Circumstantiae* 36 (06), 2180–2186. (In Chinese). doi:10.13671/j.hjkxxb.2016.0008

Bai, Y. F., Lyu, X. B., Pingcuo, , Zhang, C., and Buduo, (2018). Assessment and study of environmental air quality of 2014-2016 in Lhasa. *Meteo. Sci.Technol.* 46 (06), 212–217+224. (In Chinese). doi:10.19517/j.1671-6345.20170731

Barletta, B., Meinardi, S., Sherwood Rowland, F., Chan, C. Y., Wang, X., Zou, S., et al. (2005). Volatile organic compounds in 43 Chinese cities. *Atmos. Environ. X.* 39 (32), 5979–5990. doi:10.1016/j.atmosenv.2005.06.029

Barletta, B., Meinardi, S., Simpson, I. J., Zou, S., Rowland, F. S., and Blake, D. R. (2008). Ambient mixing ratios of nonmethane hydrocarbons (NMHCs) in two major urban centers of the Pearl River Delta (PRD) region: Guangzhou and Dongguan. *Atmos. Environ. X.* 42 (18), 4393–4408. doi:10.1016/j.atmosenv.2008.01.028

Benedict, K. B., Prenni, A. J., El-Sayed, M. M. H., Hecobian, A., Zhou, Y., Gebhart, K. A., et al. (2020). Volatile organic compounds and ozone at four national parks in the southwestern United States. *Atmos. Environ. X.* 239, 117783. doi:10.1016/j.atmosenv.2020.117783

Borbon, A., Fontaine, H., Veillerot, M., Locoge, N., and Guillermo, R. (2001). An investigation into the traffic-related fraction of isoprene at an urban location. *Atmos. Environ. X.* 35 (22), 3749–3760. doi:10.1016/S1352-2310(01)00170-4

Bufalini, J. J., Walter, T. A., and Bufalini, M. M. (1976). Ozone formation potential of organic compounds. *Environ. Sci. Technol.* 28 (9), 908–912. doi:10.1021/es60120a016

Cai, C., Geng, F., Tie, X., Yu, Q., and An, J. (2010). Characteristics and source apportionment of VOCs measured in Shanghai, China. *Atmos. Environ. X.* 44 (38), 5005–5014. doi:10.1016/j.atmosenv.2010.07.059

Carter, W. P. L. (2010). *Updated maximum incremental reactivity scale and hydrocarbon bin reactivities for regulatory applications*. Retrieved from: https://intra.engr.ucr.edu/~carter/.

Chen, S., Zheng, X. D., Lin, W. L., Zhang, Y., Dawa, Z. X., and Qi, D. L. (2015). Observational study on the ground-based UVI at dangxiong of Tibet. *J. Appl. Meteor Sci.* 26 (04), 482–491. (In Chinese). doi:10.11898/1001-7313.20150410

Chen, P., Kang, S., Li, C., Li, Q., Yan, F., Guo, J., et al. (2018). Source apportionment and risk assessment of atmospheric polycyclic aromatic hydrocarbons in Lhasa, Tibet, China. *Aerosol Air Qual. Res.* 18 (5), 1294–1304. doi:10.4209/aaqr.2017.12.0603

Cheng, X., Zhang, L. H., Li, H., Zhang, W. Q., Chen, X., Ji, Y. Y., et al. (2019). Atmospheric VOCs in a typical urban area of Beijing: Pollution characterization and health risk during the period of the first forum on the Belt and Road Initiatives. *Acta Sci. Circumstantiae* 39 (09), 2839–2851. (In Chinese). doi:10.13671/j.hjkxxb.2019.0231

Constable, J. V. H., Guenther, A. B., Schimel, D. S., and Monson, R. K. (2001). Modelling changes in VOC emission in response to climate change in the continental United States. *Glob. Chang. Biol.* 5 (7), 791–806. doi:10.1046/j.1365-2486.1999.00273.x

Cui, Y. Y., Liu, S., Bai, Z., Bian, J., Li, D., Fan, K., et al. (2018). Religious burning as a potential major source of atmospheric fine aerosols in summertime Lhasa on the Tibetan Plateau. *Atmos. Environ. X.* 181, 186–191. doi:10.1016/j.atmosenv.2018.03.025

Dai, H., Jing, S., Wang, H., Ma, Y., Li, L., Song, W., et al. (2017). VOC characteristics and inhalation health risks in newly renovated residences in Shanghai, China. *Sci. Total Environ.* 577, 73–83. doi:10.1016/j.scitotenv.2016.10.071

Duo, B., Cui, L., Wang, Z., Li, R., Zhang, L., Fu, H., et al. (2018). Observations of atmospheric pollutants at Lhasa during 2014–2015: Pollution status and the influence of meteorological factors. *J. Environ. Sci.* 63, 28–42. doi:10.1016/j.jes.2017.03.010

Gao, J. B., Xiao, Z. M., Xu, H., Li, L. W., Li, P., Tang, M., et al. (2021). Characterization and source apportionment of atmospheric VOCs in Tianjin in 2019. *Environ. Sci.* 42 (01), 55–64. (In Chinese). doi:10.13227/j.hjkx.202006257

Guo, H., Cheng, H. R., Ling, Z. H., Louie, P. K. K., and Ayoko, G. A. (2011). Which emission sources are responsible for the volatile organic compounds in the atmosphere of Pearl River Delta? *J. Hazard. Mat.* 188 (1–3), 116–124. doi:10.1016/j.jhazmat.2011.01.081

Han, C., Liu, R. R., Luo, H., Li, G. Y., Ma, S. T., Chen, J. Y., et al. (2019). Pollution profiles of volatile organic compounds from different urban functional areas in Guangzhou China based on GC/MS and PTR-TOF-MS: Atmospheric environmental implications. *Atmos. Environ. X.* 214, 116843. doi:10.1016/j.atmosenv.2019.116843

Han, T. T., Ma, Z. Q., Xu, W. Y., Qiao, L., Li, Y. R., He, D., et al. (2020). Characteristics and source implications of aromatic hydrocarbons at urban and background areas in Beijing, China. *Sci. Total Environ.* 707, 136083. doi:10.1016/j.scitotenv.2019.136083

Han, T. T., Ma, Z. Q., Li, Y. R., Pu, W. W., Wu, J., Li, Z. M., et al. (2021). Chemical characteristics and source apportionments of volatile organic compounds (VOCs) before and during the heating season at a regional background site in the North China Plain. *Atmos. Res.* 262, 105778. doi:10.1016/j.atmosres.2021.105778

Huang, C., Chen, C. H., Li, L., Cheng, Z., Wang, H. L., Huang, H. Y., et al. (2011a). Emission inventory of anthropogenic air pollutants and VOC species in the Yangtze River Delta region, China. *Atmos. Chem. Phys.* 11 (9), 4105–4120. doi:10.5194/acp-11-4105-2011

Huang, Y., Ho, S. S. H., Ho, K. F., Lee, S. C., Yu, J. Z., and Louie, P. K. K. (2011b). Characteristics and health impacts of VOCs and carbonyls associated with residential cooking activities in Hong Kong. *J. Hazard. Mat.* 186 (1), 344–351. doi:10.1016/j.jhazmat.2010.11.003

Huang, C., Wang, H. L., Li, L., Wang, Q., Lu, Q., de Gouw, J. A., et al. (2015). VOC species and emission inventory from vehicles and their SOA formation potentials estimation in Shanghai, China. *Atmos. Chem. Phys.* 15 (19), 11081–11096. doi:10.5194/acp-15-11081-2015

Jia, C., Mao, X., Huang, T., Liang, X., Wang, Y., Shen, Y., et al. (2016). Non-methane hydrocarbons (NMHCs) and their contribution to ozone formation potential in a petrochemical industrialized city, Northwest China. *Atmos. Res.* 169, 225–236. doi:10.1016/j.atmosres.2015.10.006

Klinger, L. F., Li, Q. J., Guenther, A. B., Greenberg, J. P., Baker, B., and Bai, J. H. (2002). Assessment of volatile organic compound emissions from ecosystems of China. *J. Geophys. Res.* 107, 4603–4619. doi:10.1029/2001jd001076

Kumar, A., Singh, D., Kumar, K., Singh, B. B., and Jain, V. K. (2018). Distribution of VOCs in urban and rural atmospheres of subtropical India: Temporal variation, source attribution, ratios, OFP and risk assessment. *Sci. Total Environ.* 613–614, 492–501. doi:10.1016/j.scitotenv.2017.09.096

Li, J., Xie, S., Zeng, L. M., Li, L., Li, Y., and Wu, R. (2015). Characterization of ambient volatile organic compounds and their sources in Beijing, before, during, and after Asia-Pacific Economic Cooperation China 2014. *Atmos. Chem. Phys.* 15 (14), 7945–7959. doi:10.5194/acp-15-7945-2015

Li, H., He, Q., Song, Q., Chen, L., Song, Y., Wang, Y., et al. (2017). Diagnosing Tibetan pollutant sources via volatile organic compound observations. *Atmos. Environ. X.* 166, 244–254. doi:10.1016/j.atmosenv.2017.07.031

Li, M., Zhang, Q., Zheng, B., Tong, D., Lei, Y., Liu, F., et al. (2019). Persistent growth of anthropogenic non-methane volatile organic compound (NMVOC) emissions in China during 1990–2017: Drivers, speciation and ozone formation potential. *Atmos. Chem. Phys.* 19, 8897–8913. doi:10.5194/acp-19-8897-2019

Li, Q., Su, G., Li, C., Liu, P., Zhao, X., Zhang, C., et al. (2020). An investigation into the role of VOCs in SOA and ozone production in Beijing, China. *Sci. Total Environ.* 720, 137536. doi:10.1016/j.scitotenv.2020.137536

Lin, W. L., Xu, X. B., Zheng, X. D., Dawa, J., Baima, C., and Ma, J. (2015). Two-year measurements of surface ozone at Dangxiong, a remote highland site in the Tibetan Plateau. *J. Environ. Sci.* 31, 133–145. doi:10.1016/j.jes.2014.10.022

Lin, W. L., Zhu, T., Song, Y., Zou, H., Tang, M. Y., Tang, X. Y., et al. (2008). Photolysis of surface O_3 and production potential of OH radicals in the atmosphere over the Tibetan Plateau. *J. Geophys. Res.* 113, D02309. doi:10.1029/2007JD008831

Ling, Z. H., Guo, H., Cheng, H. R., and Yu, Y. F. (2011). Sources of ambient volatile organic compounds and their contributions to photochemical ozone formation at a site in the Pearl River Delta, southern China. *Environ. Pollut.* 159, 2310–2319. doi:10.1016/j.envpol.2011.05.001

Liu, Y., Shao, M., Zhang, J., Fu, L., and Lu, S. (2005). Distributions and source apportionment of ambient volatile organic compounds in Beijing city, China. *J. Environ. Sci. Health Part A* 40 (10), 1843–1860. doi:10.1080/10934520500182842

Liu, Y., Shao, M., Lu, S., Chang, C. C., Wang, J. L., and Chen, G. (2007). Volatile organic compound (VOC) measurements in the Pearl River Delta (PRD) region, China. *Atmos. Chem. Phys.* 7 (6), 1531–1545. doi:10.5194/acp-8-1531-2008

Liu, J., Li, J., Lin, T., Liu, D., Xu, Y., Chaemfa, C., et al. (2013). Diurnal and nocturnal variations of PAHs in the Lhasa atmosphere, Tibetan Plateau: Implication for local sources and the impact of atmospheric degradation processing. *Atmos. Res.* 124, 34–43. doi:10.1016/j.atmosres.2012.12.016

Liu, Y. F., Kong, L., Liu, X., Zhang, Y., Li, C., Zhang, Y., et al. (2021). Characteristics, secondary transformation, and health risk assessment of ambient volatile organic compounds (VOCs) in urban Beijing, China. *Atmos. Pollut. Res.* 12 (3), 33–46. doi:10.1016/j.apr.2021.01.013

Lyu, X., Guo, H., Wang, Y., Zhang, F., Nie, K., Dang, J., et al. (2020). Hazardous volatile organic compounds in ambient air of China. *Chemosphere* 246, 125731. doi:10.1016/j.chemosphere.2019.125731

National Research Council (US) Committee on the Institutional Means for Assessment of Risks to Public Health (1983). *Risk assessment in the federal government: Managing the process working papers*. Washington DC: National Academies Press US. doi:10.17226/776

Niu, Z. C., Zhang, H., Xu, Y., Liao, X., Xu, L. L., and Chen, J. S. (2012). Pollution characteristics of volatile organic compounds in the atmosphere of haicang district in xiamen city, southeast China. *J. Environ. Monit.* 12, 1145–1152. doi:10.1039/c2em10884d

Norris, G., Duvall, R., Brown, S., and Bai, S. (2014). *EPA positive matrix factorization (PMF) 5.0 fundamentals and user guide*. Washington: U.S. Environmental Protection Agency Office of Research and Development.

Paatero, P., and Tapper, U. (1994). Positive matrix factorization: A non-negative factor model with optimal utilization of error estimates of data values. *Environmetrics* 5, 111–126. doi:10.1002/env.3170050203

Qi, S. H., Zhang, G., Liu, J. H., and Zhang, W. L. (2003). Polycyclic aromatic hydrocarbons (PAHs) of urban atmosphere in Lhasa City and in soil of Lhasa wetland. *Environ. Sci.* 23 (04), 349–352. (In Chinese).

Ran, L., Lin, W. L., Deji, Y. Z., La, B., Tsering, P. M., Xu, X. B., et al. (2014). Surface gas pollutants in Lhasa, a highland city of Tibet – current levels and pollution implications. *Atmos. Chem. Phys.* 14 (19), 10721–10730. doi:10.5194/acp-14-10721-2014

Santos, F. M., Gómez-Losada, Á., and Pires, J. C. M. (2021). Empirical ozone isopleths at urban and suburban sites through evolutionary procedure-based models. *J. Hazard. Mat.* 419, 126386. doi:10.1016/j.jhazmat.2021.126386

Shao, M., Yuan, B., Wang, M., and Zheng, J. Y. (2020). *Volatile organic compounds in the atmosphere: Sources and roles in atmospheric chemistry*. Beijing: SCIENCE PRESS. (In Chinese).

Shao, P., An, J., Xin, J., Wu, F., Wang, J., Ji, D., et al. (2016). Source apportionment of VOCs and the contribution to photochemical ozone formation during summer in the typical industrial area in the Yangtze River Delta, China. *Atmos. Res.* 176, 64–74. doi:10.1016/j.atmosres.2016.02.015

Shu, Y. J., He, M., Ji, J., Huang, H. B., Liu, S. W., and Leung, D. Y. C. (2019). Synergetic degradation of VOCs by vacuum ultraviolet photolysis and catalytic ozonation over Mn-xCe/ZSM-5. *J. Hazard. Mat.* 364, 770–779. doi:10.1016/j.jhazmat.2018.10.057

Song, Y., Shao, M., Liu, Y., Lu, S., Kuster, W., Goldan, P., et al. (2007). Source apportionment of ambient volatile organic compounds in Beijing. *Environ. Sci. Technol.* 41 (12), 4348–4353. doi:10.1021/es0625982

Song, M. D., Tan, Q. W., Feng, M., Qu, Y., Liu, X. G., An, J. L., et al. (2018). Source apportionment and secondary transformation of atmospheric nonmethane hydrocarbons in chengdu, southwest China. *J. Geophys. Res. Atmos.* 123, 9741–9763. doi:10.1029/2018jd028479

Tang, X. Y., Zhang, Y. H., and Shao, M. (2006). *Chemistry of the atmospheric environment*. 3rd Ed. Beijing: Higher Education Press. (In Chinese).

Tang, J. H., Chan, L. Y., Chan, C. Y., Li, Y. S., Chang, C. C., Liu, S. C., et al. (2007). Characteristics and diurnal variations of NMHCs at urban, suburban, and rural sites in the Pearl River Delta and a remote site in South China. *Atmos. Environ. X.* 41 (38), 8620–8632. doi:10.1016/j.atmosenv.2007.07.029

US EPA (2009). *Guidance for superfund volume I human health evaluation manual (Part F, supplemental guidance for inhalation risk assessment)*. EPA-540-R-070-002, OSWER 9285.9287-9282).

Wang, Y., Xu, X. B., Mao, T., and Zhang, D. Q. (2009). "Preliminary detection results of volatile organic compounds in the Atmosphere of Qomolangma region," in Proceedings of the 26th Annual Meeting of The Chinese Meteorological Society of Atmospheric Composition and Weather (Hangzhou: Climate and Environmental Change), 1. (In Chinese).

Wang, Y., Ren, X., Ji, D., Zhang, J., Sun, J., and Wu, F. (2012). Characterization of volatile organic compounds in the urban area of Beijing from 2000 to 2007. *J. Environ. Sci.* 24 (1), 95–101. doi:10.1016/s1001-0742(11)60732-8

Warneke, C., de Gouw, J. A., Holloway, J. S., Peischl, J., Ryerson, T. B., Atlas, E., et al. (2012). Multiyear trends in volatile organic compounds in Los Angeles, California: Five decades of decreasing emissions. *J. Geophys. Res.* 117, 1–10. doi:10.1029/2012jd017899

Wei, W., Wang, S., Hao, J., and Cheng, S. (2011). Projection of anthropogenic volatile organic compounds (VOCs) emissions in China for the period 2010–2020. *Atmos. Environ. X.* 45 (38), 6863–6871. doi:10.1016/j.atmosenv.2011.01.013

Xia, M. F., Li, H., Li, J. J., Chai, F. H., Li, H. J., Zhang, Y. J., et al. (2014). Characteristics and health risk assessment of atmospheric benzene homologues in summer in the northeastern urban area of Beijing, China. *Asian J. Ecotoxicol.* 9 (06), 1041–1052. (In Chinese). doi:10.7524/AJE.1673-5897-20140611001

Xue, L. K., Wang, T., Guo, H., Blake, D. R., Tang, J., Zhang, X. C., et al. (2013). Sources and photochemistry of volatile organic compounds in the remote atmosphere of Western China: Results from the Mt. Waliguan observatory. *Atmos. Chem. Phys.* 13 (17), 8551–8567. doi:10.5194/acp-13-8551-2013

Yang, T., Li, D. D., Shan, X. L., Wang, X. Z., Zhang, W. Q., and Zhang, Y. J. (2017). Pollution characteristics, source apportionment and health risk assessment of benzene homologues in the ambient air of a typical urban area in Beijing. *Asian J. Ecotoxicol.* 12 (05), 79–97. (In Chinese). doi:10.7524/AJE.1673-5897.20170217001

Yang, Y., Ji, D., Sun, J., Wang, Y., Yao, D., Zhao, S., et al. (2019). Ambient volatile organic compounds in a suburban site between Beijing and Tianjin: Concentration levels, source apportionment and health risk assessment. *Sci. Total Environ.* 695, 133889. doi:10.1016/j.scitotenv.2019.133889

Yao, Q., Cai, Z. Y., Ma, Z. Q., Han, G. Y., Liu, J. L., and Han, S. Q. (2017). Variation characteristics and health risk assessment of BTEX in Tianjin. *China Environ. Sci.* 37 (9), 3276–3284. (In Chinese).

Yin, X., de Foy, B., Wu, K., Feng, C., Kang, S., and Zhang, Q. (2019). Gaseous and particulate pollutants in Lhasa, Tibet during 2013–2017: Spatial variability, temporal variations and implications. *Environ. Pollut.* 253, 68–77. doi:10.1016/j.envpol.2019.06.113

Yu, X. L., Tang, J., Zhou, L. X., Xue, H. S., and Xue, X. J. (2001). Emission characteristics and sources of non-methane hydrocarbons at Lhasa area. *Acta Sci. Circumstantiae* 21, 203–207. (In Chinese).

Yu, J. Y., Han, Y., Chen, M. L., Zhang, H. F., Chen, Y., and Liu, J. G. (2022). Characteristics and source apportionment of ambient VOCs in Lhasa. *Environ. Sci.* 43 (01), 113–122. (In Chinese). doi:10.13227/j.hjkx.202104038

Yuan, B., Shao, M., Lu, S. H., and Wang, B. (2010). Source profiles of volatile organic compounds associated with solvent use in Beijing, China. *Atmos. Environ. X.* 44, 1919–1926. doi:10.1016/j.atmosenv.2010.02.014

Yuan, B., Hu, W. W., Shao, M., Wang, M., Chen, W. T., Lu, S. H., et al. (2013). VOC emissions, evolutions and contributions to SOA formation at a receptor site in eastern China. *Atmos. Chem. Phys.* 13 (17), 8815–8832. doi:10.5194/acp-13-8815-2013

Zhang, Y., Wang, X., Barletta, B., Simpson, I. J., Blake, D. R., Fu, X., et al. (2013). Source attributions of hazardous aromatic hydrocarbons in urban, suburban and rural areas in the Pearl River Delta (PRD) region. *J. Hazard. Mat.* 250, 403–411. doi:10.1016/j.jhazmat.2013.02.023

Zhang, J., Sun, Y., Wu, F., Sun, J., and Wang, Y. (2014). The characteristics, seasonal variation and source apportionment of VOCs at Gongga Mountain, China. *Atmos. Environ. X.* 88, 297–305. doi:10.1016/j.atmosenv.2013.03.036

Zhang, Z., Zhang, Y. L., Wang, X. M., Lu, S. J., Huang, Z., Huang, X. Y., et al. (2016). Spatiotemporal patterns and source implications of aromatic hydrocarbons at six rural sites across China's developed coastal regions. *J. Geophys. Res. Atmos.* 121 (11), 6669–6687. doi:10.1002/2016jd025115

Zhang, Y. X., An, J. L., Wang, J. Y., Shi, Y. Z., Liu, J. D., Liang, J. S., et al. (2017). Variation characteristics and health risk assessment of BTEX in the atmosphere of northern suburb of nanjing. *Environ. Sci.* 38 (02), 453–460. (In Chinese). doi:10.13227/j.hjkx.201607108

Zhang, X., Ding, X., Wang, X., Talifu, D., Wang, G., Zhang, Y., et al. (2019). Volatile organic compounds in a petrochemical region in arid of NW China: Chemical reactivity and source apportionment. *Atmosphere* 10 (11), 641. doi:10.3390/atmos10110641

Zhang, L. H., Wang, X. Z., Li, H., Cheng, N. L., Zhang, Y. J., Zhang, K., et al. (2021). Variations in levels and sources of atmospheric VOCs during the continuous haze and non-haze episodes in the urban area of beijing: A case study in spring of 2019. *Atmos. (Basel).* 12, 171–186. doi:10.3390/atmos12020171

Zhao, Q., Li, Y., Chai, X., Xu, L., Zhang, L., Ning, P., et al. (2019). Interaction of inhalable volatile organic compounds and pulmonary surfactant: Potential hazards of VOCs exposure to lung. *J. Hazard. Mat.* 369, 512–520. doi:10.1016/j.jhazmat.2019.01.104

frontiers | Frontiers in Environmental Science

TYPE Original Research
PUBLISHED 21 September 2022
DOI 10.3389/fenvs.2022.981104

OPEN ACCESS

EDITED BY
Xiaolan Li,
Institute of Atmospheric Environment, CMA, China

REVIEWED BY
Ningwei Liu,
China Meteorological Administration, Shenyang, China
Shengzhen Zhou,
Sun Yat-Sen University, China

*CORRESPONDENCE
Jizhi Wang,
jzwang@cma.gov.cn

SPECIALTY SECTION
This article was submitted to Atmosphere and Climate, a section of the journal Frontiers in Environmental Science

RECEIVED 29 June 2022
ACCEPTED 16 August 2022
PUBLISHED 21 September 2022

CITATION
Wang D, Wang J, Yang Y, Jia W, Jiang X and Wang Y (2022), Impact of meteorological conditions on tropospheric ozone and associated with parameterization methods for quantitative assessment and monitoring.
Front. Environ. Sci. 10:981104.
doi: 10.3389/fenvs.2022.981104

Impact of meteorological conditions on tropospheric ozone and associated with parameterization methods for quantitative assessment and monitoring

Deying Wang[1], Jizhi Wang[1]*, Yuanqin Yang[1], Wenxing Jia[1], Xiaofei Jiang[2] and Yaqiang Wang[1]

[1]State Key Laboratory of Severe Weather and Key Laboratory of Atmospheric Chemistry of CMA, Chinese Academy of Meteorological Sciences, Beijing, China, [2]China Meteorological Administration Training Centre, Beijing, China

In recent years, the heavy ozone pollution events around the world have shown a sudden frequently increase, which has aroused widespread concern in the government and the public. It is well known that O_3 is driven by photochemical reactions triggered by solar radiation (direct and indirect solar radiation), the O_3 concentration calculated by chemical mechanism is mostly significantly lower than the actual O_3 observation. Based on the study of the effect of meteorological conditions on the "additional increment" of O_3 in three representative regions of Beijing, Hangzhou and Guangzhou from 2015 to 2020, an innovation diagnostic theory algorithm that the cross-cutting effects of atmospheric clouds on the chemical pattern of O_3 solar radiation is established in this study. On this basis, a parametric evaluation method of O_3 is established. The novelty of this study is 1) Comprehensive influence of the meteorological conditions and photochemical reactions mechanisms on the cross-cutting effects of O_3 concentration are given. Especially low-level clouds in the troposphere, which have significantly large variable effects on the reflection and refraction of O_3 through solar radiation. Theory quantitative algorithm of cloud scattering, cloud height, cloud volume and cloud structure changes, as well as feedback effects caused by water vapor condensation, which closely related to the transformation of O_3 precursors are given. 2) Based on this, a parameterization method for quantitative O_3 assessment and monitoring, which is a Parameterization for Linking Ozone pollution with Meteorological conditions. 3) Applying the theoretical algorithm and parameterization method of this study, comparing the changes of O_3 in 2018 with 2019, an objective quantitative distinction between emission reduction and meteorological impact was made, showing that emission reduction still played a leading role, with a contribution rate of about 27%. This shows that the created quantitative algorithm of atmospheric cloud theory and the innovative parameterization method can provide an objective

quantitative basis for O_3 pollution decision-making and public emission reduction.

KEYWORDS

meteorological conditions, parameterization method, solar zenith angle, cloud scattering, Ozone pollution

Highlights

·O_3 concentrations vary with cloud reflections driven by Θ_z diurnal variations.
·High condensation under high humidity in the air is conducive to a re-increase in O_3
·Parameterize for quantitative assessment of impact of meteorological conditions on O_3
·PLOM constructs application of O_3-value add theory based on multi-factor contribution

1 Introduction

In recent years, the tropospheric (or near-surface) O_3 concentration has significantly increased. High-resolution synchronous observation revealed that the O_3 concentration in the troposphere increased by −10%–40% when the nitrogen oxide concentration decreased to a certain level during the period of the Beijing 2008 Olympic Monitoring Campaign (Zhang et al., 2009). China suffered from O_3 pollution during several consecutive high-temperature weather periods during the summers of 2017–2020. From July 17 to 20 July 2017, O_3 pollution occurred in many places in the North China Plain (NCP), Northeast China, and Northwest China, with a particularly long period in Beijing, and the frequent occurrences of heavy O_3 pollution in recent years. The formation and control of O_3 have become important issues of concern to the government and public.

Although the impact of clouds and aerosols on climate has been studied for decades, it remains a complex and unsolved problem. The aerosol effect on enhancing cloud albedo, which is often called the first aerosol indirect effect. For climate patterns where uncertainties are mostly present, the impact of atmospheric clouds is important, because it is difficult to exclude the feedback of different surface fluxes on turbulence dynamics, including the impact of cloud characteristics on the O_3 concentrations, so the influence of meteorological conditions on atmospheric tropospheric O_3 concentrations needs to be carefully studied and diagnosed (Wang and McFarquhar, 2008). (Wang and McFarquhar 2008) Modeling aerosol effects on shallow cumulus convection under various meteorological conditions observed over the Indian Ocean and implications for development of mass-flux parameterizations for climate models.

The effects of cloud cover, cloud height and cloud amount on solar radiation are directly related. The cloud amount is defined as a percentage of the horizontal domain covered by the cloud column at any level. The cloud amount continues to increase as relative humidity (RH) increases. For example, in the clean environment, the mean cloud amount increased from 6% to 11%, when RH increases from 49% to 80%. This indicates that atmospheric clouds are closely related to humidity, condensation rate, and super-saturation. These complex atmospheric cloud problems affect the solar radiation and photochemical reaction mechanism of O_3.

It is well-known that O_3 is driven by photochemical reactions initiated by solar radiation (for sure including direct and indirect solar radiation). A steady-state concentration of O_3 is expressed as follows (Madronich and Flocke, 1999; Textor et al., 2006):

$$[O_3] = \frac{j[NO_2]}{k[NO]} \tag{1}$$

where j is the photolysis frequency of NO_2, k is the rate coefficient for the O_3+NO->NO_2+O_2 reaction and the brackets denote the concentrations of O_3, NO_2 and NO.

The above relationship of NO, NO_2, and O_3 is called a steady-state relationship. Its dynamic equation is also given as (Tang et al., 2006):

$$[O_3] = \left\{\left[\left(\frac{j}{k}\right)^2 + 4\frac{j}{k}[NO_2]_0\right]^{\frac{1}{2}} - \frac{j}{k}\right\} \tag{2}$$

where the basic photochemical cycle of NO_2, NO, and O_3 is the fundamental source for O_3 genesis; j and k are constants of transformation efficiency in chemical reactions. Then it also be expressed as $\alpha = \frac{j}{k} \approx 0.01 \times 10^{-6}$, as a coefficient for the transformation efficiency (Textor et al., 2006; Wang et al., 2019).

However, in most cases, calculations of the chemical mechanism given in expression (2), even including other expression, are often underestimated compared to actual O_3 observations (Textor et al., 2006; Wang et al., 2019). Studies suggest that it is because for use in photo-chemistry models, and routinely include the effects of molecular absorbers and scatterers, clouds, aerosols, and surface reflections. So that, for different location and time of the year. Actual atmospheric conditions needed as input to the calculation are often not available (Madronich and Flocke, 1999).

So that the changes in tropospheric meteorological conditions should be one of the important factors to consider. In particular, the O_3 generation mechanism based on photochemistry and optical radiation is closely related to structural changes in the tropospheric low-layer cloud field

and their variable influence on the reflection and refraction of solar radiation. As mentioned above, the O_3 chemical mechanism is an approximation. Values j depend on molecular parameters (absorption cross sections and photo-dissociation quantum yields) that are specific to the photo-reaction of interest, and on the availability of solar radiation at any specific location in the atmosphere (Tang et al., 2006).

The quantifying the impacts of unfavorable meteorological conditions on tropospheric O_3 variation is the key issue for the Meteorological Forecasting Center to accurately assess of O_3. Nor can O_3 pollution prevention and control be decoupled from meteorological impacts. Research on the severe O_3 pollution events in the mega cities of China (Hangzhou, Guangzhou, Chengdu, and Beijing) has shown that meteorological conditions play a critical role in such phenomena (Wang and Chai, 2002; Li et al., 2015; Hu et al., 2016; Wang et al., 2019). Wang et al. (2018) selected two stations in the inland and ocean near Hong Kong to simultaneously monitor the main and secondary pollutant (e.g., O_3, NO, NO_2, and SO_2) concentrations. The results demonstrate that the O_3 concentration adjacent to the offshore point was much higher than that at the land point, indicating that the entry of continental high-pressure air mass into the sea, the tropical cyclone activities, and the interaction of the land-sea breeze all contribute to O_3 changes (Wang et al., 2018). Although there is some progress in research on the influence of meteorological conditions on air quality, it is still in the analysis stage and there is a lack of objective quantitative model-based research on the possible impact of meteorological conditions on O_3 pollution (Zhang et al., 2011; Yang et al., 2015; Hu et al., 2016). In this study, we try to adopt the parametric method to introduce the effects of cloud scattering, temperature, humidity, atmospheric density and other changes under the condition of solar zenith angle change, and explore the additional value-added effect of meteorological conditions on O_3 concentration.

As mentioned above, in particular, the O_3 generation mechanism based on photochemistry and optical radiation is closely related to structural changes in the tropospheric low-layer cloud field and their variable influence on the reflection and refraction of solar radiation. As an important factor affecting troposphere O_3, the intensity of solar ultraviolet radiation, the atmospheric channel of sunlight, and especially the impact of near-surface atmospheric meteorological conditions is extremely important. When the solar zenith angle changes, the reflection path length of solar radiation passing through clouds with different structures will naturally change; this affects and changes the O_3 content in the atmosphere (Bohn et al., 2008). All characteristics of skies with or without clouds, such as cloud height, cloud shape, cloud amount, cloud thickness, and light transmittance, affect and change the radiation path length, and then influence solar radiation. Changes in the cloud and solar zenith angle superimpose and offer feedback to further update the temporal and spatial distribution and changes in O_3 concentration. Data and research on these aspects are lacking.

An increase in O_3 concentration is closely related to the interaction between solar radiation and cloud structure (Webb and Steven, 1986; Zhao et al., 2019). Continuous cloud cover and sunlight can be often observed when looking down from aircraft. After reflection and scattering, the sky brightness increases. The differences between the cloud structure and the density of upper and lower clouds are related to the interaction between the temperature (T), pressure (P), and relative humidity (RH). The direct and feedback effects of meteorological conditions change the photochemical radiation intensity to drive the proliferation or reduction of O_3 and then affect its temporal and spatial redistribution (Bokoye et al., 2001).

Based on the principle of the PLAM index of pollution-causing meteorological conditions (Yang et al., 2009; Zhang et al., 2009, 2013, 2018), this study further investigated the relationship between O_3 pollution and meteorological conditions by parameterization, focusing on the meteorological conditions in the sensitive areas with frequent high-concentration O_3 and high-concentration regions, including the NCP, Yangtze River Delta (YRD), and Pearl River Delta (PRD). Through the analysis of multi-regional temporal and spatial observational data, this study identified the meteorological conditions affecting O_3 pollution, including the contribution of cloud reflection and the correlation between the cloud structure and solar zenith angle. The objective method to describe the relationship between O_3 pollution and meteorological conditions was quantified.

2 Data and methods

2.1 Data used in the study

Atmospheric observation data of 2015–2020 for the city areas of Beijing, Hangzhou, and Guangzhou, the major pollution influence areas of China, were supplied by the China Meteorological Information Center. Real-time and historical data of surrounding areas, including air temperature, dew temperature, air pressure, wind direction, wind speed, and visibility, were obtained from the observation stations and Hour Resolution of Automatic Weather Station (AWS) and the re-analysis data of the China Climate Center Figure Forecasting System for 2015–2020.

The geographical distribution of the NCP, YRD, and PRD regions, represented by Beijing, Hangzhou, Guangzhou, and other cities, is shown in Figure 1. The analytical data on condensation rate (f_c), wet potential temperature (θ_e), and super-saturation (S) were obtained from previous studies (Zhang et al., 2009; Wang et al., 2017; Liu et al., 2019; Wang et al., 2021). The atmospheric composition data, including $PM_{2.5}$, O_3, NO_2, SO_2, and PM_{10} over Beijing, Hangzhou, and Guangzhou in 2015–2020, were obtained from the Ministry of Ecology and Environment (http://www.zhb.gov.cn/hjzl/).

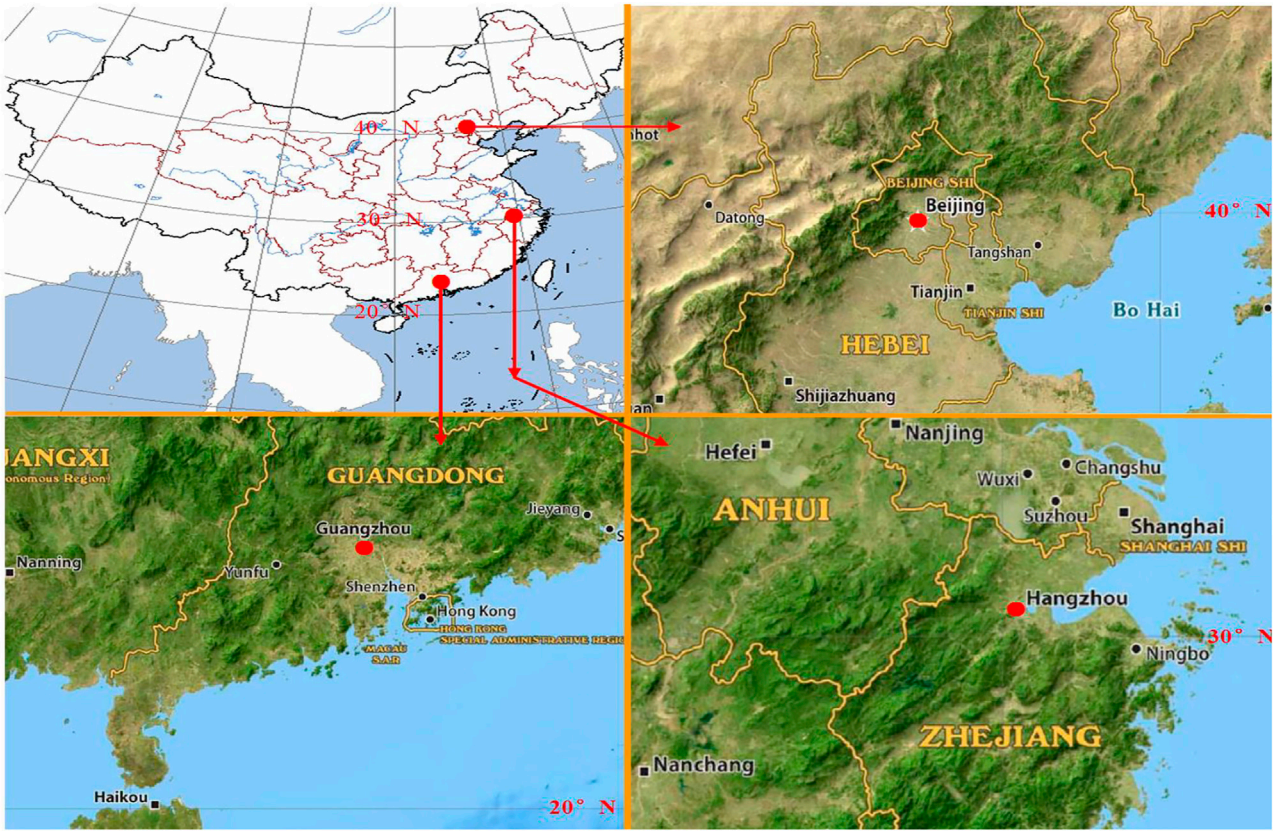

FIGURE 1
The geographical distribution of the North China Plain (NCP), Yangtze River Delta (YRD) and Pearl River Delta (PRD) regions represented by Beijing, Hangzhou, Guangzhou and other cities.

2.2 Methods

Because the levels of air pollutants, including O_3, are generally controlled by a combination of multi-meteorological variables, the impacts of individual meteorological variables on air pollution may not be significant and/or may cancel each other, as they can hardly account for the interrelation between the variables (Li et al., 2011; Wang et al., 2012). In this study, multi-sensitivity meteorological parameters were analyzed with regard to the influence of cloud scattering, solar heating, and other factors on the mechanism of O_3 changes. The new developing of the methods in this study are as follows:

2.2.1 The development of parameterization method

At present, the understanding of some atmospheric microphysical or atmospheric chemical processes related to air quality growth is not very clear and needs to be further explored. Some physical equations are inherently uncertain, or the necessary observational information under current conditions is unknown or difficult to measure precisely. For example, the physical processes of atmospheric clouds are closely related to the increase of O_3 concentration, the convection of cumulus clouds in the atmosphere, and the instantaneous mixing and change of temperature in the cloud and the ambient temperature. These processes are often difficult to write deterministic equations. Guo H-L's famous series of studies on parameterization (Kuo, 1961; Kuo, 1965; Kuo, 1974) pioneered the use of cloud microphysical processes and large-scale observational information as parametric schemes, which are widely used in numerical weather prediction. The results of the research show that the parametric method links the so-called "different magnitudes" and "incomparable" atmospheric micro-scale physical processes with large-scale processes. By parameterize and making connections between some sensitivity factors, the solution of the physical equations can be obtained.

2.2.2 The parameterization method

A parameterization method, that The Parameterization to Link Ozone-pollution with Meteorological conditions (PLOM) is mainly focused on the following sensitive influencing factors: 1) changes of solar zenith angle (Θ_z) in local time; 2) variation in and formation of

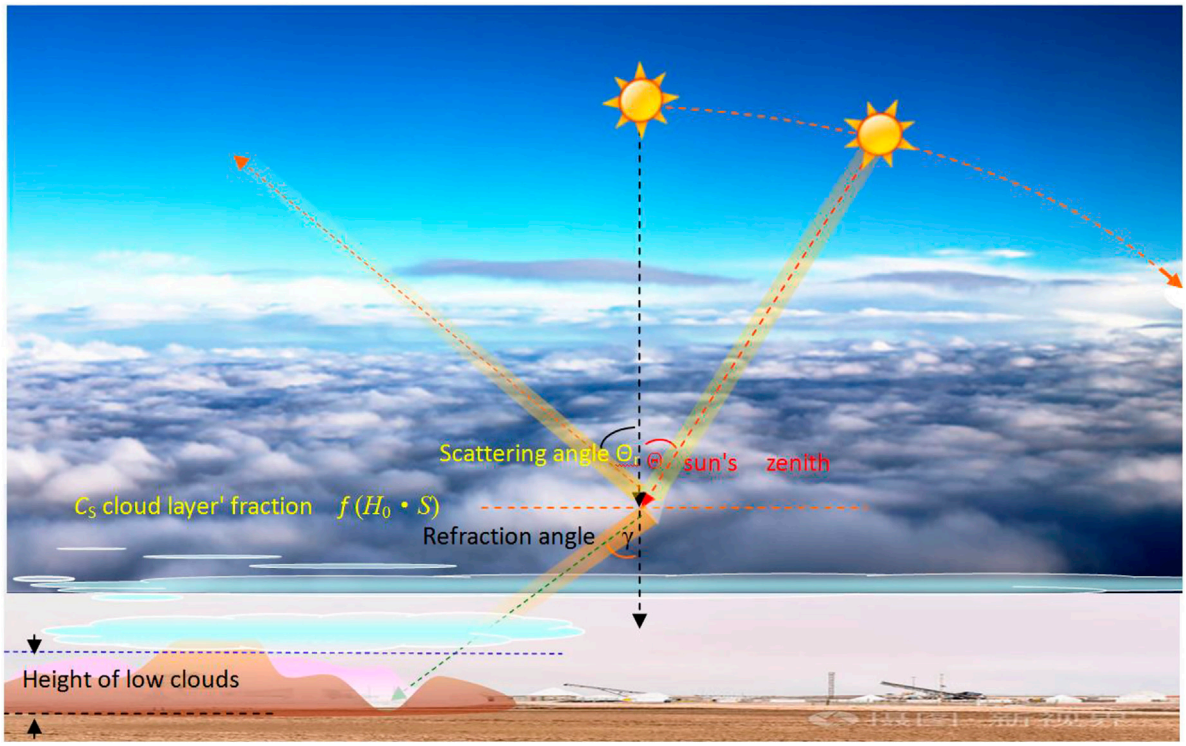

FIGURE 2
Physical model of the relationship between the reflection, refraction of solar and solar zenith angle by atmospheric clouds.

cloud scattering angle (Θ_r), and contribution of cloud scattering changes (Γ_Θ); 3) cloud structure (H_0), including cloud height, cloud amount, and cloud shape; and 4) contribution of water vapor condensation and humidification of precursor emissions to increases in O_3 concentration (ξ). The basic factors closely related to the parameterization include the atmospheric condensation rate (f_c), temperature (T), pressure (P), and atmospheric density variation (ρ).

2.2.3 Contribution of solar zenith angle parameter (Θ_z) and cloud scattering (Γ_Θ) to O_3 concentration

The contributions of the solar zenith angle parameter (Θ_z) and cloud scattering (Γ_Θ) are inseparable. Figure 2 presents a schematic diagram of the relationship between solar scattering/reflection, refraction, solar zenith angle, and atmospheric clouds. The results show that the solar reflection (diffuse reflection) rule is also applicable to scattering (Webb and Steven, 1986; Zhao et al., 2019). The solar zenith angle (Θ_z) is the angle between the incident light and the normal on the ground.

Γ_Θ is the O_3 comprehensive influence parameter under the effects of meteorological conditions and different solar zenith angles; it describes the impacts of clouds on reflection, refraction, and scattering. The reflections of sunlight by fog and cloud, and the variation in the reflection angle between air masses with different densities depend on the changes in the vertical gradient of the atmospheric pressure (P), temperature (T), and relative humidity (RH) (Zhao et al., 2019). These changes will also depend on the vertical difference in atmospheric density (ρ). They are expressed using the classical theory of atmospheric optics (Humphreys, 1940):

$$\Theta_r = \sin^{-1}\left(\frac{\rho'}{\rho}\right)^{1/2} \tag{3}$$

Where $\rho = \frac{P}{R_d T_v}$ represents the comprehensive influence of pressure (P), temperature (T), and virtual temperature [T_v, $T_v = (1 + 0.61w)$]; w is the humidity parameter mixing ratio; and $R_d = 2.8705 \times 10^{-1}$ J $g^{-1}°C^{-1}$ is the gas constant. Considering the air density difference above and below the cloud, the cloud scattering angle replaces the zenith angle under the condition of clear skies and no clouds. For a certain zenith angle during the day, the contribution of cloud scattering to the increment in O_3 concentration is:

$$\Gamma_\Theta = \mu \cos \Theta_z \begin{cases} \Theta_z = \Theta_\gamma = \sin^{-1}\left(\frac{\rho'}{\rho}\right)^{1/2} \text{considering the density difference above and below clouds} \\ \Theta_z \text{when there are no clouds and the density difference of the air layer is zero.} \end{cases} \tag{4}$$

Where μ - single scattering albedo, the efficiency coefficient associated with cloud structure (Sheng et al., 2019). Scattering albedo (μ) is related to the cloud height (H_0) of the reflected clouds, the cloud layer is higher, the scattering rate of light is higher, take 0.9–1.5. Conversely, the cloud layer is lower, the scattering rate of light is lower, generally fluctuating between 0.75 and 0.85.

As shown in Figure 2, solar radiation is reflected and scattered due to the atmospheric density difference above and below the cloud, resulting in a change in the scattering angle. γ is the refraction angle of solar radiation below the cloud in Figure 2.

Eq. 3 implies that when solar radiation encounters the influential cloud layer before reaching the ground, the density difference between the cloud and the regions above and below the cloud shall be considered; the relationship expression of Γ_Θ is $\Gamma_\Theta = \mu\cos\Theta_\gamma = \mu\cos(\sin^{-1}(\frac{\rho'}{\rho})^{1/2})$. When there are no clouds and the density difference of the atmospheric layer is zero, $\Gamma_\Theta = \mu\cos\Theta_z$.

2.2.4 Atmospheric cloud height

Atmospheric cloud structure is one of the important meteorological parameters that affect O_3 concentration; clouds play an important role in the energy balance of the earth system. The structural differences in cloud height, shape, and amount have a significant impact on the heating or cooling of different atmospheric stratifications. When clouds reflect sunlight back into space, the level above the clouds gets heated, whereas absorption of solar radiation by clouds results in cooling of the atmosphere below them. In the climate model, one of the sources of inaccuracy in prediction is the uncertainty in the description of the impact of cloud structure in the climate system, including the reflection of clouds, which is an important meteorological parameter that affects O_3 concentration (Platnick et al., 2000; Qu and Chen, 2002; Ackerman et al., 2004; Dunya et al., 2017). Under conditions that systematically affect clouds, the cloud height (H_0) is a fundamental parameter of atmospheric clouds. Solar radiation is influenced by the reflection, scattering, and refraction of clouds. H_0 can be obtained from meteorological observation reports or the air-mass lifting condensation level (LCL) (Wang et al., 2017).

To obtain the height of the cloud base of a low cloud, i.e., the LCL of the atmosphere, the following equation can be used (Yang et al., 1982; Wang et al., 2017):

$$H_0 \in P_{LCL} \approx 6.11 \times 10^2 \times \left(\frac{0.622 + 0.622\frac{e_s}{p-e_s}}{0.622\frac{e_s}{p-e_s}}\right) \quad (5)$$

where e_s represents saturated water vapor pressure. The atmospheric low cloud base height is represented by the air pressure (p). When the air pressure (p) of the air mass reaches the saturated water vapor pressure (e_s), but has not yet caused a raindrop to fall, there would be a layer of high water content in the atmosphere (Wang et al., 2017). Such areas of high water content in the atmosphere would be considered the influential atmospheric cloud systems. H is generally consistent with the actual observed low cloud height (H_0).

2.2.5 Contribution of micro scale condensation meteorological conditions to O_3 growth

It is known that NOx/VOCs sources actually dominate the generation of O_3 in the lower troposphere in large cities (Tang et al., 2006). When the VOCs/NOx ratio is appropriate, the wetting drive of the atmospheric condensation rate can accelerate and catalyze O_3 precursors to form secondary pollution, and the O_3 concentration increases exponentially (Wang et al., 2019):

$$\delta O_3 = \alpha(\chi)^{-\beta} = \xi \quad (6)$$

where χ represents O_3 precursors (NOx or VOCs), $\beta = f_c$ is the condensation function, and $\alpha = 10.0 \times 10^3$.

Day-by-day weather change is one of the important physical processes of the atmosphere. This hysterics of radiant heating under the influence of post-sunrise meteorological conditions is related to the delay in O_3 growth. In China, the YRD, the PRD, the NCP, and the Sichuan Basin (SB), the increasing of O_3 concentration in delayed power exponent effecting due to heating on low-layer atmosphere by solar radiation have been observed. As a response to the changing meteorological conditions for the diurnal variation, it is maintained for 3–6 h after sunrise, or even throughout the day, which plays an important role in the increase and decrease of NO_2 and O_3 concentrations. On the basis of multi-station data correlation fitting statistical analysis, the power exponent law is as Eq. 6. The mathematical algorithm of the power exponential growth is a typical description of nonlinear variations. By coefficient of α and β, the power exponent aptly describes the nonlinear variation of the increasing in O_3 concentration due to NO_2 reduction and its regional and seasonal differences (see Table 1). This micro-scale nonlinear contribution is combined with the cloud structure changes discussed in the next section, along with the cross-influence effect of meteorological conditions affected by the solar zenith angle, and the parameterization of PLOM is comprehensively constructed (Wang et al., 2019).

The two coefficients α and β in Eq. 6 give the meteorological characteristics that vary from region to region and from one season to another respectively. The coefficient α represents the contribution efficiency of the law of power exponent for transforming NO_2 into O_3. Study indicated that the magnitude of α for the Yangtze and Pearl River deltas was 10^2–10^3, and that for the inland SB and NCP areas was 10^1. The β denotes magnitude and sign of power, exponent and negative sign means the NO_2 concentration is correlated to the O_3 concentration decline after 3–6 h as a negative power exponent. The magnitude of β was 0.6–1.4, and the majority number is 1.0 (Wang et al., 2019).

In summary, the dimensionless index of standardized O_3 pollution meteorological conditions is expressed as:

TABLE 1 The α and β characteristics of the delayed correlation power exponent in the equation.

	α	β	Delayed time (hours)	Time
Beijing	42.8 × 101	0.9	3	December 2016
Hangzhou	11.0 × 103	1.0	3	September 2016
	19.8 × 102	1.4	6	September 2016
Guangzhou	10.5 × 103	1.7	3	December 2015
	36.4 × 102	1.4	6	December 2015
Chengdu	67.0 × 101	1.0	1	December 2015
	22.6 × 101	0.8	3	December 2015

The stations of Beijing, Hangzhou, Guangzhou and Chengdu are the representative stations of the North China Plain, the Yangtze River Delta, the Pearl River Delta and the Sichuan Basin.

$$PLOM \propto H_0\left(\mu \cos\left(\sin^{-1}\left(\frac{\rho'}{\rho}\right)^{1/2}\right)\right) + \xi \tag{7}$$

3 Results and discussion

3.1 Quantitative description based on parameterization method for severe O_3 pollution event

3.1.1 Observational facts and Parameterization to Link Ozone-pollution with Meteorological index of O_3 pollution in beijing during July 2019

To quantify the influence of meteorological conditions on O_3 pollution from multiple dimensions, typical O_3 pollution events in recent years were analyzed. During the summers of 2017–2020, a rare high-temperature event accompanied by severe O_3 pollution occurred in the NCP. The hottest month in the past 20 years was July 2019, based on the reports of the World Meteorological Organization (WMO) and the National Aeronautics and Space Administration (NASA) (http://www.CRNTT.com). 2019 was also the hottest year in Europe in this century. The temperature in France soared to 37.8°C and a new high-temperature record was set in Britain.

The Beijing Meteorological Observatory issued a yellow high-temperature warning on the afternoon of July 1. The temperature in Beijing continued to rise in July, with the daily maximum temperature going above 35–37°C for many days, and the maximum temperature hovering close to 40°C, with strong ultraviolet intensity and a sharp increase in O_3 concentration.

Figure 3 shows the hourly variations in the PLOM index calculated using the parameterization method in Eq. 7, as well as the temperature, O_3 concentration, and NO_2 concentration. As shown, high temperature and high O_3 pollution occurred frequently in Beijing in July 2019. Temperatures above 35°C and O_3 concentrations above 220 μg m^{-3} were observed in the periods shown in the yellow box of Figure 3. The peak values of temperature (above 37°C) and O_3 concentration (266 and 245 μg m^{-3}) were recorded on July 4 and 21. Moreover, the temperature had a significant diurnal variation synchronized with the O_3 concentration. It is notable that the PLOM index can describe the diurnal variation characteristics consistent with the O_3 concentration for typical severe O_3 pollution cases in Beijing. Figure 3 also shows that the concentrations of NO_2 and O_3 changed in an inverse manner. This indicates that increases in O_3 concentration can be captured under the meteorological conditions of the micro-scale condensation (f_c) described by the PLOM index (see Eq. 7) (Wang et al., 2019). This is an alternative superimposed contribution to the O_3 concentration due to the impact of micro-scale meteorological conditions.

3.1.2 Ability of Parameterization to Link Ozone-pollution with Meteorological index to express seasonal and regional impact of O_3 pollution in China

Figure 4A shows the correlation between the O_3 concentration and PLOM index in Beijing from July 1 to 31, 2019. For two consecutive summers in 2019 and 2020, Beijing suffered from a severe heat wave. Under the high temperature and high humidity "sauna" weather conditions, severe O_3 pollution was encountered in Beijing. Figure 4 indicates that the PLOM index has the important ability to present the O_3 pollution. The PLOM index also has consistent and good expressive ability for O_3 pollution in different years, seasons, and regions. The O_3 concentration positively correlated with the PLOM index; the correlation confirmation coefficients (R^2) were 0.42, 0.53, 0.62, and 0.53 for Beijing for July 2019 and 2020, Hangzhou for September 2015, and Guangzhou for July 2019, respectively, and the significance levels (p) were less than 0.01. Therefore, the PLOM index has important expressive ability to diagnose the influence of meteorological conditions on the change of troposphere O_3 pollution in three representative O_3 pollution areas in China, and the physical mechanisms established by the index are discussed below.

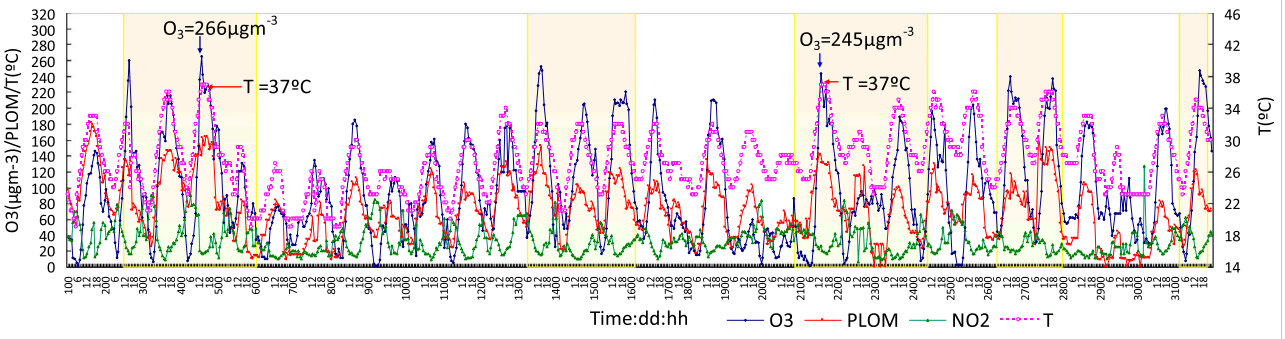

FIGURE 3
Hourly series of PLOM index, temperature, O_3 and NO_2 concentrations from 1 to 31 July, 2019.

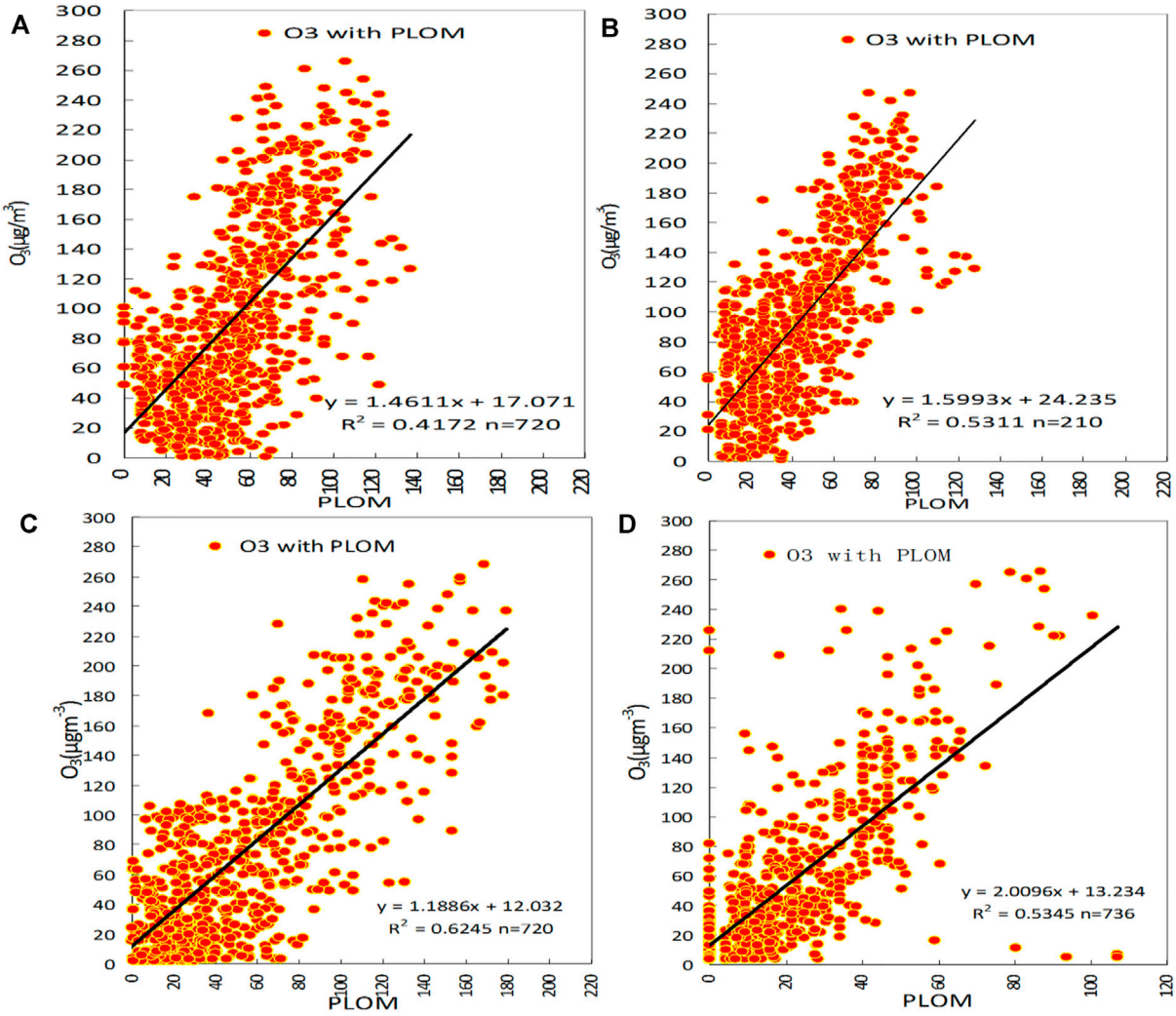

FIGURE 4
(A): Correlation analysis between O_3 concentration and PLOM index from 1 to 31 July, 2019 in Beijing, **(B)**: from 1 to 31 July, 2020 in Beijing, **(C)**: from 1 to 30 September, 2015 in Hangzhou and **(D)**: from 1 to 31 July, 2019 in Guangzhou.

3.2 Contribution of cloud scattering to O_3 under the solar zenith angle changes—driving mechanism based on daily weather condition changes

3.2.1 Cloud scattering effects of different cloud-layer density changes on increase in O_3 concentration

As shown in Figure 2, the zenith angle (Θ_z) is the angle between the sun's incident light and the straight line perpendicular to the ground. Γ_Θ is the impact on O_3 concentration due to the effect of the cloud structure on the reflection, refraction, and scattering of sunlight under different zenith angles under a particular meteorological condition. This depends on the reflection angle (Θ_r) due to the changes in the atmospheric vertical structure, including changes in air pressure (P), temperature (T), and RH distribution with variation in density between the air masses.

From the scattering angle of Eq. 3, the influence of meteorological parameters on the scattering at a certain solar altitude angle can be obtained. The difference in meteorological attributes (temperature (T), pressure (P), water vapor mixing ratio (w)) above and below the cloud is the key to the scattering/reflection and refraction effect of sunlight, which has an effect on the O_3 concentration. At the below-cloud level, solar radiation is refracted through the cloud, and the radiation intensity decreases, whereas scattering and reflection in the above-cloud level increase the solar radiation intensity (irradiance). The change in radiation intensity not only increases or decreases the tropospheric O_3 concentration but also has an important feedback effect, because sunlight reflection will change the densities of the upper and lower levels again. According to Eq. 3, the scattering, reflection, and refraction angles of sunlight entering the atmosphere can be distorted again, and the scattering effect and radiation intensity can be further changed to re-influence the cyclic feedback effect. The parameterization method reveals the impact of meteorological conditions on solar illumination and describes the quantitative influence on the re-contribution to O_3 distribution by connecting the atmospheric attributes (T, P, HR, and ρ) in and above the cloud.

The scattering angle can be calculated using Eq. 3; for the convenience of comparison, the lower layer is assumed to have a 925 hPa height. When the cloud height corresponds to the specified isobaric surface height of 850 (1,500 m) and 700 hPa (3,000 m), the changes in the scattering and reflection angle of solar radiation caused by the change in vertical density (ρ'/ρ) between the upper and lower clouds can be calculated.

Figure 5 indicates the change in scattering angle of solar radiation due to the vertical density difference (ρ'/ρ) between the upper and lower clouds with a cloud height of 1,500 and 3,000 m calculated using Eq. 3. The atmospheric density difference above and below clouds has a significant impact on the scattering of solar radiation. When the density difference changes from 0.6 to 1, the scattering angle changes from 45° to 90°.

There is no difference in density between the cloud and above-cloud level, i.e., ρ'/ρ = 1, which indicates that the cloud has a similar "mirror" reflection effect, the maximum scattering angle is 90°, and the positive contribution to the increase in O_3 concentration is zero. The density ratio (ρ'/ρ) decreases with an increase in the lower atmospheric density. When the density ratio is halved, the reflection angle decreases to 45°, and the contribution can reach the maximum. As shown in Figures 5A,B, the smaller the reflection angle, the greater the positive contribution to the increase in O_3 concentration. This situation just corresponds to the dry and clean meteorological conditions when cold air is inserted into the lower atmosphere. Once the cloud structure changes and the density above and below the cloud changes, the initial cloud reflection changes the solar radiation intensity, as well as enhances radiation above the cloud and increases the O_3 concentration. Changes in a cloud environment and meteorological conditions lead to cooling below the cloud, and ρ'/ρ further decreases (Figure 5A). Based on Eq. 4, the cosine effect will provide feedback and the cloud effect will increase the cloud reflection (Γ_Θ) contribution again, further aggravating the increment in O_3 concentration. Cloud height has an obvious impact on the density difference above and below the cloud. Below 1,500 m, the density difference is typically −0.9–1 and the scattering angle is −85–70°. When the cloud height is 3,000 m, the density difference is −0.7–0.9 and the scattering angle is −70–58°. A change in illuminance depends on the density difference of reflective clouds. A smaller reflection angle corresponds to a greater contribution to the increase in sky brightness and a greater positive contribution to an increase in O_3 concentration. It is also associated with the height of scattering and reflecting clouds; when the cloud is higher, the reflection angle is smaller, and the illumination increases. On the contrary, when the cloud is lower, the reflection angle is larger, and the illumination decreases.

As mentioned above in the Section 2.2.3, when considering the density difference above and below clouds, reflection from fogs and clouds or at any surface of sufficient size (greater than wave-length, dimensions) between masses of air at the same pressure but of unequal density, namely variers from the angle of the zenith (Θ_Z) to the reflection angle with clouds. The contribution of O_3 of reflection effect due to reflection angle (Θ_r) gives as (Humphreys, 1940; Tverski, 1954):

$$\Gamma_\Theta = \Theta_z = \Theta_y \sin^{-1}\left(\frac{\rho'}{\rho}\right)^{1/2} \quad \text{considering the density difference above and below clouds} \tag{8}$$

Based on Eq. 8, the cosine effect will provide feedback and the cloud effect will increase the cloud reflection (Γ_Θ) contribution again, further aggravating the increment in O_3 concentration. Including the cloud height has an obvious impact on the density difference above and below the cloud. The feedback mechanism is as follows: during the initial phase, cloud reflection can increase solar radiation intensity above the cloud layer, causing O_3 concentration to increase. It also causes cooling below the clouds. So that it is

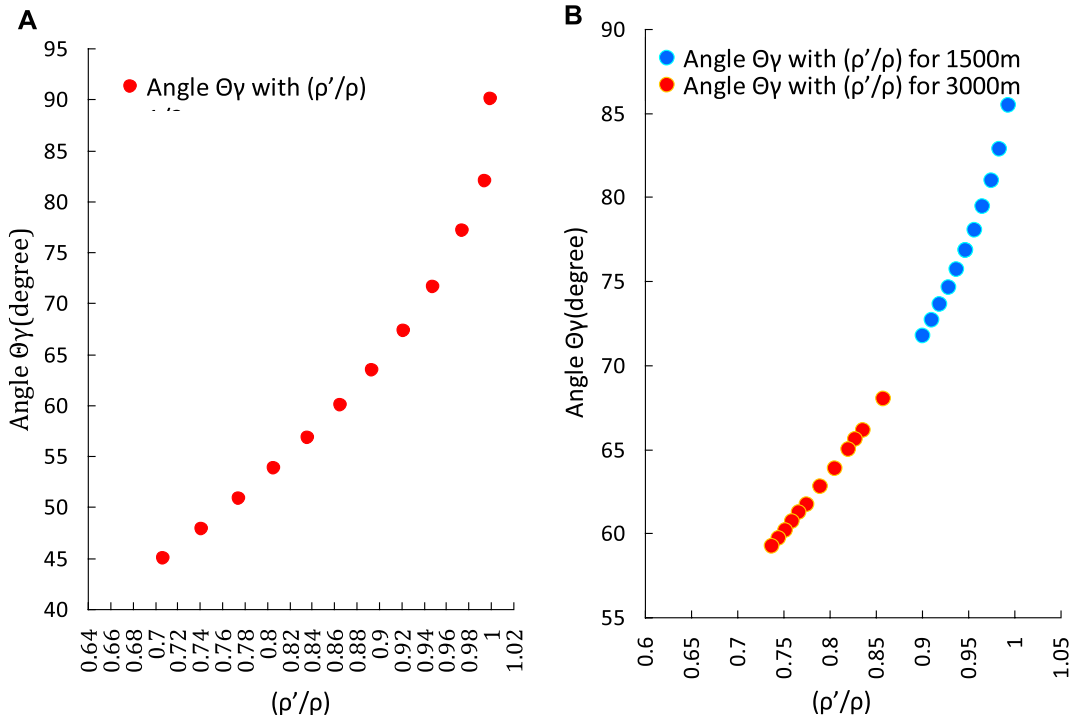

FIGURE 5
(A): The changes of sunlight reflection angle varies with vertical density difference (ρ'/ρ) between above and below of cloud layer, **(B)**: The changes of sunlight reflection angle varies with the vertical density difference (ρ'/ρ) in above and below cloud with the heights of the clouds for 1,500 m and 3,000 m respectively.

further reduced by Eq. 8, resulting (ρ'/ρ)to be increased and the angle of reflection getting increasing (Figure 5A). That is based on Eq. 8, the cosine effect will provide feedback that will again increase the contribution of cloud reflection through (Γ_{Θ}), further exacerbating the increase in O_3 concentration. So, the Eq. 8, as the first term in the PLOM index, describes the direct and feedback contribution of the scattering angle parameter. The second term in the PLOM index, describes contribution of micro scale condensation meteorological conditions to O_3 growth (Wang et al., 2022).

In conclusion, these results show that when the cloud structure changes, the densities of the upper and lower levels change, the solar radiation intensity changes, the radiation above the cloud increases, and the O_3 concentration increases. At the same time, cloud reflection has a dual effect, which will provide feedback and aggravate the increment in O_3 concentration again. The direct and feedback contributions of scattering angle parameters are comprehensively presented in the PLOM index.

3.2.2 Typical cases for contribution of cloud height, cloud scattering, and precursor wetting to increase in O_3 concentrations

Figure 6 shows a typical case of O_3 pollution mentioned above. The variations in various parameters based on the periodic change in the solar zenith angle during the typical peak period of O_3 concentration in Beijing from July 1 to 6, 2019 is given. The rise in cloud height (H0) at daytime and the decrease at night (Figure 6A) was closely linked to the diurnal variation in the solar zenith angle. An increase in daytime δO_3 was observed (Figure 6B). This is the diurnal change of cloud height, the O_3 precursor conversion complements the increment of O_3 (δO_3), i.e. satisfies Eq. 6: $\delta O_3 = \alpha\chi^{-\beta}$. As shown in Figure 6B, the peak of the increment in δO3 is as high as 50–60 μg m^{-3}. When the solar zenith angle is at the zenith (indicated by “”), cloud scattering contributes the most to the increment in O_3 concentration (Figure 6C).

Combined with the impacts of the multi-sensitive meteorological factors discussed herein, the observed O_3 concentration finally increased. The peak value of O_3 concentration was 266 μg m^{-3}, which appeared at 13:00 on July 4. The increment in O_3 concentration can be extended from the zenith angle peak in the evening. The characteristics of the contribution to the increase in O_3 concentration by the influences of precursors and cloud scattering are shown in Figure 6.

Figures 7A,B show the time series of cloud height (H_0) and the contribution of precursor wetting process to O_3 ($\delta O_3 = \alpha\chi^{-\beta}$), respectively during the period of 7–12 February, 2020 in Beijing. Figures 7C,D) show the correlation analysis of

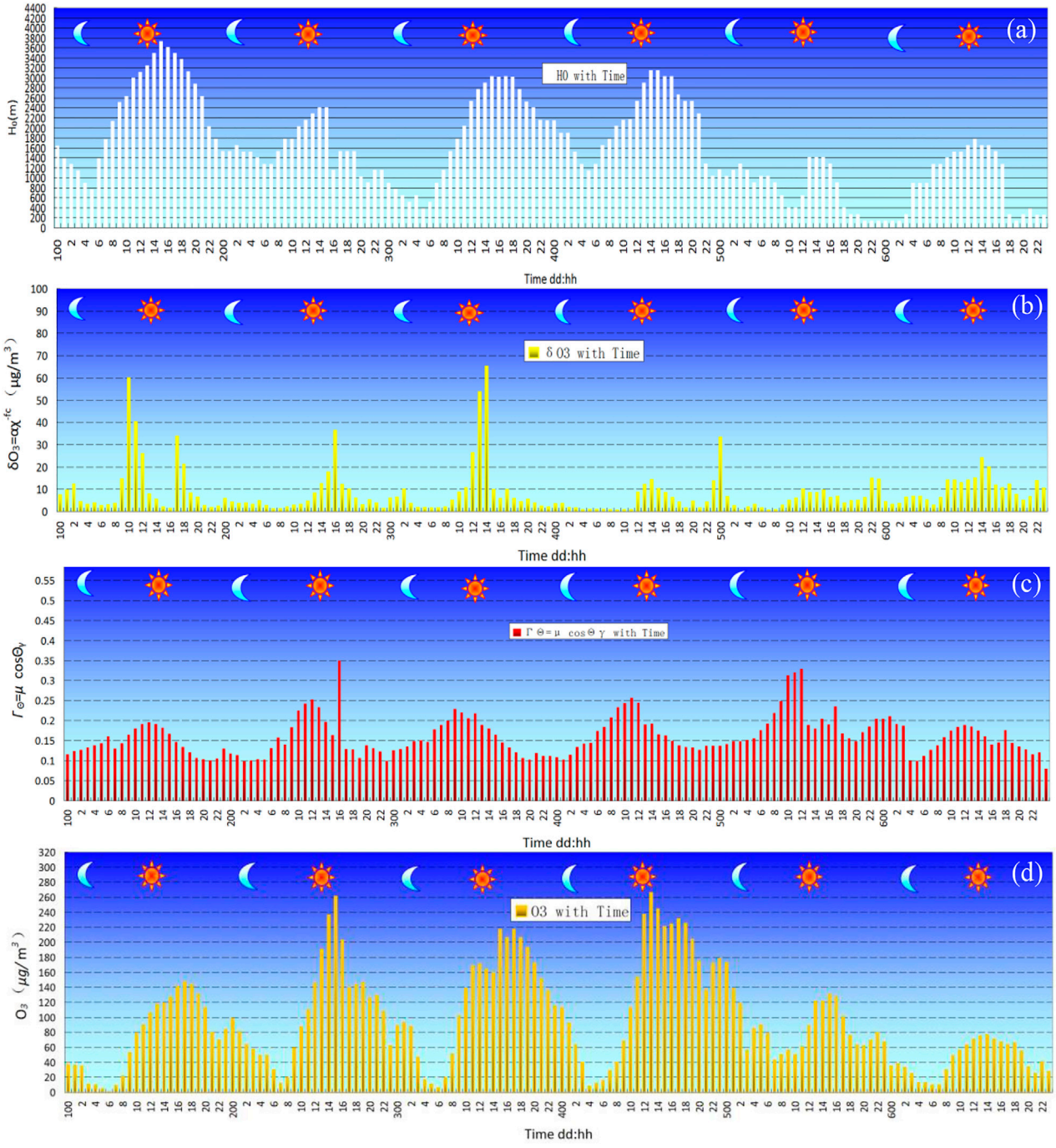

FIGURE 6
(A):Time series of cloud height (H_0), **(B)**: the contribution of precursor wetting process to O_3, **(C)**: the contribution of cloud scattering on O_3 ($\Gamma_\Theta = \mu\cos\Theta_Z$) and **(D)**: the observed O_3 concentration based on the diurnal variation of solar zenith angle during the O_3 peak period in Beijing from 1 to 6 July, 2019.

atmospheric condensation rate (F_c) with O_3 concentration changes for 1 to 6 July 2019 in Beijing corresponding to Figures 6A,B and for 7 to 12 February, 2020 in Beijing (d) corresponding to Figures 7A,B, respectively. It can be seen from the figure that in both summer and winter, it can be observed that with the increase of Fc, the O_3 concentration shows a positive correlation of e-exponential growth, and the correlation confirmation coefficient (R_2) significance level

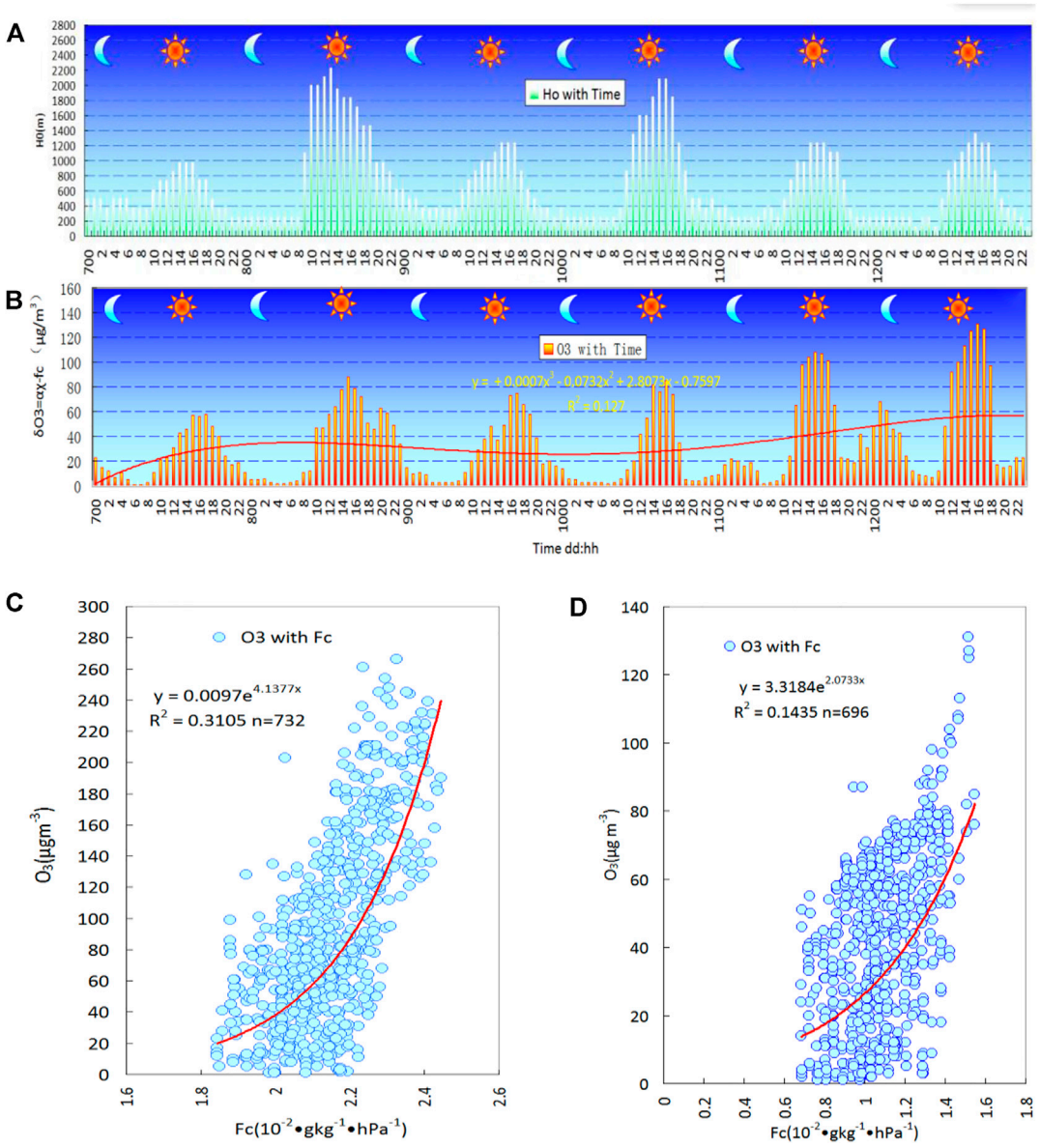

FIGURE 7
During period from February 7 to 12 2020 in Beijing, **(A)**: for hourly the time series of cloud high (H0) in local time, and **(B)**: the time series of precursor wetting process of O_3 in local time. **(C)**: Correlation analysis of Fc with O_3 for 1 to 6 July 2019 for Beijing, corresponding to Figure 6D and **(D)**: 7 to 12 February, 2020 for Beijing, corresponding to Figure 7B.

exceeds 0.001. This suggests that the increase in condensation rate (F_c) is conducive to accelerating and catalyzing the formation of an increase in O_3 concentration.

In summary, it can be seen that the influence of meteorological conditions on the increase in O_3 concentration can aggravate O_3 pollution. The above evidence of the value-added effect of changes in high-resolution meteorological elements on O_3 concentration shows that although the existing understanding based on the chemical mechanism of O_3 formation is based on an approximation of an incomplete knowledge of photochemistry, the increase in O_3 concentration can be extended from the zenith angle peak described in PLOM, which means that wavelength-dependent photochemistry is linked to the influence of clouds on optical characteristics, and the effects of cloud height (the height of the pollution mixed layer) are also included in the design of PLOM. The increase in condensation rate (F_c) in the air is also conducive to accelerating and catalyzing the formation of an increase in O_3 concentration. Therefore, it is practical and necessary for this study, to establish quantitative PLOM parameters, focusing on

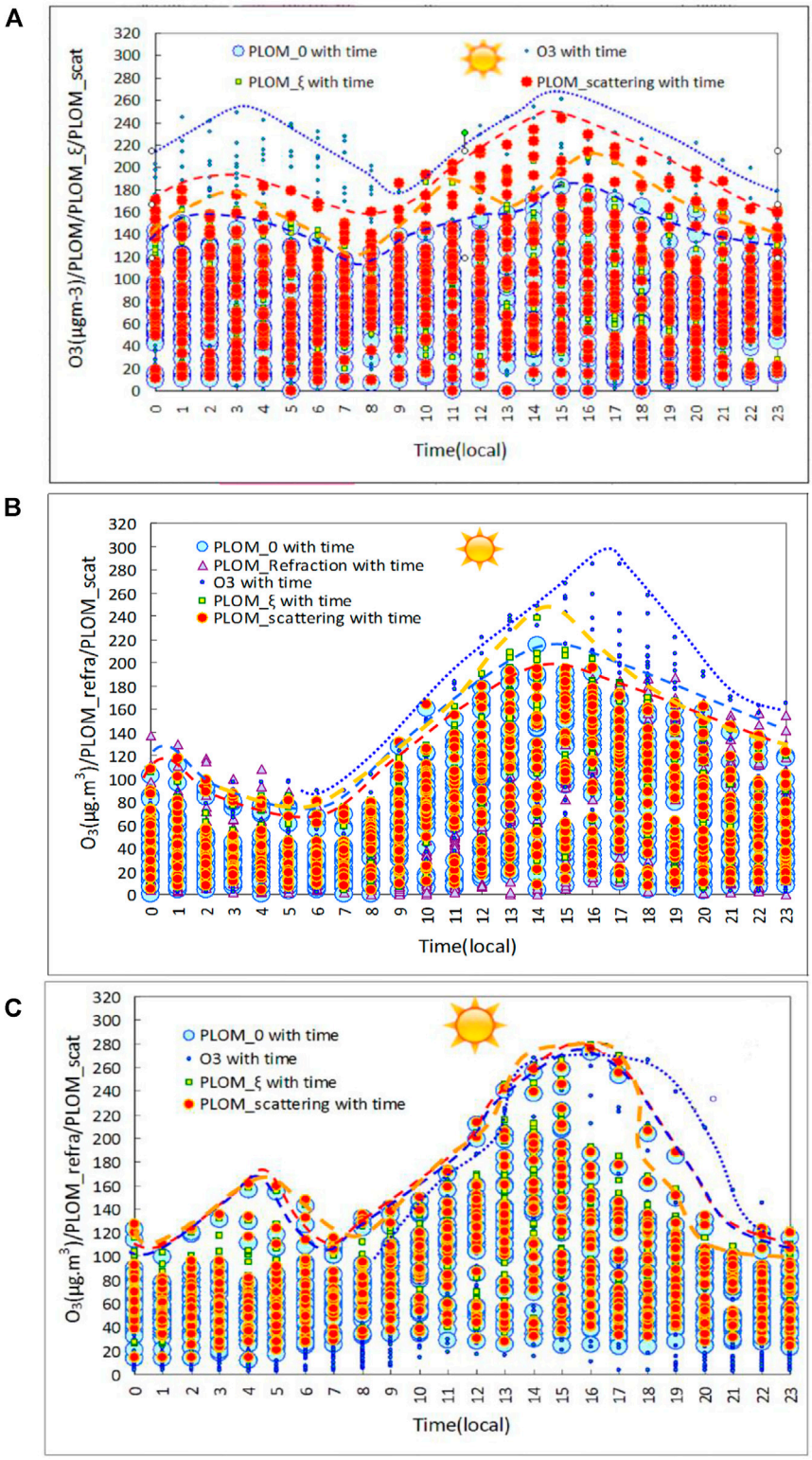

FIGURE8
(A): Time series of PLOM_0 (blue dotted line), PLOM with scattering effect (red dashed line), PLOM_$\xi(\delta O_3 = \alpha(NO_2)^{-fc})$with contributed by O_3 precursors (yellow dashed line), as well as O_3 concentration (blue thin dotted line) in Beijing from 1 to 31 July, 2019. **(B)**: Similar to **(A)**, but in Hangzhou from 1 to 30 September, 2015. **(C)**: in Guangzhou from 1 to 31 July, 2019. The red fill circle and red dashed line represent the distributions of PLOM and the outline of its maximum values, includes additional cloud scattering effects at daytime respectively. The filled circle with relative larger

(*Continued*)

FIGURE8 (Continued)
light blue fill and blue dashed line represent the values of PLOM_0 and outline of its maximum values, respectively. Small rectangular icons with green boxes and yellow fills, along with yellow dotted lines, represent the distributions of PLOM_ξ ($\delta O_3 = \alpha(NO_2)^{-fc}$)and the outline of its maximum values, respectively. The blue small circle and thin dotted line represent the observed values of O_3 and outline of its maximum values of O_3, respectively. The triangle describes the contributions of sunlight refraction to O_3 weakening.

and supplementing the additional effect of meteorological conditions on increasing more O_3 values.

3.2.3 Diurnal variation characteristics of O_3 increases due to cloud scattering

In order to consider the PLOM parametric description based on the effect of solar altitude angle diurnal changes on O_3 in the establishment of the PLOM index, consider the contribution of higher atmospheric condensation rate (f_c) to fine particulate matter and O_3 precursors, which is conducive to O_3 growth. This is because the impact of changes in atmospheric condensation rate (f_c) can also cover the indirect contribution of clouds to O_3 growth, including the contribution of diurnal variations in cloud height (height of the mixed layer of pollution) to O_3 growth (see Figures 6, 7). Based on the describing ability of PLOM mentioned above, by using a kind of the daily cycle synthesis profile analysis method (Wang et al., 2019), an analyzing of the different regional differences in the hourly distribution of cloud scattering effects of each parameter in NCP, YRD and PRD during severe O_3 pollution was given as shown in Figure 8.

Figure 8 shows the diurnal cycle synthetic sections of the hourly distribution of the effects of cloud scattering and the hourly distribution of O_3 precursor conversion with O_3 concentration during the severe O_3 pollution period in Beijing from July 1 to 31, 2019 (Figure 8A), in Hangzhou from September 1 to 30, 2015 (Figure 8B), and in Guangzhou from July 1 to 31, 2019 (Figure 8C).

The solar zenith angle has some different effect on the diurnal variation in O_3 concentration in the inland and coastal areas. The solar zenith angle $\Theta_z = 0^\circ$ represents noon (local time). Unlike the near-coastal areas close to Hangzhou and Guangzhou, the diurnal variation in O_3 concentration shows a significant double peak in Beijing, which occurs at 03:00-08:00 (4–9 h before noon) and 14:30 (2.5 h after noon). The O_3 concentration was as high as 250 μg m^{-3} in the morning and 266 μg m^{-3} at 14:00. The peak value of O_3 was observed in the afternoon only in Hangzhou and Guangzhou, at 17:30 and 16:00, respectively, lagging behind noon by 4–5.5 h, 1.5-3 h behind that in the NCP. The contribution of O_3 precursors to the increase in O_3 concentration was 28% in Beijing, and 11% and 13% in Hangzhou and Guangzhou, respectively (Table 2 and Figures. 8A–C). The bimodal distribution of O_3 concentration in the morning and afternoon in Beijing was 10 h ahead of and 4 h behind noon. The Hangzhou and Guangzhou lag was 2.5–4.5 h.

Micrometeorological conditions had a greater influence on the wetting process of O_3 precursors, and the lag period and influence intensity were significantly different between the north and south areas. In addition, the contribution of cloud scattering to the increment in O_3 concentration was 19%, 8%, and 4% in Beijing, Hangzhou, and Guangzhou, respectively (indicated by the red dotted line and red solid circle in Figure 8). The impact intensity in the NCP was more than twice that in the YRD and PRD, and the peak lagged about 2.5–4.5 h behind noon. The loss rate of tropospheric O_3 concentration caused by cloud refraction in Hangzhou was −6%, and the lag time was up to 6 h.

In summary, meteorological conditions, including the scattering and refraction of sunlight by clouds and atmospheric condensation, have an obvious effect on the wetting process of O_3 precursors. They also have a significant impact on the occurrence time and intensity of the tropospheric O_3 concentration peak, which shows that the PLOM index is of great significance in the diagnosis and prediction of the temporal and spatial distribution of severe O_3 pollution.

3.3 Quantitative comparative analysis of application of Parameterization to Link Ozone-pollution with Meteorological index to meteorological conditions and emission reduction during typical severe pollution cases

Zhang et al. (2009; 2018b) proposed a quantitative and objective evaluation method based on the PLAM index for the contribution of meteorological conditions and emission to aerosol pollution. This method can provide an important objective basis for the government to assess and make emission reduction decisions (Zhang et al., 2009; Wang et al., 2018). For aerosol pollution, the objective and quantitative discrimination of the rate of change of the contribution of meteorological conditions is $\lambda = (\alpha_B - \alpha_A)/\alpha_B$. α_B and α_A represent the slope of the fitting curve between the PLAM index and aerosol pollution concentration (e.g., $PM_{2.5}$) during the different periods (B and A), respectively (Zhang et al., 2018b). The PLAM index discrimination principle is also applicable to the PLOM index in this study. Figure 9 shows the comparison between PLOM during severe O_3 pollution in 2019 and the same period in 2018. For severe O_3 pollution in 2019, compared with meteorological conditions in the same periods in 2018, the discrimination is $\lambda = (\alpha_{2018} - \alpha_{2019})/\alpha_{2018}$.

TABLE 2 Effects of Θ_z on tropospheric ozone concentrations based on cloud scattering, refraction, and ozone precursors.

City	Peak time of O_3	Hours ahead of/ behind Θ_z = 0	Contribution rate of O_3 affected by ξ (%)	Hours behind Θ_z = 0° due to ξ influences	Contribution rate of O_3 affected by cloud scattering (%)	Hours behind Θ_z = 0° due to cloud scattering influences	Contribution rate of O_3 affected by cloud reflections
BJ	01:00/14:30	10/2.5	28	4.0	19	2.5	—
HZ	17:30	/5.5	11	2.5	8	2.5	−6%
GZ	16:30	/4.5	13	4.5	4	4.5	—

TABLE 3 Comparison of contribution of meteorological conditions in 2019 and 2018.

Year	Contrast studies	α	Average O_3 concentration
2018	Observation in 2018	2.16	90.8 μg m^{-3}
2019	Observation in 2019	1.46	95.5 μg m^{-3}
2019	If no emission reduction in 2019	—	119.9 μg m^{-3}
2019 to 2018	λ = (α2018 - α2019)/α2018	0.32	—

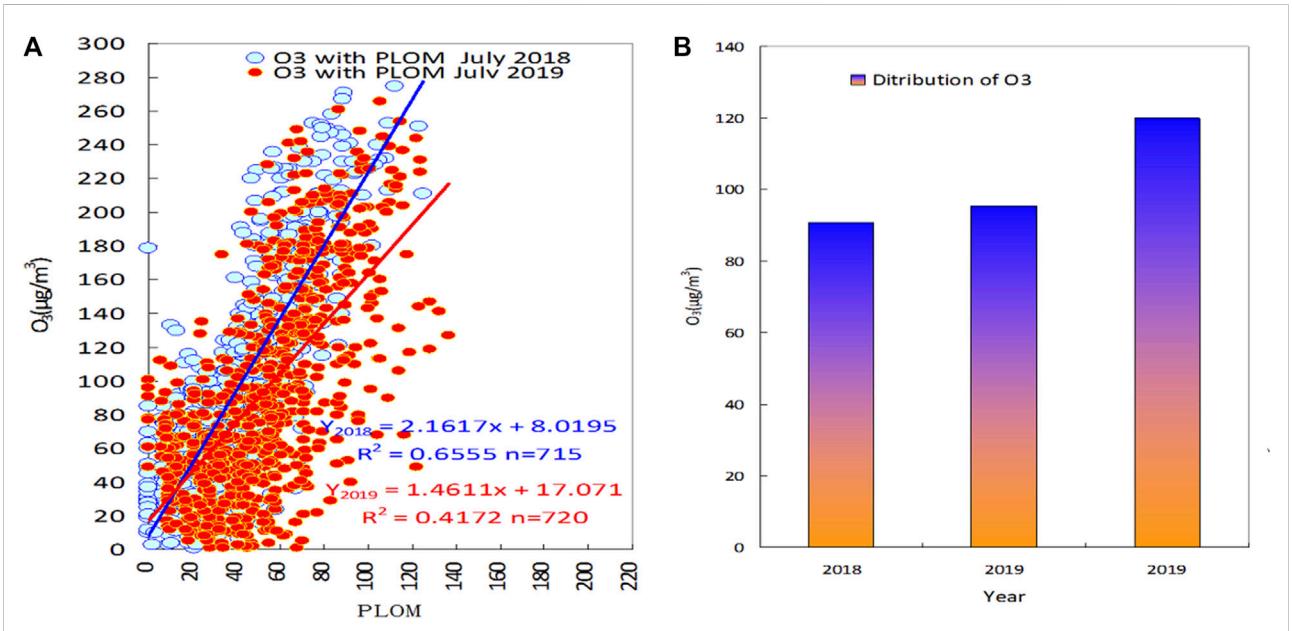

FIGURE 9
(A): Comparison analyses of contribution of meteorological conditions between typical severe O_3 pollution in 2019 and 2018; **(B)**: The observational O_3 concentration in 2018 and 2019 (left and medium), and regardless of emission reductions, O_3 concentrations in 2019 (right).

Compared with the observed change in O_3 concentration in 2018, the O_3 concentration was expected to increase by 32% due to unfavorable meteorological conditions in 2019; however, the actual observation only increased by −4.9%, indicating that the emission reductions still contributed to a reduction in O_3 concentration by −27.1%.

The variation rate of unfavorable meteorological conditions for O_3 concentration was 32% in 2019; under the same meteorological conditions, the average value of O_3 concentration can be the higher value of 119.9 μg m^{-3} in 2019 (see Figure 9B (right)). The monthly average observed value of O_3 concentration was 95.5 μg m^{-3}, a decrease of 25–30%, which

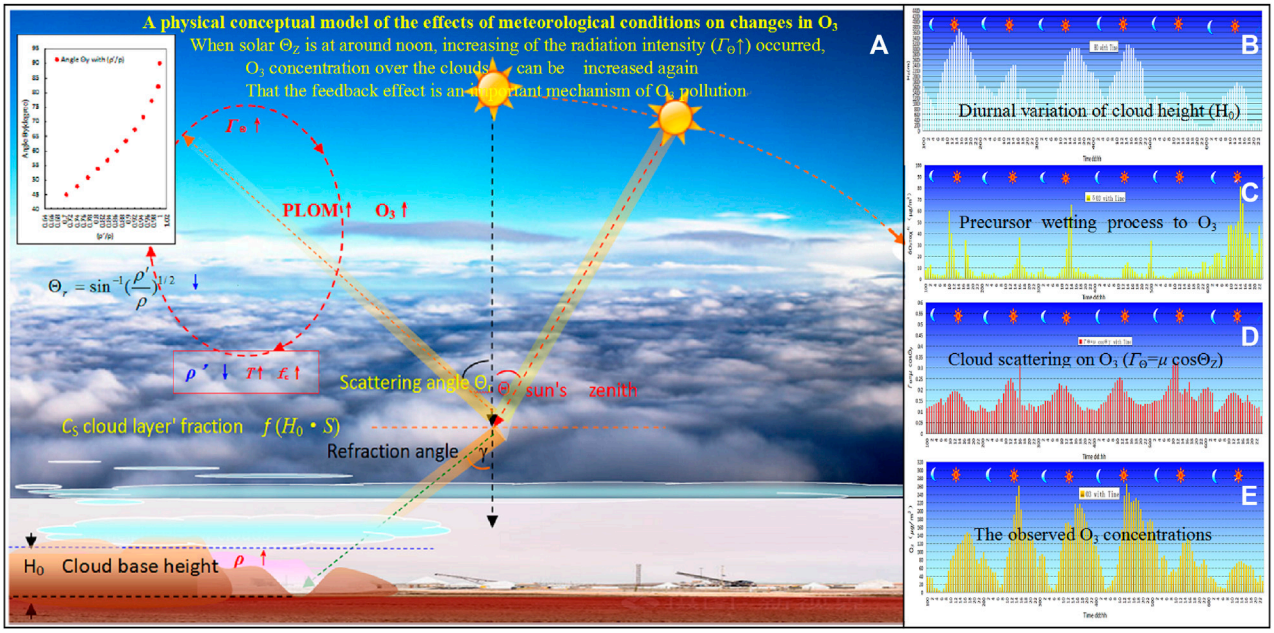

FIGURE 10
Conceptual diagram of the effect of meteorological conditions on ozone pollution.

indicates the importance of the contribution of emission reduction measures (Table 3).

4 Conclusion

The relationship between tropospheric O_3 pollution and meteorological conditions in the main sensitive areas in China was analyzed and demonstrated, by using the atmospheric component data for Beijing, Hangzhou, and Guangzhou. Based on quantitative description theories of cloud scattering, cloud height, cloud volume, and cloud structure changes, as well as feedback effects caused by water vapor condensation, a parametric PLOM index model for the analysis and diagnosis of O_3 pollution events was established. Clouds are representative parameters that affect the multi-parametric variations of meteorological conditions, and it covers both direct and indirect effects. The design of the PLOM index introduces changes in cloud structure, so that the effects of cloud shape, cloud height, solar zenith angle, cloud scattering, etc. Are included. And a closer relationship with water vapor condensation related to the transformation of O_3 precursors, leading to the temporal and spatial variations in the tropospheric O_3 concentration is included also. The comprehensive structure of the index puts forward a diagnostic quantitative model and physical concept for the influence of meteorological conditions on the variation in O_3 concentration, as shown in the Figure 10. The major findings were as follows:

(1) Under conditions with influence clouds, the incremental values of O_3 concentrations exhibit a process of cyclic feedback and reinforcement. When the difference in the cloud scattering angle (Θ_r) above the cloud and in the cloud is smaller (e.g., 0–45°), the solar radiation (luminance) increases, and the PLOM index and O_3 concentration increase again.

(2) Under the condition of having influence clouds, feedback effect is an important mechanism of O_3 pollution due to density decreases (increases) in the upper (lower) level over (below) the cloud, which is associated with solar radiation intensity over the clouds.

(3) The PLOM index diagnosis of typical severe O_3 pollution cases shows the effect of cloud scattering significantly contributes to the increase in tropospheric O_3 concentration. The contribution rates were 19%, 8%, and 4% in Beijing, Hangzhou, and Guangzhou, respectively. The significant regional difference in precursor wetting triggered by micrometeorological impacts on the increase in O_3 concentration indicates that it has a more obvious impact inland.

(4) The PLOM index has universality and expressive ability. The correlation analysis of four typical cases of severe O_3 pollution in Beijing (0.42), Hangzhou (0.53), and Guangzhou (0.62) revealed that the PLOM index positively correlated with the change in O_3 concentration.

(5) The PLOM index established in this study can provide a quantitative and objective basis, and decision-making guidance, for the Meteorological Forecasting Center's

consultation to accurately assess the relative contribution of emission reduction and meteorological conditions.

Data availability statement

The original contributions presented in the study are included in the article/Supplementary Material, furtherinquiries can be directed to the corresponding author.

Author contributions

JW, DW, and YY designed the research and led the overall scientific questions. YY, DW, XJ, WJ, and YW carried out data processing and analysis. WJ and XJ helped with data processing. DW wrote the first draft of the manuscript and then JW revised the manuscript. All authors read and approved the final version.

Funding

This study is supported jointly by the Major National Natural Science Foundation of China Project (42090031), the National Natural Science Foundation of China Project (U19A2044), National Natural Science Foundation of China (41675121), the Basic Scientific Research Progress of the Chinese Academy of Meteorological Sciences (2016Z001), the National Key Project of Basic Research (2014CB441201, 453172).

Acknowledgments

The authors would like to thank Academician Zhang X.Y. for his valuable suggestions and comments.

Conflict of interest

The authors declare that the research was conducted in the absence of any commercial or financial relationships that could be construed as a potential conflict of interest.

Publisher's note

All claims expressed in this article are solely those of the authors and do not necessarily represent those of their affiliated organizations, or those of the publisher, the editors and the reviewers. Any product that may be evaluated in this article, or claim that may be made by its manufacturer, is not guaranteed or endorsed by the publisher.

References

Ackerman, A. S., Kirkpatrick, M. P., Stevens, D. E., and Toon, O. B. (2004). The Impact of humidity above stratiform clouds on indirect aerosol climate forcing. *Nature* 21, 1014–1017. doi:10.1038/nature03174

Bohn, B., Corlett, G. K., Gillmann, M., Sanghavi, S., Stange, G., Tensing, E., et al. (2008). Photolysis frequency measurement techniques: Results of a comparison within the ACCENT project. *Atmos. Chem. Phys.* 8, 5373–5391. doi:10.5194/acp-8-5373-2008

Bokoye, A. I., Royer, A., O'Neil, N. T., Cliche, P., Fedosejevs, G., Teillet, P., et al. (2001). Characterization of atmospheric aerosols across Canada from a ground-based sunphotometer network: Aerocan. *Atmosphere-Ocean* 39 (4), 429–456. doi:10.1080/07055900.2001.9649687

Dunya, A., Philippe, K., Alain, S., Bock, O., Irbah, A., Bekki, S., et al. (2017). Enhanced MODIS atmospheric total water vapour content trends in response to arctic amplification. *Atmosphere* 8 (12), 241. doi:10.3390/atmos8120241

Hu, Y. T., Zhao, P., Niu, J. F., Sun, Z., Zhu, L., and Ni, G. (2016). Canopy stomatal uptake of NOX, SO2 and O3 by mature urban plantations based on sap flow measurementflow measurement. *Atmos. Environ. X.* 125, 165–177. doi:10.1016/j.atmosenv.2015.11.019

Humphreys, W. J. (1940). *Physics of the air*. 3rd Ed., 676. Part3:Chaptre1).

Kuo, H. L. (1961). Convection in conditionally unstable Atmosphere. *Tellus* 13, 441–459. doi:10.1111/j.2153-3490.1961.tb00107.x

Kuo, H. L. (1974). Further studies of the parameterization of the influence of cumulus convection on large-scale flow. *J. Atmos. Sci.* 31, 1232–1240. doi:10.1175/1520-0469(1974)031<1232:fsotpo>2.0.co;2

Kuo, H. L. (1965). On formation and intensification of tropical cyclones through latent heat release by cumulus convection. *J. Atmos. Sci.* 22, 40–63. doi:10.1175/1520-0469(1965)022<0040:ofaiot>2.0.co;2

Li, J., Chen, H. B., Li, Z. Q., Wang, P., Cribb, M., and Fan, X. (2015). Low-level temperature inversions and their effect on aerosol condensation nuclei concentrations under different large-scale synoptic circulations. *Adv. Atmos. Sci.* 32 (7), 898–908. doi:10.1007/s00376-014-4150-z

Li, Y., Wang, W., Wang, J. Z., Zhang, X., Lin, W., and Yang, Y. (2011). Impact of air pollution control measures and weather conditions on asthma during the 2008 Summer Olympic Games in Beijing. *Int. J. Biometeorol.* 55, 547–554. doi:10.1007/s00484-010-0373-6

Liu, L. K., Zhang, X. Y., Zhong, J. T., Wang, J., and Yang, Y. (2019). The 'two-way feedback mechanism' between unfavorable meteorological conditions and cumulative PM2.5 mass existing in polluted areas south of Beijing. *Atmos. Environ. X.* 208, 1–9. doi:10.1016/j.atmosenv.2019.02.050

Madronich, S., and Flocke, S. (1999). *The role of solar radiation in atmospheric chemistry*. Berlin, Heidelberg: The Handbook of Environmental Chemistry.

Platnick, S., Durkee, P. A., Nielsen, K., Taylor, J. P., Tsay, S. C., King, M. D., et al. (2000). The role of background cloud microphysics in the radiative formation of ship tracks. *J. Atmos. Sci.* 57, 2607–2624. doi:10.1175/1520-0469(2000)057<2607:trobcm>2.0.co;2

Qu, H., and Chen, S. B. (2002). The application prospect of the medium resolution imaging spectrometer (MODIS) data in geosciences. *World Geol.* 21, 176–180.

Sheng, Z. Z., Che, H. Z., Chen, Q., Xia, X., Liu, D., Wang, Z., et al. (2019). Aerosol vertical distribution and optical properties of different pollution events in Beijing in autumn 2017. *Atmos. Res.* 215, 193–207. doi:10.1016/j.atmosres.2018.08.029

Tang, X. Y., Zhang, Y. H., and Shao, M. (2006). *Atmospheric environmental chemistry*. China: Higher Education Press.

Textor, C., Schulz, M., Guibert, S., Kinne, S., Balkanski, Y., Bauer, S., et al. (2006). Analysis and quantification of the diversities of aerosol life cycles within AeroCom. *Atmos. Chem. Phys.* 6, 1777–1813. doi:10.5194/acp-6-1777-2006

Tverski, P. H. (1954). *Introduction to meteorology*. Russian: Hydrometeorology Press.

Wang, D. Y., Wang, J. Z., Yang, Y. Q., Liangke, L., Junting, Z., and Yaqiang, W. (2021). Formation mechanism of heavy haze-fog associated with the interactions

between different scales of atmospheric processes in China. *Atmos. Pollut. Res.* 12, 101085. doi:10.1016/j.apr.2021.101085

Wang, H. L., and McFarquhar, G. M. (2008). Modeling aerosol effects on shallow cumulus convection under various meteorological conditions observed over the Indian Ocean and implications for development of mass-flux parameterizations for climate models. *J. Geophys. Res.* 113 (D20), D20201. doi:10.1029/2008jd009914

Wang, H., Lyu, X. P., Guo, H., Wang, Y., Zou, S., Ling, Z., et al. (2018). Ozone pollution around a coastal region of South China Sea:interaction between marine and continental air. *Atmos. Chem. Phys.* 18, 4277–4295. doi:10.5194/acp-18-4277-2018

Wang, J. Z., Gong, S., Zhang, X. Y., Yang, Y. Q., Hou, Q., Zhou, C. H., et al. (2012). A parameterized method for air-quality diagnosis and its applications. *Adv. Meteorology* 238589, 1–10. doi:10.1155/2012/238589

Wang, J. Z., Yang, Y. Q., Jiang, X. F., Wang, D. Y., Zhong, J. T., and Wang, Y. Q. (2022). Observational study of the PM2.5 and O3 superposition-composite pollution event during spring 2020 in Beijing associated with the water vapor conveyor belt in the northern hemisphere. *Atmos. Environ. X.* 272, 118966. doi:10.1016/j.atmosenv.2022.118966

Wang, J. Z., Yang, Y. Q., Zhang, X. Y., Liu, H., Che, H., Shen, X., et al. (2017). On the influence of atmospheric super-saturation layer on China's heavy haze-fog events. *Atmos. Environ. X.* 171, 261–271. doi:10.1016/j.atmosenv.2017.10.034

Wang, J. Z., Yang, Y. Q., Zhang, Y. M., Niu, T., Jiang, X., Wang, Y., et al. (2019). Influence of meteorological conditions on explosive increase in O3 concentration in troposphere. *Sci. Total Environ.* 652, 1228–1241. doi:10.1016/j.scitotenv.2018.10.228

Wang, S. L., and Chai, F. H. (2002). A study on O3 pollutions in Beijing, 2002. *Geo-Science (in Chin.* 22 (3), 360–364.

Webb, A. R., and Steven, M. D. (1986). Daily totals of solar UVB radiation estimated from routine meteorological measurements. *J. Climatol.* 6, 405–411. doi:10.1002/joc.3370060406

Yang, D. S., Liu, Y. B., and Liu, S. K. (1982). Dynamics of meteorology. 297–359.

Yang, Y. Q., Wang, J. Z., Hou, Q., and Yaqiang, W. (2009). A plam index for Beijing stabilized weather forecast in summer over Beijing. *J. Appl. Meteorol. Sci. (in Chin.* 20, 643–649.

Yang, Y. R., Liu, X. G., Qu, Y. J., An, J. L., Jiang, R., Zhang, Y. H., et al. (2015). Characteristics and formation mechanism of continuous hazes in China: A case study during the autumn of 2014 in the north China plain. *Atmos. Chem. Phys.* 15 (14), 8165–8178. doi:10.5194/acp-15-8165-2015

Zhang, X. Y., Sun, J. Y., Wang, Y. Q., Li, W. J., Zhang, Q., Wang, W. G., et al. (2013). Factors contributing to haze and fog in China (in Chinese). *Chin. Sci. Bull.* 58, 1178–1187.

Zhang, X. Y., Wang, Y. Q., Lin, W. L., Zhang, Y. M., Zhang, X. C., Gong, S., et al. (2009). Changes of atmospheric composition and optical properties over beijing 2008 olympic monitoring Campaign. *Bull. Am. Meteorol. Soc.* 90 (11), 1633–1652. doi:10.1175/2009bams2804.1

Zhang, X. Y., Zhong, J. T., Wang, J. Z., Wang, Y., and Liu, Y. (2018). The interdecadal worsening of weather conditions affecting aerosol pollution in the Beijing area in relation to climate warming. *Atmos. Chem. Phys.* 18, 5991–5999. doi:10.5194/acp-18-5991-2018

Zhang, Y. M., Wang, J. Z., Yang, Y. Q., Li, D., Wang, Y. Q., Che, H., et al. (2018). Contribution distinguish between emission reduction and meteorological conditions to "Blue Sky". *Atmos. Environ. X.* 190, 209–217. doi:10.1016/j.atmosenv.2018.07.015

Zhang, Y. M., Zhang, X. Y., Sun, J. Y., Lin, W. L., Gong, S. L., Shen, X. J., et al. (2011). Characterization of new particle and secondary aerosol formation during summertime in Beijing, China. *Tellus B* 63, 382–394. doi:10.3402/tellusb.v63i3.16221

Zhao, Q., Yao, W., Zhang, C., Wang, X., and Wang, Y. (2019). Study on the influence of fog and haze on solar radiation based on scattering-weakening effect. *Renew. Energy* 134, 178–185. doi:10.1016/j.renene.2018.11.027

frontiers | Frontiers in Environmental Science

TYPE Original Research
PUBLISHED 10 October 2022
DOI 10.3389/fenvs.2022.1002412

OPEN ACCESS

EDITED BY
Gen Zhang,
Chinese Academy of Meteorological Sciences, China

REVIEWED BY
Chi Yang,
Nanjing University of Information Science and Technology, China
Chong Shi,
Aerospace Information Research Institute (CAS), China
Zirui Liu,
Institute of Atmospheric Physics (CAS), China

*CORRESPONDENCE
Jing Li,
jing-li@pku.edu.cn

SPECIALTY SECTION
This article was submitted to Atmosphere and Climate, a section of the journal Frontiers in Environmental Science

RECEIVED 25 July 2022
ACCEPTED 31 August 2022
PUBLISHED 10 October 2022

CITATION
Xiong C, Li J, Liu Z and Zhang Z (2022), The dominant role of aerosol-cloud interactions in aerosol-boundary layer feedback: Case studies in three megacities in China.
Front. Environ. Sci. 10:1002412.
doi: 10.3389/fenvs.2022.1002412

The dominant role of aerosol-cloud interactions in aerosol-boundary layer feedback: Case studies in three megacities in China

Changrui Xiong[1], Jing Li[1]*, Zhenxin Liu[2] and Zhenyu Zhang[1]

[1]Department of Atmospheric and Oceanic Sciences, School of Physics, Peking University, Beijing, China, [2]School of Environmental Science and Engineering, Nanjing University of Information Science and Technology, Nanjing, China

Interactions between aerosols and meteorology have received increasing attention in recent decades. Through interactions with radiation, aerosols involve in thermodynamic processes and cause cloud adjustment, referred to as the direct and semi-direct effects respectively. They also involve in cloud microphysical processes by severing as cloud condensation nuclei or ice nuclei, referred to as indirect effect. Aerosol direct effect is found to potentially exacerbate air quality by stabilizing the planetary boundary layer (PBL). However, their impacts through the interaction with clouds, including semi-direct and indirect effect remain unclear. In this study, we conducted model simulations to evaluate the direct, semi-direct and indirect effects of aerosols in PBL structure and surface $PM_{2.5}$ concentration during three heavy haze events under overcast conditions. Overall, the aerosol-PBL feedback results in a 22%–36% decrease of PBL height and 5%–28% increase of $PM_{2.5}$ concentration. The indirect effect always has the largest impact on PBL and $PM_{2.5}$ pollution, accounting for 59%–84% of the changes. The semi-direct effect is the weakest on average, although it can exceed the direct effect at certain times and locations. Black carbon aerosols play the vital role in both the direct and semi-direct effects. Our findings promote the understanding of heavy haze formation, and highlight the dominant role of aerosol-cloud interaction in the feedback process of aerosols to PBL structure and air quality.

KEYWORDS

semi-direct effect, aerosol-radiation interactions, aerosol-cloud interactions, black carbon aerosol, planetary boundary layer, WRF-Chem

Introduction

Rapid industrialization and urbanization in China have been accompanied by frequent occurrence of heavy haze in the past decade (Chandran Govindaraju and Tang, 2013; Li et al., 2016). High intensity of anthropogenic emissions (Chan and Yao 2008; Huang et al., 2014a), fast formation of secondary aerosols (Huang et al., 2014b;

Huang et al., 2021), as well as unfavorable meteorological conditions are identified as the main causes of aerosol pollution (Wu et al., 2013; Miao et al., 2017; Shu et al., 2017; Zhang et a., 2018a; Ning et al., 2018). Specifically, as air pollutants emitted from the ground are generally located within the planetary boundary layer, the structure and process of the PBL are critical in the formation of pollution events (Li et al., 2017; Miao and Liu, 2019; Miao et al., 2021).

Aerosol pollutions, on the other hand, interact with the atmosphere *via* complex mechanisms, which include the direct, semi-direct and indirect effect (IPCC, 2013). These interactions could in turn alter PBL height and structure, and thus inducing feedbacks to the surface pollutions. By scattering and/or absorbing radiation, aerosol direct effect may lead to cooling at surface and warming aloft in the daytime, which suppresses the development of PBL (Ding et al., 2013; Wilcox et al., 2016; Zhong et al., 2019; Su et al., 2020). This further induces a positive feedback to air pollution through the accumulation of primary pollutants as well as the acceleration of secondary aerosols formation (Petäjä et al., 2016; Tie et al., 2017; Liu et al., 2018a; Miao et al., 2019). More specifically, black carbon (BC) has been identified as the key component in exacerbation of air quality, due to its strong light absorption and radiative heating effect (Bond et al., 2013; Wang et al., 2013; Ding et al., 2016; Wang et al., 2018; Liu et al., 2019). Previous studies have estimated that magnitude of surface $PM_{2.5}$ concentration enhancement through aerosol direct effect vary from a few percent to around 30% throughout severe haze events over Northern China (Wang et al., 2014a; Wang et al., 2014b; Wang et al., 2015; Wu et al., 2019; Li et al., 2020; Wang et al., 2021). However, these studies mainly focus on the direct effect under clear sky conditions. There is still lack of investigation of the semi-direct and indirect effect when there are clouds.

Over Southern China, heavy pollution and clouds frequently coexist during the winter season (King et al., 2013; Song et al., 2017; Ye et al., 2018), which involves active interaction between aerosols and clouds. It is therefore crucial to evaluate the feedbacks of aerosols to PBL and surface pollution under cloudy conditions. Previous studies have revealed that BC may heat the cloud layer and promote cloud evaporation (semi-direct effect; Hansen et al., 1997; Ackerman et al., 2000; Koch and Del Genio, 2010). The reduction of cloud cover can increase the shortwave flux reaching the surface, which may offset or even dominate over the direct effect (Forkel et al., 2012; Liu et al., 2018b). Given its opposite impact through direct and semi-direct effect, it is intriguing to know whether BC will enhance or reduce pollution under cloudy conditions. In addition, Zhao et al. (2017) also pointed out the critical role of indirect effect in aerosol-PBL feedback, which increases cloud droplet number concentration (CDNC) and liquid water path (LWP), decreases net shortwave flux at surface and suppresses the development of PBL, therefore resulting in an up to 25% enhancement of aerosol concentration.

Although considerable efforts have been made to quantify aerosol feedbacks, the relative effect of aerosol-cloud interaction to the direct effect remain uncertain as previous studies give different estimates (Zhang et al., 2015; Gao et al., 2015; Gao et al., 2016; Zhang et al., 2017; Zhang et al., 2018b; Gao et al., 2020). Moreover, few studies have investigated the mechanism of aerosol semi-direct effect on PBL and surface pollution, or quantified its contribution. However, it is necessary to isolate the direct and semi-direct effect as their impact on PBL become much more complex when they coexist. In light of the above discussion, here we aim to evaluate the individual contribution of aerosol direct, semi-direct as well as indirect effects to PBL structure and surface pollution during haze events under cloudy conditions, and to identify the dominant effect.

Methods

Model configurations

In this study, we use Weather Research and Forecasting model coupled to Chemistry (WRF-Chem) (Grell et al., 2005) to investigate aerosol effects during the typical haze events in three megacities in China characterized with high cloud fraction. This model fully couples meteorology with chemistry, which simulates aerosol radiative effect (including direct and semi-direct effect) as well as indirect effect. We conduct the simulation with three nested domains. The horizontal resolutions are 30 km, 6 km, and 3 km for domain 1 (outmost), domain 2 (middle), and domain 3 (innermost), respectively. The outermost domain 1 covers most parts of China. While the innermost nested domain 3 covers the studied city, including Shanghai, Wuhan and Zhengzhou respectively, with 130 × 130 grid cells (Figure 1). The vertical grids include 47 layers from the surface to 100 hPa with denser layers within the PBL. Meteorological initial and lateral boundary conditions are obtained from the National Centers for Environmental Prediction's Final Analysis data at 1-degree horizontal resolution and 6-h temporal intervals. Four dimensional data assimilation (FDDA) is utilized during the model spin up period, which lasted for 3 days. Surface and radiosondes observational weather data are also assimilated in the simulations using WRF OBSGRID program, which significantly improves the simulated cloud properties. Note that all the assimilation is turned off in the innermost domain throughout the experiment to allow full aerosol-cloud-radiation interactions. Anthropogenic emissions in China are obtained from the Multi-resolution Emission Inventory for China (MEIC) (Liu et al., 2016). Daily biomass burning emissions in 2016 at spatial resolution of 1 km are obtained from the Fire Inventory from NCAR version-1.5 (FINNV1.5) (Wiedinmyer et al., 2011). Biogenic emissions are calculated online in WRF-Chem using the MEGAN algorithm version 2 (Guenther et al., 2006). Dust emissions follows Shao. (2001).

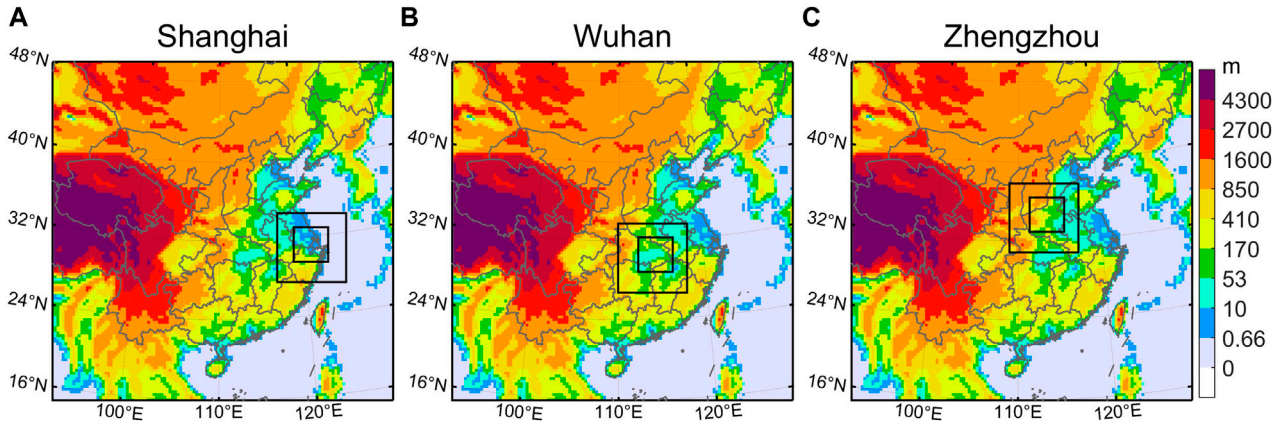

FIGURE 1
The WRF-Chem modeling domain for the case of **(A)** Shanghai, **(B)** Wuhan, and **(C)** Zhengzhou. The outmost region represents domain 1, while the black rectangle in the middle represents domain 2, and the innermost black rectangle represents domain 3.

The Carbon-Bond Mechanism version Z (CBM-Z) gas-phase chemistry mechanism (Zaveri and Peters, 1999) as well as the Model for Simulating Aerosol Interactions and Chemistry (MOSAIC 4-bins) aerosol module (Zaveri et al., 2008) are employed in the model. For aerosol radiative effect, aerosol optical properties are calculated based on the Mie theory assuming internally mixing of chemical compositions (Barnard et al., 2010), and passed to RRTMG radiation scheme (Iacono et al., 2008). For aerosol indirect effect, aerosol activations are parameterized with the scheme of Abdul-Razzak and Ghan (2002). CDNC derived according to the aerosol activations is passed to the RRTMG radiation and Lin microphysics scheme (Lin et al., 1983), to affect the optical properties of cloud and the collision and coalescence rates of cloud droplets to form raindrops, respectively. In addition, we increase the lower limit of the PBL mixing coefficient for aerosols and gases in order to improve model representation of vertical distribution as well as diurnal variation of PM2.5 concentration, following Du et al. (2020). Main physical and chemical parametrizations adopted in this study are as summarized in Supplementary Table S1.

To achieve better representativeness, we adopt an ensemble approach in our simulation of Shanghai case. The initial ensemble is generated with the three-dimensional variational data assimilation system of the WRF (WRF-3DVAR) (Barker et al., 2004) using cv5 option. Perturbation standard deviations generated based on model error covariance are approximately 1 K for the potential temperature, 1 g/kg for the water vapor mixing ratio, 0.5 m/s for the horizontal wind components and 0.2 hPa for the pressure. Perturbations are added to the initial field of the base simulation (first member) in the innermost domain to form a total of 10 ensemble members in our study. Our method in generating ensemble initials using WRF-3DVAR follows Barker (2005) and Meng and Zhang. (2008).

Isolating the direct and semi-direct effect

In particular, we develop a novel scheme, as shown in Figure 2, to separate the direct and semi-direct effect of aerosols. A set of three model experiments are designed: without aerosol radiative feedback (ExpA), with aerosols radiative feedback (ExpC), and an intermediate experiment (ExpB). Among them, the differences between ExpA and ExpC represent total aerosol radiative effect. While in ExpB, cloud properties are imported from ExpA and aerosol optical properties are imported from ExpC, which are the key procedures to isolate the direct and semi-direct effect. As can be seen, the only differences between ExpA and ExpB are the aerosol optical properties, which represent direct effect. The only differences between ExpB and ExpC are the cloud properties, which represent semi-direct effect. Similar framework in isolating direct effect and cloud response has been adopted in previous studies, in which aerosol optical properties and clouds are imported into multiple diagnostic radiation routines, in order to separate the radiative forcing by these effects (Liu et al., 2018b; Ghan et al., 2012). In our study, aerosol optical properties and clouds are imported into the meteorology chemistry model WRF-Chem to force the simulation, so that we can not only evaluate changes of radiative flux from radiation module, such as net shortwave flux at surface shown in this study, but also evaluate changes of PBL structure and surface $PM_{2.5}$ concentration due to direct or semi-direct effect.

More specifically, our experiments are conducted in two steps. In step one, ExpA and ExpC are conducted without and with aerosol radiative feedback, respectively, during which aerosol optical properties and cloud properties are exported and saved. In step two, we perform ExpB with cloud properties imported from ExpA and aerosol optical properties imported

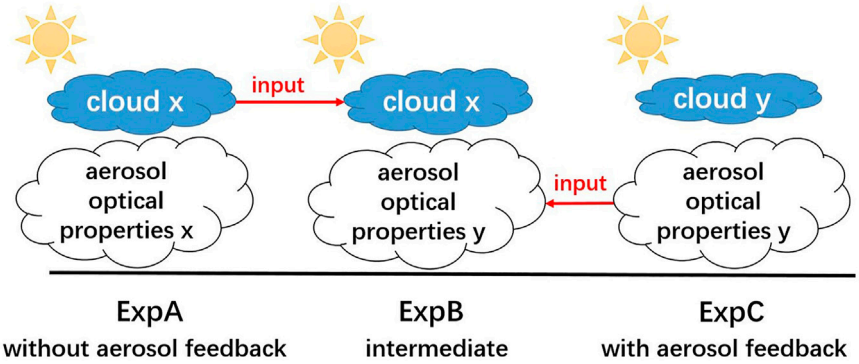

FIGURE 2
Schematic illustration of the experiment design in isolating aerosol direct and semi-direct effect using WRF-Chem. ExpA is conducted without aerosol feedback, ExpC is conducted with aerosol feedback. While in ExpB, cloud properties are imported from ExpA and aerosol optical properties are imported from ExpC. Therefore, the only differences between ExpA and ExpB are the aerosol optical properties, which represent the direct effect. The only differences between ExpB and ExpC are the cloud properties, which represent the semi-direct effect.

from ExpC. We also re-run ExpA and ExpC with cloud and aerosol optical properties imported from their respective output from step one. All model settings are the same in three experiments except for the imported variables during step two.

Our imported variables of aerosol optical properties include shortwave aerosol optical depth, single-scattering albedo, and asymmetry factor at all four wavelengths, as well as longwave aerosol optical depth at all sixteen wavelengths in WRF-Chem. Our imported variables of cloud properties consist of number concentrations of cloud droplet as well as mixing ratios of water vapor and five hydrometeors, including cloud droplets, cloud ice, rain, snow and graupel. Note that microphysics latent heat is also imported, since it is entirely dependent on cloud properties (neglecting the influence of temperature change on specific heat of vaporization, which is about 0.1% per degree centigrade at 10°C). Three-dimensional cloud properties are imported at an interval of 36 s, which is three times the integration time step, and aerosol optical properties are imported at an interval of 5 min, shorter than the interval between radiation module calls. To reduce the error induced by the time interval of data input, temporal resolutions of the imported data are set sufficiently high, as described above. These data require large computer storage. Therefore, our experiment runs are shorter than 1 day due to the limited storage.

Scenario design

Table 1 shows the scenarios in our study, and their corresponding experiments in the above framework are shown in Figure 2. For isolating the direct and semi-direct effects by all aerosols, ExpC represents the BASE300 scenario where all aerosols radiative feedback is turned on. ExpA represents the AeroRadoff scenario, in which aerosol radiative effect is turned off (i.e., aerosol optical depth are set to zero), and the intermediate ExpB represents the AeroRadoff_int scenario. Therefore, direct and semi-direct effect by all aerosol species can be calculated as AeroRadoff_int minus AeroRadoff and BASE300 minus AeroRadoff_int, respectively. For isolating the direct and semi-direct effects by BC, ExpC also represents the BASE300 scenario, while ExpA represents the AeroRadexBC scenario, in which only BC radiative effect is turned off (i.e., mass, volume and number concentrations of BC are set to zero in the Mie-scattering module), and the intermediate ExpB represents the AeroRadexBC_int scenario. Therefore, direct and semi-direct effect by BC can be calculated as AeroRadexBC_int minus AeroRadexBC and BASE300 minus AeroRadexBC_int, respectively. Note that CDNC is fixed at 300 cm^{-3} in all five scenarios for the evaluation of aerosol radiative effect, including BASE300, AeroRadoff, AeroRadexBC, AeroRadoff_int and AeroRadexBC_int, in order to fix the indirect effect.

Indirect effect is calculated based on BASEprogn and CDNC20 scenarios in which different settings of cloud droplet number concentration (CDNC) are adopted, following Zhao et al. (2017) and Zhang et al. (2018b). The first one is conducted with prognostic CDNC, which represents indirect effect in actual polluted conditions. While the second one is conducted with prescribed spatially uniform CDNC of 20 cm^{-3}, which represents indirect effect in clean conditions. Aerosol radiative feedback is turned off (aerosol optical depth are set to zero) in the above two scenarios in order to fix aerosol radiative effect. Total aerosol effect (including direct, semi-direct and indirect effect) is calculated based on the difference between BASEreal and CDNC20 scenarios. The BASEreal scenario is conducted with prognostic CDNC and aerosol radiative feedback.

TABLE 1 Scenarios for modeling aerosol effects, and their corresponding experiment in the framework of isolating aerosol direct and semi-direct effect illustrated in Figure 2. The first five scenarios, including BASE300, AeroRadoff, AeroRadexBC, AeroRadoff_int, and AeroRadexBC_int, are designed to evaluate the direct and semi-direct effect. BASEprogn and CDNC20 scenarios are designed to evaluate the indirect effect. Total aerosol effect is calculated based on the difference between BASEreal and CDNC20 scenarios.

Scenario name	Scenario description	Experiment
BASE300	With prescribed CDNC of 300 cm^{-3}, with aerosol radiative feedback	ExpC
AeroRadoff	The same as BASE300 except that aerosol radiative feedback is turned off	ExpA
AeroRadexBC	The same as BASE300 except that BC radiative feedback is turned off	ExpA
AeroRadoff_int	Intermediate scenario between BASE300 and AeroRadoff	ExpB
AeroRadexBC_int	Intermediate scenario between BASE300 and AeroRadexBC	ExpB
BASEprogn	With prognostic CDNC, without aerosol radiative feedback	—
CDNC20	With prescribed CDNC of 20 cm^{-3}, without aerosol radiative feedback	—
BASEreal	With prognostic CDNC and aerosol radiative feedback	—

Process analysis scheme

From the original WRF-Chem model output variables, it is difficult to quantify the contribution of each detailed physical process. This brings obstacles to the analysis of how aerosols affect changes of temperature and water vapor. Therefore in our process analysis scheme, the temperature or water vapor change is decomposed into contributions of individual physical process. To be more specific, we first decouple the air masses and map factors from the tendencies of each physical process in the original Runge-Kutta 3rd order scheme, and then integrate these tendencies over time separately, so that they can be directly compared with the total change of variables, including temperature and water vapor. Since during each integration time step in the original WRF-Chem, the change of temperature or water vapor mixing ratio is calculated as the sum of each individual physical process, therefore total change of model temperature or water vapor integrated over time is equal to the sum of our integrated tendencies from each physical process. Note that interaction between different processes may be possible but is not considered in the model. Detailed analysis are given in Section 3.3

Results

Model evaluations

We selected three cases in this study, including the case of Shanghai on 19 Nov 2016, case of Wuhan on 4 Jan 2016 and case of Zhengzhou on 12 Feb 2016. All three cases are characterized by high cloud cover and heavy pollution. The model performances are evaluated against the Level 2 Cloud product from the Moderate Resolution Imaging Spectroradiometer (MODIS) on the Aqua satellite, radiosondes as well as *in-situ* observations of meteorological factors and $PM_{2.5}$ concentration (Figure 3; Supplementary Figures S1–S3). Note that for the case of Shanghai, observations are compared to model simulation of the first ensemble member, since all other ensemble members are perturbed based on it. We can see from Supplementary Figure S1 that all three cases are characterized with heavy pollution and high cloud fraction, yet with different amounts of LWP. From 7:00 to 17:00 LT, mean LWP in the base simulation (BASEreal) over the box region of Figures 3D–F are 128.1, 186.4 and 304.0 g/m^2, respectively. Simulated mean $PM_{2.5}$ concentrations corresponding to *in-situ* sites are 120.3, 186.9 and 197.8 μg/m^3, respectively (Figures 3G–I). It can be seen that the model simulations capture the mean $PM_{2.5}$ concentration as well as the spatial distribution of clouds very well. Note that most previous model experiments of aerosol effects have substantially underestimated the cloud fraction and LWP over China in winter, by more than 30 and 50%, respectively. This has been a common problem in chemical transport models (Chen et al., 2015; Cai et al., 2016; Liu et al., 2016; Zhao et al., 2017), which can result in considerable underestimation of semi-direct and indirect effects in aerosol-PBL feedbacks. To address this problem, we assimilated the radiosonde observational dataset in the simulations (see Section 2.1), which significantly improves the simulated cloud properties.

Quantifying the aerosol effects

In all three cases characterized by heavy pollution and high cloud fraction, aerosol total effect (BASEreal minus CDNC10) results in significant decrease in surface net shortwave flux and PBL height in the daytime (from 7:00 to 17:00 LT), which greatly enhances $PM_{2.5}$ pollution. Over the box regions of Shanghai, Wuhan and Zhengzhou (Figures 3D–F), decrease of net shortwave flux due to aerosol total effect are −106.9 ± 25.7 (−48.4 ± 11.7%), −96.6 (−62.2%) and −49.6 W/m^2 (−60.5%), respectively. Decreases of PBL height due to aerosol total effect are −187.1 ± 53.0 (−30.3 ± 8.6%), −129.4 (−35.8%) and −78.3 m (−21.5%), which increase surface $PM_{2.5}$ concentration by +24.3 ± 10.4 (+27.0 ± 11.6%), +12.0 (+7.9%) and +8.5 μg/m^3 (+4.5%),

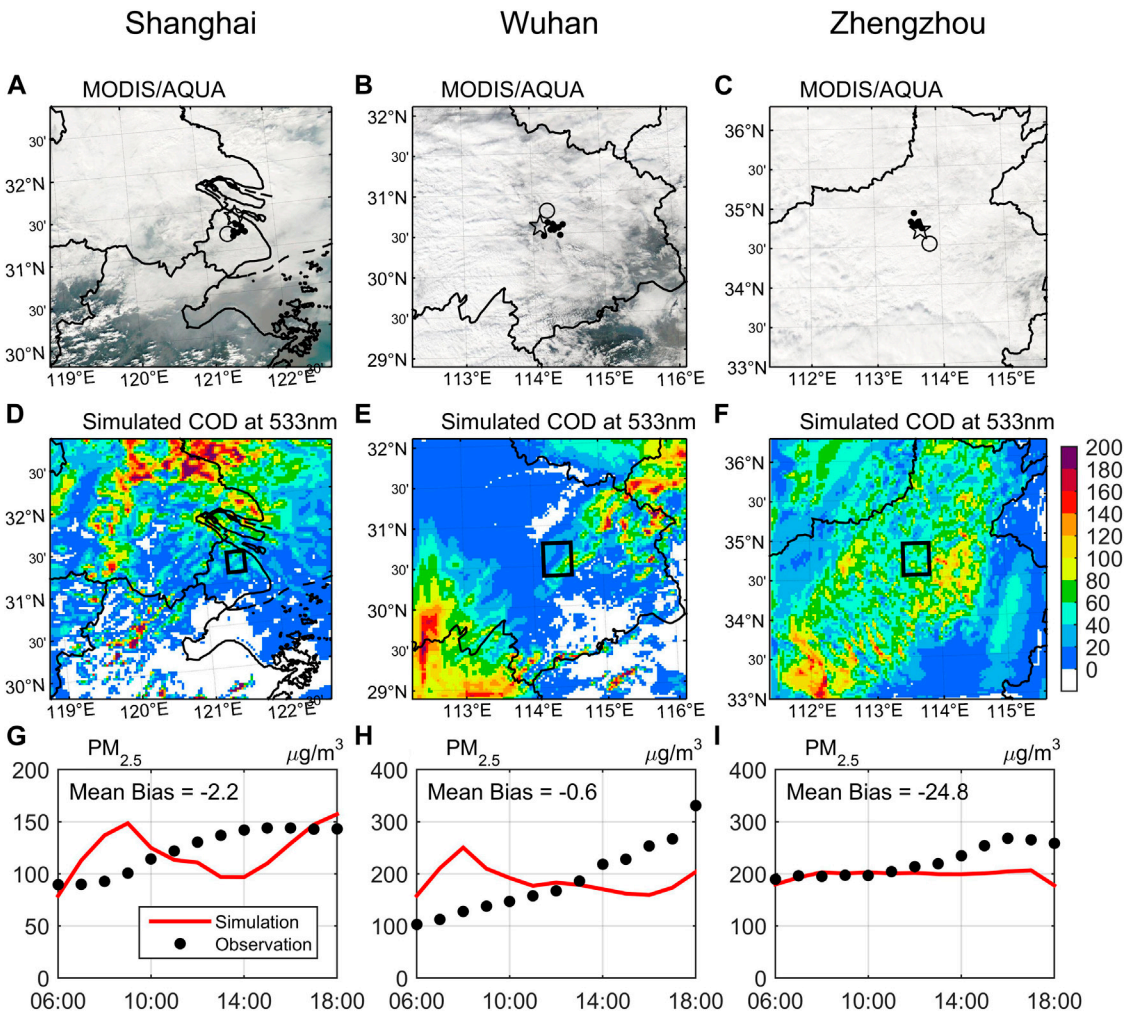

FIGURE 3
Evaluation of model performance. Left, middle and right column represents the cases of Shanghai (2016.11.19), Wuhan (2016.01.04) and Zhengzhou (2016.02.12), respectively. **(A–C)** Spatial distribution of corrected reflectance (true color) of MODIS/AQUA projected onto the simulation domain. Black dots, circles as well as pentagrams mark the locations of the *in-situ* measurements for $PM_{2.5}$ concentrations and meteorological factors, as well as radiosondes observations, respectively. **(D–F)** Spatial distribution of simulated cloud optical depth (COD) at 14:00LT. **(G–I)** Time series of simulated and observed $PM_{2.5}$ concentrations at ground stations.

respectively (Figures 4A–C, Supplementary Figures S4A–C, S7A–C). This considerable enhancement of $PM_{2.5}$ pollution highlights the importance of aerosol-PBL feedback under cloudy conditions.

We mainly discuss the case of Shanghai in the following main body part, while the detailed results of the other two cases are shown in the Supplementary Material (Supplementary Figures S4–S9). To be more specific, the direct effect is evaluated from the AeroRadoff_int and AeroRadoff scenarios (Figures 4D–F). This effect reduces net shortwave flux at surface and PBL height by −31.0 ± 12.6 W/m^2 (−14.0 ± 5.7%) and −61.1 ± 27.0 m (−9.9 ± 4.4%), respectively, leading to an increase of $PM_{2.5}$ concentration by 5.9 ± 2.1 μg/m^3 (+6.6 ± 2.3%), averaged over the box region in Shanghai. The aerosol semi-direct effect is determined based on the BASE300 and AeroRadoff_int scenarios, which is generally opposite to and weaker than the direct effect on average according to Figures 4G–I. Over the box region in Shanghai, aerosol semi-direct effect changes surface net shortwave flux, PBL height and $PM_{2.5}$ concentration by +0.7 ± 5.7 W/m^2 (+0.3 ± 2.7%), +10.4 ± 9.3 m (+1.7 ± 1.5%) and −0.14 ± 1.1 μg/m^3 (−0.15 ± 1.2%), respectively. However, note from Supplementary Figures S7F,I that magnitude of semi-direct effect exceed the direct effect locally in the case of Wuhan at 34.0°N, 112.4°E. Furthermore, it can be seen from Figures 4J–L that the indirect effect (BASEprogn minus CDNC20) dramatically alters net shortwave flux at surface and PBL height by −82.5 ± 32.9 W/m^2 (−37.3 ± 14.9%) and −140.8 ± 69.1 m (−22.8 ± 11.2%), respectively, thereby increasing $PM_{2.5}$

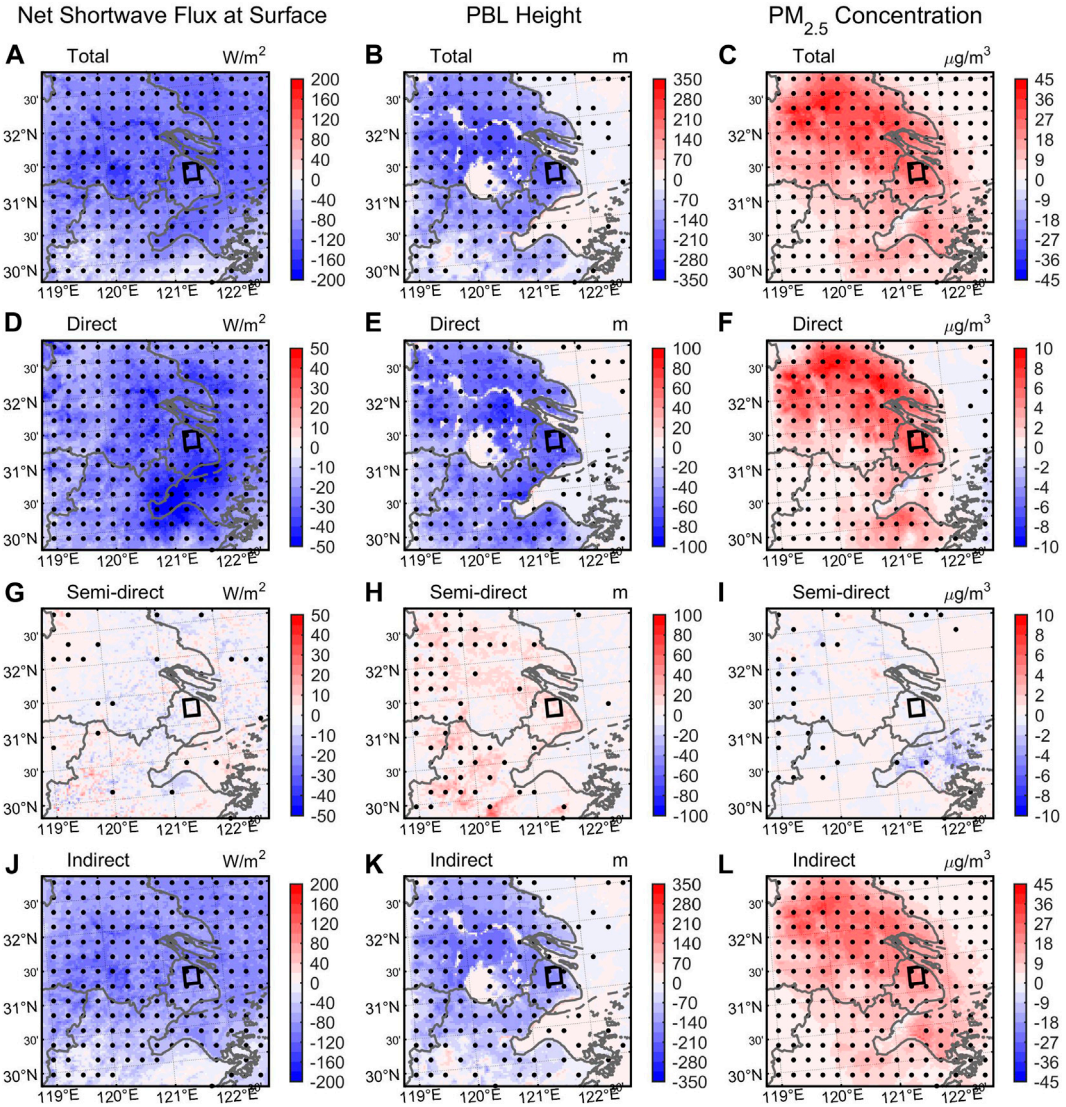

FIGURE 4
Spatial distribution of ensemble mean aerosol effect on net shortwave flux at surface (left column), PBL height, (middle column), PM2.5 concentration (right column) in the Shanghai Case, averaged from 7:00 to 17:00 LT. **(A–C)** The total effect, calculated as BASEreal minus CDNC20. **(D–F)** The direct effect, calculated as AeroRadoff_int minus AeroRadoff. **(G–I)** The semi-direct effect, calculated as BASE300 minus AeroRadoff_int. **(J–L)** The indirect effect, calculated as BASEprogn minus CDNC20. Stilted grids indicate significant differences at the 5% significance level. The box regions in the city center are used for calculating mean values in the horizontal direction.

concentration by 18.5 ± 9.9 μg/m^3 (+20.6 ± 11.1%) over the box region of Shanghai, largely exceeding the changes induced by the direct and semi-direct effect. It is also noted that the spatial pattern of aerosol total effect is closely related to that of the indirect effect. Therefore, indirect effect plays the dominant role in decreasing surface net shortwave flux and PBL height, as well as in increasing $PM_{2.5}$ concentration in the Shanghai Case.

Figure 5 compares the time series of ensemble mean and standard deviation of aerosol effects over the box region of Shanghai. The indirect effect, scaled by a factor of 0.5 in this figure, again turns out to be the dominant effect on surface shortwave flux, PBL height and $PM_{2.5}$ concentration, which also has the largest spread. Direct effect by all aerosol species has greater impact and uncertainty than the semi-direct effect on the whole, and their signs are generally opposite. Still, magnitude of semi-direct effect can exceed direct effect at certain times. For example, magnitude of $PM_{2.5}$ concentration change due to semi-direct effect (−3.6 μg/m^3; −3.9%) exceeded the direct effect (+3.2 μg/m^3; +3.5%) at 10:00 LT in ensemble member 10 (figure not shown).

Because BC is previously indicated as an important contributor of aerosol radiative effect (e.g., Bond et al., 2013;

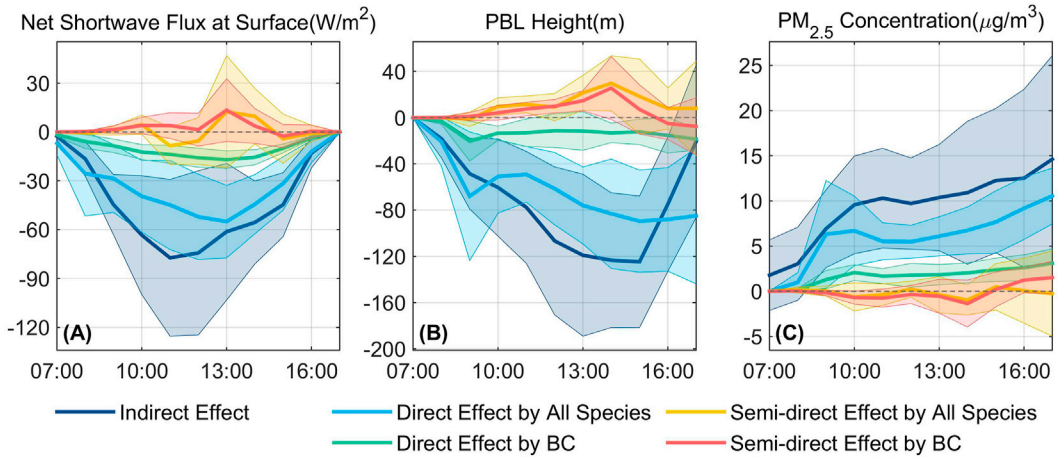

FIGURE 5
Time series of ensemble mean aerosol effect on **(A)** net shortwave flux at surface, **(B)** PBL height and **(C)** PM2.5 concentration in the Shanghai case, averaged over the box region marked in Figure 3D. Shaded areas represent ensemble standard deviations. Note that indirect effect is scaled by a factor of 0.5 in this figure.

Wang et al., 2013; Ding et al., 2016), we separately examine the radiative effect of BC by switching its radiative feedback on and off in BASE300 and AeroRadexBC scenarios, respectively. Similarly, the differences between AeroRadexBC_int and AeroRadexBC scenarios represent BC's direct effect, and the differences between the BASE300 and AeroRadexBC_int scenarios represent its semi-direct effect. Although mass concentration of BC only accounts for about 5% of $PM_{2.5}$, its direct effect on net shortwave flux at surface, PBL height and $PM_{2.5}$ concentration reaches ~30% of all aerosol species (Figure 5). Its semi-direct effect is also roughly equal to that of all aerosol species, indicating that BC played the dominant role in semi-direct effect, which is in accordance with Fan et al. (2008). We also notice that semi-direct effect by BC is generally opposite to its direct effect. It is noted that although semi-direct by BC is weaker than its direct effect on surface net shortwave flux, PBL height as well as $PM_{2.5}$ concentration on average, the spreads of its semi-direct effect are greater than its direct effect. Ensemble mean magnitude of increase of PBL height by BC semi-direct effect (+25.6 m; +2.6%) even exceeded the decrease by its direct effect (−13.2 m; −1.3%) at 14:00 LT. The reduction of $PM_{2.5}$ concentration due to BC semi-direct exceeded its direct effect at 14:00 LT in ensembles 1, 2 and 6 (figure not shown).

The time for the maximum ensemble mean reduction of $PM_{2.5}$ concentration due to the semi-direct effect is 14:00 LT for BC (−1.4 μg/m^3; −2.0%) as well as all aerosol species (−1.0 μg/m^3; −1.4%), which roughly correspond to the time for the maximum increase of PBL height, but is an hour after the maximum increase of surface shortwave flux. The cause of this delay is that surface shortwave flux largely determines the growth rate of PBL (Stull, 1988), while the height of PBL is determined by its integral.

The direct and semi-direct effect of BC as well as all aerosol species, together with the indirect effect in all three cases, are compared in Figure 6. The indirect effect, scaled by a factor of 0.5, has the largest impact on average among all aerosol effects, highlighting its dominant role under cloudy scenes (increasing $PM_{2.5}$ concentration by +3% ~ +21%). Direct effect exhibits the second largest impact on average, increasing $PM_{2.5}$ concentration by +1% ~ +7% (+1% ~ +2%) due to all aerosol species (only BC). Both direct and indirect effects reduce surface shortwave flux, suppress the development of the PBL and enhance $PM_{2.5}$ pollution. The semi-direct effect shows the least impact in these cases, which either decreases or slightly increases $PM_{2.5}$ concentration by −0.2% ~ +0.02% (−0.3% ~ −0.07%) for all aerosol species (BC only), caused by the complex responses of clouds with either decreased or slightly increased LWP.

Analyzing aerosol-PBL feedback through semi-direct effect

Next, we examine detailed changes of the physical processes caused by the semi-direct effect, which refers to the impact of cloud response to aerosol-radiation interactions on PBL structure and $PM_{2.5}$ concentration. Two key questions are: 1) How aerosol-radiation interactions affect the cloud? 2) How cloud response affects PBL structure and $PM_{2.5}$ concentration? We give a special emphasize on BC, since in the last section we have demonstrated that BC dominates in the semi-direct effect. The time-height cross section of the variables related to BC and cloud in Shanghai

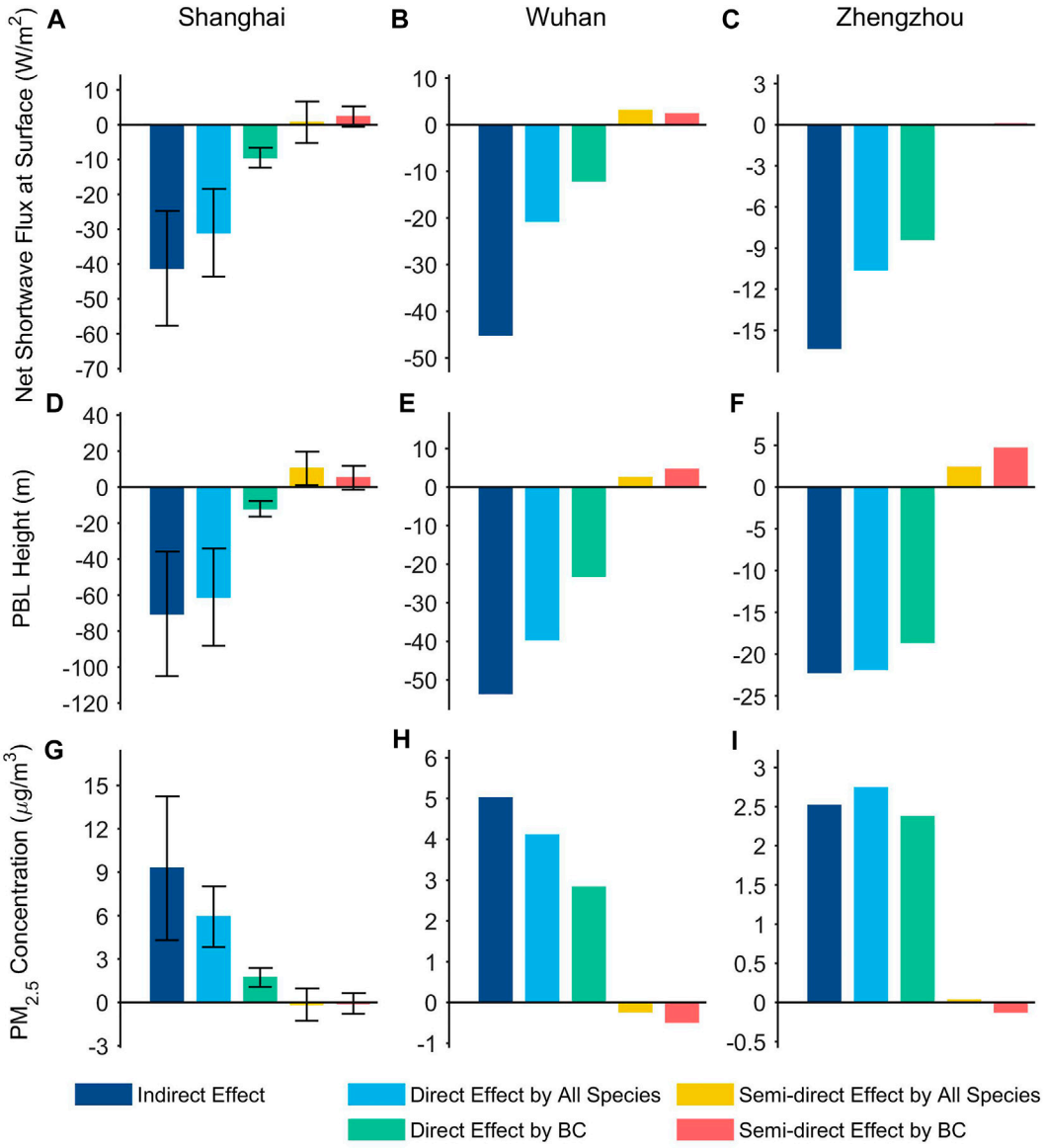

FIGURE 6
Bar plot of aerosol effect in cases of Shanghai (left column), Wuhan (middle column) and Zhengzhou (right column). **(A–C)** Aerosol effect on net shortwave flux at surface. **(D–F)** Aerosol effect on PBL height. **(G–I)** Aerosol effect on surface PM2.5 concentration. All variables are averaged from 7: 00 to 17:00 LT over the box regions marked in Figure 3. For the case of Shanghai, bars and error bars represent ensemble means and standard deviations, respectively. Note that the indirect effect is scaled by a factor of 0.5 in this figure.

case are analyzed in Figure 7. For the base simulation (BASE300), clouds reside below 1,000 m near the PBL top in the morning and extend to about 2,000 m in the afternoon (Figure 7A). On the other hand, BC aerosols are mostly located within the PBL, with only a small portion above its top (Figure 7D). Due to the radiative effect of BC, cloud fraction reduced in the morning (before 13:00 LT) but increased in the afternoon (after 14:00 LT) (Figure 7B). This pattern corresponds to the change of RH, caused by the rise of temperature in the morning and increase of water vapor in the afternoon (Figures 7C,E,F).

We further use the process analysis scheme described in Section 2.4 to investigate the underlying causes of temperature and water vapor change. Figure 8A shows the temperature change due to the radiative effect of BC. Figures 8B–F shows the contribution of each detailed physical process, the sum of which is equal to the total temperature change. We can see that the increase in temperature above the PBL is mainly caused by shortwave heating of BC, which leads to the reduction of cloud fraction in the morning. On the other hand, change of water vapor mixing ratio is also isolated in Figure 9, showing that the

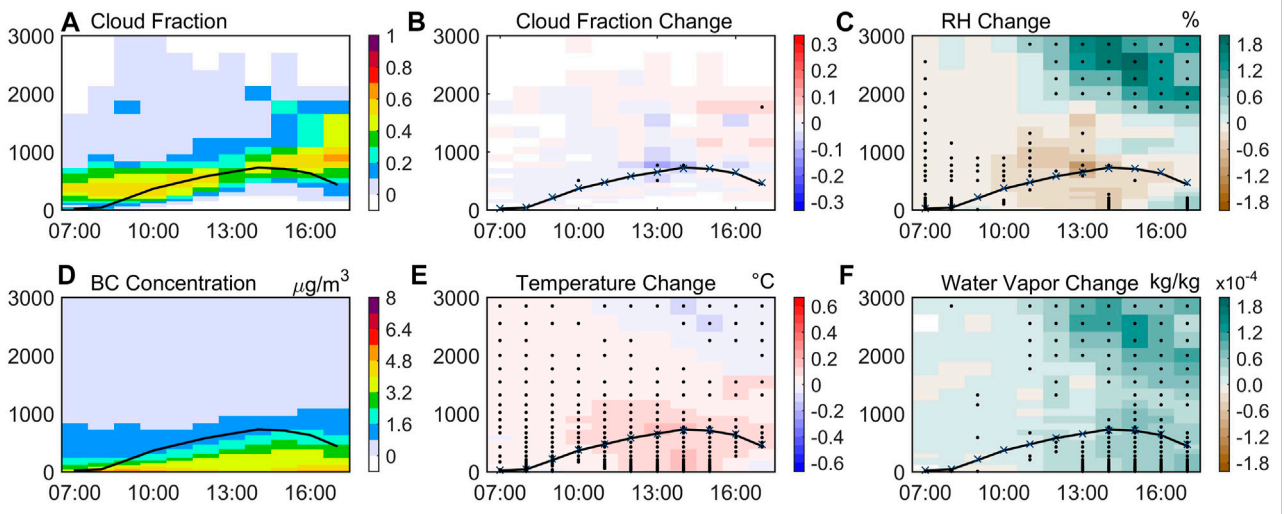

FIGURE 7
Time series of ensemble mean vertical distributions (time-height section) of variables in the Shanghai case, averaged over the box region shown in Figure 3D. **(A)** Simulated cloud fraction. **(D)** Simulated BC concentration. **(B,C,E,F)** Change of simulated cloud fraction, relative humidity, temperature and water vapor mixing ratio caused by BC radiative effect, respectively. Black solid lines represent PBL height in the simulation with BC radiative feedback (BASE300). Blue crosses represent PBL height in the simulation with aerosol radiative feedback except BC. (AeroRadexBC). Stilted grids indicate significant differences at the 5% significance level.

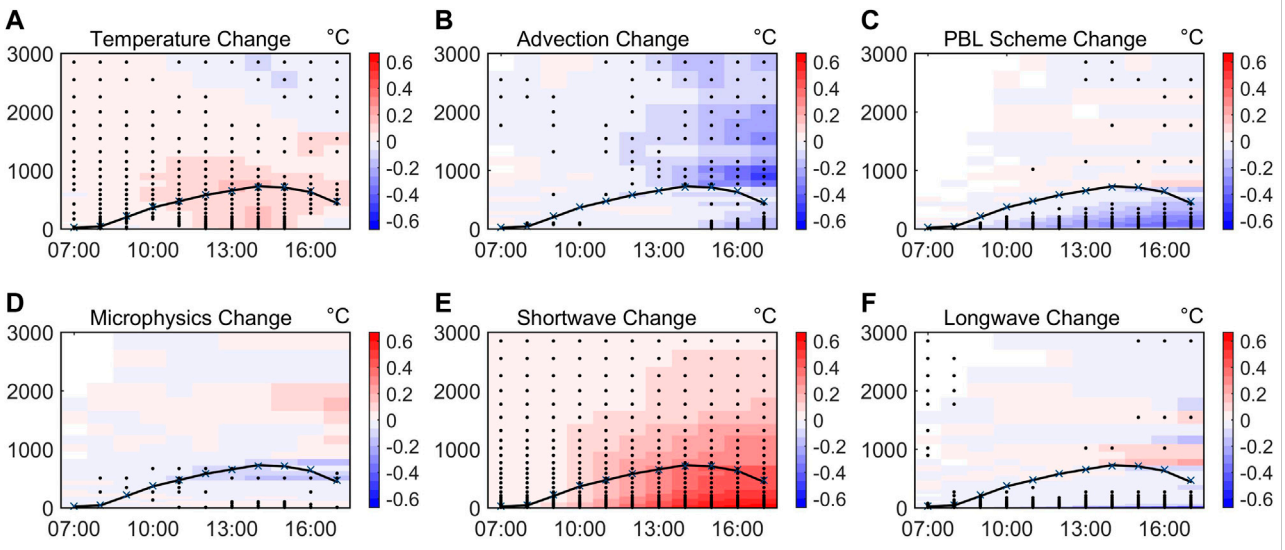

FIGURE 8
Process analysis of ensemble mean temperature change by BC radiative effect in time-height section in the Shanghai case, averaged over the box region shown in Figure 3D. **(A)** Simulated temperature change. **(B–F)** Simulated accumulated temperature change due to advection, PBL scheme (including surface heat flux and vertical turbulent mixing), microphysics process, shortwave heating and longwave heating, respectively. The sum of each individual process **(B–F)** equals to the total temperature change in **(A)**. Black solid lines represent PBL height in the simulation with aerosol radiative feedback (BASE300). Blue crosses represent PBL height in the simulation with aerosol radiative feedback except BC. (AeroRadexBC). Stilted grids indicate significant differences at the 5% significance level.

change of advection results in the increase of water vapor above the PBL, which serves to increase cloud fraction in the afternoon.

Cloud responses could further influence PBL structure and $PM_{2.5}$ concentration. In the morning, the reduction of cloud fraction gives rise to the increase of surface shortwave flux, together with latent heat cooling near PBL top (Figure 5A, Figure 8D), both of which promoted the development of PBL and reduced $PM_{2.5}$ concentration (Figures 5B,C). However, the

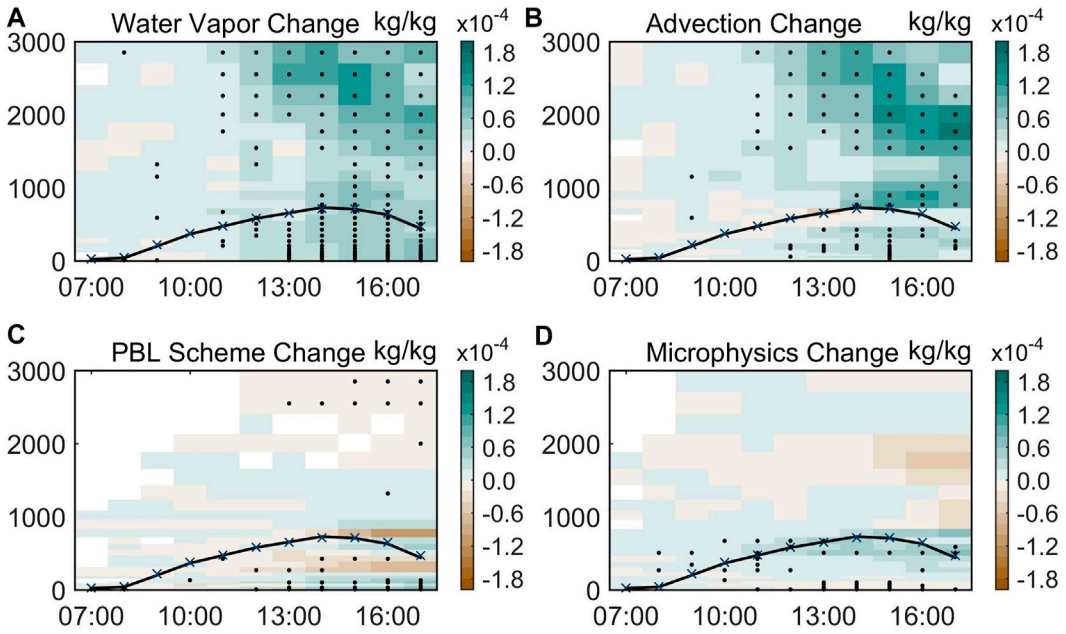

FIGURE 9
Process analysis of ensemble mean water vapor change by BC radiative effect in time-height section in the Shanghai case, averaged over the box region shown in Figure 3D. **(A)** Simulated water vapor change. **(B–D)** Simulated accumulated water vapor change due to advection, PBL scheme (including surface evaporation and vertical turbulent mixing) and microphysics process, respectively. The sum of each individual process **(B–D)** equals to the total temperature change in **(A)**. Black solid lines represent PBL height in the simulation with aerosol radiative feedback (BASE300). Blue crosses represent PBL height in the simulation with aerosol radiative feedback except BC. (AeroRadexBC). Stilted grids indicate significant differences at the 5% significance level.

increase of cloud fraction in the afternoon induces a decrease of surface shortwave flux, which inhibits the further development of PBL and enhances $PM_{2.5}$ pollution (Figure 5). The opposite impact of semi-direct effect in the morning and afternoon, as described above, weakens the magnitude of its average impact throughout daytime (from 7:00 LT to 17:00 LT), which also partly explains why influences of semi-direct effect are small on average (Figure 6).

Analyzing aerosol-PBL feedback through the indirect effect

Previous studies showed that the indirect effect could increase CDNC in warm clouds, which subsequently suppresses precipitation and increases LWP (Twomey, 1977; Albrecht, 1989). Both increased CDNC and LWP could result in a dramatic increase of COD, far exceeding the change caused by the aerosol radiative effect (Figure 10). This increased COD decreases net shortwave flux at surface, suppresses the development of the PBL and consequently enhances $PM_{2.5}$ pollution. Furthermore, increased LWP and reduced precipitation could promote cloud chemistry and weaken wet scavenging of pollutant particles, both contributing to the growth of $PM_{2.5}$ concentration. To evaluate the effect of these processes, we turn off cloud processing of aerosols (including cloud chemistry and wet scavenging) in the BASEprogn and CDNC20 scenarios and compare the differences. Without cloud processing of aerosols, mean changes of net shortwave flux at surface, PBL height and $PM_{2.5}$ concentration induced by the indirect effect are $-79.7 \pm 33.4\ W/m^2$ ($-36.1 \pm 15.1\%$), -137.4 ± 71.0 m ($-22.2 \pm 11.5\%$) and $+9.0 \pm 6.0\ \mu g/m^3$ ($+10.1 \pm 6.7\%$), respectively. This increase in $PM_{2.5}$ is much lower than that with cloud processing of aerosols (Section 3.2), indicating the important role of the latter process. Although large uncertainties in cloud processing of aerosols with model simulations exist (Gong et al., 2011; Lu and Fung, 2018), simulated indirect effect without this process is still larger than direct and semi-direct effect, which further confirmed the dominant role of indirect effect on PBL structure and $PM_{2.5}$ pollution.

Conclusion and discussions

In this study, we investigate the relative contributions of direct, semi-direct and indirect effects of aerosols in PBL-aerosol interaction under cloudy skies. We develop a new method to

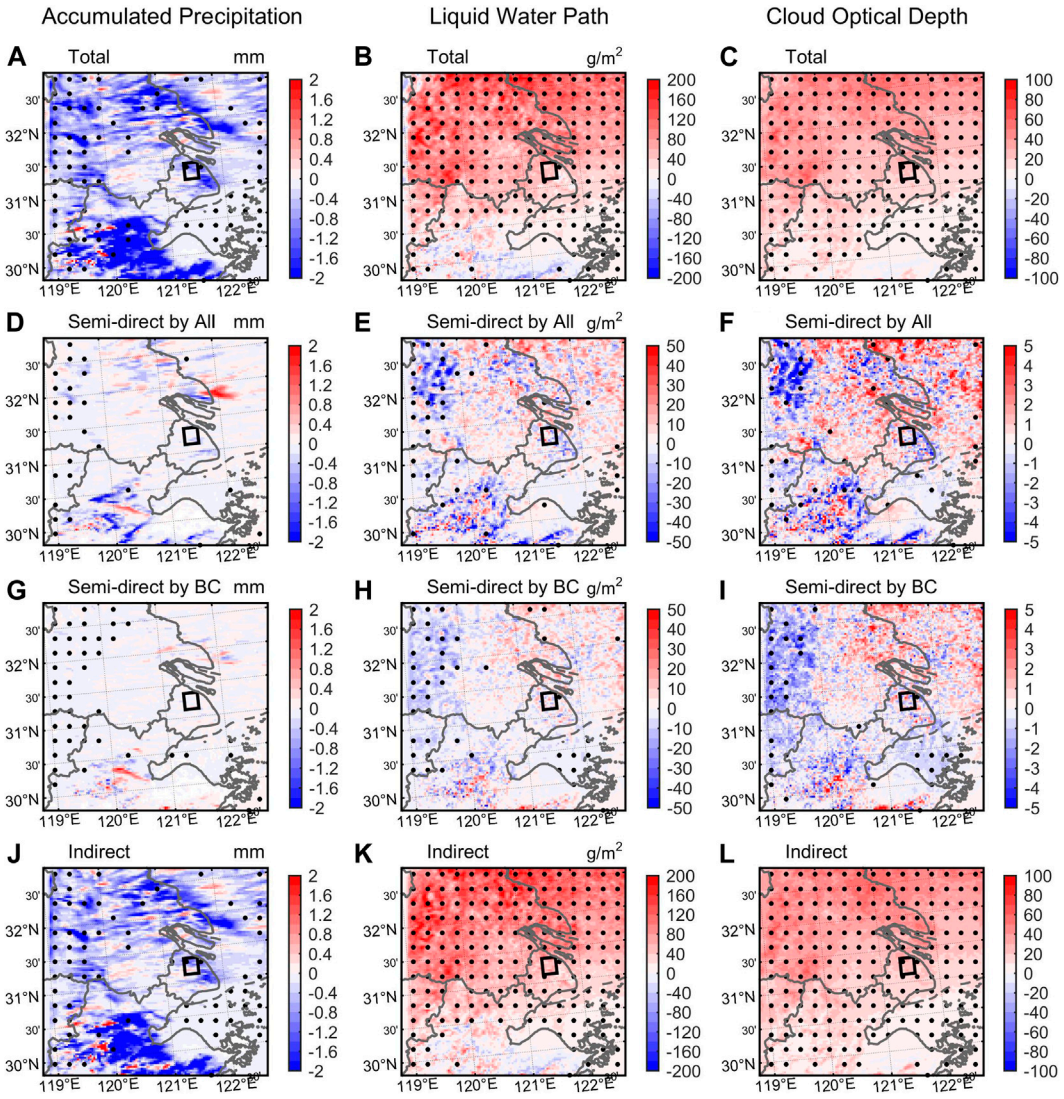

FIGURE 10
Spatial distribution of ensemble mean aerosol effect on accumulated precipitation (left column), liquid water path, (middle column), cloud optical depth (right column) in the Shanghai Case, averaged from 7:00 to 17:00 LT. **(A–C)** The total effect. **(D–F)** The semi-direct effect by all aerosol species. **(G–I)** The semi-direct effect by BC only. **(J–L)** The indirect effect. Stilted grids indicate significant differences at the 5% significance level. The box regions in the city center are used for calculating mean values in the horizontal direction.

isolate the direct and semi-direct effect of aerosols in WRF-Chem, and compare their impacts with the indirect effect. Three haze events characterized with high cloud cover but different amounts of LWP are investigated. Our results show that the indirect effect have the dominant impact, which substantially increases COD, decreases surface net shortwave flux and PBL height and increases $PM_{2.5}$ concentration by as much as +3% ~ +21%. Enhanced cloud chemistry and weakened wet scavenging due to the indirect effect also elevate $PM_{2.5}$ pollution level. Direct effect generally shows the second largest impact, which also decreases surface shortwave flux and PBL height, thereby increasing $PM_{2.5}$ concentration by +1% ~ +7%. Semi-direct effect has the least impact on average, but can still exceed direct effect at certain times and locations, which alters PBL structure through changes of COD and latent heat release and changes $PM_{2.5}$ concentration by −0.2% ~ +0.02%. In addition, we found that BC's direct effect is about 30% of all aerosols (changing $PM_{2.5}$ concentration by +1% ~ +2%), and its semi-direct effect is roughly equal to that of all aerosols (changing $PM_{2.5}$ concentration by −0.3% ~ −0.07%), indicating its unique role in aerosol radiative feedbacks.

Our study suggests that the impacts of aerosols through clouds, especially the indirect effect, play the dominant role in their feedback processes to PBL structure and air quality under

cloudy conditions. Note that most previous studies may substantially underestimate the indirect effect due to the underestimation of cloud fraction and LWP (see Section 3.1). Short-term aerosol indirect effect on surface pollution under persistent cloud cover were not compared to direct effect in these studies, so that the dominant role of aerosol-cloud interaction has not been pointed out. Some studies also showed that semi-direct effect could dominate over the indirect effect. However, these studies mainly focused on cloud fraction, convective available potential energy (CAPE) or precipitation (Ackerman et al., 2000; Koren et al., 2008; Rosenfeld et al., 2008; Fan et al., 2015), whereas in terms of the change of PBL structure and $PM_{2.5}$ pollution, COD should be considered as a more influential factor, because change in COD is directly associated with the surface shortwave flux change which drives the development of PBL. Other studies also showed different results from ours that semi-direct effect may either dominate over or be overtaken by the direct effect through long-term model experiments (Forkel et al., 2012; Zhang et al., 2018b). These discrepancies may be attributed to differences in the temporal and spatial modeling scales, average cloud cover during the experiments, aerosol species and their vertical distributions. Therefore, further research on the sensitivity of PBL-aerosol interaction to different BC fractions, aerosol and cloud vertical distributions, as well as different cloud cover conditions is needed for more generalized conclusions. So far, the interactions between aerosols and clouds still represent the largest uncertainty in climate models. More observational studies are also needed to verify and to evaluate these aerosol feedbacks.

Data availability statement

We acknowledge National Climate Data Center and China National Environmental Monitoring Center for providing in-situ meteorological factors (https://gis.ncdc.noaa.gov/maps/ncei/cdo/hourly) and PM2.5 concentration observational datasets (https://quotsoft.net/air/). We acknowledge University of Wyoming for providing radiosondes observational datasets (http://weather.uwyo.edu/upperair/sounding.html) for model evaluation. Observational datasets of cloud properties for model evaluation are obtained from MODIS data website (https://ladsweb.modaps.eosdis.nasa.gov/search/). As for WRF-Chem model simulations, we thank National Center for Atmospheric Research (NCAR) and University Corporation for Atmospheric Research (UCAR) for providing meteorological initial and lateral boundary conditions (http://rda.ucar.edu/datasets/ds083.2/), surface and radiosondes observational weather data for model assimilation (https://rda.ucar.edu/datasets/ds461.0/; https://rda.ucar.edu/datasets/ds351.0/), chemical initial and boundary conditions, biomass burning emissions, biogenic emissions as well as source codes of WRF-Chem (https://www2.acom.ucar.edu/wrf-chem). Anthropogenic emission are developed by MEIC model group of Tsinghua University (http://www.meicmodel.org/dataset-mix.html).

Author contributions

Conceptualization, formal analysis, writing—original draft, writing—review, and editing: CX and JL; Methodology: CX and ZL; Data curation: CX and ZZ; Supervision, funding acquisition: JL.

Funding

This study is funded by National Natural Science Foundation of China (NSFC) Grant No. 41975023.

Conflict of interest

The authors declare that the research was conducted in the absence of any commercial or financial relationships that could be construed as a potential conflict of interest.

Publisher's note

Supplementary material

The Supplementary Material for this article can be found online at: https://www.frontiersin.org/articles/10.3389/fenvs.2022.1002412/full#supplementary-material

References

Abdul-Razzak, H., and Ghan, S. J. (2002). A parameterization of aerosol activation 3. Sectional representation. *J. Geophys. Res.* 107 (3), 1–6. doi:10.1029/2001jd000483

Ackerman, A. S., Toon, O. B., Stevens, D. E., Heymsfield, A. J., Ramanathan, V., and Welton, E. J. (2000). Reduction of tropical cloudiness by soot. *Science* 288 (5468), 1042–1047. doi:10.1126/science.288.5468.1042

Albrecht, B. A. (1989). Aerosols, cloud microphysics, and fractional cloudiness. *Science* 245 (4923), 1227–1230. doi:10.1126/science.245.4923.1227

Barker, D. M., Huang, W., Guo, Y. R., Bourgeois, A. J., and Xiao, Q. N. (2004). A three-dimensional variational data assimilation system for MM5: Implementation and initial results. *Mon. Wea. Rev.* 132 (4), 897–914. doi:10.1175/1520-0493(2004)132<0897:ATVDAS>2.0.CO;2

Barker, D. M. (2005). Southern high-latitude ensemble data assimilation in the antarctic mesoscale prediction system. *Mon. Weather Rev.* 133 (12), 3431–3449. doi:10.1175/MWR3042.1

Barnard, J. C., Fast, J. D., Paredes-Miranda, G., Arnott, W. P., and Laskin, A. (2010). Technical note: Evaluation of the WRF-chem "Aerosol chemical to aerosol optical Properties" module using data from the MILAGRO campaign. *Atmos. Chem. Phys.* 10 (15), 7325–7340. doi:10.5194/acp-10-7325-2010

Bond, T. C., Doherty, S. J., Fahey, D. W., Forster, P. M., Berntsen, T., DeAngelo, B. J., et al. (2013). Bounding the role of black carbon in the climate system: A scientific assessment. *J. Geophys. Res. Atmos.* 118 (11), 5380–5552. doi:10.1002/jgrd.50171

Cai, C., Zhang, X., Wang, K., Zhang, Y., Wang, L., Zhang, Q., et al. (2016). Incorporation of new particle formation and early growth treatments into WRF / Chem:Model improvement, evaluation, and impacts of anthropogenic aerosols over East Asia. *Atmos. Environ.* 124, 262–284. doi:10.1016/j.atmosenv.2015.05.046

Chan, C. K., and Yao, X. (2008). Air pollution in mega cities in China. *Atmos. Environ.* 42 (1), 1–42. doi:10.1016/j.atmosenv.2007.09.003

Chandran Govindaraju, V. G. R., and Tang, C. F. (2013). The dynamic links between CO2 emissions, economic growth and coal consumption in China and India. *Appl. Energy* 104, 310–318. doi:10.1016/j.apenergy.2012.10.042

Chen, Y., Zhang, Y., Fan, J., Leung, L. R., and Zhang, Q. (2015). Application of an online-coupled regional climate model, WRF-CAM5, over east asia for examination of ice nucleation schemes: Part I. comprehensive model evaluation and trend analysis for 2006 and 2011. *Climate* 3, 627–667. doi:10.3390/cli3030627

Ding, A. J., Fu, C. B., Yang, X. Q., Sun, J. N., Petäjä, T., Kerminen, V. M., et al. (2013). Intense atmospheric pollution modifies weather: A case of mixed biomass burning with fossil fuel combustion pollution in eastern China. *Atmos. Chem. Phys.* 13 (20), 10545–10554. doi:10.5194/acp-13-10545-2013

Ding, A. J., Huang, X., Nie, W., Sun, J. N., Kerminen, V. M., Petäjä, T., et al. (2016). Enhanced haze pollution by black carbon in megacities in China. *Geophys. Res. Lett.* 43 (6), 2873–2879. doi:10.1002/2016GL067745

Du, Q., Zhao, C., Zhang, M., Dong, X., Chen, Y., Liu, Z., et al. (2020). Modeling diurnal variation of surface PM2.5 concentrations over east China with WRF-chem: Impacts from boundary-layer mixing and anthropogenic emission. *Atmos. Chem. Phys.* 20 (5), 2839–2863. doi:10.5194/acp-20-2839-2020

Fan, J., Rosenfeld, D., Yang, Y., Zhao, C., Leung, L. R., and Li, Z. (2015). Substantial contribution of anthropogenic air pollution to catastrophic floods in Southwest China. *Geophys. Res. Lett.* 42, 1–10. doi:10.1002/2015GL064479. Received

Fan, J., Zhang, R., Tao, W. K., and Mohr, K. I. (2008). Effects of aerosol optical properties on deep convective clouds and radiative forcing. *J. Geophys. Res.* 113 (8), 1–16. doi:10.1029/2007JD009257

Forkel, R., Werhahn, J., Hansen, A. B., McKeen, S., Peckham, S., Grell, G., et al. (2012). Effect of aerosol-radiation feedback on regional air quality - a case study with WRF/Chem. *Atmos. Environ.* 53, 202–211. doi:10.1016/j.atmosenv.2011.10.009

Gao, M., Carmichael, G. R., Wang, Y., Saide, P. E., Yu, M., Xin, J., et al. (2016). Modeling study of the 2010 regional haze event in the North China Plain. *Atmos. Chem. Phys.* 16 (3), 1673–1691. doi:10.5194/acp-16-1673-2016

Gao, M., Han, Z., Tao, Z., Li, J., Kang, J. E., Huang, K., et al. (2020). Air quality and climate change, topic 3 of the model inter-comparison study for asia phase III (MICS-Asia III) - Part 2: Aerosol radiative effects and aerosol feedbacks. *Atmos. Chem. Phys.* 20 (2), 1147–1161. doi:10.5194/acp-20-1147-2020

Gao, Y., Zhang, M., Liu, Z., Wang, L., Wang, P., Xia, X., et al. (2015). Modeling the feedback between aerosol and meteorological variables in the atmospheric boundary layer during a severe fog-haze event over the North China Plain. *Atmos. Chem. Phys.* 15 (8), 4279–4295. doi:10.5194/acp-15-4279-2015

Ghan, S. J., Liu, X., Easter, R. C., Zaveri, R., Rasch, P. J., Yoon, J. H., et al. (2012). Toward a minimal representation of aerosols in climate models: Comparative decomposition of aerosol direct, semidirect, and indirect radiative forcing. *J. Clim.* 25 (19), 6461–6476. doi:10.1175/JCLI-D-11-00650.1

Gong, W., Stroud, C., and Zhang, L. (2011). Cloud processing of gases and aerosols in air quality modeling. *Atmosphere* 2 (4), 567–616. doi:10.3390/atmos2040567

Grell, G. A., Peckham, S. E., Schmitz, R., McKeen, S. A., Frost, G., Skamarock, W. C., et al. (2005). Fully coupled "online" chemistry within the WRF model. *Atmos. Environ.* 39 (37), 6957–6975. doi:10.1016/j.atmosenv.2005.04.027

Guenther, A., Karl, T., Harley, P., Wiedinmyer, C., Palmer, P. I., and Geron, C. (2006). Estimates of global terrestrial isoprene emissions using MEGAN (model of emissions of gases and aerosols from nature). *Atmos. Chem. Phys.* 6 (11), 3181–3210. doi:10.5194/acp-6-3181-2006

Hansen, J., Sato, M., and Ruedy, R. (1997). Radiative forcing and climate response. *J. Geophys. Res.* 102, 6831–6864. doi:10.1029/96jd03436

Huang, R. J., Zhang, Y., Bozzetti, C., Ho, K. F., Cao, J. J., Han, Y., et al. (2014b). High secondary aerosol contribution to particulate pollution during haze events in China. *Nature* 514 (7521), 218–222. doi:10.1038/nature13774

Huang, X., Ding, A., Gao, J., Zheng, B., Zhou, D., Qi, X., et al. (2021). Enhanced secondary pollution offset reduction of primary emissions during COVID-19 lockdown in China. *Natl. Sci. Rev.* 8 (2), 137. doi:10.1093/nsr/nwaa137

Huang, Y., Shen, H., Chen, H., Wang, R., Zhang, Y., Su, S., et al. (2014a). Quantification of global primary emissions of PM2.5, PM10, and TSP from combustion and industrial process sources. *Environ. Sci. Technol.* 48 (23), 13834–13843. doi:10.1021/es503696k

Iacono, M. J., Delamere, J. S., Mlawer, E. J., Shephard, M. W., Clough, S. A., and Collins, W. D. (2008). Radiative forcing by long-lived greenhouse gases: Calculations with the AER radiative transfer models. *J. Geophys. Res.* 113 (13), 2–9. doi:10.1029/2008JD009944

King, M. D., Platnick, S., Menzel, W. P., Ackerman, S. A., and Hubanks, P. A. (2013). Spatial and temporal distribution of clouds observed by MODIS onboard the terra and aqua satellites. *IEEE Trans. Geosci. Remote Sens.* 51 (7), 3826–3852. doi:10.1109/TGRS.2012.2227333

Koch, D., and Del Genio, A. D. (2010). Black carbon semi-direct effects on cloud cover: Review and synthesis. *Atmos. Chem. Phys.* 10 (16), 7685–7696. doi:10.5194/acp-10-7685-2010

Koren, I., Martins, J. V., Remer, L. A., and Afargan, H. (2008). Smoke invigoration versus inhibition of clouds over the amazon. *Science* 321, 946–949. doi:10.1126/science.1159185

Li, J., Han, Z., Wu, Y., Xiong, Z., Xia, X., Li, J., et al. (2020). Aerosol radiative effects and feedbacks on boundary layer meteorology and PM2.5 chemical components during winter haze events over the Beijing-Tianjin-Hebei region. *Atmos. Chem. Phys.* 20 (14), 8659–8690. doi:10.5194/acp-20-8659-2020

Li, J., Li, C., Zhao, C., and Su, T. (2016). Changes in surface aerosol extinction trends over China during 1980-2013 inferred from quality-controlled visibility data. *Geophys. Res. Lett.* 43 (16), 8713–8719. doi:10.1002/2016GL070201

Li, Z., Guo, J., Ding, A., Liao, H., Liu, J., Sun, Y., et al. (2017). Aerosol and boundary-layer interactions and impact on air quality. *Natl. Sci. Rev.* 4 (6), 810–833. doi:10.1093/nsr/nwx117

Lin, Y. L., Farley, R. D., and Orville, H. D. (1983). Bulk parameterization of the snow field in a cloud model. *J. Clim. Appl. Meteorology* 22, 1065–1092. doi:10.1175/1520-0450(1983)022<1065:BPOTSF>2.0.CO;2

Liu, D., Zhao, D., Xie, Z., Yu, C., Chen, Y., Tian, P., et al. (2019). Enhanced heating rate of black carbon above the planetary boundary layer over megacities in summertime. *Environ. Res. Lett.* 14 (12), 124003. doi:10.1088/1748-9326/ab4872

Liu, Q., Jia, X., Quan, J., Li, J., Li, X., Wu, Y., et al. (2018a). New positive feedback mechanism between boundary layer meteorology and secondary aerosol formation during severe haze events. *Sci. Rep.* 8 (1), 1–8. doi:10.1038/s41598-018-24366-3

Liu, X. Y., Zhang, Y., Zhang, Q., and He, K.-B. (2016). Application of online-coupled WRF/Chem-MADRID in East Asia: Model evaluation and climatic effects of anthropogenic aerosols. *Atmos. Environ.* 124, 321–336. doi:10.1016/j.atmosenv.2015.03.052

Liu, Z., Yim, S. H. L., Wang, C., and Lau, N. C. (2018b). The impact of the aerosol direct radiative forcing on deep convection and air quality in the pearl river delta region. *Geophys. Res. Lett.* 45 (9), 4410–4418. doi:10.1029/2018GL077517

Lu, X., and Fung, J. C. H. (2018). Sensitivity assessment of PM2.5 simulation to the below-cloud washout schemes in an atmospheric chemical transport model. *Tellus B Chem. Phys. Meteorology* 70 (1), 1–17. doi:10.1080/16000889.2018.1476435

Meng, Z., and Zhang, F. (2008). Tests of an ensemble Kalman filter for mesoscale and regional-scale data assimilation. Part III: Comparison with 3DVAR in a real-

data case study. *Mon. Weather Rev.* 136 (2), 522–540. doi:10.1175/2007MWR2106.1

Miao, Y., Che, H., Zhang, X., and Liu, S. (2021). Relationship between summertime concurring PM2.5 and O3 pollution and boundary layer height differs between Beijing and Shanghai, China. *Environ. Pollut.* 268, 115775. doi:10.1016/j.envpol.2020.115775

Miao, Y., Guo, J., Liu, S., Liu, H., Li, Z., Zhang, W., et al. (2017). Classification of summertime synoptic patterns in Beijing and their associations with boundary layer structure affecting aerosol pollution. *Atmos. Chem. Phys.* 17 (4), 3097–3110. doi:10.5194/acp-17-3097-2017

Miao, Y., Li, J., Miao, S., Che, H., Wang, Y., Zhang, X., et al. (2019). Interaction between planetary boundary layer and PM2.5 pollution in megacities in China: A review. *Curr. Pollut. Rep.* 5 (4), 261–271. doi:10.1007/s40726-019-00124-5

Miao, Y., and Liu, S. (2019). Linkages between aerosol pollution and planetary boundary layer structure in China. *Sci. Total Environ.* 650, 288–296. doi:10.1016/j.scitotenv.2018.09.032

Ning, G., Wang, S., Yim, S. H. L., Li, J., Hu, Y., Shang, Z., et al. (2018). Impact of low-pressure systems on winter heavy air pollution in the northwest Sichuan Basin, China. *Atmos. Chem. Phys.* 18 (18), 13601–13615. doi:10.5194/acp-18-13601-2018

Petäjä, T., Järvi, L., Kerminen, V. M., Ding, A. J., Sun, J. N., Nie, W., et al. (2016). Enhanced air pollution via aerosol-boundary layer feedback in China. *Sci. Rep.* 6, 1–6. doi:10.1038/srep18998

Rosenfeld, D., Lohmann, U., Raga, G. B., O'Dowd, C. D., Kulmala, M., Fuzzi, S., et al. (2008). Flood or drought: How do aerosols affect precipitation? *Science* 321 (5894), 1309–1313. doi:10.1126/science.1160606

Shao, Y. (2001). A model for mineral dust emission. *J. Geophys. Res.* 106 (3), 20239–20254. doi:10.1029/2001jd900171

Shu, L., Xie, M., Gao, D., Wang, T., Fang, D., Liu, Q., et al. (2017). Regional severe particle pollution and its association with synoptic weather patterns in the Yangtze River Delta region, China. *Atmos. Chem. Phys.* 17 (21), 12871–12891. doi:10.5194/acp-17-12871-2017

Song, C., Wu, L., Xie, Y., He, J., Chen, X., Wang, T., et al. (2017). Air pollution in China: Status and spatiotemporal variations. *Environ. Pollut.* 227, 334–347. doi:10.1016/j.envpol.2017.04.075

Stocker, T. F., et al. (2013). *Climate Change 2013: The Physical Science Basis. Contribution of Working Group I to the Fifth Assessment Report of the Intergovernmental Panel on Climate Change*. Cambridge University Press.

Stull, R. B. (1988). *An introduction to boundary layer meteorology*. Dordrecht: Springer Netherlands. doi:10.1007/978-94-009-3027-8An introduction to boundary layer meteorology

Su, T., Li, Z., Li, C., Li, J., Han, W., Shen, C., et al. (2020). The significant impact of aerosol vertical structure on lower atmosphere stability and its critical role in aerosol-planetary boundary layer (PBL) interactions. *Atmos. Chem. Phys.* 20 (6), 3713–3724. doi:10.5194/acp-20-3713-2020

Tie, X., Huang, R. J., Cao, J., Zhang, Q., Cheng, Y., Su, H., et al. (2017). Severe pollution in China amplified by atmospheric moisture. *Sci. Rep.* 7 (1), 1–8. doi:10.1038/s41598-017-15909-1

Twomey, S. (1977). The influence of pollution on the shortwave albedo of clouds. *J. Atmos. Sci.*, 34(1), 1149–1152. doi:10.1175/1520-0469doi:10.1175/1520-0469(1977)034<1149:tiopot>2.0.co;2

Wang, H., Shi, G. Y., Zhang, X. Y., Gong, S. L., Tan, S. C., Chen, B., et al. (2015). Mesoscale modelling study of the interactions between aerosols and PBL meteorology during a haze episode in China Jing-Jin-Ji and its near surrounding region - Part 2: Aerosols' radiative feedback effects. *Atmos. Chem. Phys.* 15 (6), 3277–3287. doi:10.5194/acp-15-3277-2015

Wang, J., Wang, S., Jiang, J., Ding, A., Zheng, M., Zhao, B., et al. (2014a). Impact of aerosol-meteorology interactions on fine particle pollution during China's severe haze episode in January 2013. *Environ. Res. Lett.* 9 (9), 094002. doi:10.1088/1748-9326/9/9/094002

Wang, Y., Khalizov, A., Levy, M., and Zhang, R. (2013). New Directions: Light absorbing aerosols and their atmospheric impacts. *Atmos. Environ.* 81, 713–715. doi:10.1016/j.atmosenv.2013.09.034

Wang, Z. F., Li, J., Wang, Z., Yang, W. Y., Tang, X., Ge, B. Z., et al. (2014b). Modeling study of regional severe hazes over mid-eastern China in January 2013 and its implications on pollution prevention and control. *Sci. China Earth Sci.* 57 (1), 3–13. doi:10.1007/s11430-013-4793-0

Wang, Z., Huang, X., and Ding, A. (2018). Dome effect of black carbon and its key influencing factors: A one-dimensional modelling study. *Atmos. Chem. Phys.* 18 (4), 2821–2834. doi:10.5194/acp-18-2821-2018

Wang, Z., Huang, X., Ding, K., Ren, C., Cao, L., Zhou, D., et al. (2021). Weakened aerosol-PBL interaction during COVID-19 lockdown in northern China. *Geophys Res. Lett.* 48 (3), 1–10. doi:10.1029/2020GL090542

Wiedinmyer, C., Akagi, S. K., Yokelson, R. J., Emmons, L. K., Al-Saadi, J. A., Orlando, J. J., et al. (2011). The Fire INventory from NCAR (FINN): A high resolution global model to estimate the emissions from open burning. *Geosci. Model Dev.* 4 (3), 625–641. doi:10.5194/gmd-4-625-2011

Wilcox, E. M., Thomas, R. M., Praveen, P. S., Pistone, K., Bender, F. A. M., and Ramanathan, V. (2016). Black carbon solar absorption suppresses turbulence in the atmospheric boundary layer. *Proc. Natl. Acad. Sci. U.S.A.* 113 (42), 11794–11799. doi:10.1073/pnas.1525746113

Wu, J., Bei, N., Hu, B., Liu, S., Zhou, M., Wang, Q., et al. (2019). Aerosol-radiation feedback deteriorates the wintertime haze in the North China Plain. *Atmos. Chem. Phys.* 19 (13), 8703–8719. doi:10.5194/acp-19-8703-2019

Wu, M., Wu, D., Fan, Q., Wang, B. M., Li, H. W., and Fan, S. J. (2013). Observational studies of the meteorological characteristics associated with poor air quality over the Pearl River Delta in China. *Atmos. Chem. Phys.* 13 (21), 10755–10766. doi:10.5194/acp-13-10755-2013

Ye, W. F., Ma, Z. Y., and Ha, X. Z. (2018). Spatial-temporal patterns of PM2.5 concentrations for 338 Chinese cities. *Sci. Total Environ.* 631-632, 524–533. doi:10.1016/j.scitotenv.2018.03.057

Zaveri, R. A., Easter, R. C., Fast, J. D., and Peters, L. K. (2008). Model for simulating aerosol interactions and chemistry (MOSAIC). *J. Geophys. Res.* 113 (13), 1–29. doi:10.1029/2007JD008782

Zaveri, R. A., and Peters, L. K. (1999). A new lumped structure photochemical mechanism for large-scale applications. *J. Geophys. Res.* 104 (D23), 30387–30415. doi:10.1029/1999JD900876

Zhang, B., Wang, Y., and Hao, J. (2015). Simulating aerosol-radiation-cloud feedbacks on meteorology and air quality over eastern China under severe haze conditions in winter. *Atmos. Chem. Phys.* 15 (5), 2387–2404. doi:10.5194/acp-15-2387-2015

Zhang, X., Zhang, Q., Hong, C., Zheng, Y., Geng, G., Tong, D., et al. (2018b). Enhancement of PM2.5 Concentrations by aerosol-meteorology interactions over China. *J. Geophys. Res. Atmos.* 123 (2), 1179–1194. doi:10.1002/2017JD027524

Zhang, X., Zhong, J., Wang, J., Wang, Y., and Liu, Y. (2018a). The interdecadal worsening of weather conditions affecting aerosol pollution in the Beijing area in relation to climate warming. *Atmos. Chem. Phys.* 18 (8), 5991–5999. doi:10.5194/acp-18-5991-2018

Zhang, Y., Wang, K., and He, J. (2017). Multi-year application of WRF-CAM5 over East Asia-Part II: Interannual variability, trend analysis, and aerosol indirect effects. *Atmos. Environ.* 165, 222–239. doi:10.1016/j.atmosenv.2017.06.029

Zhao, B., Liou, K. N., Gu, Y., Li, Q., Jiang, J. H., Su, H., et al. (2017). Enhanced PM2.5 pollution in China due to aerosol-cloud interactions. *Sci. Rep.* 7 (1), 1–11. doi:10.1038/s41598-017-04096-8

Zhong, J., Zhang, X., Wang, Y., Wang, J., Shen, X., Zhang, H., et al. (2019). The two-way feedback mechanism between unfavorable meteorological conditions and cumulative aerosol pollution in various haze regions of China. *Atmos. Chem. Phys.*, 19, 3287–3306. doi:10.5194/acp-19-3287-2019

frontiers | Frontiers in Environmental Science

TYPE Original Research
PUBLISHED 21 October 2022
DOI 10.3389/fenvs.2022.1024795

OPEN ACCESS

EDITED BY
Gen Zhang,
Chinese Academy of Meteorological Sciences, China

REVIEWED BY
Yun Lin,
Joint Institute for Regional Earth System Science and Engineering, College of Physical Sciences, University of California, Los Angeles, United States
Shupeng Zhu,
University of California, Irvine, United States

*CORRESPONDENCE
Wei Tang,
tangwei@craes.org.cn

SPECIALTY SECTION
This article was submitted to Atmosphere and Climate, a section of the journal Frontiers in Environmental Science

RECEIVED 22 August 2022
ACCEPTED 06 October 2022
PUBLISHED 21 October 2022

CITATION
Du X, Tang W, Zhang Z, Chen J, Han L, Yu Y, Li Y, Li H, Chai F and Meng F (2022), Responses of ozone concentrations to the synergistic control of NO_x and VOCs emissions in the Chengdu metropolitan area. *Front. Environ. Sci.* 10:1024795. doi: 10.3389/fenvs.2022.1024795

Responses of ozone concentrations to the synergistic control of NO_x and VOCs emissions in the Chengdu metropolitan area

Xiaohui Du[1,2,3], Wei Tang[1]*, Zhongzhi Zhang[1], Junhui Chen[4], Li Han[4], Yang Yu[1], Yang Li[1], Yingjie Li[4], Hong Li[1], Fahe Chai[1] and Fan Meng[2]

[1]Atmospheric Environment Institute, Chinese Research Academy of Environmental Sciences, Beijing, China, [2]State Key Laboratory of Environmental Criteria and Risk Assessment, Chinese Research Academy of Environmental Sciences, Beijing, China, [3]College of Water Sciences, Beijing Normal University, Beijing, China, [4]Sichuan Academy of Environmental Sciences, Chengdu, China

Simulations of 108 emission reduction scenarios for NO_x and VOCs using Comprehensive Air Quality Model with Extensions (CAMx) were conducted for eight cities in the Chengdu metropolitan area (CMA). The isopleth diagrams were drawn to explore the responses and differences of ozone (O_3) concentrations to NO_x and VOCs emission changes under Chengdu, CMA and Sichuan Province emission reduction scenarios. The results show that the O_3-sensitive regimes of eight cities may change under different emission reduction scenarios. Under Chengdu emission reduction scenario, the Chengdu city is in the transition regime and O_3 formation will shift from transition to VOC-limited when the VOCs emissions decreased by 50%, and the decreases in O_3 concentrations caused by VOCs emission reductions are small. For the CMA and Sichuan Province emission reduction scenarios, all cities are NO_x-limited in the baseline cases and with at least a 66% and a 77% reduction in NO_x emissions, respectively, the daily maximum 8-h average O_3 (MDA8) can attain the O_3 standard (160 μg m^{-3}). Although reductions in VOCs emissions can also lessen the O_3 concentration, the effectiveness is relatively small. The changes in O_3 concentrations under different VOCs to NO_x emission reduction ratios indicate that all cities achieve a relatively high O_3 concentration decrement with low VOCs to NO_x emission reduction ratios and that the decreasing O_3 concentrations caused by non-local emission reductions are much higher than those achieved by local emission reductions. In addition, the decreases in O_3 concentrations in Chengdu are quite close when the total NO_x and VOCs emissions reduction percentages are less than 30% under the CMA and Sichuan emission reduction scenarios.

KEYWORDS

ozone modeling, emission reduction scenarios, O3-sensitive regimes, empirical kinetic modeling approach, Chengdu metropolitan area

1 Introduction

High ozone (O_3)concentrations threaten human health and shorten human life (Amann et al., 2008). The mechanism of O_3 formation and destruction is very complex. O_3 can be generated *via* a series of complex chemical reactions between nitrogen oxides (NO_x) and volatile organic compounds (VOCs) under sunlight conditions (Haagen-Smit, 1952; Yu, 2019; Li et al., 2022). Therefore, it is useful to study the relationship between the changes of NO_x and VOCs emissions and O_3 pollution in oreder to develop mitigation strategies that effectively reduce O_3 concentrations. The Chengdu metropolitan area (CMA) has become a large urban agglomeration in southwestern China due to its rapid industrial development and population growth (Yang et al., 2020), leading to a significant increase in air pollutant emissions and air pollution problems (Zhou et al., 2019). O_3 concentrations in CMA have gradually increased from 2015 to 2019. The number of days when the daily maximum 8-h average O_3 concentration (MDA8) in CMA exceeded the secondary standard of the Ambient Air Quality Standard (GB3095-2012) increased by 95 days, and the total number of exceeding days for 2019 reached 331 days in CMA. The number of days with excessive O_3 concentrations in Chengdu accounted for 1/6 of the polluted days in 2019. Therefore, it is essential to control regional O_3 pollution in the CMA region.

Studies show that when NO_x emissions are at very high level, the reaction of NO_x with OH radicals will inhibit the formation of O_3. However, when VOCs emissions increase concurrently, O_3 concentrations increase. At very high VOCs emissions, the rate of self-reaction of HO_2 is much greater than its reaction with NO, and increasing NO_x emissions will enhance O_3 formations as well (Zhang, 2013; Itahashi et al., 2015, 2020; Kim et al., 2017; Wickham et al., 2019). This indicates that the relationships among O_3-NO_x-VOC need to be considered in conjunction with NO_x and VOCs emission reductions to prevent O_3 pollution. The 'Ozone Pollution Prevention and Control Action Program' implemented in 2017 in Chengdu demonstrated that scientific emission reduction ratio of VOCs to NO_x could reduce the O_3 concentration in Chengdu more effectively (Wu and Xie, 2017). Other studies conducted in different regions also revealed that appropriate VOCs to NO_x ratios could enhance the reduction of O_3 concentrations (Chen et al., 2019; He et al., 2019; Wang et al., 2019).

The response of O_3 to NO_x and VOCs emissions can be determined by setting different NO_x and VOCs emissions abatement scenarios to simulate the changes in O_3 concentrations, and the sensitivities of O_3 to VOCs and NO_x emissions can be explored by plotting empirical kinetic modeling approach (EKMA) curves based on various emission reduction scenarios (Qu et al., 2014; Ou et al., 2016; Tan et al., 2018; Cui et al., 2021; Jiang et al., 2021; Liu et al., 2021). Although the contributions from local emissions play an important role in O_3 foramtion in CMA (Yang et al., 2020; Yang et al., 2021), studies investigating the separate effects of local and regional emissions on O_3 concentrations in the CMA region have not been widely conducted.

In this study, 108 emission reduction scenarios for NO_x and VOCs emissions, including 36 scenarios for the Chengdu city, 36 scenarios for the CMA region and 36 scenarios for Sichuan Province are conducted using the Comprehensive Air Quality Model with Extensions (CAMx) model, to explore the different effects of local and regional emissions on O_3 concentrations and to develop a more refined O_3 abatement policy for the Chengdu city. The effects of changes in NO_x and VOCs emissions from different source regions on the O_3 concentrations are compared and discussed. The results provide the scientific supports for developing O_3 control measures at municipal and regional levels in the CMA region.

2 Method and material

2.1 Model description and settings

CAMx, version 7.1 (ENVIRON, 2020), is a third-generation three-dimensional (3D) air quality model and can be applied to multi-scale integrated simulation studies of photochemical smog and fine particulate matter in a 3D nested grid. It can provide several extensions, such as source apportionment techniques, sensitivity analysis, process analysis, *etc.* These extension modules have been widely used in China and abroad (Chatani et al., 2020; A. M. Dunker, 2015; Alan M. Dunker et al., 2015; Yarwood et al., 2013).

In this study, the horizontal resolution of the master grid is 36 × 36 km (Figure 1A), covering the whole China, Northeast Asia and some parts of Southeast Asia. The nested grid is 12 × 12 km, covering Sichuan Province and its surrounding areas (Figure 1B). The model is divided into 20 layers vertically. The Weather Research and Forecasting (WRF v3.9.1.1) model (Skamarock et al., 2019) is used to provide meteorological conditions, with the input data (6 h interval) from the National Centers for Environmental Prediction (NCEP) Final Analysis (FNL). The gas-phase chemical mechanism is SAPRC07 and the coarse/fine aerosol chemistry scheme is used for the aerosol chemistry mechanism. The photolysis rates used in the model are calculated using the O_3 column concentrations from the Ozone Monitoring Instrument (OMI) data.

The emissions inventory for the master grid (36 km) is based on the Multi-resolution Emission Inventory for China (MEIC 2016, Li et al., 2017) and Regional Emission Inventory in Asia (REAS2.1, Kurokawa et al., 2013). The emission inventory used for the nest grid (12 km) is according to MEIC2016 and adjusted by the localized air pollutant emission inventory. VOCs emission is subdivided into 116 species using the VOCs species consolidation methods

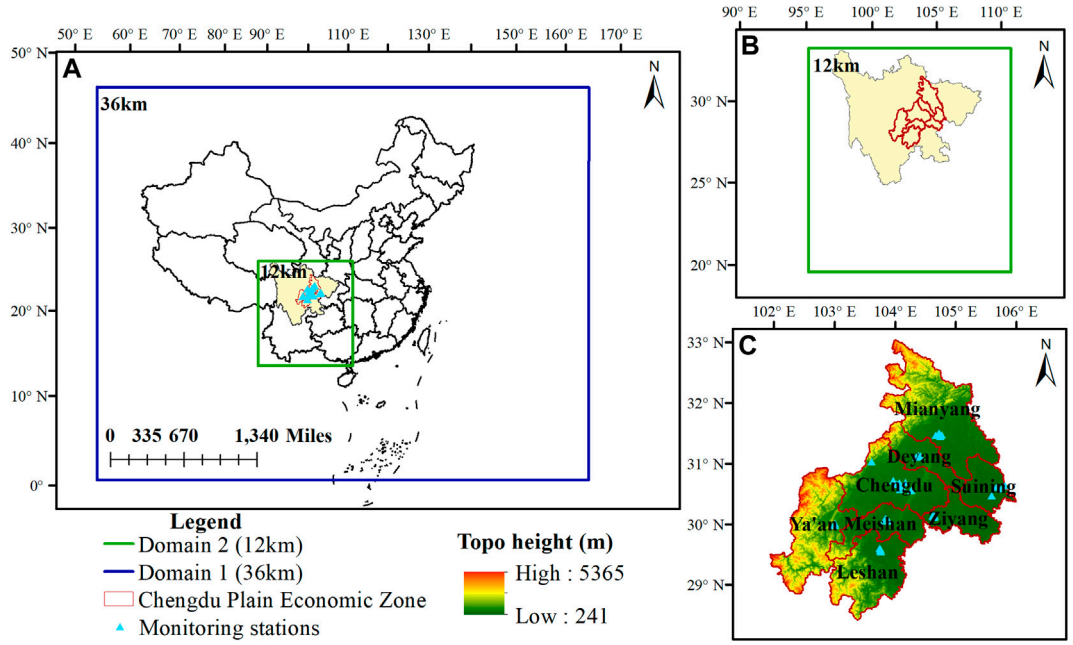

FIGURE 1
Modeling domains for **(A)** East Asia, **(B)** Sichuan and its surrounding area and **(C)** the CMA region. The blue triangles in (C) represent national air quality monitoring stations.

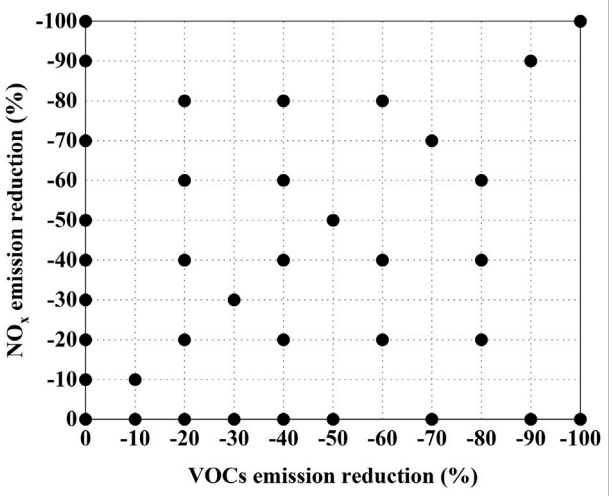

FIGURE 2
NOx and VOCs emission reductions matrix

introduced by Carter. (2000), Li et al. (2014) and Carter and Heo. (2013) for allocation of VOCs species for the SAPRC07 mechanism. The biogenic emissions used in the simulations are generated by the Model of Emissions of Gases and Aerosols from Nature (MEGANv3.1; Guenther et al., 2019).

2.2 Simulation scenarios design

One baseline scenario and 108 emission reduction scenarios are designed in this study. Of the 108 scenarios, 36 are region-wide NO_x and VOCs emissions reductions for Chengdu with emissions outside Chengdu remaining unchanged; 36 are region-wide emission reduction scenarios for eight cities in the CMA region (Chengdu, Deyang, Mianyang, Meishan, Leshan, Ziyang, Suining and Ya'an) with emissions outside CMA remaining unchanged; 36 are region-wide emission reduction scenarios for entire Sichuan Province with emissions outside Sichuan Province remaining unchanged. Figure 2 shows the matrix of different NO_x and VOCs emission reductions. The origin (x = y = 0) represents the baseline scenario and the dots identify the proportions of NO_x and VOCs emissions reduction percentages that are applied for Chengdu, CMA and Sichuan Province. Referring to Ou et al. (2016), Chen et al. (2019) and Luo et al. (2021) for the setting of emission reduction scenarios, since those nearest the baseline cases represent more feasible emissions reductions, the emissions reduction percentages are spaced at 10% intervals when the emissions reduction percentages are 50% or less and at 20% intervals when the emissions reduction percentages exceeded 50%. In order to investigate the changes in O_3 concentrations at different emissions reduction ratios of VOCs to NO_x, 12 scenarios with different reduction percentages of NO_x and VOCs emissions are designed (e.g., 20% reduction for NO_x and 40% reduction for VOCs). All simulations are conducted for the August

TABLE 1 Comparisons of observed and simulated MDA8 O_3 concentrations on polluted days in eight cities in August 2019 (MDA8 O_3 concentrations exceeding 160 μg m^{-3}).

City name	Observed MDA8 O_3	Simulated MDA8 O_3	Fractional bias (%)	Number of pollution days
Chengdu	194.64	175.42	−10.80	14
Deyang	209.14	179.11	−14.09	7
Leshan	177.50	199.99	12.12	6
Meishan	188.00	182.30	−3.55	10
Mianyang	179.17	171.52	−5.52	6
Suining	179.43	223.51	21.59	7
Ya'an	170.00	167.54	−1.93	4
Ziyang	178.33	193.49	6.63	9

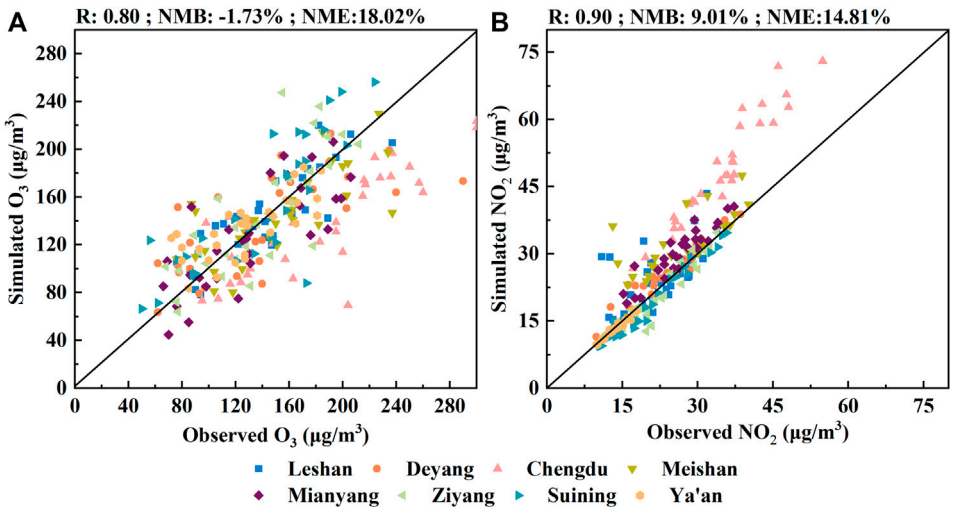

FIGURE 3
Comparisons of **(A)** daily maximum 8-h average O_3 and **(B)** daily averaged NO_2 concentrations in eight cities of the CMA region in August 2019.

2019 period, and the other input parameters used for all simulations are unified. Finally, the responses of O_3 to NO_x and VOCs emission reductions are calculated based on the 108 emission reduction scenarios and are visualised *via* O_3-NO_x-VOC isopleths.

Considering that pollution control measures are mainly targeted at stages of heavy pollution, O_3 polluted days in each city are selected as those for which the observed and simulated MDA8 O_3 concentrations are simultaneously greater than 160 μg m^{-3}, and the number of O_3 polluted days during August 2019 are counted (Table 1), the simulated MDA8 O_3 concentrations for each city are averaged over the modeling grids where the monitoring stations are located. The factional bias between observed and simulated MDA8 O_3 concentrations are calculated for each city, showing that the model is well performed for simlulating the polluted days with most of biases less than 20%.

3 Results and discussions

3.1 Model evaluation

The evaluation of the model performance for O_3 and NO_2 concentrations in cities of the CMA region is illustrated in Figure 3. The observed MDA8 O_3 concentrations and the daily NO_2 concentrations averaged over the monitoring sites in each city are used against the simulated data. The simulated MDA8 O_3 concentrations in August 2019 are extracted from the modeling grids where the monitoring stations are located. A total of 37 national monitoring stations in the eight cities in CMA are chosen for model validations (Figure 1C). The statistical metrics, correlation coefficient (R), normalised mean bias (NMB) and normalised mean error (NME) show that the correlations between simulated and observed O_3 and NO_2 concentrations

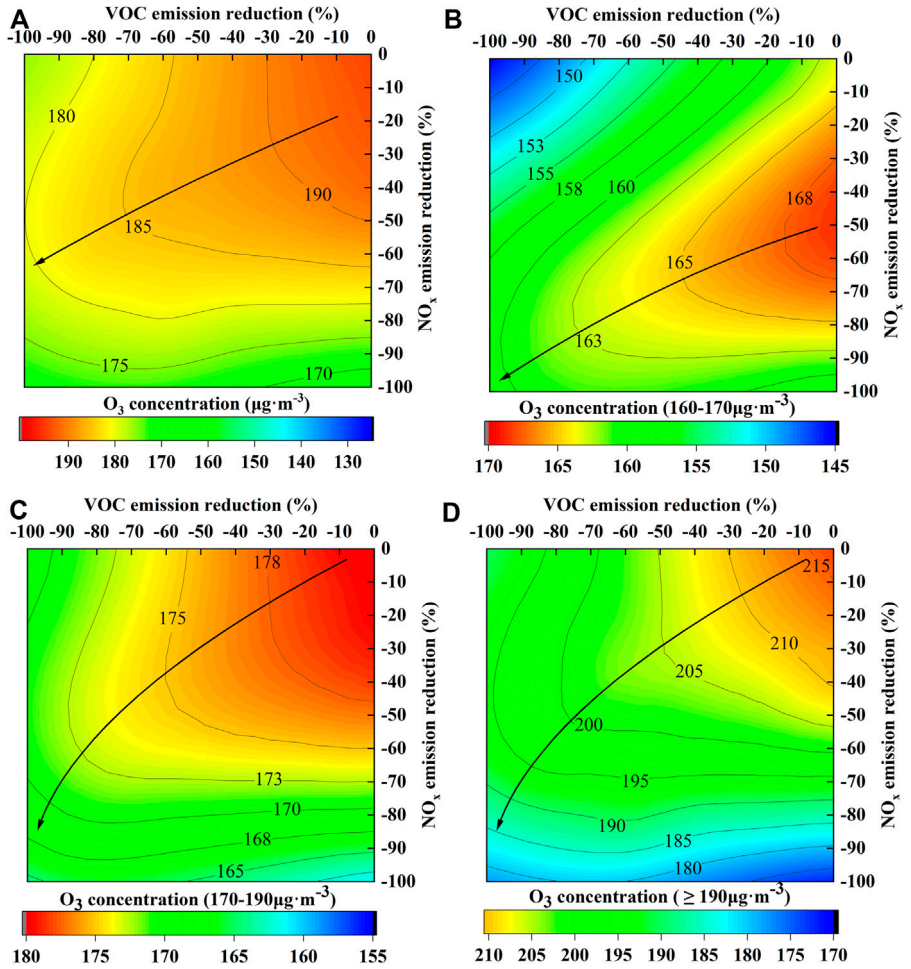

FIGURE 4
Isopleth diagrams of MDA8 O_3 varing with VOCs and NO_x emission reductions in Chengdu for **(A)** all polluted days, **(B)** polluted days with MDA8 O_3 concentrations in the range of 160–170 μg m^{-3}, **(C)** polluted days with MDA8 O_3 concentrations in the range of 170–190 μg m^{-3} and **(D)** polluted days with MDA8 O_3 concentrations greater than 190 μg m^{-3} (the black arrows are ridgelines).

are both greater than 0.8, the NMB values of O_3 and NO_2 are −1.73% and 9.01%, and the NME values of O_3 and NO_2 are 18.02% and 14.81%, indicating that the model generally performs well over the CMA region (Emery et al., 2017).

3.2 Responses of O_3 to NO_x and VOCs emission reductions

3.2.1 Reduction scenarios in chengdu

A baseline and thirty-six abatement scenarios were conducted to investigate the effects of local and regional emission reductions on MDA8 O_3 concentrations in Chengdu. Isopleth diagrams of average MDA8 O_3 concentration are plotted on polluted days during August 2019 with NO_x and VOCs emissions reduced only for Chengdu (Figure 4A), following the method as described in Section 2.2 (Table 1). The decreases in O_3 concentrations due to the reductions of local NO_x and VOCs emissions for Chengdu are small, even with a 100% reduction of local emissions, which only brings down the MDA8 O_3 concentration close to 170 μg m^{-3}. The isopleth diagrams illustrate that the MDA8 O_3 concentration for the baseline scenario is skewed towards the transition regime (Figure 4A). When the VOCs emissions gradually reduce and NO_x emissions remain the same or decrease less than the VOCs emissions, the O_3-sensitive regime in Chengdu gradually moves toward VOC-limited.

The average MDA8 O_3 polluted days during August 2019 in Chengdu are divided into three categories based on the following concentration ranges, 160–170 μg m^{-3}, 170–190 μg m^{-3} and ≥190 μg m^{-3} (Figures 4B–D). When the MDA8 O_3 concentrations at the range of 160–170 μg m^{-3}, Chengdu is in VOC-limited regime and a decrease in NO_x emissions enhancing

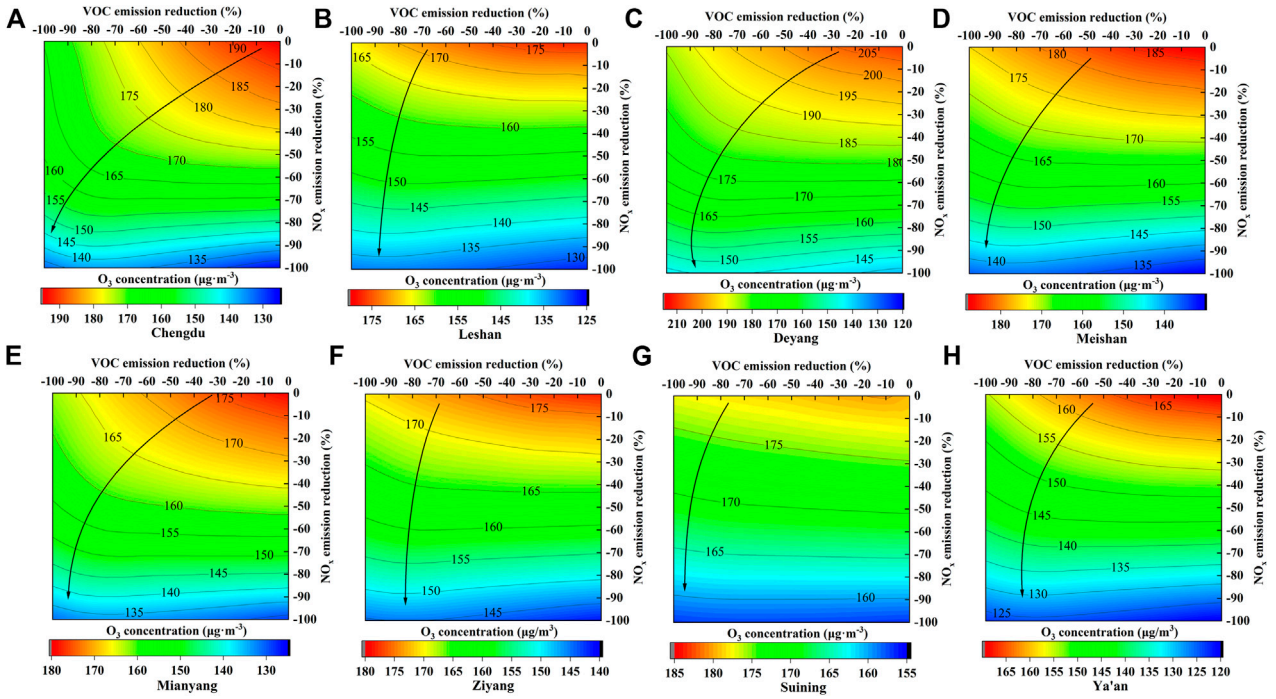

FIGURE 5
Isopleth diagrams of MDA8 O_3 varing with VOCs and NO_x emission reductions for the CMA scenario ((**A**) Chengdu, (**B**) Leshan, (**C**) Deyang, (**D**) Meishan, (**E**) Mianyang, (**F**) Ziyang, (**G**) Suining, (**H**) Ya'an; the black lines with arrows are ridgelines).

O_3 concentrations. However, a 20% reduction in VOCs emissions in Chengdu can bring down the MDA8 O_3 concentration to 160 μg m^{-3}. When the MDA8 O_3 concentration above 170 μg m^{-3}, Chengdu is in a transition regime. At the range of 170–190 μg m^{-3}, MDA8 O_3 concentrations in Chengdu are only likely to reach 160 μg m^{-3} when NO_x emissions decreased by almost 100%. At the O_3 level above 190 μg m^{-3}, the MDA8 O_3 concentrations in Chengdu cannot reach 160 μg m^{-3} if only local emissions are reduced. It indicates that at light levels of O_3 pollution, reducing local emission can attain O_3 standard, while at more severe levels of O_3 pollution, considering regional control measures are necessary in Chengdu.

3.2.2 Reduction scenarios in CMA

In the emission reduction scenario for eight cities in CMA, the isopleth diagrams of MDA8 O_3 illustrates that all cities are mainly NO_x-limited in the baseline scenario except for Chengdu, which is in a transition regime (Figure 5). In Chengdu, the reduction of both NO_x and VOCs emissions resulted in a decrease in O_3 concentration. When NO_x and VOCs emission reductions exceeded 40%, the gradient of O_3 concentration decrement caused by NO_x reduction is greater than that from VOCs reduction. Similar trend is also observed for Deyang. The O_3 isopleths for Leshan, Meishan, Mianyang and Ya'an show that the effects of VOCs emission reductions on O_3 concentrations are small, with only a decrease of O_3 concentration around 5 μg m^{-3} by more than 50% reductions. The nearly horizontal contours of Suining and Ziyang indicate that these two cities are NO_x-limited and reducing NO_x emissions inhibits O_3 formations. Therefore, priorly reducing NO_x emissions in the eight cities of CMA will bring down O_3 concentrations more effectively.

The responses of O_3 concentrations to NO_x and VOCs emissions vary in different cities in the CMA region. The averaged MDA8 O_3 concentrations in cities such as Leshan, Mianyang and Ya'an can attain the standard (160 μg m^{-3}) when NO_x emissions in CMA are reduced by 22–53%. Cities such as Chengdu, Ziyang, Deyang and Meishan need to reduce NO_x emissions in CMA by 60–77% to reach the standard. Although the MDA8 O_3 concentrations in Suining are lower than most of the other cities, the reduction of NO_x emissions in CMA causes a small gradient in the decrease of O_3, resulting in more than 89% reduction of NO_x emissions in CMA to lower down O_3 concentrations below 160 μg m^{-3}. It indicates that synergistic precursor emission reductions from the CMA region or outside CMA are required to achieve more effective O_3 controls.

3.2.3 Reduction scenarios in Sichuan Province

Isopleth diagrams of the averaged MDA8 O_3 concentrations *versus* the VOCs and NO_x emission reduction percentages for

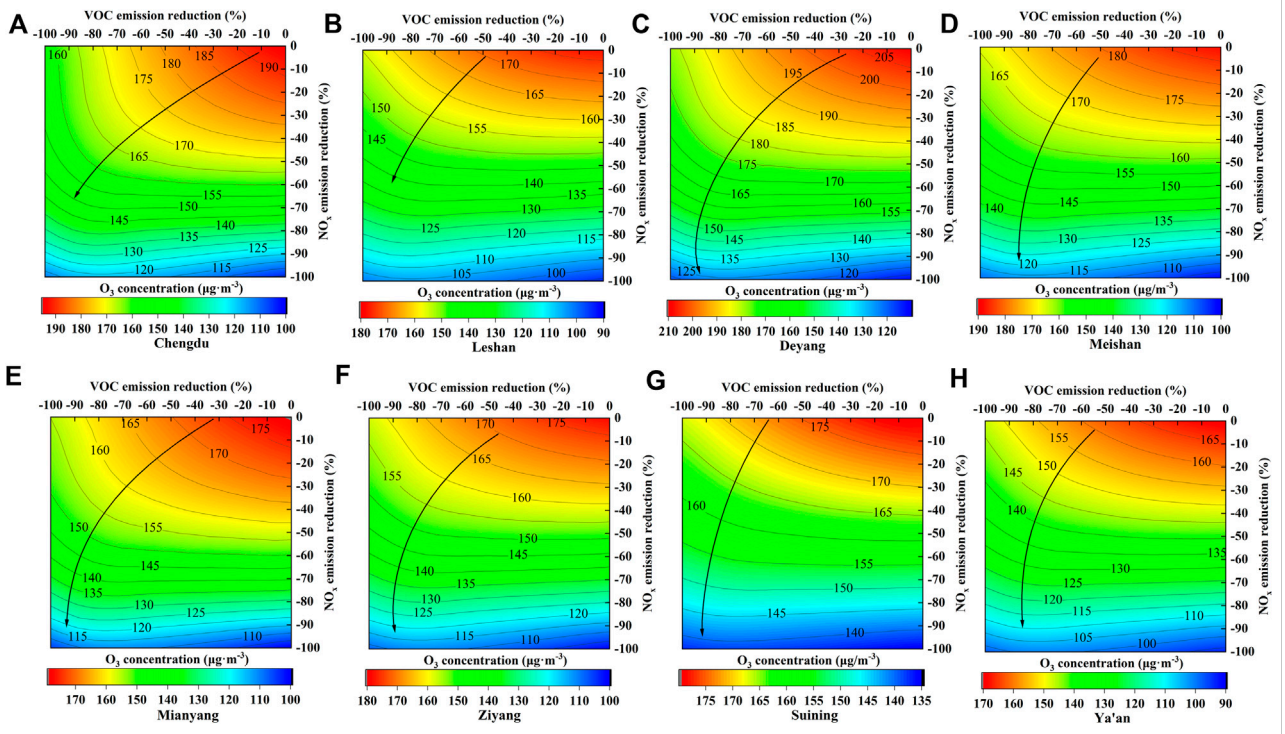

FIGURE 6
Isopleth diagrams of MDA8 O_3 varing with VOCs and NO_x emission reductions for the Sichuan Province scenario ((**A**) Chengdu, (**B**) Leshan, (**C**) Deyang, (**D**) Meishan, (**E**) Mianyang, (**F**) Ziyang, (**G**) Suining, (**H**) Ya'an; the black lines with arrows are ridgelines).

Sichuan Province are shown in Figure 6. It shows that reducing NO_x and VOCs emissions in Sichuan Province cause a larger gradient in the decrease of MDA8 O_3 concentrations compared to those shown in Figure 4 and Figure 5. Although the responses of O_3 concentrations to NO_x and VOCs emissions in most cities are NO_x-limited, the same percentage of VOCs emission reductions in Figure 6 causes a greater decrease in MDA8 O_3 concentrations than in Figure 4 and Figure 5. In Leshan, Mianyang and Meishan, around 30% VOCs emission reductions result in a 5 μg m^{-3} decrease in the O_3 concentrations. Similarly, the MDA8 O_3 concentrations in eight cities reach the 160 μg m^{-3} much faster in the emission reduction scenarios for Sichuan Province. Cities such as Ziyang, Suining, Leshan, Mianyang and Ya'an, NO_x emissions dropped by around 20–45%, and cities such as Chengdu, Deyang and Meishan, NO_x emissions dropped by approximately 48–66%, respectively, MDA8 O_3 concentrations can attain the standard of 160 μg m^{-3}.

The effects of NO_x and VOCs emission reductions from different regions on O_3 concentrations vary significantly among cities. Figure 7 shows the maximum decrements in MDA8 O_3 concentrations for each city under the 100% NO_x and VOCs emission reductions for the CMA region and Sichuan Province. The emission reductions for Sichuan Province result in a maximum decrease in MDA8 O_3 concentrations above 77.4 μg m^{-3} (40%) for most cities, with a maximum of approximately 83.9 μg m^{-3} (47%) in Leshan. The exception is in Suining, which has the smallest decrease in O_3 concentrations among these cities, with a maximum decrease of about 44 μg m^{-3} (25%) in two different regional emission reduction scenarios. A study by Lu et al. (2019) revealed that the background O_3 concentrations from May to August accounted for approximately 50.3% of total O_3 concentrations in the Sichuan Basin, indicating that a 100% reduction of anthropogenic emissions in Sichuan Province may cause less than 50% decrease of total O_3 concentrations.

The maximum decrease in O_3 concentrations in Deyang and Chengdu under the CMA emission reduction scenario is around 71.4 μg m^{-3} (34.1%) and 68.8 μg m^{-3} (35.4%), respectively, and the maximum decrease in O_3 concentrations in Chengdu and Deyang under the Sichuan Province emission reduction scenario is about 97.5 μg m^{-3} (46.6%) and 91.0 μg m^{-3} (46.8%), respectively. The decreases in O_3 concentrations under the Sichuan Province emission reduction scenario are approximately 12% larger compared to the CMA emission reduction scenario, especially in Leshan, Mianyang and Ziyang, decreases in O_3 concentrations under the Sichuan

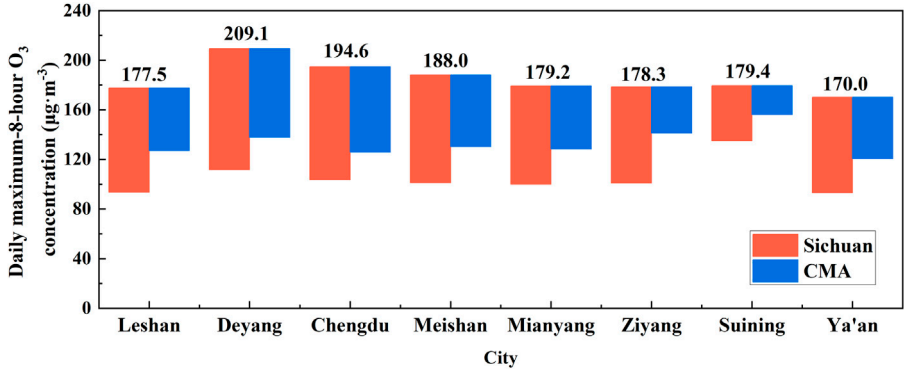

FIGURE 7
The effects of 100% NO_x and VOCs emission reductions on MDA8 O_3 concentrations in eight cities for the CMA and Sichuan Province scenarios.

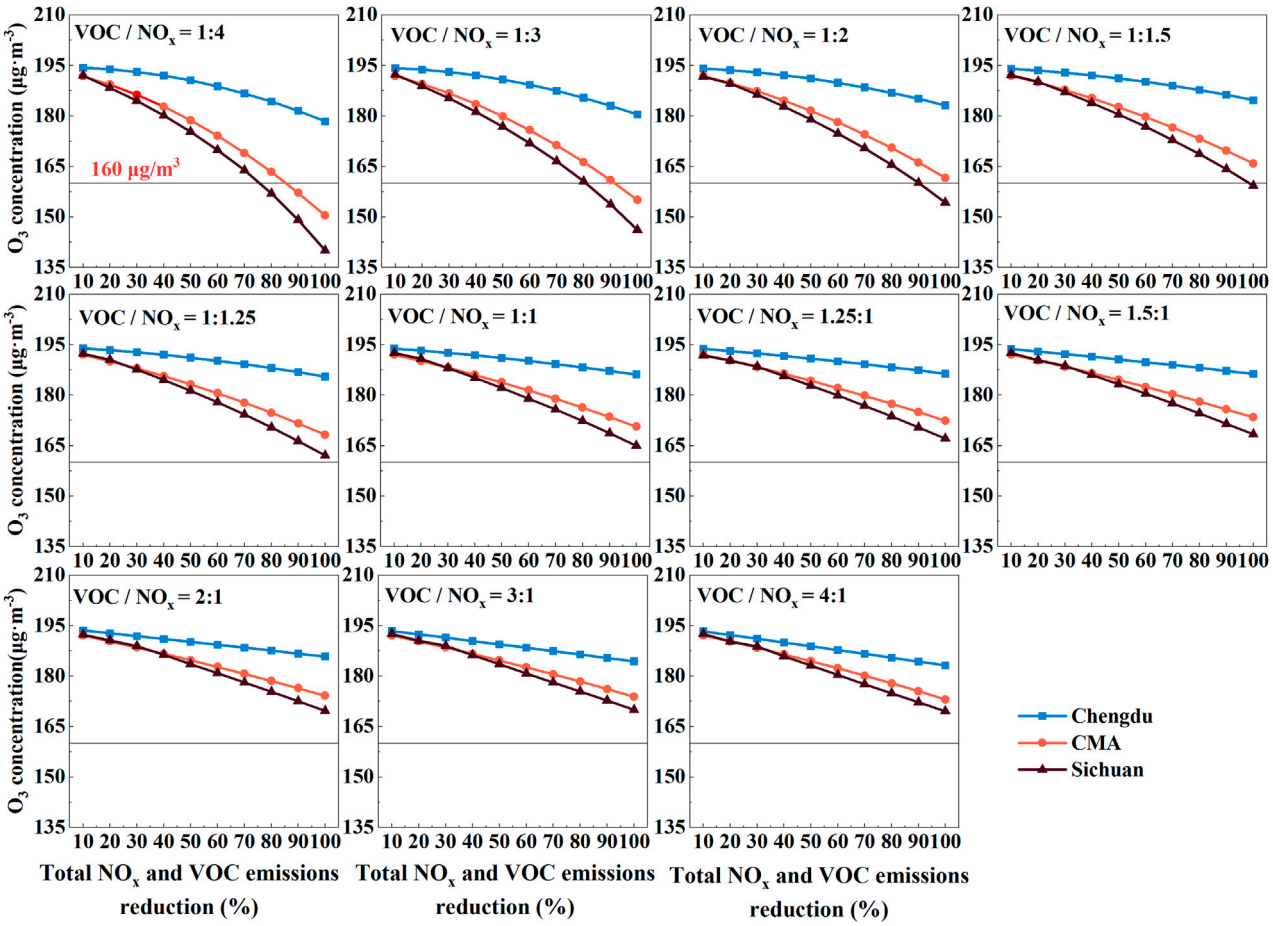

FIGURE 8
Effects of the emission reductions with different VOCs to NO_x ratios on the changes in MDA8 O_3 concentrations under Chengdu, CMA and Sichuan Province scenarios.

Province emission reduction scenario are about 20% higher than those under the CMA emission reduction scenario.

3.3 Differences in O_3 reduction effectiveness

Figures 4–6 illustrate the effects of local and regional emission perturbations on O_3 concentrations. Comparing the O_3 isopleth diagrams for Chengdu, CMA and Sichuan Province emission reduction scenarios reveals that, although the baseline scenario showing Chengdu is in a VOC-limited regime, the reductions of local VOCs emissions have small impact on the decrease of O_3 concentrations. When local VOCs emissions decreased by 60%, the decrease of O_3 concentrations in Chengdu is less than 5 μg m^{-3}. In contrast, under emission reduction scenarios for the CMA and Sichuan Province, to achieve a 5 μg m^{-3} decrease in MDA8 O_3 concentrations in Chengdu only required a reduction of NO_x or VOCs emissions of less than 20%, and even a smaller reduction rate is demanded if both NO_x and VOCs emissions are reduced. It indicates that the regional and transported emission sources on O_3 concentrations should be considered in emission control strategies.

Referring to the emission ratios of VOCs to NO_x in other studies (Chen et al., 2019; Wang et al., 2019; Yao et al., 2021), 11 different emission reduction ratios of VOCs to NO_x emissions (VOCs/NO_x = 1:4, 1:3, 1:2, 1:1.5, 1:1.25, 1:1, 1.25:1, 1.5:1, 2:1, 3:1, 4:1) within 100% emission reductions under Chengdu, CMA, and Sichuan Province scenarios are conducted to investigate the changes for MDA8 O_3 in Chengdu (Figure 8). When the emission reduction ratio of VOCs/NO_x is greater than 1, the decreasing trend of the averaged MDA8 O_3 concentration is closer to linear and the decrement in the averaged MDA8 O_3 concentration is significantly smaller than those when the ratio is less than 1. In contrast, the decreasing trend in the averaged MDA8 O_3 concentration is non-linear when the emission reduction ratio of VOCs/NO_x is equal to or less than one and the smaller the ratio (the larger reduction of NO_x emission) the faster the O_3 decrease. The largest decrease in the averaged MDA8 O_3 concentration is at the VOCs/NO_x ratio of 1:4.

Among the emission reduction scenarios in different regions, the decrease in the averaged MDA8 O_3 concentration under the Chengdu emission reduction scenario is significantly smaller than those under the other two regional emission reduction scenarios (the CMA and Sichuan Province). However, when the total VOCs and NO_x emission reductions are less than 30%, especially at high ratio of VOCs/NO_x, the decrease in the averaged MDA8 O_3 concentration under these two emission reduction scenarios is almost identical.

4 Conclusion

108 scenarios of NO_x and VOCs emission reductions for different regions were simulated using the CAMx model and the relationship among O_3-NO_x-VOC was obtained in this study. The responses of O_3 formation to the changes in NO_x and VOCs emissions in the CMA region were demonstrated by the O_3 isopleth diagrams. In addition, 11 emission reduction cases with different VOCs-to-NO_x ratios were investigated to explore the changes in O_3 concentrations under different reduction ratios of precursor emissions.

It was found that the O_3-sensitive regimes in Chengdu city was in a transition zone, while the other cities in the CMA region were in the NO_x-limited zone. Eight cities could meet the MDA8 O_3 concentration standard when NO_x emissions in the CMA region were reduced by 77% or more. However, if only cut VOCs emissions, even with a 100% reduction, it failed to attain O_3 standard of 160 μg m^{-3} for all cities in the CMA region. The results showed that under the NO_x and VOCs emission reduction scenario in Sichuan Province, the most effective way to reduce the peak MDA8 O_3 concentration was to control NO_x emissions, with a 66% reduction in NO_x emissions enabling cities in the CMA region to reach the MDA8 O_3 standard (160 μg m^{-3}). However, in reality, it is quite difficult to achieve 66% NO_x emission reductions in a short time period. Hence, in order to reach the MDA8 O_3 standard in all cities in the CMA region, joint regional pollutant prevention and control abatement measures outside of Sichuan Province may need to be considered. Although a decrease in VOCs emissions could also reduce the MDA8 O_3 concentration, the effects were smaller than that achieved with a decrease in NO_x emissions, and cutting VOCs emissions alone may not be able to achieve the MDA8 O_3 standard in some cities, such as Deyang, Meishan, and Suining. Overall, the NO_x and VOCs emission reductions in Sichuan Province could reach a 50% higher O_3 concentration decrease than the emission reductions in the CMA region, such as in the Ziyang city, but the other cities such as Deyang, Chengdu and Suining, such differences were not significant.

The MDA8 O_3 concentration decreases resulting from different VOCs to NO_x emission reduction ratios for the eight cities in the CMA region showed that all cities reach higher MDA8 O_3 decreases due to NO_x emissions control. In addition, the effects of non-local emission reductions on MDA8 O_3 decreases were much higher than those from local emission reductions. Furthermore, in the emission reduction scenarios for the CMA and Sichuan Province, the decreases in MDA8 O_3 were almost identical for NO_x and VOCs emission reductions at less than 30%, suggesting that if the non-local NO_x and VOCs emission reductions were small, effects of expanding the emission control area from CMA to Sichuan Province on MDA8 O_3 were insignificant.

O_3 is highly transportable and biogenic VOCs emissions were relatively high in summer, contributing high background O_3 concentrations and increasing the difficulties in O_3 control. Although most cities in the CMA region were NO_x-limited on the regional basis, the synergistic control of NO_x and VOCs emissions was still an effective way to reduce O_3 concentrations in the short term. On the other hand, persistently controlling regional NO_x emissions should become a control measure in a long run to further reduce O_3 levels regionally.

Data availability statement

The raw data supporting the conclusions of this article will be made available by the authors, without undue reservation.

Author contributions

XD and WT contributed significantly to the conception of the study and to model data analysis and manuscript preparation; ZZ, YY and YL conducted simulations and model performance evaluations; JC, LH, YL prepared emission inventory for the modeling; HL, FC and FM helped perform the analysis with constructive discussions. All authors contributed to the article and approved the submitted version.

Funding

This work was supported by National Key Research and Development Project (NO. 2017YFC0213003, NO. 2018YFC0213504, NO. 2016YFC0208905).

Acknowledgments

The authors would like to thank Jiemeng Bao and Zhenhai Wu for providing measurement data.

Conflict of interest

The authors declare that the research was conducted in the absence of any commercial or financial relationships that could be construed as a potential conflict of interest.

Publisher's note

References

Amann, M., Derwent, D., Forsberg, B., Hanninen, O., Hurley, F., Krzyzanowski, M., et al. (2008). *World Health Organization: Health risks of ozone from long-range transboundary air pollution*. Geneva, Switzlerand: World Health Organisation Regional Office for Europe. Available at: http://www.euro.who.int/__data/assets/pdf_file/0005/78647/E91843.pdf (Accessed October 18, 2017).

Carter, W. P. L., and Heo, G. (2013). Development of revised SAPRC aromatics mechanisms. *Atmos. Environ.* 77, 404–414. doi:10.1016/j.atmosenv.2013.05.021

Carter, W. P. L. (2000). Implementation of the saprc-99 chemical mechanism into the models-3 framework. Report, 1–101.

Chatani, S., Shimadera, H., Itahashi, S., and Yamaji, K. (2020). Comprehensive analyses of source sensitivities and apportionments of PM_{2.5} and ozone over Japan via multiple numerical techniques. *Atmos. Chem. Phys.* 20 (17), 10311–10329. doi:10.5194/acp-20-10311-2020

Chen, X., Situ, S., Zhang, Q., Wang, X., Sha, C., Zhouc, L., et al. (2019). The synergetic control of NO2 and O3 concentrations in a manufacturing city of southern China. *Atmos. Environ.* 201 (2), 402–416. doi:10.1016/j.atmosenv.2018.12.021

Cui, M., An, X., Xing, L., Li, G., Tang, G., He, J., et al. (2021). Simulated sensitivity of ozone generation to precursors in beijing during a high O3 episode. *Adv. Atmos. Sci.* 38 (7), 1223–1237. doi:10.1007/s00376-021-0270-4

Dunker, A. M., Koo, B., and Yarwood, G. (2015). Source apportionment of the anthropogenic increment to ozone, formaldehyde, and nitrogen dioxide by the path-integral method in a 3D model. *Environ. Sci. Technol.* 49 (11), 6751–6759. doi:10.1021/acs.est.5b00467

Dunker, A. M. (2015). Path-integral method for the source apportionment of photochemical pollutants. *Geosci. Model Dev.* 8 (6), 1763–1773. doi:10.5194/gmd-8-1763-2015

Emery, C., Liu, Z., Russell, A. G., Odman, M. T., Yarwood, G., and Kumar, N. (2017). Recommendations on statistics and benchmarks to assess photochemical model performance. *J. Air Waste Manag. Assoc.* 67 (5), 582–598. doi:10.1080/10962247.2016.1265027

ENVIRON (2020). *CAMx (comprehensive air quality model with extensions) user's guide version 7.10*. Novato, CA: ENVIRON International Corporation.

Guenther, A., Jiang, X., Shah, T., Huang, L., Kemball-Cook, S., and Yarwood, G. (2019). "Model of emissions of gases and aerosol from nature version 3 (MEGAN3)," in *Air pollution modeling and its application XXVI* (Cham: Springer), 187.

Haagen-Smit, A. J. (1952). Chemistry and physiology of Los Angeles smog. *Ind. Eng. Chem.* 44 (6), 1342–1346. doi:10.1021/ie50510a045

He, Z., Wang, X., Ling, Z., Zhao, J., Guo, H., Shao, M., et al. (2019). Sources of methacrolein and methyl vinyl ketone and their contributions to methylglyoxal and formaldehyde at a receptor site in Pearl River Delta. *J. Environ. Sci.* x, 1–10. doi:10.1016/j.jes.2018.12.001

Itahashi, S., Hayami, H., and Uno, I. (2015). Comprehensive study of emission source contributions for tropospheric ozone formation over East Asia. *J. Geophys. Res. Atmos.* 120 (1), 331–358. doi:10.1002/2014JD022117

Itahashi, S., Mathur, R., Hogrefe, C., Napelenok, L. S., and Zhang, Y. (2020). Modeling stratospheric intrusion and trans-Pacific transport on tropospheric ozone using hemispheric CMAQ during April 2010 - Part 2: Examination of emission impacts based on the higher-order decoupled direct method. *Atmos. Chem. Phys.* 20 (6), 3397–3413. doi:10.5194/acp-20-3397-2020

Jiang, Z., Shi, H., Zhao, B., Gu, Y., Zhu, Y., Miyazaki, K., et al. (2021). Modeling the impact of COVID-19 on air quality in southern California: Implications for future control policies. *Atmos. Chem. Phys.* 21 (11), 8693–8708. doi:10.5194/acp-21-8693-2021

Kim, E., Kim, B. U., Kim, H. C., and Kim, S. (2017). The variability of ozone sensitivity to anthropogenic emissions with biogenic emissions modeled by MEGAN and BEIS. *Atmosphere* 8 (10), 187–225. doi:10.3390/atmos8100187

Kurokawa, J., Ohara, T., Morikawa, T., Hanayama, S., Janssens-Maenhout, G., Fukui, T., et al. (2013). Emissions of air pollutants and greenhouse gases over Asian regions during 2000–2008: Regional Emission inventory in Asia (REAS) version 2. *Atmos. Chem. Phys.* 13 (21), 11019–11058. doi:10.5194/acp-13-11019-2013

Li, M., Liu, H., Geng, G., Hong, C., Liu, F., Song, Y., et al. (2017). Anthropogenic emission inventories in China: A review. *Natl. Sci. Rev.* 4 (6), 834–866. doi:10.1093/nsr/nwx150

Li, M., Zhang, Q., Streets, D. G., He, K. B., Cheng, Y. F., Emmons, L. K., et al. (2014). Mapping Asian anthropogenic emissions of non-methane volatile organic compounds to multiple chemical mechanisms. *Atmos. Chem. Phys.* 14 (11), 5617–5638. doi:10.5194/acp-14-5617-2014

Li, Z., Yu, S., Li, M., Chen, X., Zhang, Y., Song, Z., et al. (2022). The modeling study about impacts of emission control policies for Chinese 14th five-year plan on $PM_{2.5}$ and O_3 in yangtze river delta, China. *Atmosphere* 13 (1), 26. doi:10.3390/atmos13010026

Liu, C., Zhang, L., Wen, Y., and Shi, K. (2021). Sensitivity analysis of O3 formation to its precursors-Multifractal approach. *Atmos. Environ.* 251, 118275. doi:10.1016/j.atmosenv.2021.118275

Lu, X., Zhang, L., Chen, Y., Zhou, M., Zheng, B., Li, K., et al. (2019). Exploring 2016-2017 surface ozone pollution over China: Source contributions and meteorological influences. *Atmos. Chem. Phys.* 19 (12), 8339–8361. doi:10.5194/acp-19-8339-2019

Luo, H., Zhao, K., Yuan, Z., Yang, L., Zheng, J., Huang, Z., et al. (2021). Emission source-based ozone isopleth and isosurface diagrams and their significance in ozone pollution control strategies. *J. Environ. Sci. (China)* 105, 138–149. doi:10.1016/j.jes.2020.12.033

Ou, J., Yuan, Z., Zheng, J., Huang, Z., Shao, M., Li, Z., et al. (2016). Ambient ozone control in a photochemically active region: Short-term despiking or long-term attainment? *Environ. Sci. Technol.* 50 (11), 5720–5728. doi:10.1021/acs.est.6b00345

Qu, Y., An, J., Li, J., Chen, Y., Li, Y., Liu, X., et al. (2014). Effects of NOx and VOCs from five emission sources on summer surface O3 over the Beijing-Tianjin-Hebei region. *Adv. Atmos. Sci.* 31 (4), 787–800. doi:10.1007/s00376-013-3132-x

Skamarock, W. C., Klemp, J. B., Dudhia, J., Gill, D. O., Zhiquan, L., Berner, J., et al. (2019). A description of the advanced research WRF model version 4. NCAR technical note NCAR/TN-475+STR. AvaliableAt: http://library.ucar.edu/research/publish-technote.

Tan, Z., Lu, K., Jiang, M., Su, R., Dong, H., Zeng, L., et al. (2018). Exploring ozone pollution in chengdu, southwestern China: A case study from radical chemistry to O3-VOC-NOx sensitivity. *Sci. Total Environ.* 636, 775–786. doi:10.1016/j.scitotenv.2018.04.286

Wang, N., Lyu, X., Deng, X., Huang, X., Jiang, F., and Ding, A. (2019). Aggravating O 3 pollution due to NO x emission control in eastern China. *Sci. Total Environ.* 677, 732–744. doi:10.1016/j.scitotenv.2019.04.388

Wickham, J., Stehman, S., Gass, L., Dewitz, J., Sorenson, D., Granneman, B., et al. (2019). EPA public access. *Adv. Ecol. Res.* 60, 1–24. doi:10.1016/j.scitotenv.2019.01.116.Source

Wu, R., and Xie, S. (2017). Spatial distribution of ozone formation in China derived from emissions of speciated volatile organic compounds. *Environ. Sci. Technol.* 51 (5), 2574–2583. doi:10.1021/acs.est.6b03634

Yang, X., Wu, K., Lu, Y., Wang, S., Qiao, Y., Zhang, X., et al. (2021). Origin of regional springtime ozone episodes in the Sichuan Basin, China: Role of synoptic forcing and regional transport. *Environ. Pollut.* 278, 116845. doi:10.1016/j.envpol.2021.116845

Yang, Y., Lan, H., and Li, J. (2020). Spatial econometric analysis of the impact of socioeconomic factors on PM2.5 concentration in China's inland cities: A case study from chengdu plain economic zone. *Int. J. Environ. Res. Public Health* 17 (1), 74. doi:10.3390/ijerph17010074

Yao, S., Wei, W., Cheng, S., Niu, Y., and Guan, P. (2021). Impacts of meteorology and emissions on O_3 pollution during 2013–2018 and corresponding control strategy for a typical industrial city of China. *Atmosphere* 12 (5), 619. doi:10.3390/atmos12050619

Yarwood, G., Emery, C., Jung, J., Nopmongcol, U., and Sakulyanontvittaya, T. (2013). A method to represent ozone response to large changes in precursor emissions using high-order sensitivity analysis in photochemical models. *Geosci. Model Dev.* 6 (5), 1601–1608. doi:10.5194/gmd-6-1601-2013

Yu, S. (2019). Fog geoengineering to abate local ozone pollution at ground level by enhancing air moisture. *Environ. Chem. Lett.* 17 (1), 565–580. doi:10.1007/s10311-018-0809-5

Zhang, W. (2013). Direct sensitivity techniques in regional air quality models: Development and application. Atlanta, Georgia: Georgia Institute of Technology. Doctoral dissertation. Available at: https://smartech.gatech.edu/bitstream/handle/1853/52941/ZHANG-DISSERTATION-2013.pdf?sequence=1&isAllowed=y.

Zhou, Z., Tan, Q., Deng, Y., Wu, K., Yang, X., and Zhou, X. (2019). Emission inventory of anthropogenic air pollutant sources and characteristics of VOCs species in Sichuan Province, China. *J. Atmos. Chem.* 76 (1), 21–58. doi:10.1007/s10874-019-9386-7

frontiers | Frontiers in Environmental Science

TYPE Original Research
PUBLISHED 09 November 2022
DOI 10.3389/fenvs.2022.1052646

OPEN ACCESS

EDITED BY
Gen Zhang,
Chinese Academy of Meteorological Sciences, China

REVIEWED BY
Jing Chen,
Beijing Normal University, China
Chenglong Zhang,
Research Center for Eco-environmental Sciences (CAS), China

*CORRESPONDENCE
Runli Gao,
gaorunli@163.com
Haitao Wang,
dr_wht@163.com

†These authors have contributed equally to this work

SPECIALTY SECTION
This article was submitted to Atmosphere and Climate, a section of the journal Frontiers in Environmental Science

RECEIVED 24 September 2022
ACCEPTED 28 October 2022
PUBLISHED 09 November 2022

CITATION
Hao S, Liu X, Sun C, Zhang Y, Gao R, Wang H and Wang X (2022), Experimental study of the adsorption of 2-Chloroacetophenone at the air-environmental water interface. *Front. Environ. Sci.* 10:1052646. doi: 10.3389/fenvs.2022.1052646

Experimental study of the adsorption of 2-Chloroacetophenone at the air-environmental water interface

Shangpeng Hao[1], Xuefeng Liu[1†], Chao Sun[1], Yuanpeng Zhang[1], Runli Gao[1]*, Haitao Wang[1]* and Xiaolu Wang[2]

[1]State Key Laboratory of NBC Protection for Civilian, Beijing, China, [2]Department of Automation, Tsinghua University, Beijing, China

The widespread surface of the air-water interface plays a crucial role in the partitioning processes between the atmosphere and the hydrosphere. As one of the prime CWAs (Chemical Warfare Agents) abandoned by Japanese, the unfound 2-Chloroacetophenone posed a severe threat to the Chinese people. In this study, the interface partition constant of 2-Chloroacetophenone was obtained by measuring the mass uptake vapor on different environmental water films with various thicknesses. The surface tension, dissolved organic matter, and salinity of the environmental samples were analyzed. The partition constant of 2-Chloroacetophenone in pure water, river water and sea water samples at 288 K were 1182.2 ± 49.9, 1606.6 ± 101.3 and 408.9 ± 18.3, respectively. Surface adsorption is the predominant mechanism. The results also indicate that the adsorption partitioning ability of 2-Chloroacetophenone at the air/water interface was negatively correlated with surface tension. 2-Chloroacetophenone is more likely to adsorb at the gas/water interface with lower surface tension.

KEYWORDS

air-water interface, partition constant, 2-Chloroacetophenone, surface microlayer, flow-tube reactor

Introduction

2-Chloroacetophenone, one of the primarily used riot control agents with the military designation of CN, can cause uncontrolled sneezing, coughing, eye irritation and lacrimation (Olajos and Salem, 2001; Blain, 2003). It was first synthesized in 1871 and had served in military action for a long history (Olajos and Salem, 2001). CN was also used as the main active ingredient in a liquid mixture under the tradename "Mace" for riot control and law enforcement.

The chemical formula of CN is shown in Figure 1. At room temperature, CN is colorless crystals solid. CN has low solubility in water but is soluble in alcohols, ethers and

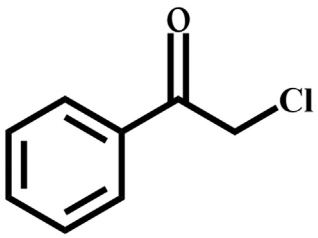

2-Chloroacetophenone (CN)

FIGURE 1
Chemical formula of 2-chloroacetophenone (CN).

other organic solvents. The vapor pressure of CN at 20°C is 4.1×10^{-3} mmHg. The hydrolysis of CN in water is very slow. CN acts directly on the mucous membranes. Exposure to high concentrations of CN aerosol can cause intense ocular and respiratory irritation and associated burning and pain sensation in the eyes, nose, throat and lungs. Some symptoms can persist for 20 min. The maximum safe dose for short-term inhalation is 500 mg/m^3 (Blain, 2003). And the safety threshold in an aqueous environment is 0.36 μg/L (Hu et al., 2008).

After World War I, CN began to appear as a chemical warfare agent in military operations and exercises. Since the 1930s, tons of agents called "Midori" or "green color agent" was manufactured and shipped to China by the Japanese army (Tu, 2010; Brombach, 2011). At the end of the war, a large amount of CN was directly dumped into water area in China by the Japanese army to cover up the evidence of their criminal use. These abandoned chemical agents had been found in nearly 100 locations in China. There are still considerable amounts of agents that remain undetected. These agents had become a serious threat to residents, causing severe pollution and ecological damage. This project was undertaken to evaluate the atmospheric fate of CN.

The air-water interface is the most widespread surface in the environment. The uppermost 1 μm to 1 mm of the surface of the ocean and the river, which also call the Surface Microlayer, is mainly composed of various biogenic organics species (Peleg et al., 2016; Stirchak et al., 2021). Some organic compounds, such as n-alkanoic acids (fatty acids) and humic-like substances (HULIS), are surface-active substances and can affect the surface tension of water (Tinel et al., 2016; Chiu et al., 2017). These compounds are also present in atmospheric water films such as fog, mist, dew, cloud droplets surface and can affect the nucleation and the growth of aerosols and the absorption of gas molecules. Cappiello analyzed water-soluble organic matter (WSOC) in fog water samples by MS/MS and found the presence of HULIS (Cappiello et al., 2003).

The main purpose of this study is to develop an understanding of the partitioning processes between the atmosphere and the hydrosphere. The adsorption behavior is strongly associated with the target molecule's polarity and size and the film surface's polarity, which could be measured by the air/water partition constant (K_{AI}) (Jing et al., 2006; Goss, 2010; Chen et al., 2011). However, the presence of surfactants may increase the water solubility of gaseous substances through micelle trapping mechanisms or intermolecular interactions. It also may cause a decrease in the permeability of gaseous substances on aqueous surfaces (Chen and Valsaraj, 2007). Furthermore, the spices may be involved in surface reactions to cause unpredictable results. Chen investigated the effect of surfactants on the adsorption of naphthalene at the gas-water interface using Suwannee River fulvic acid (SRFA) (Chen and Valsaraj, 2007). When the concentration of River fulvic acid in water was low, the increase of naphthalene adsorption by aqueous films was limited. And the concentration of naphthalene in aqueous films even exceeded the solubility in pure water when the concentration of SRFA was high, indicating that the presence of HULIS in natural aqueous films promoted the adsorption of naphthalene. Some studies had also shown that long-chain fatty acid monomolecular layers covering the surface of aqueous film inhibit the uptake of N_2O_5 and anthracene (Thornton and Abbatt, 2005; McNeill et al., 2006).

In this study, a flow-tube reactor was used to obtain the equilibrium concentration of CN between the water film and the gas phase. The objective of this work was to obtain the partition constant of CN and to investigate the impact of different surface samples on the partitioning results.

Materials and methods

Materials

Standard reagents: Methanol (chromatographic pure, Fisher Chemical, Germany); NaCl (chromatographic pure, Beijing Chemical Manufacturer, China); TENAX TA supporter (60/80 mesh size, BUCHEM BV, Holland); CN (99.89%), provided by the State Key Laboratory of NBC Protection for Civilian (Duan et al., 2020).

Environmental water samples: The river water samples were collected from the Yangtze River in Yichang, Hubei Province (salinity 0.2 g/L); The sea water samples were taken from the surface layer of the South China Sea in Guangdong Province (salinity 17.125 g/L). All environmental water samples used were unfiltered.

Equipment and instrument

Equipment: 7890A Gas chromatograph (equipped with hydrogen ion flame detector, Agilent Technologies,

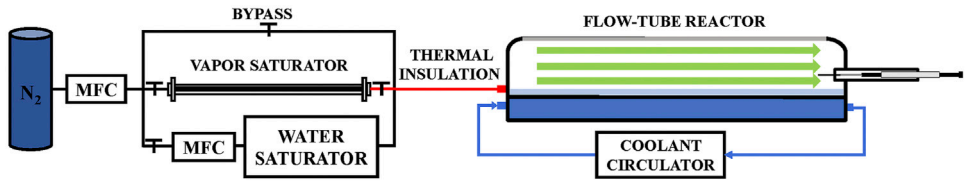

FIGURE 2
Flow tube reactor.

United States); Solid-phase microextraction device (SPME, Supelco, United States); 85 μm CAR/PDMS fiber (Supelco; United States); Magnetic heating stirrer (MS-H-Pro, Dalong Xingchuang Instruments, China); Ultrapure water system (CR- 20B+, Gaosen instrument equipment, China); Thermostat oil-bath cauldron (OSB-2000, EMELA); Flow injection fluorescence (R-6000, Shimadzu, Japan); Laboratory conductivity meter (ST3100C, OHAUS, United States); Optical contact angle meter (OCA-20, Dataphysics, Germany); Electronic balance (CPA225D, Sartorius Group, Germany), Mass flow controller, range 0–500 ml min^{-1} (SY-9312D, ShengYe Technology Company of Beijing, China).

The adsorption experiments were performed on a flow-tube reactor described in our previous work (Hao et al., 2021). Some modifications have been made in Figure 2 for the detection of CN. The equipment was mainly constant with a vapor saturator device, a flow-tube reactor, and a coolant circulator system. The whole device and the quartz boat were held in a horizontal position. The partition experiment was conducted in the flow-tube reactor. CN is adsorbed on a thin water film coated on the bottom surface of a rectangular quartz trough (length 490 mm, width 30 mm, and height 5 mm). The bottom surface area of the quartz trough is 147 cm^2. The circulating coolant in the reactor controls the temperature of the water film. The reactor was sealed using a suitable seal strip. The instrument status was monitored by a variety of sensors. Temperature sensors inserted through the reactor body are placed only millimeters from the glass trough bottom. The temperature of the water film is monitored consistently throughout the experiment. The internal pressure of the reactor was measured by a pressure sensor system. The sensor used ensures the reproducibility and reliability of the experiment.

The concentration of gas-phase CN is hard to quantify by the gas chromatograph directly. So, we use SPME technique to capture the CN in the reactor. During the experiment, the SPME fibers were inserted into the reactor and released into the GC inlet for analysis.

The whole system was operated in a ventilated environment. Nitrogen was used as the carrier gas at a flow rate of 60 ml/min. The flow rate was controlled by the SY-9312D mass flow controller. The carrier gas was humidified by passing through a vessel containing water to avoid the volatilization of the water film during the experiment.

Experimental details

The bottom of the quartz boat was soaked in 50% w/v NaOH for 1 h, followed by rinsing with Milli-Q water. The volume of water added controlled the thickness of the film. The temperature of the water film was kept at 15°C which makes the data correspond to the average temperature of the atmosphere. 2, 5, 8, 11, and 15 ml of ultrapure water were added into the quartz trough to form water films with thicknesses of 136, 340, 544, 748, and 1,020 μm, respectively.

The vapor saturator device generated the gas-phase CN. At 20°C, CN is a flaky white crystal, and the vapor needs to be transferred to the flow tube reactor for the partitioning experiment. TENAX TA has been used in riot control agent analysis (Carrick et al., 2001). We present a scheme to spike TENAX TA supporter into a thermal desorption tube. The supporter was coated with CN by mixing it with a CN-methanol solution. Methanol has a lower boiling point (64.8°C), so it was first to evaporate when heated. After that, CN has been adsorbed onto the surface of the supporter and was released in a stream of nitrogen gas. The support was transformed into a stainless-steel tube and covered by glass wool. Since the melting point of CN is 54°C, heating the thermal desorption tube would lead to rapid volatilization of CN. Therefore, the temperature of the vapor generator was kept at 20°C in all experiments.

The quartz boat was covered with water film and placed in the reactor, and then the vapor was passed through to carry out the experiment. The concentration of CN in the gas phase and aqueous phase was measured using SPME separately. The reactor and the lines were purified with pure nitrogen to avoid residues after the experiment.

Environmental water experiment: The effects of mineral content and dissolved organic matter (DOM) on the interfacial partitioning in different environmental water were studied. Experiments were conducted with the samples collected

from the Yangtze River and the South China Sea at the same temperature and water film thickness.

Sample analysis

In this experiment, SPME combined with GC-FID was used to analyze CN in the gas phase and aqueous phase.

An 85 μm CAR/PDMS fiber was inserted into the flow tube reactor to capture CN in the gas phase. The SPME fiber was exposed for 10 min. And the fiber was inserted into the injection port of the GC for desorption. Samples were collected at 10, 30, and 50 min, respectively.

The aqueous samples were collected at the end of the partitioning experiment. The concentration of CN in aqueous phase was determined using the same fiber. In the previous work, the effects of extraction temperature, extraction time, stirring speed, salinity, and resolution time on the extraction effect were investigated (Hao et al., 2022). The best extraction conditions were obtained as follows: extraction temperature 40°C, extraction time 30 min, stirring speed 1500 r/min, NaCl 2 mol/L, and resolution time 2 min.

Quantification of CN in the aqueous and gas phase was calculated based on two calibration curves. A calibration curve for aqueous samples was obtained by a serial dilution from standard stock solution (10 mg/ml) to the lowest concentration (10 μg/ml) calibration standard. In each analysis, eighty microliters of water samples were diluted to 4 ml with ultrapure water for SPME. These samples were extracted for 30 min under the same extraction conditions to obtain a standard curve for the aqueous phase. The curve for the gas phase was from the standard gas method, which will be described in the following part.

Analysis was conducted on a 7890A gas chromatograph (FID, Agilent Technologies, United States) at 250°C. The injector temperature was set at 250°C. Nitrogen was used as carrier gas at a pressure of 20 psi. Hydrogen and air were used as detector gases at 40 and 300 ml/min flow, respectively. The analytical column was DB-5MS, 30 m × 0.25 m, 0.25 μm thickness (Agilent Technologies). The temperature program of the GC was from 80°C (1 min) to 250°C (8 min) at 20°C/min.

Data progressing

The concentration of CN in the water films was accumulated by both adsorption and absorption processes, which can be described by the following equation (Chen et al., 2011):

$$C_W^T = C_W + \frac{K_{AI}}{\delta} C_g \quad (1)$$

where: C_W^T is the overall equilibrium concentration for CN, C_W is the bulk water phase concentration of cyclohexanone, C_g is the concentration in the gas phase, δ is the thickness of water film, K_{AI} is the partition constant at the air-water interface.

According to Eq. 1, the y-axis intercept and slope of the curve are the values of bulk phase concentration (C_W) and the partition constant K_{AI}, respectively. In combination with the value of C_g, the interfacial partition constant K_{AI} was obtained.

Analysis of environment water

The samples' DOM in river water and sea water was measured using a Shimadzu F-6000 fluorescence spectrophotometer from Japan. The sample was placed in a 1 cm quartz cuvette with a scanning speed of 12,000 nm/min. The excitation wavelength (λEx) in the range of 200–900 nm (slit width 5 nm) was used, and fluorescence was recorded (λEm) in the range of 200–900 nm (slit width 5 nm).

The surface tension of ultrapure water and the real samples were measured using the pendant droplet method with a contact angle meter. An inverted pendant drop was suspended from a stainless-steel needle. A digital video camera captured the images of the drops. Ten milliliters of ultrapure water and environmental water were weighed. The density of each sample was measured and used to calculate the surface tension of different samples. The salinity (SAL), total dissolved solids (TDS), and conductivity of environmental water were determined using a laboratory conductivity meter.

Results and discussion

Standard curves

The SPME-GC response was obtained using the standard gas method. A gas-tight syringe was used to extract the headspace gas from a vial filled with CN. The temperature of the vial was maintained at 20°C. Then the gas samples were injected into a brown bottle (1.15 L) to get gas mixtures. The bottle was sealed with a sealing film (Parafilm) and placed in a thermostat oil-bath cauldron at 15°C. The concentration of CN in the bottle was calculated by the following equation.

$$n_s = \frac{P_S \cdot V}{RT} \quad (2)$$

Where: P_s (mmHg) is the saturated vapor pressure of CN (4.1×10^{-3} mmHg at 20°C), V (L) is the extraction volume, n_s (μg/L) is the amount of the CN introduced into the brown bottle, R is the gas constant, T (K) is the sample temperature.

A glass-tight syringe was used to draw 50, 100, 200, 400, and 500 ml of headspace gas. The CAR/PDMS extraction fiber was inserted into the sealing film and extracted for 10 min. After each set of experiments, the syringe and the bottle were heated to avoid residual. Different concentrations of gas mixtures were prepared for the standard curve and analyzed by GC-FID.

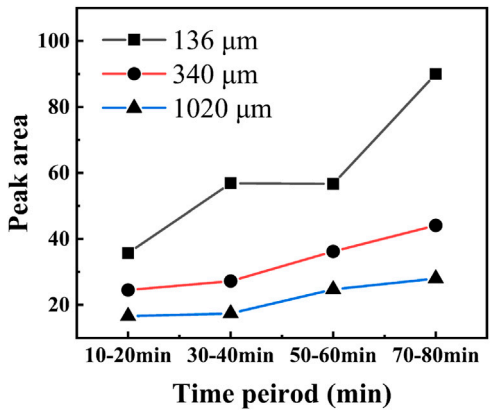

FIGURE 3
Trend of gas phase concentration of CN.

The standard curve for the SPME is y = 16.069x-14.792, and the correlation coefficient is 0.9897, indicating that the method's linearity is acceptable.

The variation of CN concentration in gas-phase

We selected four time periods to explore the rule of gas phase concentration with different water film thicknesses. From the beginning of the experiment, CN was collected from the gas phase at 10–20, 30–40, 50–60 and 70–80 min, respectively. The result is shown in Figure 3. It can be seen from the figure that the concentration of CN in the reactor showed an increasing trend, and the concentration of CN decreased as the thickness of the water film increased. For the water film with a thickness of 136 μm, part of the bottom surface of the quartz boat will be exposed when covered for more than 1 h. So, 60 min was chosen as the experiment time.

Ultrapure water adsorption distribution constant determination

The uptake experiments with ultrapure water were first conducted at 288 K. The thickness of the water films ranged from 136 to 1020 μm. The concentration of CN was plotted as a function of the gas phase concentration/film thickness to determine the partitioning constant (K_{AI}). Figure 4A shows the fitted line of the experimental data.

As shown in Table 1, the average gas-phase concentration for different water film experiments ranged from 2.11 to 3.29 mg/L. The overall concentrations of CN in the water film ranged from 4.92 to 30.7 mg/L. The interfacial partition constant K_{AI} at 288 K is 1182.2 ± 49.9. With the increase in film thickness, the overall equilibrium concentration of CN in the aqueous film decreased. Surface adsorption became the dominant partition mechanism as the film thickness decreased. The correlation coefficient of the linear fit was 0.9947, indicating a good correlation between the two parameters.

River water adsorption experiments

Five experiments were performed at 288 K. The bottom surface of the boat was coated with the water sample collected from the Yangtze River. The thicknesses of the river water films were 136, 340, 544, 748, and 1,020 μm, respectively. As can be seen from Table 2, the overall concentrations of CN in water film determined in river water ranged from 1.65 to 20.18 μg/L. The partition constant K_{AI} was 1606.6 ± 101.3 at 288 K. As shown in Figure 4B, the correlation coefficient of the linear fit was 0.9941. The partition constant of CN in river water was higher than that

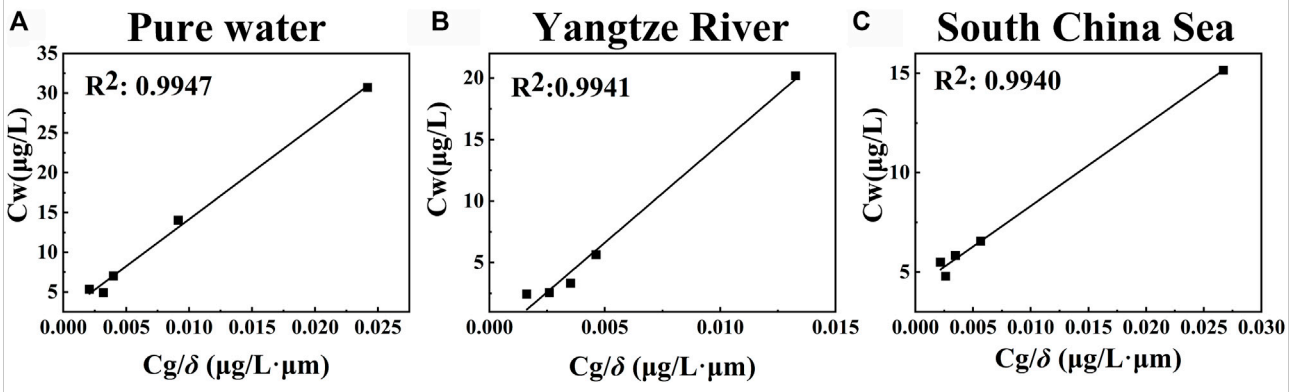

FIGURE 4
Uptake of CN from the gas-phase on water films with varying thicknesses and different sample.

TABLE 1 Interface air-water partition constants of CN for ultrapure water.

	δ (μm)	Cg/(μg/L)	C_W/(μg/L)	K_{AI}
Ultrapure water	136	3.29	30.70	1182.2 ± 49.9
	340	3.11	14.00	
	544	2.16	7.01	
	748	2.39	4.92	
	1020	2.11	5.33	

[a]Uncertainties for K_{AI} were based on standard errors for the linear regression as shown in Figure 4A.

TABLE 2 Interface air-water partition constants of CN for river water.

	δ (μm)	C_g/(μg/L)	C_W/(μg/L)	K_{AI}
Yangtze river	136	1.80	20.18	1606.6 ± 101.3
	340	1.57	5.63	
	544	1.91	3.31	
	748	1.94	2.55	
	1020	1.65	1.65	

[a]Uncertainties for K_{AI} were based on standard errors for the linear regression as shown in Figure 4B.

TABLE 3 Interface air-water partition constants of CN for sea water.

	δ (μm)	Cg/(μg/L)	C_W/(μg/L)	K_{AI}
Sea water	136	3.63	15.16	408.9 ± 18.3
	340	1.93	6.55	
	544	1.89	5.83	
	748	1.97	4.79	
	1020	2.22	5.48	

[a]Uncertainties for K_{AI} were based on standard errors for the linear regression as shown in Figure 4C.

of ultrapure water. CN was easily adsorbed at the air-water interface of river water.

Sea water adsorption experiments

Five experiments were performed with the surface sample collected from the south China sea in 288 K. The concentration of CN was analyzed using the SPME-GC method. Table 3 below illustrates that the overall concentration of CN ranged from 4.79 to 15.16 μg/L. The results of the correlational analysis are presented in Figure 4C. The correlation coefficient of the two paraments was 0.9940. And the interfacial adsorption partition constant K_{AI} was 408.9 ± 18.3 at 288 K.

Water quality analysis

The collected environmental water samples were analyzed using a laboratory conductivity meter. As shown in Table 4, the salinity, total dissolved matter content, and conductivity of the seawater were much higher than those of the river water.

Dissolved organic matter (DOM) is the main light-absorbing substance in water, and fluorescence technology has proved to be a valuable tool for providing information on the composition of DOM in water (Stedmon, 2003; Sanchez et al., 2013; Cincotta et al., 2019). The fluorescence spectrophotometer results for ultrapure water, river water, and seawater are shown in Figure 5.

Compared to pure water, river water and sea water contains light-absorbing material, and the fluorescence was measured at $\lambda_{Ex}/\lambda_{Em}$ = 300/400 nm for sea water. As reported by Fellman and Stedmon, this part of the components was identified as HULIS. The DOM in the collected sea water samples was mainly composed of HULIS (Fellman et al., 2010; Murphy et al., 2010).

As shown in Table 5, the density and surface tension of different samples were measured. Prior studies have noted that the salt in the aqueous cause an increase in surface tension. The result also indicated that the surface tension of seawater was higher than that of salt solution at the same concentration (Zhao and Kang, 2017). It can be seen that river water has slightly lower surface tension than ultrapure water, and the value of surface tension increased with the salinity and the presence of humus.

Comparative analysis

The overall CN in the aqueous films was accumulated through interfacial adsorption and bulk phase absorption processes. In the previous work, we determined Henry's constant of CN by a gas-liquid system partitioning device. The experiments were carried out in environmental samples from the same source. As shown in Figure 6, the partition constant and Henry's constant of CN in the different aqueous samples were different, and the differences were mainly in the river water.

TABLE 4 Salinity, total dissolved solid (TDS) and conductivity of environmental water samples.

Environmental water	SAL (%)	TDS (g/L)	Conductivity (ms/cm)
River water	0.38	0.2	0.4
Sea water	20.71	17.13	34.25

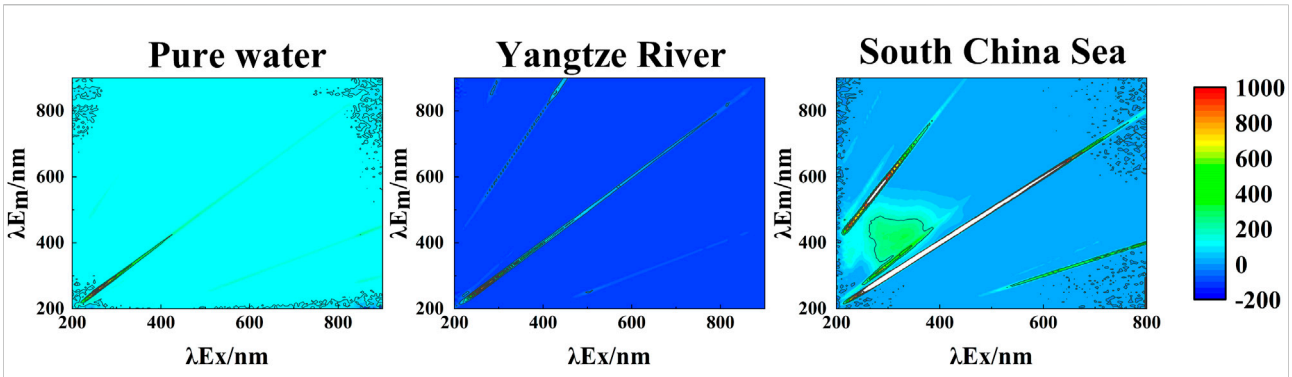

FIGURE 5
Fluorescence intensity measurements of different samples.

TABLE 5 Surface tension of ambient water.

	Ultrapure water	Yangtze river	South China sea
Density (g/ml^3)	1.004	1.008	1.028
Surface tension (mN/m)	72.9	71.5	74.7

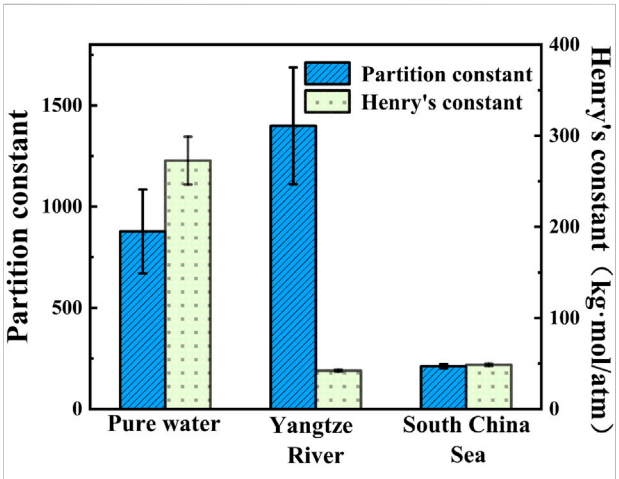

FIGURE 6
Comparison of partition constant and Henry's constant for CN.

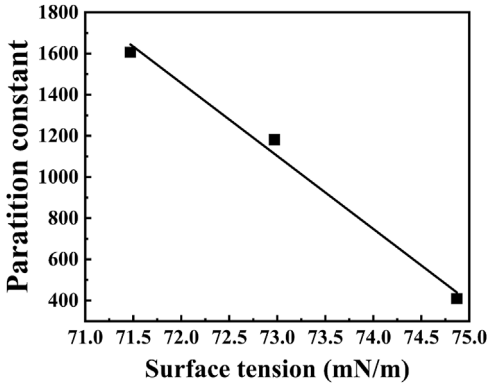

FIGURE 7
Effect of surface tension on partition constant.

Based on Eq. 1, the intercept of the fitted line in Figure 4 is the value of bulk phase concentration. The least amount of CN was dissolved in the bulk phase of river water, which is consistent with the results of Henry's constant. As shown in Figure 7, the partition constants of different water samples had a reverse correlation with their surface tensions, and with lower surface tension, CN is more likely to adsorb at the gas/water interface. The surfactant substance in the river reduces the surface tension, and the interfacial adsorption of CN is enhanced by micelle trapping mechanisms or intermolecular bonding. These results match those observed in an earlier study of naphthalene by Jing Chen (Chen and Valsaraj, 2007). The sea water samples have the minimum bulk phase absorption. Although humic substances have been found in seawater from fluorescence measurements, the sea water sample has the highest surface tension, probably because its salinity is significantly higher than that of river water and ultrapure water.

The present study suggests that the influence of surface-active substances and ionic strength of environmental water on the bulk phase absorption and interfacial adsorption of CN should be considered comprehensively. The surface tension

can be used as a reference to evaluate the adsorption behavior of CN preliminary.

Conclusion

In this study, the interfacial partition constants (K_{AI}) of CN in different film thicknesses and several environmental samples were determined using a flow-tube reactor. SPME was used to uptake and quantify the concentration of CN in the aqueous phase and gas phase. The salinity, DOM and surface tension of different samples were tested, respectively.

Surface adsorption became the dominant absorption mechanism for CN as the film thickness decreased. The adsorption partitioning ability of CN at the air/water interface was negatively correlated with surface tension. CN is more likely to adsorb at the gas/water interface with lower surface tension. The maximum interface adsorption for CN was found at the air/river water interface, and the partition constant at the air/river water interface was 1606.6 ± 101.3. The K_{AI} of CN in ultrapure water and sea water samples at 288 K were 1182.2 ± 49.9, 408.9 ± 18.3. Fluorescence measurements indicated that light-absorbing substances exist in seawater and river water, and humis substances were founded in seawater. The presence of salts and HULIS in seawater reduces the bulk phase uptake and interfacial desorption of CN.

Data availability statement

The original contributions presented in the study are included in the article/supplementary material, further inquiries can be directed to the corresponding author.

Author contributions

Conceptualization and design HW, RG; methodology SH, XL; writing original draft preparation, SH, CS; data analysis, SH, XL; manuscript review and editing, HW, XL, SH, CS. All authors have read and agreed to the published version of the manuscript.

Funding

This work was supported by the National Key Research and Development Program of China (Grant No. 2021YFB3301100) and the National Natural Science Foundation of China (Grant Nos. 21876202 and 21177158).

Conflict of interest

The authors declare that the research was conducted in the absence of any commercial or financial relationships that could be construed as a potential conflict of interest.

Publisher's note

All claims expressed in this article are solely those of the authors and do not necessarily represent those of their affiliated organizations, or those of the publisher, the editors and the reviewers. Any product that may be evaluated in this article, or claim that may be made by its manufacturer, is not guaranteed or endorsed by the publisher.

References

Blain, P. (2003). Tear gases and irritant incapacitants. *Toxicol. Rev.* 22 (2), 103–110. doi:10.2165/00139709-200322020-00005

Brombach, M. (2011). Abandoned chemical weapons in China: The unresolved Japanese legacy. *Glob. Green U. S. A. U. S. Affil. Green Cross Int.* 21, 1–33.

Cappiello, A., Simoni, E., Fiorucci, C., Mangani, F., Palma, P., Trufelli, H., et al. (2003). Molecular characterization of the water-soluble organic compounds in fogwater by ESIMS/MS. *Environ. Sci. Technol.* 37 (7), 1229–1240. doi:10.1021/es0259990

Carrick, W., Cooper, D., and Muir, B. (2001). Retrospective identification of chemical warfare agents by high-temperature automatic thermal desorption-gas chromatography-mass spectrometry. *J. Chromatogr. A* 925 (1-2), 241–249. doi:10.1016/s0021-9673(01)01024-x

Chen, J., Ehrenhauser, F., Liyana-Arachchi, T., Hung, F., Wornat, M., and Valsaraj, K. (2011). Adsorption of gas-phase phenanthrene on atmospheric water and ice films. *Polycycl. Aromat. Compd.* 31 (4), 201–226. doi:10.1080/10406638.2011.585370

Chen, J., and Valsaraj, K. (2007). Uptake and UV-photooxidation of gas-phase polyaromatic hydrocarbons on the surface of atmospheric water films. 2. Effects of dissolved surfactants on naphthalene photooxidation. *J. Phys. Chem. A* 111 (20), 4289–4296. doi:10.1021/jp068394p

Chiu, R., Tinel, L., Gonzalez, L., Ciuraru, R., Bernard, F., George, C., et al. (2017). UV photochemistry of carboxylic acids at the air-sea boundary: A relevant source of glyoxal and other oxygenated VOC in the marine atmosphere. *Geophys. Res. Lett.* 44 (2), 1079–1087. doi:10.1002/2016gl071240

Cincotta, M., Perdrial, J., Shavitz, A., Libenson, A., Shanley, J., Perdrial, N., et al. (2019). Scientific data management in the age of big data: An approach supporting a resilience index development effort. *Front. Environ. Sci.* 7, 1–13. doi:10.3389/fenvs.2019.00072

Duan, J., Li, B., Liu, H., Gao, R., Zhang, Y., and Wang, H. (2020). Determination of the purity of chloroacetophenone by the monpeak method of differential scanning calorimetry. *Chem. Anal. Meterage* 29 (05), 11–14. (in Chinese). doi:10.3969/j.issn.1008-6145.2020.05.003

Fellman, J., Hood, E., and Spencer, R. (2010). Fluorescence spectroscopy opens new windows into dissolved organic matter dynamics in freshwater ecosystems: A review. *Limnol. Oceanogr.* 55 (6), 2452–2462. doi:10.4319/lo.2010.55.6.2452

Goss, K. (2010). The air/surface adsorption equilibrium of organic compounds under ambient conditions. *Crit. Rev. Environ. Sci. Technol.* 34 (4), 339–389. doi:10.1080/10643380490443263

Hao, S., Sun, C., Zhang, Y., Wang, H., Zhao, W., Wang, X., et al. (2021). Adsorption of gas-phase cyclohexanone on atmospheric water films. *Atmosphere* 12 (12), 1705. doi:10.3390/atmos12121705

Hao, S., Wang, H., Zhao, W., Sun, C., Gao, R., and Zhang, Y. (2022). Simultaneous determination of trace level riot control agents in environmental water by solid-phase microextraction and gas chromatography coupled with a Flame Ionization Detector. *J. Sep. Sci.* 45 (14), 2612–2620. doi:10.1002/jssc.202100851

Hu, B., Li, Y., Yang, N., Gao, C., Wang, H., and Zhang, J. (2008). Determination of the environmentally safe threshold value of chloroacetophenone in waters. *Acta Sci. Circumstantiae* 28 (1), 125–131. (in Chinese). doi:10.3321/j.issn:0253-2468.2008.01.020

Jing, C., Franz, S., Kalliat, T., and Mary, M. (2006). Uptake and UV-photooxidation of gas-phase PAHs on the surface of atmospheric water films. 1. Naphthalene. *J. Phys. Chem. A* 110 (29), 9161–9168. doi:10.1021/jp062560b

Mcneill, V., Patterson, J., Wolfe, G., and Thornton, J. (2006). The effect of varying levels of surfactant on the reactive uptake of N₂O₅ to aqueous aerosol. *Atmos. Chem. Phys.* 6, 1635–1644. doi:10.5194/acp-6-1635-2006

Murphy, K., Butler, K., Spencer, R., Stedmon, C., Boehme, J., and Aiken, G. (2010). Measurement of dissolved organic matter fluorescence in aquatic environments: An interlaboratory comparison. *Environ. Sci. Technol.* 44 (24), 9405–9412. doi:10.1021/es102362t

Olajos, E., and Salem, H. (2001). Riot control agents: Pharmacology, toxicology, biochemistry and chemistry. *J. Appl. Toxicol.* 21 (5), 355–391. doi:10.1002/jat.767

Peleg, A., Barak, H., Adina, P., and Eyal, R. (2016). The impact of dry atmospheric deposition on The sea-surface microlayer in the SE mediterranean sea: An experimental approach. *Front. Mar. Sci.* 3, 222. doi:10.3389/fmars.2016.00222

Sanchez, N., Skeriotis, A., and Miller, C. (2013). Assessment of dissolved organic matter fluorescence PARAFAC components before and after coagulation-filtration in a full scale water treatment plant. *Water Res.* 47 (4), 1679–1690. doi:10.1016/j.watres.2012.12.032

Stedmon, C., Markager, S., and Bro, R. (2003). Tracing dissolved organic matter in aquatic environments using a new approach to fluorescence spectroscopy. *Mar. Chem.* 82 (3-4), 239–254. doi:10.1016/S0304-4203(03)00072-0

Stirchak, L., Abis, L., Kalalian, C., George, C., and Donaldson, D. (2021). Differences in photosensitized release of VOCs from illuminated seawater versus freshwater surfaces. *ACS Earth Space Chem.* 5 (9), 2233–2242. doi:10.1021/acsearthspacechem.1c00063

Thornton, J., and Abbatt, J. (2005). N(2)O(5) reaction on submicron sea salt aerosol: Kinetics, products, and the effect of surface active organics. *J. Phys. Chem. A* 109 (44), 10004–10012. doi:10.1021/jp054183t

Tinel, L., Rossignol, S., Bianco, A., Passananti, M., Perrier, S., Wang, X., et al. (2016). Mechanistic insights on the photosensitized chemistry of a fatty acid at the air/water interface. *Environ. Sci. Technol.* 50 (20), 11041–11048. doi:10.1021/acs.est.6b03165

Tu, A. (2010). Chemical weapons abandoned by the imperial Japanese army in Japan and China at the end of World war II. *Toxin Rev.* 30 (1), 1–5. doi:10.3109/15569543.2011.542111

Zhao, L., and Kang, X. (2017). Relationship between coefficient of seawater surface tension and concentration, temperature. *J. Heilongjiang Univ. Sci. Technol.* 17 (8), 32–35. (in Chinese).

frontiers | Frontiers in Environmental Science

TYPE Correction
PUBLISHED 13 December 2022
DOI 10.3389/fenvs.2022.1108423

OPEN ACCESS

APPROVED BY
Frontiers Editorial Office,
Frontiers Media SA, Switzerland

*CORRESPONDENCE
Runli Gao,
gaorunli@163.com
Haitao Wang,
dr_wht@163.com

SPECIALTY SECTION
This article was submitted to Atmosphere and Climate, a section of the journal Frontiers in Environmental Science

RECEIVED 26 November 2022
ACCEPTED 06 December 2022
PUBLISHED 13 December 2022

CITATION
Hao S, Liu X, Sun C, Zhang Y, Gao R, Wang H and Wang X (2022), Corrigendum: Experimental study of the adsorption of 2-chloroacetophenone at the air-environmental water interface. *Front. Environ. Sci.* 10:1108423. doi: 10.3389/fenvs.2022.1108423

Corrigendum: Experimental study of the adsorption of 2-chloroacetophenone at the air-environmental water interface

Shangpeng Hao[1], Xuefeng Liu[1], Chao Sun[1], Yuanpeng Zhang[1], Runli Gao[1]*, Haitao Wang[1]* and Xiaolu Wang[2]

[1]State Key Laboratory of NBC Protection for Civilian, Beijing, China, [2]Department of Automation, Tsinghua University, Beijing, China

KEYWORDS

air water interface, partition constant, 2-Chloroacetophenone, surface microlayer, flow-tube reactor

A Corrigendum on
Experimental study of the adsorption of 2-chloroacetophenone at the air-environmental water interface

by Hao S, Liu X, Sun C, Zhang Y, Wang H and Wang X (2022). Front. Environ. Sci. 10:1052646. doi: 10.3389/fenvs.2022.1052646

In the original article, there was an error in the Author list and author "Runli Gao" was erroneously excluded. The corrected Author list appears above. The newly added author has been added to the correspondence section.

The **Author Contributions** statement is subsequently corrected as follows:

"Conceptualization and design HW, RG; methodology SH, XL; writing original draft preparation, SH, CS; data analysis, SH, XL; manuscript review and editing, HW, XL, SH, CS All authors have read and agreed to the published version of the manuscript."

The authors apologize for this error and state that this does not change the scientific conclusions of the article in any way. The original article has been updated.

Publisher's note

frontiers | Frontiers in Environmental Science

TYPE Original Research
PUBLISHED 25 November 2022
DOI 10.3389/fenvs.2022.1068861

OPEN ACCESS

EDITED BY
Chaoyang Xue,
UMR7328 Laboratoire de physique et chimie de l'environnement et de l'Espace (LPC2E), France

REVIEWED BY
Taosheng Jin,
Nankai University, China
Nicholas Kiprotich Cheruiyot,
Cheng Shiu University, Taiwan

*CORRESPONDENCE
Yifeng Xue,
xueyifeng@cee.cn

SPECIALTY SECTION
This article was submitted to Atmosphere and Climate, a section of the journal Frontiers in Environmental Science

RECEIVED 13 October 2022
ACCEPTED 16 November 2022
PUBLISHED 25 November 2022

CITATION
Ai Y, Cui Y, Ge Y, Wu X, Wu T, Liu X, Shen Y, Liu M, Wan Y, Yi H and Xue Y (2022), Study on the control targets and measures for total diesel consumption from mobile sources in Beijing, China. *Front. Environ. Sci.* 10:1068861. doi: 10.3389/fenvs.2022.1068861

Study on the control targets and measures for total diesel consumption from mobile sources in Beijing, China

Yi Ai[1], Yangyang Cui[2], Yunshan Ge[1], Xuefang Wu[2], Tongran Wu[2], Xinyu Liu[2], Yan Shen[2], Mingyu Liu[3], Yunfei Wan[2,4], Huawei Yi[2] and Yifeng Xue[2]*

[1]School of Mechanical Engineering, Beijing Institute of Technology, Beijing, China, [2]National Engineering Research Center of Urban Environmental Pollution Control, Beijing Municipal Research Institute of Eco-Environmental Protection, Beijing, China, [3]Beijing Vehicle Emission Management Center, Beijing, China, [4]College of Resource Environment and Tourism, Capital Normal University, Beijing, China

Based on the current air pollution control and CO_2 emission reduction policies, this study analyzed the energy structure, number of motor vehicles and nonroad mobile machinery, energy consumption and pollutant emissions in Beijing. Furthermore, the diesel consumption characteristics and challenges for emission reduction in key fields were investigated, such as medium- and heavy-duty diesel trucks, long-distance passenger and tourist diesel vehicles, and nonroad machinery, which are areas with difficult-to-reduce diesel consumption. Control targets and measures for total diesel consumption were also proposed. The results indicated that the higher diesel consumption per unit area in Beijing is related to the larger passenger car and freight truck populations. In recent decades, the number of diesel vehicles has increased, the vehicle type structure has been optimized, the proportion of vehicles with high emission standards has increased, and the absolute pollutant emissions have decreased. Among these, nitrogen oxides (NO_x), fine particulate matter ($PM_{2.5}$) and volatile organic compound (VOC) emissions of different models decreased by 39.5%, 75.3% and 42.8%, respectively, while carbon dioxide (CO_2) emissions from diesel combustion decreased by 32%. Moreover, medium and large passenger vehicles, medium- and heavy-duty trucks and construction machinery are the main contributors to diesel consumption. These vehicle types are also difficult to control and reduce, and their replacement by new-energy vehicles is relatively limited. The main control measures for diesel consumption are as follows. First, a green transportation mode can be adopted for goods that can be converted from roads to railways. Second, fuel consumption reduction for nonroad mobile machinery can be realized by tightening fuel consumption limits, setting appropriate maximum retirement life, establishing low- or ultralow-emission zones, and establishing demonstration plots for electric vehicle (EV) substitution for mobile machinery. To improve the air quality and take the lead in carbon neutrality in the future, Beijing must further accelerate the energy structure adjustment and the development of new-energy vehicles in the transportation sector. Carbon neutralization is an important opportunity for diesel

consumption reduction, and the synergistic control of atmospheric pollution and carbon emissions from diesel combustion must be strengthened.

KEYWORDS

mobile source, diesel consumption, total pollutants control, control measures, atmospheric pollution, carbon dioxide

1 Introduction

After years of efforts, the total emissions of motor vehicles and nonroad mobile machinery in Beijing continue to decline (Fu et al., 2012; Yao et al., 2014; Zhang et al., 2014; Lv et al., 2016). However, due to the high motor vehicle population, overall emissions remain very high, and the proportion of motor vehicles and nonroad mobile machinery emissions in local pollution sources continues to rise (Song et al., 2006; Lee et al., 2008; Ni et al., 2017; Wu et al., 2022). In 2018, source apportionment of fine particulate matter ($PM_{2.5}$) showed that the contribution of mobile-source emissions in the local $PM_{2.5}$ pollution reached 45%, the largest source of local $PM_{2.5}$ in Beijing. Therefore, the task of emission management and reduction remains arduous (Zhang et al., 2017; Fan et al., 2018; Gao et al., 2020; Zhang et al., 2020).

Diesel vehicles in Beijing account for only 5% of all vehicles, but single-vehicle emissions are relatively high. The nitrogen oxides (NO_x) emissions of diesel vehicles account for approximately 80% of the total NO_x emissions from motor vehicles (Xue et al., 2022); therefore, diesel vehicles are a significant source of NO_x emissions. Beijing's 2019 Action Plan for Pollution Prevention and Control proposes promoting the control and reduction of total diesel consumption by vehicles in Beijing and accelerating the construction of an indicator system of statistics, monitoring, and total reduction for diesel consumption by vehicles in public transport, tourism, freight transport, sanitation, and postal services.

Therefore, in this study, based on Beijing registration data, the emission factor method is used to calculate the emissions of air pollutants from mobile sources, and carbon dioxide (CO_2) emissions are measured according to the CO_2 emission accounting guidelines. Additionally, the existing policies related to the pollution control of diesel vehicles in Beijing are evaluated. Pollution emission control measures are proposed, considering air quality improvement, emission reduction needs, diesel consumption characteristics, and existing problems in emission reduction.

2 Materials and methods

In this study, through data collection, investigation and expert consultations, the current diesel consumption and carbon emission reduction policies in Beijing are reviewed; fuel reduction measures for medium- and heavy-duty diesel trucks, long-distance passenger transport and tourist vehicles, and nonroad mobile machinery are studied; control targets for total diesel consumption are proposed; and the impact on air quality is analyzed.

2.1 Data sources

The data include the number of various motor vehicles, the types and number of nonroad mobile machinery units, and energy data. The number of motor vehicles is obtained from the Beijing Traffic Management Bureau, the types and number of nonroad mobile machinery units are based on the Beijing nonroad mobile machinery information code registration data, and the energy data are obtained from the Statistical Yearbook released by the Beijing Municipal Bureau of Statistics. (as can be seen in Table 1).

2.2 Calculation method of atmospheric pollutant emissions from diesel combustion

2.2.1 Calculation method for diesel motor vehicle emissions

The air pollutant emissions of diesel vehicles in Beijing are calculated based on registration data, road length, and the emission factor method (Gu et al., 2019; Hao et al., 2022).

$$E_1 = \sum_i P_i \times EF_i \times VKT_i \times 10^{-6}, \quad (1)$$

where E_1 is the annual emission of pollutants corresponding to vehicle emission source i, in tonnes; EF_i is the emission factor, which is the amount of pollutants emitted by type i diesel vehicles per kilometer, in g/km; P_i is the number of registered diesel vehicles in Beijing; and VKT_i is the average annual mileage of type i diesel vehicles, in km/vehicle.

2.2.2 Calculation method for diesel nonroad mobile machinery emissions

For construction machinery and agricultural machinery, emissions are calculated by using the emission factor based on the mechanical power with the following formula:

TABLE 1 Data sources of activity levels for mobile-source emissions.

Category	Source
Number of various diesel vehicles and emission standards	Beijing Traffic Management Bureau
Number of various diesel machinery units and emission standards	Registration data
Energy data	Beijing Statistical Yearbook

TABLE 2 CO_2 emission coefficients for different energy types.

Energy	CO_2 coefficient	Unit
Coal	2.66	tonnes of CO_2/tonnes of standard coal
Fuel	1.73	
Gas	1.26	
Electricity	0.6168	kg/kWh

$$E = \sum_{j}\sum_{k}\sum_{n}\left(P_{j,k,n} \times G_{j,k,n} \times LF_{j,k,n} \times hr_{j,k,n} \times EF_{j,k,n}\right) \times 10^{-6}, \quad (2)$$

where E is the emission of various pollutants from nonroad mobile machinery, in tonnes; j is the type of nonroad mobile machinery; k is the emission standard; n is the power range; P is the number of nonroad mobile machinery units registered in Beijing, with vehicle as the unit; G is the average rated net power, in kilowatts/vehicle; LF is the load factor; hr is the total hours of use per year, in hours; EF is the pollutant emission factor, in g/kWh, and the mobile source survey method and emission coefficient in the Second National Pollution Source Census in China are applied.

2.3 CO_2 emission accounting method

CO_2 emissions include emissions from terminal coal consumption, terminal fuel consumption, terminal gas consumption, and regional electricity consumption.

$$E_i = F_i \times EF_i, \quad (3)$$

where i refers to the various energy types, such as coal, fossil fuel and gas. Ei represents CO_2 emissions from type i. EF_i represents the emission factor of type i, as shown in Table 2, and the EFs of coal, fossil fuel and gas were 2.66, 1.73, and 1.56 tonnes of CO_2 per ton of standard coal, respectively (NDRC Energy Research Institute, 2011). The local power grid emission factor is 0.6168 CO_2 emissions ($kgCO_2$/kWh).

2.4 Model simulation

The ADMS-Urban model is used to quantify the impact of air pollutant emissions from vehicles on the surrounding atmospheric environment; it is a steady-state atmospheric dispersion modeling system developed by Cambridge Environmental Research Consultants (CERC). Based on atmospheric boundary layer parameters, the ADMS-Urban model can better handle the complex topography and wind conditions of megacities (Righi et al., 2009; Audrius and Auksė, 2015). First, the traffic flow coefficients are assigned to roads of different levels, and a 1 km × 1 km grid is used for Beijing. Second, the data mentioned above are used to calculate the emissions of air pollutants in each grid, and the dispersion concentration of air pollutants in Beijing throughout the year is then simulated to obtain the dispersion concentration map of various pollutants. At present, ADMS-Urban is widely used and can accurately simulate the diffusion of traffic pollutants. The uncertainty of its simulation results is related mainly to meteorological conditions. Generally, when wind speed or direction changes sharply, the simulation value of ADMS-Urban is lower than the actual monitoring value, while when weather conditions are relatively stable, the simulation results are more accurate.

The total amount of various pollutants, meteorological data, typical road vehicle flow data, and model parameters are imported into the model. In the simulation of pollutant dispersion in the Beijing area, the total pollutant data for Beijing are used, and the data are gridded for the dispersion simulation. The data source is based on the amount of pollutant emissions from vehicles in Beijing. The meteorological data required for the model simulations are from the China Meteorological Data Service Centre (http://data.cma.cn), and the model defaults are used for other data, such as road slopes and loads.

3 Results and discussion

3.1 Air pollutant emissions from diesel vehicles in Beijing

Figure 1 shows the changes in diesel vehicles and diesel consumption in Beijing from 2013 to 2020. The overall diesel consumption from 2013 to 2020 decreased, with interannual fluctuations. In 2020, the diesel consumption of diesel vehicles in Beijing was 0.90 million tonnes, which is significantly lower than that in 2019 and is related mainly to the decline in passenger and

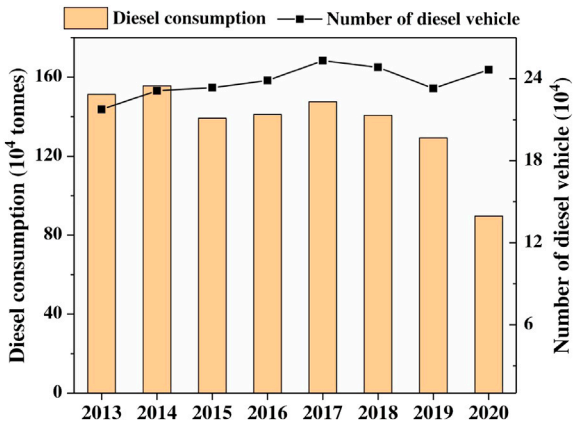

FIGURE 1
Changes in the number of diesel vehicles and diesel consumption from 2013 to 2020.

freight traffic due to the coronavirus 2019 (COVID-19) pandemic. In the long term, diesel consumption also declined by 41% from 1.51 million tonnes in 2013 as a result of the adjustment of the diesel vehicle structure, i.e., new diesel vehicles replacing old ones, since the fuel consumption of new diesel vehicles is significantly lower. *Fuel consumption limits for heavy-duty commercial vehicles were* implemented in 2014 (GB 30510-2014) and 2018 (GB 30510-2018), clearly and effectively reducing the fuel consumption of new vehicles. In the second year after implementation, i.e., 2015 and 2019, diesel consumption in Beijing was greatly reduced.

As shown in Figure 2, the changes and proportions of air pollutant emissions from diesel vehicles in Beijing show that from 2013 to 2020, the adjustment and optimization of vehicle structure caused declines of 39.5%, 75.3%, and 42.8% in the NO_x, $PM_{2.5}$, and volatile organic compound (VOC) emissions, respectively, of different vehicle types, with $PM_{2.5}$ decreasing most significantly. Large diesel passenger cars and trucks contributed significantly to NO_x and $PM_{2.5}$. There were also significant differences in the contributions of vehicles with different emission standards. The ownership of medium-sized diesel trucks meeting China III emission levels accounts for 37%, contributing 46% of NO_x and 45% of $PM_{2.5}$ emissions; the ownership of heavy-duty diesel trucks meeting China III emission standards accounts for 11%, contributing 15% of NO_x emissions and 13% of $PM_{2.5}$ emissions. The emissions of pollutants from vehicles at or below China III emission standards were also relatively high, and their percentage of pollutant emissions exceeded the proportion of vehicles. It is necessary to further promote the adoption of measures to ensure that the emission standards are met and to accelerate the elimination and updating of these vehicles.

3.2 CO_2 emissions

According to the corresponding assessment criteria of the Work Plan for the Evaluation of the Responsibility of Energy Saving and Carbon Reduction Targets in Beijing during the 13th Five-Year Plan Period, the annual CO_2 emissions during 2013–2020 in Beijing are calculated as shown in Figure 3. CO_2 emissions peaked at 151 million tonnes in 2019, followed by a plateau period. Thanks to the large-scale coal-to-clean energy policy, CO_2 emissions declined from 2015 to 2017, followed by a slight rebound from 2018 to 2019. The proportion of CO_2 emissions from coal continuously declined, the proportion of emissions from electricity significantly increased, and the proportion of emissions from fossil fuel remained stable.

CO_2 emissions from diesel combustion decreased from 3.85 million tonnes in 2013 to 2.24 million tonnes in 2020, a reduction of 41%. The contribution of diesel combustion to total CO_2 emissions decreased from 3% in 2013 to 2% in 2020 (as can be seen in Figure 4). At present, some road transport enterprises are included in the list of key carbon emission units. For the future prevention and control of air pollution from road transport vehicles, more road transport enterprises, especially those with numerous medium- and heavy-duty trucks and medium and large passenger vehicles, should be highlighted based on the current carbon emission management mechanism.

3.3 The control target of total diesel consumption from mobile sources in Beijing and its impact on air quality

Based on the actual situation in Beijing, the total amount of diesel should be set, and the diesel consumption in key industries should be controlled, including road transportation (passenger and freight transport), the construction industry, and the building materials industry, which are best combined with key carbon emission units (Jiang et al., 2008; Kim et al., 2010). The annual diesel consumption reduction targets of each industry should be reasonably allocated, and diesel consumption statistics should be collected and monitored. Based on publicity and policy implementation, key diesel vehicle users should be guided to increase their awareness of energy conservation and emissions reduction, to actively update and eliminate low-standard diesel vehicles and machinery with high energy consumption and emissions levels, and to gradually upgrade to new standards or new-energy vehicles and machinery (Axsen and Kurani, 2010; Bessa and Matos, 2012; Yang et al., 2018).

The control target of total diesel consumption is closely related to the targets of air quality improvement and carbon neutrality in Beijing. In 2020, the concentration of $PM_{2.5}$ in Beijing decreased to 38 μg/m^3 for the first time, which is related to

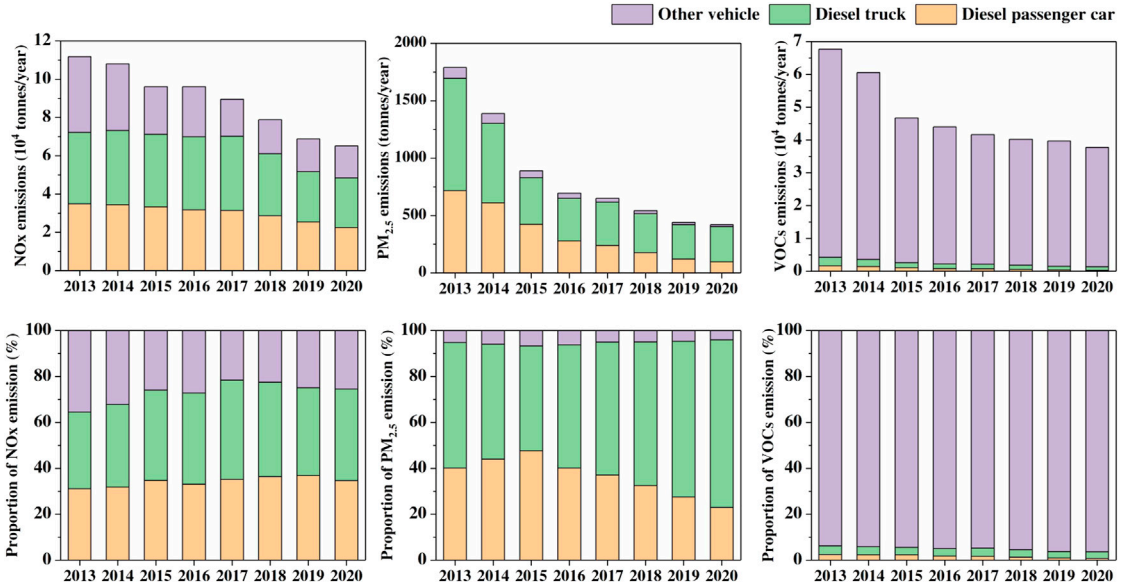

FIGURE 2
Changes and proportions of pollutant emissions from diesel vehicles.

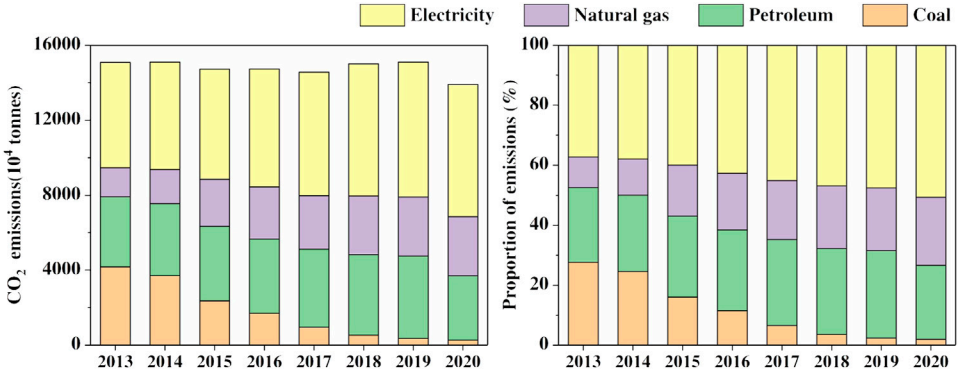

FIGURE 3
Changes in CO_2 emissions and proportions of CO_2 emissions in Beijing.

the decrease in the activity level of pollution sources caused by COVID-19 (Cao et al., 2021). This decrease is also an environmental benefit of air pollution control measures. To achieve air quality standards and meet the World Health Organization (WHO)'s recommended health limits for $PM_{2.5}$ in the future, there is still a need to strengthen air pollution control, especially concerning the continuous reduction of emissions from mobile pollution sources. Therefore, based on future air quality improvement targets in Beijing (low, medium, and high $PM_{2.5}$ concentration scenarios will be 25, 20, and 15 μg/m^3, respectively, in 2035), reductions of at least 40%, 45%, and 50% in the low, medium, and high gasoline and diesel consumption scenarios, respectively, in Beijing should be met by 2035 (Figure 5A).

To meet the target of carbon neutrality by 2050 and the carbon reduction target of halving greenhouse gas emissions by 2035, reductions of at least 45%, 50%, and 60% in the low, medium, and high diesel consumption scenarios or gasoline and diesel consumption scenarios, respectively, in Beijing should be met by 2035 (Figure 5B).

For major diesel vehicle types, there should be no diesel consumption by small passenger vehicles by 2035, by which time all buses should also be electric vehicles (EVs). The development of new-energy tourist buses and medium and large buses can be

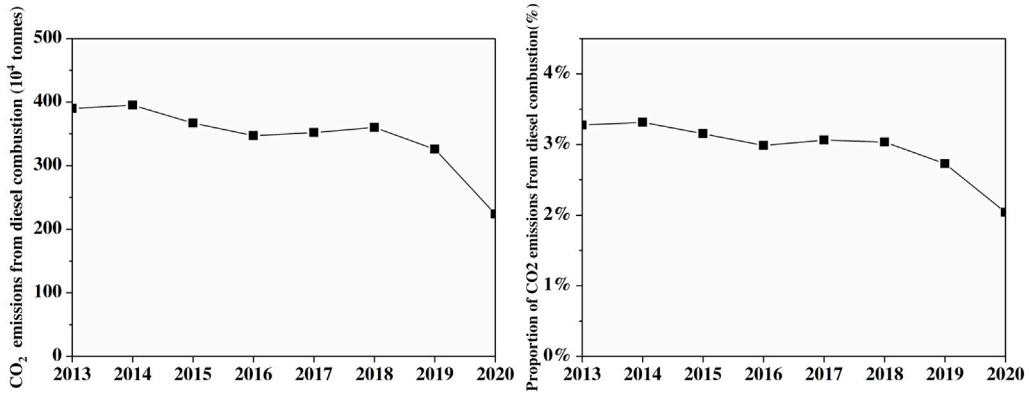

FIGURE 4
Changes in CO_2 emissions from diesel combustion and the proportion of CO_2 emissions from diesel combustion in Beijing.

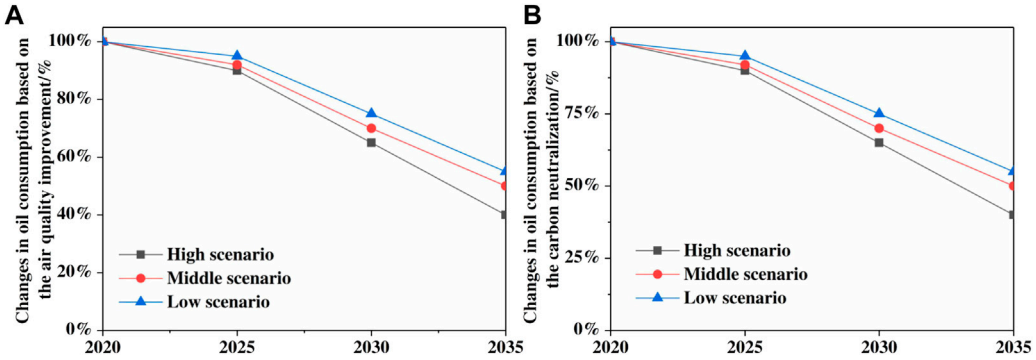

FIGURE 5
Changes in fuel consumption due to air quality improvement **(A)** and carbon neutrality **(B)**.

accelerated by the establishment of a zero-emission zone in the city center to increase the proportion of these vehicles. Light trucks are being phased out naturally, and the economic stimulus for accelerating the phaseout and renewal of older vehicles and policies facilitating access to new-energy vehicles could increase the proportions of the latter. Due to the implementation of the new energy development strategy for medium- and heavy-duty trucks, technological progress and lower production costs, and the anticipation of a ban on the sale of traditional-fuel vehicles, the adoption of new-energy medium- and heavy-duty trucks could be accelerated. Based on the bottom-up measures for key diesel vehicles, it is estimated that diesel consumption in the low, medium, and high scenarios in 2035 could be reduced, respectively, by 54%, 62%, and 69% (Figure 6) compared to 2020, which would essentially meet Beijing's carbon emission reduction targets.

The ADMS-Urban model is used to simulate the effects of pollution emissions from diesel combustion on primary $PM_{2.5}$, VOC, and NO_x concentrations in 2020 and the decreases in major atmospheric pollutant concentrations due to reduced diesel consumption under different control scenarios in 2035.

The impact of diesel vehicles on the surrounding air quality in Beijing in 2020 is obtained through simulation, as shown in Figure 7. Five traffic stations are selected as sensitive receptors, and the annual average concentrations of NO_x, $PM_{2.5}$, and VOCs are 17.6, 0.4 and 0.8 μg/m^3, respectively.

Under the low diesel reduction scenario, the annual average concentrations of the three major atmospheric pollutants due to diesel vehicles are reduced by approximately 53%, and the annual average concentrations of NO_x, $PM_{2.5}$, and VOCs at the five traffic stations with sensitive receptors are 10.51 μg/m^3, 0.14 μg/m^3 and 0.48 μg/m^3, respectively. Under the medium diesel reduction scenario, the annual average concentrations of the three major atmospheric pollutants due to diesel vehicles are reduced by approximately 65%, and the annual average

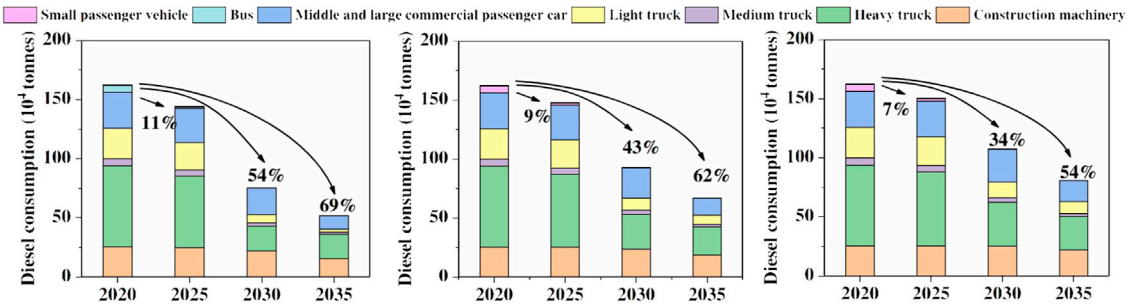

FIGURE 6
Fuel consumption of different types of vehicles in the low, medium, and high scenarios.

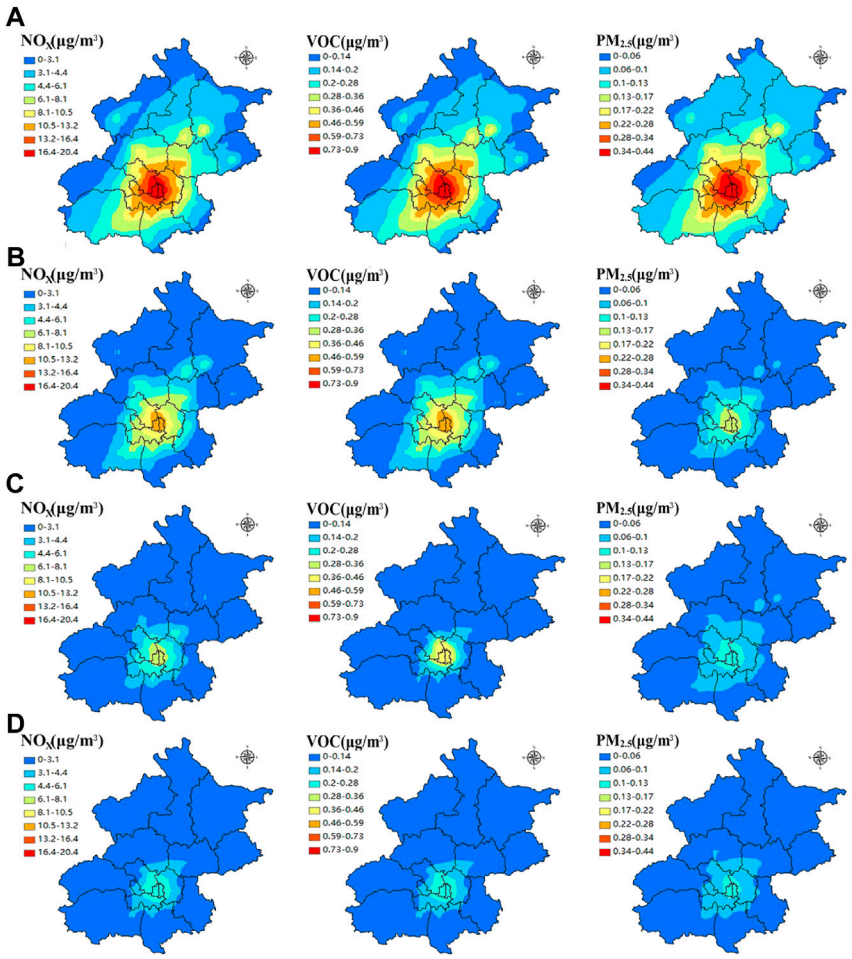

FIGURE 7
Impacts of diesel vehicles in Beijing in 2020 **(A)** and high- **(B)**, medium- **(C)**, and low-control scenarios **(D)** in 2035 on air quality.

concentrations of NO_x, $PM_{2.5}$, and VOCs at the five traffic stations with sensitive receptors are 6.69 μg/m^3, 0.1 μg/m^3, and 0.32 μg/m^3, respectively.

Under the high diesel reduction scenario, the annual average concentrations of the three major atmospheric pollutants due to diesel vehicles are reduced by approximately 74%, and the annual

average concentrations of NO_x, $PM_{2.5}$, and VOCs at the five traffic stations with sensitive receptors are 2.26 μg/m^3, 0.07 μg/m^3, and 0.24 μg/m^3, respectively.

3.4 Recommendations for coordinated control of diesel vehicle pollution in Beijing

To reduce the pollution emissions from diesel vehicles, over the past decade, Beijing has actively adopted legislation (*Beijing Regulations on the Prevention and Control of Emissions from Motor Vehicles and Nonroad Mobile Machinery*), upgraded diesel vehicle and oil product standards, implemented a subsidy policy for the elimination of old diesel vehicles, and strengthened emission supervision and law enforcement (online supervision, remote sensing monitoring, etc.). These measures and policies have effectively promoted the adjustment and optimization of the diesel vehicle structure in Beijing, and the proportion of vehicles with high emission scores has continuously increased. Some key models of new energy have been well developed, especially in the light truck and bus industries. However, several problems remain: (1) It is necessary to further optimize the traffic structure and increase the proportion of railway transport. (2) The efficiency of transport should be further improved. The current transport intensity is still high. (3) The low level of new-energy development of medium-heavy goods vehicles and buses is insufficient to support the realization of higher air quality improvement and carbon neutrality goals.

3.4.1 Promoting optimization of the energy structure of freight vehicles

In addition to ensuring major livelihood, emergency, and special scenarios, policies should be developed starting from the licensing process to ensure that new and updated light trucks are essentially new-energy vehicles. A series of incentive plans for new-energy trucks in Beijing should be formulated to expand the incentive range from light trucks under 4.5 tonnes to medium- and heavy-duty trucks. A series of priority passage policies for new-energy logistics distribution vehicles should be formulated and implemented, and all vehicles with truck passes should be purely EVs or hydrogen fuel cell vehicles, thus promoting EVs through policies that begin with licensing and use processes.

3.4.2 Push-pull combination to promote the elimination of old vehicles and upgrading to electric vehicles

The current policies and measures should be continued, including the subsidy for the elimination of gasoline vehicles meeting the China III emission standard, the ban on gasoline vehicles meeting China I and II emission standards within the Fifth Ring Road during weekdays, and the city-wide ban on diesel trucks meeting the China III emission standard. Additionally, phaseout subsidies and restrictions on vehicles with higher emission standards and more vehicle models should be studied. In 2022, light gasoline vehicles meeting the China III emission standard should be banned within the Fifth Ring Road during weekdays; in 2023, phaseout subsidies for gasoline vehicles meeting the China IV emission standard and large and medium-sized passenger vehicles meeting the China III emission standard should be implemented; in 2024, diesel trucks meeting the China IV emission standard should be banned in Beijing; and in 2025, light gasoline vehicles meeting the China IV emission standard and large and medium-sized passenger vehicles meeting the China III emission standard should be banned within the Fifth Ring Road.

3.4.3 Promoting the transportation of bulk goods by rail and establishing a green freight transport mode of electrified railway plus new-energy vehicles

Adjustment of the freight transportation structure must be continuously promoted. The special implementation plans for medium- and long-term transportation structural adjustment should be studied and formulated, infrastructure facilities should be improved, and the use of rail transportation for bulk goods, such as sand and gravel aggregates, commercial vehicles, steel, and productive coal, should be promoted. The construction of green sand and gravel bases should be promoted to further increase the proportion of sand and gravel transportation by rail and new-energy vehicles.

4 Conclusion

This study analyzes the energy structure, number of motor vehicles and nonroad mobile machinery units, and their energy consumption and emissions in Beijing. It combines the current air pollutant and CO_2 emissions in Beijing and proposes synergistic control measures and recommendations for the existing policies and problems related to diesel vehicle pollution control in Beijing. The main conclusions are as follows:

From 2013 to 2020, the adjustment and optimization of vehicle structure caused decreases of 39.5%, 75.3%, and 42.8% in the NO_x, $PM_{2.5}$, and VOC emissions of different vehicle types, respectively, with $PM_{2.5}$ reduction being the most significant. Diesel trucks contribute significantly to NO_x and $PM_{2.5}$ emissions. CO_2 emissions from diesel combustion decreased from 3.85 million tonnes in 2013 to 2.24 million tonnes in 2020, a reduction of 41%. The contribution of diesel combustion to total CO_2 emissions decreased from 3% in 2013 to 2% in 2020.

To improve air quality and take the lead in carbon neutrality in the future, Beijing must further accelerate energy structure adjustment and the development of new-energy vehicles in the transportation sector. Existing policies are insufficient to promote the updating of in-use vehicles into new-energy vehicles, and the purchase cost, technology, and supporting

facilities have not reached the ideal standard. In the future, full-scale electrification depends on social consensus and transformation, the establishment and guarantee of relevant systems, the safe supply of electricity, and breakthroughs in EV control and fast charging technologies. The need for large-scale production and reduced purchase cost must also be addressed.

Carbon neutralization is an important opportunity for diesel reduction to strengthen the synergistic control of atmospheric pollution and carbon emissions from diesel combustion. Energy consumption reduction is a systematic project, but it is not appropriate to control the consumption of diesel and gasoline separately, and coordination should be enhanced. Diesel consumption and emissions can be reduced through dual control of the number of industries and the total amount of emissions. Combined with the management of carbon transportation and carbon emission units, the prevention and reduction of energy and emissions in key vehicle-using industries should be promoted.

Data availability statement

The original contributions presented in the study are included in the article/Supplementary Material; further inquiries can be directed to the corresponding author.

Author contributions

Conceptualization, YA; methodology, YC and YG; formal analysis, XW, TW, and XL; data curation, YS, ML, YW, and HY; writing—original draft preparation, YA; writing—review and editing, XY.

Conflict of interest

The authors declare that the research was conducted in the absence of any commercial or financial relationships that could be construed as a potential conflict of interest.

The reviewer TJ declared a past co-authorship with the author YA to the handling editor.

Publisher's note

All claims expressed in this article are solely those of the authors and do not necessarily represent those of their affiliated organizations, or those of the publisher, the editors and the reviewers. Any product that may be evaluated in this article, or claim that may be made by its manufacturer, is not guaranteed or endorsed by the publisher.

References

Audrius, D., and Auksė, M. (2015). The statistical evaluation and comparison of ADMS-Urban model for the prediction of nitrogen dioxide with air quality monitoring network. *Environ. Monit. Assess.* 187 (578), 578–612. doi:10.1007/s10661-015-4810-1

Axsen, J., and Kurani, K. S. (2010). Anticipating plug-in hybrid vehicle energy impacts in California: Constructing consumer-informed recharge profiles. *Transp. Res. Part D Transp. Environ.* 15 (4), 212–219. doi:10.1016/j.trd.2010.02.004

Bessa, R. J., and Matos, M. A. (2012). Economic and technical management of an aggregation agent for electric vehicles: A literature survey. *Euro. Trans. Electr. Power* 22 (3), 334–350. doi:10.1002/etep.565

Cao, X. Z., Tian, Y., Shen, Y., Wu, T. R., Li, R. F., Liu, X. Y., et al. (2021). Emission variations of primary air pollutants from highway vehicles and implications during the COVID-19 pandemic in beijing, China. *Int. J. Environ. Res. Public Health* 118 (8), 4019. doi:10.3390/ijerph18084019

Fan, C. Y., Song, C. L., Lv, G., Wang, G. Y., Zhou, H., and Jing, X. J. (2018). Evaluation of carbonyl compound emissions from a non-road machinery diesel engine fueled with a methanol/diesel blend. *Appl. Therm. Eng.* 129, 1382–1391. doi:10.1016/j.applthermaleng.2017.10.086

Fu, M. L., Ge, Y. S., Tan, J. W., Zeng, T., and Liang, B. (2012). Characteristics of typical non-road machinery emissions in China by using portable emission measurement system. *Sci. Total Environ.* 437, 255–261. doi:10.1016/j.scitotenv.2012.07.095

Gao, C. K., Gao, C. B., Song, K. H., Xing, Y. H., and Chen, W. W. (2020). Vehicle emissions inventory in high spatial–temporal resolution and emission reduction strategy in Harbin-Changchun Megalopolis. *Process Saf. Environ. Prot.* 138, 236–245. doi:10.1016/j.psep.2020.03.027

Gu, X. K., Yin, S. S., Lu, X., Zhang, H., Wang, L. L., Bai, L., et al. (2019). Recent development of a refined multiple air pollutant emission inventory of vehicles in the Central Plains of China. *J. Environ. Sci.* 84 (10), 80–96. doi:10.1016/j.jes.2019.04.010

Hao, L. J., Zhao, Z. H., Yin, H., Wang, J. F., Li, L. J., Lu, W. H., et al. (2022). Study of durability of diesel vehicle emissions performance based on real driving emission measurement. *Chemosphere* 297, 134171. doi:10.1016/j.chemosphere.2022.134171

Jiang, J., Gu, F., Gennish, R., Moore, D. J., Harris, G., and Ball, A. D. (2008). Monitoring of diesel engine combustions based on the acoustic source characterisation of the exhaust system. *Mech. Syst. Signal Process.* 22, 1465–1480. doi:10.1016/j.ymssp.2007.12.003

Kim, C. H., Qi, G. S., Dahlberg, K., and Li, W. (2010). Strontium-doped perovskites rival platinum catalysts for treating NO_x in simulated diesel exhaust. *Science* 327, 1624–1627. doi:10.1126/science.1184087

Lee, S. J., Jeong, S. J., Kim, W. S., and Lee, C. B. (2008). Computational study on the effects of volume ratio of DOC/DPF and catalyst loading on the PM and NOx emission control for heavy-duty diesel engines. *Int. J. Automot. Technol.* 9 (6), 659–670. doi:10.1007/s12239-008-0078-6

Lv, B., Zhang, B., and Bai, Y. (2016). A systematic analysis of $PM_{2.5}$ in beijing and its sources from 2000 to 2012. *Atmos. Environ. X.* 124, 98–108. doi:10.1016/j.atmosenv.2015.09.031

NDRC Energy Research Institute (2011). Data from: Guidelines for the preparation of provincial GHG inventories. http://www.cbcsd.org.cn/sjk/nengyuan/standard/home/20140113/download/shengjiwenshiqiti.pdf.

Ni, X. Y., Huang, H., and Du, W. P. (2017). Relevance analysis and short-term prediction of $PM_{2.5}$ concentrations in beijing based on multi-source data. *Atmos. Environ. X.* 150, 146–161. doi:10.1016/j.atmosenv.2016.11.054

Righi, S., Lucialli, P., and Pollini, E. (2009). Statistical and diagnostic evaluation of the ADMS-Urban model compared with an urban air quality monitoring network. *Atmos. Environ. X.* 43 (25), 3850–3857. doi:10.1016/j.atmosenv.2009.05.016

Song, Y., Xie, S., Zhang, Y., Zeng, L., Salmon, L. G., and Zheng, M. (2006). Source apportionment of $PM_{2.5}$ in beijing using principal component analysis/absolute principal component scores and unmix. *Sci. Total Environ.* 372 (1), 278–286. doi:10.1016/j.scitotenv.2006.08.041

Wu, T. R., Cui, Y. Y., Lian, A. P., Tian, Y., Li, R. F., Liu, X. Y., et al. (2022). Vehicle emissions of primary air pollutants from 2009 to 2019 and projection for the 14th Five-Year Plan period in Beijing, China. *J. Environ. Sci.* 124, 513–521. doi:10.1016/j.jes.2021.11.038

Xue, Y. F., Liu, X. Y., Cui, Y. Y., Shen, Y., Wu, T. R., Wu, B. B., et al. (2022). Characterization of air pollutant emissions from construction machinery in Beijing and evaluation of the effectiveness of control measures based on information code registration data. *Chemosphere* 303, 135064. doi:10.1016/j.chemosphere.2022.135064

Yang, F., Xie, Y., Deng, Y., and Yuan, C. (2018). Predictive modeling of battery degradation and greenhouse gas emissions from U.S. state-level electric vehicle operation. *Nat. Commun.* 9 (1), 2429–29. doi:10.1038/s41467-018-04826-0

Yao, Z., Wei, H., Perugu, H., Liu, H., and Li, Z. X. (2014). Sensitivity analysis of project level MOVES running emission rates for light and heavy duty vehicles. *J. Traffic Transp. Eng.* 1 (2), 81–96. doi:10.1016/S2095-7564(15)30092-1

Zhang, Q. J., Yang, L., Ma, C., Zhang, Y. J., Wu, L., and Mao, H. J. (2020). Emission characteristics and chemical composition of particulate matter emitted by typical non-road construction machinery. *Atmos. Pollut. Res.* 11 (4), 679–685. doi:10.1016/j.apr.2019.12.018

Zhang, S. J., Wu, Y., Wu, X. M., Li, M. L., Ge, Y. S., Liang, B., et al. (2014). Historic and future trends of vehicle emissions in beijing, 1998–2020: A policy assessment for the most stringent vehicle emission control program in China. *Atmos. Environ. X.* 89, 216–229. doi:10.1016/j.atmosenv.2013.12.002

Zhang, S. J., Wu, Y., Zhao, B., Wu, X. M., Shu, J. W., and Hao, J. (2017). City-specific vehicle emission control strategies to achieve stringent emission reduction targets in China's Yangtze River Delta region. *J. Environ. Sci.* 51 (1), 75–87. doi:10.1016/j.jes.2016.06.038

frontiers | Frontiers in Environmental Science

TYPE Mini Review
PUBLISHED 04 January 2023
DOI 10.3389/fenvs.2022.1082623

OPEN ACCESS

EDITED BY
Chaoyang Xue,
UMR7328 Laboratoire de physique et chimie de l'environnement et de l'Espace (LPC2E), France

REVIEWED BY
Chen Xu,
Institute of Atmospheric Physics (CAS), China
Qian Chen,
Nanjing University of Information Science and Technology, China

*CORRESPONDENCE
Wei Wei,
weiw@cma.gov.cn

SPECIALTY SECTION
This article was submitted to Atmosphere and Climate, a section of the journal Frontiers in Environmental Science

RECEIVED 28 October 2022
ACCEPTED 12 December 2022
PUBLISHED 04 January 2023

CITATION
Wei W, Zhang H, Zhang X and Che H (2023), Low-level jets and their implications on air pollution: A review. *Front. Environ. Sci.* 10:1082623. doi: 10.3389/fenvs.2022.1082623

Low-level jets and their implications on air pollution: A review

Wei Wei[1,2]*, Hongsheng Zhang[3], Xiaoye Zhang[2] and Huizheng Che[2]

[1]CMA Earth System Modeling and Prediction Centre, Beijing, China, [2]State Key Laboratory of Severe Weather, Chinese Academy of Meteorological Sciences, Beijing, China, [3]Laboratory for Climate and Ocean-Atmosphere Studies, Department of Atmospheric and Oceanic Sciences, School of Physics, Peking University, Beijing, China

Low-level jets (LLJ) are a common phenomenon in the atmospheric boundary layer and have been reported worldwide. Additionally, they have considerable relevance in a series of fields. This review aimed to document their implications on air quality, specifically particulate matter, mineral dust, and ozone in recent literature focus on i) generalizing long-range advection of pollutants by the low-level jets; ii) analysing vertical transport due to low-level jets-enhanced turbulence mixing and the corresponding mechanisms for different pollutants; and iii) introducing the performance of state-of-the-art numerical models. Finally, we suggest that high-resolution spatiotemporal observations of the pollutants and turbulence must be conducted, and current parameterization schemes should be improved to better represent the low-level jets and nocturnal boundary layer structures for reproducing the complicated interactions between the low-level jets and pollutants.

KEYWORDS

low-level jets, regional transport, vertical dispersion, intermittent turbulence, PM2.5, ozone

1 Introduction

Low-level jets (LLJs) are a common phenomenon in the atmospheric boundary layer (ABL) and have been widely observed worldwide, including in North America (Smith et al., 2019), South America (Sánchez et al., 2022), East Asia (Wei et al., 2014; Miao et al., 2018), Europe (Tuononen et al., 2017), and Africa (King et al., 2021). However, there is no universal consensus on the definition of the LLJs (Fiedler et al., 2013). To summarize the definitions in previous literatures, the term LLJ used here refers to a stream of fast-moving flow with maximum wind speed and vertical wind shear in the lower part of the troposphere (Stull, 1988).

The occurrence and variation of the LLJs are modulated by a combination of mechanisms on different temporal and spatial scales. Blackadar's (1957) pioneering work proposed that inertial oscillations of ageostrophic components contribute to the diurnal cycle of the LLJs. The "Blocking Theory" (Wexler, 1961) attributed the speeding-up of flows to the blockage of terrains, such as the Rocky Mountains, an analogy to the

Gulf Stream in oceanography. The thermal—wind relationship leads to coastal jets because of the differential heating and cooling between the land and oceans (Lima et al., 2019). Sloping terrains and the associated horizontal temperature gradients are other ways for providing baroclinicity that the LLJs need to develop (Gebauer and Shapiro, 2019).

The LLJs are primarily a process in the ABL and are highly relevant in many fields, such as wind energy (Wimhurst and Greene, 2019), precipitation (Du et al., 2012), fog (Wu et al., 2020), urban heat islands (Hu et al., 2013a), wildfires (Čavlina Tomašević et al., 2022), aviation safety (Gultepe et al., 2019), and migration pathways of birds (Wainwright et al., 2016). This review aimed to examine how the LLJs impact pollutant transport locally and inter-regionally, considering mineral dust, fine particulate matter ($PM_{2.5}$), and ozone (O_3). Specifically, this paper focuses on the following:

Present the current state of knowledge of the LLJ—pollutant interaction mechanism.

Document the state-of-the-art methods to analyse the LLJs, including numerical models and signal analysis techniques.

Outline the remaining gaps between the current progress and future research.

2 Regional transport

The belt of high wind speed, one of the dominant features of the LLJs, is a crucial process in the long-range transport of the pollutants. The contribution of LLJ advection to a certain region depends on the season, wind direction, and location of pollutant sources. In the Sahara Desert, dust is primarily advected below 800 hPa to South America in winter and spring and to the Caribbean at 500 hPa in summer and autumn (Gläser et al., 2015). In the southwestern China, up to 80% of the summertime O_3 accumulation is because of horizontal transport (Yang et al., 2020). The LLJs are crucial to the redistribution of O_3 between source locations and downwind regions (Bao et al., 2008; Klein et al., 2019). Li et al. (2019) revealed that southerly LLJs could transport large amounts of $PM_{2.5}$ from upstream regions, leading to accumulation of the pollutants in the downstream zones. In contrast, the occurrence of the LLJs positively contributes to the dilution of pollutants in Beijing (Miao et al., 2019). In Tianjin, China, southwesterly LLJs transport polluted air masses from the southern industrial regions, deteriorating local air quality, whereas the northerly or southeasterly LLJs are helpful in improving visibility (Wu et al., 2020). In general, the existence of the LLJs favors the dilution of pollutants, whereas downwind regions suffer from pollutant advection by the LLJs.

In addition, the transport of precursors and moisture by the LLJs facilitates the formation of pollution periods. In the North China Plain, southwesterly LLJs establish a moisture channel from the South China Sea to the Bohai Rim Region, contributing to the frequent $PM_{2.5}$ events in winter (Ju et al., 2020).

3 Vertical transport of mineral dust

Although the long-range transport of chemical species by the LLJs between different regions has been studied previously, the vertical flux associated with them has not been intensely investigated (Figure 1). Recent studies have revealed that vertical dispersion induced by the LLJs may play a crucial role in the local air quality.

The downward momentum flux caused by the LLJs is recognized as one of the key mechanisms of dust emissions in the Sahara Desert, in addition to monsoon surges (Cuesta et al., 2010), cold pool outflows (Allen et al., 2013), and dry convective plumes (Ansmann et al., 2009). The LLJs develop in the ABL after sunset because of the inertial oscillations (Blackadar, 1957). The wind shear near the jet core creates turbulence in the upper layer and it is transported downward, generating peak winds near the surface. There is a time lag of several hours between the maximal wind speed of the LLJs and that at the surface layer, with the former occurring before sunrise and the latter occurring mid-morning. Dust is emitted once the surface wind exceeds the local dust emission threshold (Allen and Washington, 2014). Observations and model simulations (Todd et al., 2008) have confirmed that LLJ-induced downward momentum initiates mid-morning dust events. Approximately 60% of the total dust can be attributed to the peak wind caused by nocturnal LLJs (Fiedler et al., 2013). The LLJs are a common phenomenon in the Sahara Region and an average of 29% at night was observed (Fiedler et al., 2013). Frequently occurring LLJs are key drivers of the local dust emissions. According to satellite observations from 2006 to 2008 (Schepanski et al., 2009), the surface peak wind associated with the nocturnal LLJs accounted for 65% of dust source activations during the mid-morning across North Africa, which is larger than the values at midday. Once uplifted, the dust is horizontally transported by the LLJs to America, Europe, and beyond.

4 Vertical transport of $PM_{2.5}$

Due to the consumption of fossil fuels and the stable atmosphere, $PM_{2.5}$ pollution tends to occur frequently during winter, especially in densely populated metropolises. One feature of $PM_{2.5}$ pollutions in winter is persistent and it threatens public health (Dominici et al., 2014). Persistent heavy pollution events are divided into two stages (Zhong et al., 2017; Wei et al., 2018; Zhong et al., 2018; Ren et al., 2019a): the cumulative stage during which particles accumulate is due to the high emissions, adverse synoptic weather conditions, regional transport, and secondary pollutant production and the dissipation stage is characterized by an abrupt decline in $PM_{2.5}$ levels. Numerous studies (Wei et al., 2018; Ren et al., 2019a; Ren et al., 2019c; Li et al., 2020; Wei et al., 2020; Li et al., 2021) have revealed that the LLJs play a key role in the dissipation stage of $PM_{2.5}$.

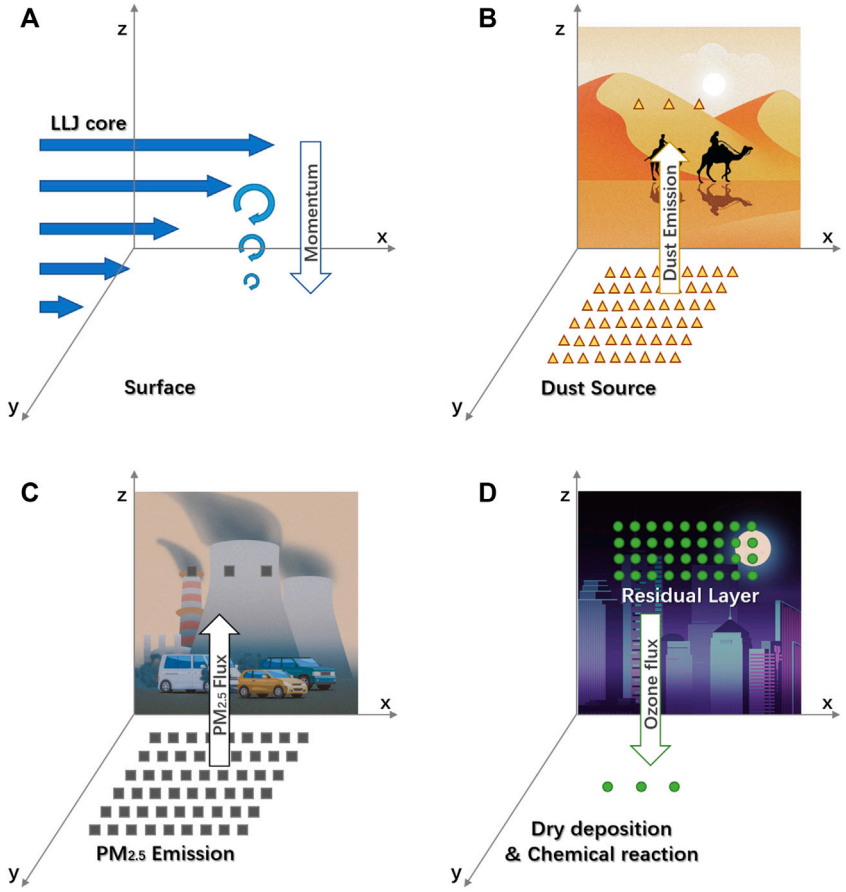

FIGURE 1
Schematic of vertical interaction between LLJs and pollutants with transport of **(A)** momentum, **(B)** dust, **(C)** fine particulate matter, and **(D)** ozone.

Inversion layer frequently develops in winter and traps $PM_{2.5}$ emitted from the ground within a shallow layer. According to the "barrier effect" theory (Ren et al., 2021), turbulence disappears at some heights and laminar flow develops during heavily polluted periods, which serves as a barrier layer impeding vertical turbulence transport. In the presence of the LLJs, turbulence bursts produced by aloft wind shear enhance vertical mixing, break the decoupled ABL structure, and rebuild the heat/momentum/material exchange between different heights. Field observations (Li et al., 2020) confirmed that the LLJs frequently occurred during the transition between the two stages. Miao et al. (2018) investigated the climatology of the LLJs in the Beijing Region and discovered that they frequently occurred in spring and winter and were mostly concentrated during nighttime. The consistency between the LLJs and severe $PM_{2.5}$ events implies that they play a crucial role in $PM_{2.5}$ pollution, which has been confirmed in a wide range of areas in China.

The LLJs can affect the diffusion of $PM_{2.5}$ indirectly *via* propagating internal gravity waves (IGWs), in addition to their direct impact on pollutant transport. The IGWs are a type of wavelike motion in the stable boundary layer (SBL) triggered by the LLJs (Jia et al., 2019). One puzzling phenomenon of heavy pollution is that $PM_{2.5}$ concentrations at different levels experience non-simultaneous drops or inverse variations (Ren et al., 2020). In the presence of the LLJs, the IGWs are generated and propagated downward, intermittently triggering turbulence layer by layer (Wei et al., 2022). The vertical spreading of the IGWs is responsible for short-term $PM_{2.5}$ removals during the cumulative stage and asynchronous variation at different heights.

5 Vertical transport of tropospheric O_3

As a volatile secondary photochemical pollutant, O_3 concentration at the surface undergoes a marked diurnal

variation: i) High emission of precursors and photodissociation leads to high O_3 concentration during the daytime. ii) After sunset, the photochemical production shuts down and O_3 is removed *via* dry deposition and chemical reactions within the surface layer. Meanwhile the aloft residual layer traps O_3. iii) The following morning, strong turbulence develops and fully mixes the aloft O_3. In this scenario, nocturnal O_3 concentration at the surface should be near zero owing to the absence of production, removal processes, and a decoupled SBL. However, nighttime O_3 spikes have been frequently reported in different regions since the 1970s (Samson, 1978; Reitebuch et al., 2000).

At night, the surface layer decouples with the aloft residual layer, thus making the residual layer a "reservoir" of daytime pollutants. In the presence of the LLJs, the strong wind shear near the jet core generates turbulence bursts, enhancing the vertical mixing between the two layers. Thus, the O_3 restored in the residual layer leaks into the surface layer. Studies (Reitebuch et al., 2000; Hu et al., 2012; Hu et al., 2013b) have verified that the concentration of O_3 in the residual layer, accompanied by O_3 spikes near the surface, is highly variable, implying active vertical exchanges. This aloft turbulence source associated with the LLJs depicts a reversed vertical structure from the traditional SBL, where most of the turbulence is produced by surface friction and transported upward. The turbulence induced by the LLJs is highly sporadic and is marked by intermittent bursts which remains an intriguing problem. Apart from the LLJs, other mechanisms causing intermittent turbulence include Kelvin–Helmholtz instabilities, gravity waves, wake vortices, and density currents (Wei et al., 2017). Considering that favorable synoptical patterns for the LLJs are also beneficial to heavy O_3 periods in some regions (Ryan, 2004), the importance of the LLJs in O_3 pollution cannot be ignored.

The maxima O_3 concentrations at nighttime may not be comparable to those in the afternoon. However, relevant research still has implications: i) The LLJs are important contributors to the horizontal transport. Considering that the vertical O_3 flux leads to a leaky residual-layer reservoir, the impact of pollutants carried by the LLJs downwind may be relieved. ii) O_3 dispersed to the surface is permanently removed *via* dry deposition at night. As photochemical production does not occur, the net effect is that the total amount of O_3 is reduced, further easing the next-morning O_3 levels. iii) In persistent O_3 periods, the amount of O_3 removed by nighttime vertical mixing is crucial for the total O_3 budget over several days (Banta et al., 2007). iv) Nighttime spikes have been reported in different chemical species, including hydrogen peroxide (Das and Aneja, 1994), isoprene (Starn et al., 1998), volatile organic compounds (VOCs) (Ganzeveld et al., 2008), carbon dioxide (CO_2) (Hicks et al., 2015), and $PM_{2.5}$ (Wei et al., 2018). Therefore, the studies on the LLJ–O_3 mechanism also have implications for other pollutants.

6 Models and analyses methods

Model simulation has become a useful tool for investigating the LLJs and their interactions with air pollutions. Based on the inertial oscillation theory, numerical models can reproduce the diurnal variation in the LLJs (van de Wiel et al., 2010). However, the underestimation of the maximal wind speed and deviations of profiles by the numerical models have been widely reported (Smith et al., 2018; Haikin and Castelli, 2022). The simulation bias of the maximal wind strength and profiles could further affect the wind shear and turbulence mixing. The simulation of the nocturnal LLJ is highly sensitive to the vertical resolution, planetary boundary layer (PBL) schemes and surface-layer parameterizations. Refining vertical spacing is helpful to improve the LLJs while the computational cost and model stability should be considered.

The simulation bias in the diurnal variation of $PM_{2.5}$ levels is largely due to turbulence mixing during nighttime. Considering that the LLJs and serious $PM_{2.5}$ pollution tend to occur in stabilized atmosphere, local closure PBL schemes are suitable for the simulation of the LLJs and $PM_{2.5}$ events (Jia and Zhang, 2020). Some literatures (Udina et al., 2020; Yang et al., 2021) have confirmed that the Mellor—Yamada—Janjic scheme (Janjic, 2002) shows better performance compared with other schemes, while it still cannot reproduce the different stages of haze events. The turbulence mixing coefficient is one of the key parameters to control the PBL mixing. Du et al. (2020) revealed that increasing the threshold of turbulence mixing coefficient was helpful to the simulation of diurnal variation of $PM_{2.5}$. Jia et al. (2021) developed a turbulence diffusion term for aerosols and embedded it into a mesoscale model for the first time.

The high wind speed of the LLJs is crucial to achieving long-range transport of dust. The underestimation of the jet core speed implies a weakened region-to-region transport simulation. In addition, parameterization of the mineral dust budget depends on the simulation of the downward momentum flux (Pérez et al., 2011; Knippertz and Todd, 2012). However, a weakened LLJ strength can lead to an underestimation of the dust emissions, as the surface wind speed is not strong enough to reach the dust emission threshold. Besides, the overestimation of LLJ strength and vertical mixing at night alters the diurnal variation of the wind field in the ABL (Sandu et al., 2013).

The tropospheric O_3 concentration during the daytime can be simulated in accordance with the field observations, although distinct differences exist at night. The primary reason for this is the representation of the nighttime turbulence transport by the LLJs. Although the horizontal structure of the LLJs can be reasonably simulated, the results of the simulated LLJ vertical profiles are far from satisfactory. Sensitivity simulations (Hu et al., 2012) elucidated that longer turbulence lengths and long-tail stability functions are more suitable for O_3 and LLJs modelling, implying that turbulence mixing during nighttime requires careful treatment.

TABLE 1 Summary of main studies (mostly after 2012) on the LLJs and chemical species transport in different regions.

Research focus	Regions and references
Dust	Africa: Knippertz and Todd, (2012); Fiedler et al. (2013); Allen and Washington, (2014); Gläser et al. (2015); Schepanski et al. (2015); Kalenderski and Stenchikov, (2016); Wiggs et al. (2022)
	East Asia: Ge et al. (2016); Zhou et al. (2019); Han et al. (2022)
	West Asia: Gandham et al. (2022) the dust belt: Shi et al. (2021); Tindan et al. (2022)
$PM_{2.5}$	Asia: Chen et al. (2018); Wei et al. (2018); Wei et al. (2020); Ren et al. (2019a); Ren et al. (2019b); Ren et al. (2019c); Li et al. (2019); Miao et al. (2019); Jin et al. (2020); Li et al. (2020); Li et al. (2021); Wei et al. (2022); Mei et al. (2022)
	South America: Martin et al. (2018); Rodriguez-Gomezetal et al. (2022)
	North America: Dreessen et al. (2016); Wang et al. (2018)
O_3	Europe: Kulkarni et al. (2016); Klein et al. (2019)
	North America: Hu et al. (2012); Hu et al. (2013b); Ryan, (2004); Caputi et al. (2019)
	South America: Martins et al. (2018); Melo et al. (2019)
	Asia: Zhu et al. (2020); Zhao et al. (2022)
CO_2	Africa: Han et al. (2015)
Black Carbon	South America: Martins et al. (2018)
Sulphur and NO	Europe: Arkadievi Obolkin et al. (2014)

Turbulence intermittency has still not been effectively considered in the numerical models, although field observations have confirmed its importance in the transport of O_3 (Salmond and McKendry, 2002; Salmond and McKendry, 2005), $PM_{2.5}$ (Wei et al., 2018; Ren et al., 2019b), and CO_2 (ElMadany et al., 2014; Hicks et al., 2015). The classical Monin—Obukhov similarity theory (MOST, Monin and Obukhov, 1954), which has been widely adopted in atmospheric and environmental models, is only suitable for unstable ABL or traditional surface-forced SBL. Large uncertainties may exist when applying the MOST-based models to intermittent turbulence. Furthermore, no overarching agreement has yet been reached an appropriate method to describe the turbulence intermittency in the ABL. The traditional Fourier transform cannot be applied to the analysis of non-linear and non-stationary turbulence bursts. The wavelet analysis was used to separate the LLJ-induced intermittent turbulence during O_3 periods (Salmond, 2004). Based on the self-adaptive Hilbert—Huang transform (Huang et al., 1998), several indexes have been proposed to quantify the strength of the turbulence intermittency (Wei et al., 2018; Ren et al., 2019b; Ren et al., 2019c).

7 Summary and discussion

This review summarized the current state of interactions between the LLJs and pollutants from the perspective of observations, models, and mechanisms. With the literature of the three most-studied species (i.e., mineral dust, $PM_{2.5}$, and O_3), the effects of the LLJs can be divided into long-range horizontal transport and local vertical dispersion. Recent works have been listed in Table 1. The fast-moving stream of the LLJs is an important pathway for the region-to-region transport of moisture, precursors, and pollutants. Whether the LLJ is a boon or bane for the local air quality depends on the season, wind direction, and location of the pollutant sources. Recently, vertical mixing induced by the LLJs has been under the spotlight for explaining the local variation of pollutant levels. The downward transport of intermittent turbulence resulting from the LLJs is crucial for re-coupling nocturnal SBLs, enhancing vertical mixing, transporting pollutants downward/upward, and worsening/improving the air quality. What the three species have in common is that the downward momentum due to LLJs strengthens the turbulence mixing and pollutants transport. Specifically, O_3 dissipates downward from the aloft "reservoir", leading to O_3 peaks at night. The mineral dust was uplifted from the underground the next morning. The $PM_{2.5}$ is mostly transported upward and diluted over a deeper layer. The intermittency of LLJ-induced turbulence perplexes the mechanism of the vertical dissipation of pollutants.

In the future, high-resolution turbulence and pollutant observational data is needed to investigate the complicated vertical LLJ—pollutant interaction and establish the turbulence diffusion relationship of pollutants. Most current work is based on surface observations of pollutants and turbulence. However, to study the fine structure of the SBL, continuous profiles are required. A meteorological tower can provide multilevel observations, however, its spatial resolution is far from satisfactory. Radiosonde data suffers from a low time resolution. Carrying out intensive observation period experiments can be a good way for addressing these problems. Remote sensing technologies, such as Lidar are helpful methods to obtain continuous observation. Furthermore, the current findings were mostly obtained from one site. There is a large scope for further research on the spatial distribution of intermittent turbulence and pollutants based on multi-site observation.

The numerical models perform well in the simulation of the horizontal structure of the LLJs, while the vertical distribution remains unsatisfactory. PBL schemes need to be further improved for better representing nighttime processes. Accurate simulation of the LLJ profiles and development is

crucial for nocturnal turbulence mixing. In addition, present models do not consider the turbulence intermittency, and most studies on the LLJ-burst interplay focus on O_3 and $PM_{2.5}$. How this mechanism impacts the variation of other chemical species, such as nitrogen oxides (NO), VOCs, and carbon monoxide, remains to be assessed.

Author contributions

All authors listed have made a substantial, direct, and intellectual contribution to the work and approved it for publication.

Funding

This work is supported by the National Natural Science Foundation of China (42090031, 92044301, 91544216, 41705003) and Natural Science Foundation of Liaoning Province (No.2020-MS-350).

Conflict of interest

The authors declare that the research was conducted in the absence of any commercial or financial relationships that could be construed as a potential conflict of interest.

Publisher's note

All claims expressed in this article are solely those of the authors and do not necessarily represent those of their affiliated organizations, or those of the publisher, the editors and the reviewers. Any product that may be evaluated in this article, or claim that may be made by its manufacturer, is not guaranteed or endorsed by the publisher.

References

Allen, C. J. T., Washington, R., and Engelstaedter, S. (2013). Dust emission and transport mechanisms in the central Sahara: Fennec groundbased observations from bordj badji mokhtar, june 2011. *J. Geophys. Res. Atmos.* 118, 6212–6232. doi:10.1002/jgrd.50534

Allen, C. J., and Washington, R. (2014). The low-level jet dust emission mechanism in the central Sahara: Observations from bordj-badji mokhtar during the june 2011 fennec intensive observation period. *J. Geophys. Res. Atmos.* 119 (6), 2990–3015. doi:10.1002/2013jd020594

Ansmann, A., Tesche, M., Knippertz, P., Bierwirth, E., Althausen, D., Müller, D., et al. (2009). Vertical profiling of convective dust plumes in southern Morocco during SAMUM. *Tellus B* 61 (1), 340–353. doi:10.3402/tellusb.v61i1.16833

Arkadievich Obolkin, V., Lvovich Potemkin, V., Leonidovich Makukhin, V., Vladimirovna Chipanina, Y., and Iozovna Marinayte, I. (2014). Low-level atmospheric jets as main mechanism of long-range transport of power plant plumes in the Lake Baikal Region. *Int. J. Environ. Stud.* 71 (3), 391–397. doi:10.1080/00207233.2014.918396

Banta, R. M., Mahrt, L., Vickers, D., Sun, J., Balsley, B. B., Pichugina, Y. L., et al. (2007). The very stable boundary layer on nights with weak low-level jets. *J. Atmos. Sci.* 64 (9), 3068–3090. doi:10.1175/jas4002.1

Bao, J. W., Michelson, S. A., Persson, P. O. G., Djalalova, I. V., and Wilczak, J. M. (2008). Observed and WRF-simulated low-level winds in a high-ozone episode during the Central California Ozone Study. *J. Appl. Meteorology Climatol.* 47 (9), 2372–2394. doi:10.1175/2008JAMC1822.1

Blackadar, A. K. (1957). Boundary layer wind maxima and their significance for the growth of nocturnal inversions. *Bull. Am. Meteorological Soc.* 38, 283–290. doi:10.1175/1520-0477-38.5.283

Caputi, D. J., Faloona, I., Trousdell, J., Smoot, J., Falk, N., and Conley, S. (2019). Residual layer ozone, mixing, and the nocturnal jet in California's San Joaquin Valley. *Atmos. Chem. Phys.* 19 (7), 4721–4740. doi:10.5194/acp-19-4721-2019

Čavlina Tomašević, I., Cheung, K. K., Vučetić, V., Fox-Hughes, P., Horvath, K., Telišman Prtenjak, M., et al. (2022). The 2017 Split wildfire in Croatia: Evolution and the role of meteorological conditions. *Nat. Hazards Earth Syst. Sci. Discuss.* 22, 3143–3165. doi:10.5194/nhess-22-3143-2022

Chen, Y., An, J., Sun, Y., Wang, X., Qu, Y., Zhang, J., et al. (2018). Nocturnal low-level winds and their impacts on particulate matter over the Beijing area. *Adv. Atmos. Sci.* 35 (12), 1455–1468. doi:10.1007/s00376-018-8022-9

Cuesta, J., Lavaysse, C., Flamant, C., Mimouni, M., and Knippertz, P. (2010). Northward bursts of the west african monsoon leading to rainfall over the hoggar massif, Algeria. *Q. J. R. Meteorol. Soc.* 136, 174–189. doi:10.1002/qj.439

Das, M., and Aneja, V. P. (1994). Measurements and analysis of concentrations of gaseous hydrogen peroxide and related species in the rural central piedmont region of North Carolina. *Atmos. Environ.* 28, 2473–2483. doi:10.1016/1352-2310(94)90398-0

Dominici, F., Greenstone, M., and Sunstein, C. R. (2014). Particulate matter matters. *Science* 344 (6181), 257–259. doi:10.1126/science.1247348

Dreessen, J., Sullivan, J., and Delgado, R. (2016). Observations and impacts of transported Canadian wildfire smoke on ozone and aerosol air quality in the Maryland region on June 9–12, 2015. *J. Air & Waste Manag. Assoc.* 66 (9), 842–862. doi:10.1080/10962247.2016.1161674

Du, Q., Zhao, C., Zhang, M., Dong, X., Chen, Y., Liu, Z., et al. (2020). Modeling diurnal variation of surface PM_{2.5} concentrations over East China with WRF-chem: Impacts from boundary-layer mixing and anthropogenic emission. *Atmos. Chem. Phys.* 20, 2839–2863. doi:10.5194/acp-20-2839-2020

Du, Y., Zhang, Q., Ying, Y., and Yang, Y. (2012). Characteristics of low-level jets in shanghai during the 2008–2009 warm seasons as inferred from wind profiler radar data. *J. Meteorological Soc. Jpn. Ser. II* 90 (6), 891–903. doi:10.2151/jmsj.2012-603

Fiedler, S., Schepanski, K., Heinold, B., Knippertz, P., and Tegen, I. (2013). Climatology of nocturnal low-level jets over North Africa and implications for modeling mineral dust emission. *J. Geophys. Res. Atmos.* 118 (12), 6100–6121. doi:10.1002/jgrd.50394

Gandham, H., Dasari, H. P., Karumuri, A., Ravuri, P. M. K., and Hoteit, I. (2022). Three-dimensional structure and transport pathways of dust aerosols over West Asia. *npj Clim. Atmos. Sci.* 5 (1), 45–15. doi:10.1038/s41612-022-00266-2

Ganzeveld, L., Eerdekens, G., Feig, G., Fischer, H., Harder, H., Konigstedt, R., et al. (2008). Surface and boundary layer exchanges of volatile organic compounds, nitrogen oxides and ozone during the GABRIEL campaign. *Atmos. Chem. Phys.* 8, 6223–6243. doi:10.5194/acp-8-6223-2008

Ge, J. M., Liu, H., Huang, J., and Fu, Q. (2016). Taklimakan Desert nocturnal low-level jet: Climatology and dust activity. *Atmos. Chem. Phys.* 16 (12), 7773–7783. doi:10.5194/acp-16-7773-2016

Gebauer, J. G., and Shapiro, A. (2019). Clarifying the baroclinic contribution to the Great Plains low-level jet frequency maximum. *Mon. Weather Rev.* 147 (9), 3481–3493. doi:10.1175/mwr-d-19-0024.1

Gläser, G., Wernli, H., Kerkweg, A., and Teubler, F. (2015). The transatlantic dust transport from north Africa to the americas—its characteristics and source regions. *J. Geophys. Res. Atmos.* 120 (21), 11231–11252. doi:10.1002/2015jd023792

Gultepe, I., Sharman, R., Williams, P. D., Zhou, B., Ellrod, G., Minnis, P., et al. (2019). A review of high impact weather for aviation meteorology. *Pure Appl. Geophys.* 176 (5), 1869–1921. doi:10.1007/s00024-019-02168-6

Haikin, N., and Castelli, S. T. (2022). On the effect of a low-level jet on atmospheric pollutant dispersion: A case study over a coastal complex domain, employing high-resolution modelling. *Boundary-Layer Meteorol.* 182 (3), 471–495. doi:10.1007/s10546-021-00661-x

Han, Z., Ge, J., Chen, X., Hu, X., Yang, X., and Du, J. (2022). Dust activities induced by nocturnal low-level jet over the taklimakan Desert from WRF-chem simulation. *J. Geophys. Res. Atmos.* 127 (12), e2021JD036114. doi:10.1029/2021jd036114

Hicks, B. B., O'Dell, D. L., Eash, N. S., and Sauer, T. J. (2015). Nocturnal intermittency in surface CO2 concentrations in sub-Saharan Africa. *Agric. For. Meteorology* 200, 129–134. doi:10.1016/j.agrformet.2014.09.007

Hu, X. M., Doughty, D. C., Sanchez, K. J., Joseph, E., and Fuentes, J. D. (2012). Ozone variability in the atmospheric boundary layer in Maryland and its implications for vertical transport model. *Atmos. Environ.* 46, 354–364. doi:10.1016/j.atmosenv.2011.09.054

Hu, X. M., Klein, P. M., Xue, M., Lundquist, J. K., Zhang, F., and Qi, Y. (2013a). Impact of low-level jets on the nocturnal urban heat island intensity in Oklahoma City. *J. Appl. Meteorology Climatol.* 52 (8), 1779–1802. doi:10.1175/jamc-d-12-0256.1

Hu, X. M., Klein, P. M., Xue, M., Zhang, F., Doughty, D. C., Forkel, R., et al. (2013b). Impact of the vertical mixing induced by low-level jets on boundary layer ozone concentration. *Atmos. Environ.* 70, 123–130. doi:10.1016/j.atmosenv.2012.12.046

Huang, N. E., Shen, Z., Long, S. R., Wu, M. C., Shih, H. H., Zheng, Q., et al. (1998). The empirical mode decomposition and the Hilbert spectrum for nonlinear and non-stationary time series analysis. *Proc. R. Soc.* 454, 903–995. doi:10.1098/rspa.1998.0193

Janjic, Z. I. (2002). Nonsingular implementation of the Mellor–Yamada level 2.5 scheme in the NCEP meso model. *NCEP Off. note* 437, 61.

Jia, M., Yuan, J., Wang, C., Xia, H., Wu, Y., Zhao, L., et al. (2019). Long-lived high-frequency gravity waves in the atmospheric boundary layer: Observations and simulations. *Atmos. Chem. Phys.* 19 (24), 15431–15446. doi:10.5194/acp-19-15431-2019

Jia, W., and Zhang, X. (2020). The role of the planetary boundary layer parameterization schemes on the meteorological and aerosol pollution simulations: A review. *Atmos. Res.* 239, 104890. doi:10.1016/j.atmosres.2020.104890

Jia, W., Zhang, X., Zhang, H., and Ren, Y. (2021). Application of turbulent diffusion term of aerosols in mesoscale model. *Geophys. Res. Lett.* 48 (11), e2021GL093199. doi:10.1029/2021gl093199

Jin, X., Cai, X., Yu, M., Song, Y., Wang, X., Kang, L., et al. (2020). Diagnostic analysis of wintertime PM2. 5 pollution in the North China Plain: The impacts of regional transport and atmospheric boundary layer variation. *Atmos. Environ.* 224, 117346. doi:10.1016/j.atmosenv.2020.117346

Ju, T., Wu, B., Wang, Z., Liu, J., Chen, D., and Zhang, H. (2020). Relationships between low-level jet and low visibility associated with precipitation, air pollution, and fog in Tianjin. *Atmosphere* 11 (11), 1197. doi:10.3390/atmos11111197

Kalenderski, S., and Stenchikov, G. (2016). High-resolution regional modeling of summertime transport and impact of African dust over the Red Sea and Arabian Peninsula. *J. Geophys. Res. Atmos.* 121 (11), 6435–6458. doi:10.1002/2015jd024480

King, J. A., Engelstaedter, S., Washington, R., and Munday, C. (2021). Variability of the Turkana low-level jet in reanalysis and models: Implications for rainfall. *J. Geophys. Res. Atmos.* 126 (10), e2020JD034154. doi:10.1029/2020jd034154

Klein, A., Ravetta, F., Thomas, J. L., Ancellet, G., Augustin, P., Wilson, R., et al. (2019). Influence of vertical mixing and nighttime transport on surface ozone variability in the morning in Paris and the surrounding region. *Atmos. Environ.* 197, 92–102. doi:10.1016/j.atmosenv.2018.10.009

Knippertz, P., and Todd, M. C. (2012). Mineral dust aerosols over the Sahara: Meteorological controls on emission and transport and implications for modeling. *Rev. Geophys.* 50, RG1007. doi:10.1029/2011rg000362

Kulkarni, P. S., Dasari, H. P., Sharma, A., Bortoli, D., Salgado, R., and Silva, A. M. (2016). Nocturnal surface ozone enhancement over Portugal during winter: Influence of different atmospheric conditions. *Atmos. Environ.* 147, 109–120. doi:10.1016/j.atmosenv.2016.09.056

Li, Q., Wu, B., Liu, J., Zhang, H., Cai, X., and Song, Y. (2020). Characteristics of the atmospheric boundary layer and its relation with PM2.5 during haze episodes in winter in the North China Plain. *Atmos. Environ.* 223, 117265. doi:10.1016/j.atmosenv.2020.117265

Li, Q., Zhang, H., Cai, X., Song, Y., and Zhu, T. (2021). The impacts of the atmospheric boundary layer on regional haze in North China. *npj Clim. Atmos. Sci.* 4 (1), 9–10. doi:10.1038/s41612-021-00165-y

Li, X., Hu, X. M., Ma, Y., Wang, Y., Li, L., and Zhao, Z. (2019). Impact of planetary boundary layer structure on the formation and evolution of air-pollution episodes in Shenyang, Northeast China. *Atmos. Environ.* 214, 116850. doi:10.1016/j.atmosenv.2019.116850

Lima, D. C., Soares, P. M., Semedo, A., Cardoso, R. M., Cabos, W., and Sein, D. V. (2019). A climatological analysis of the Benguela coastal low-level jet. *J. Geophys. Res. Atmos.* 124 (7), 3960–3978. doi:10.1029/2018jd028944

Martins, L. D., Hallak, R., Alves, R. C., de Almeida, D. S., Squizzato, R., Moreira, C. A., et al. (2018). Long-range transport of aerosols from biomass burning over southeastern South America and their implications on air quality. *Aerosol Air Qual. Res.* 18 (7), 1734–1745. doi:10.4209/aaqr.2017.11.0545

Mei, M., Ding, Y., Wang, Z., Liu, Y., and Zhang, Y. (2022). Effects of the East Asian subtropical westerly jet on winter persistent heavy pollution in the Beijing–Tianjin–Hebei region. *Int. J. Climatol.* 42 (5), 2950–2964. doi:10.1002/joc.7400

Melo, A. M., Dias-Junior, C. Q., Cohen, J. C., Sá, L. D., Cattanio, J. H., and Kuhn, P. A. (2019). Ozone transport and thermodynamics during the passage of squall line in Central Amazon. *Atmos. Environ.* 206, 132–143. doi:10.1016/j.atmosenv.2019.02.018

Miao, Y., Guo, J., Liu, S., Wei, W., Zhang, G., Lin, Y., et al. (2018). The climatology of low-level jet in Beijing and Guangzhou, China. *J. Geophys. Res. Atmos.* 123 (5), 2816–2830. doi:10.1002/2017jd027321

Miao, Y., Liu, S., Sheng, L., Huang, S., and Li, J. (2019). Influence of boundary layer structure and low-level jet on PM2.5 pollution in beijing: A case study. *Int. J. Environ. Res. public health* 16 (4), 616. doi:10.3390/ijerph16040616

Monin, A., and Obukhov, A. (1954). Basic laws of turbulent mixing in the surface layer of the atmosphere. *Contrib. Geophys Inst. Acad. Sci. USSR* 151, 163–187.

Pérez, C., Haustein, K., Janjic, Z., Jorba, O., Huneeus, N., Baldasano, J. M., et al. (2011). Atmospheric dust modeling from meso to global scales with the online NMMB/BSC-Dust model - Part 1: Model description, annual simulations and evaluation. *Atmos. Chem. Phys.* 11, 13001–13027. doi:10.5194/acp-11-13001-2011

Reitebuch, O., Strassburger, A., Emeis, S., and Kuttler, W. (2000). Nocturnal secondary ozone concentration maxima analysed by sodar observations and surface measurements. *Atmos. Environ.* 34 (25), 4315–4329. doi:10.1016/s1352-2310(00)00185-0

Ren, Y., Zhang, H., Wei, W., Cai, X., Song, Y., and Kang, L. (2019a). A study on atmospheric turbulence structure and intermittency during heavy haze pollution in the Beijing area. *Sci. China Earth Sci.* 62 (12), 2058–2068. doi:10.1007/s11430-019-9451-0

Ren, Y., Zhang, H., Wei, W., Wu, B., Cai, X., and Song, Y. (2019b). [Standards and quality control points of alginate-based medical devices]. *Atmos. Chem. Phys.* 19 (2), 1041–1044. doi:10.7507/1002-1892.201812002

Ren, Y., Zhang, H., Wei, W., Wu, B., Liu, J., Cai, X., et al. (2019c). Comparison of the turbulence structure during light and heavy haze pollution episodes. *Atmos. Res.* 230, 104645. doi:10.1016/j.atmosres.2019.104645

Ren, Y., Zhang, H., Zhang, X., Wei, W., Li, Q., Wu, B., et al. (2021). Quantitative verification of the turbulence barrier effect during heavy haze pollution events. *Sci. Total Environ.* 753, 045005. doi:10.1088/2515-7620/ac6381

Rodríguez-Gómez, C., Echeverry, G., Jaramillo, A., and Ladino, L. A. (2022). The negative impact of biomass burning and the Orinoco low-level jet on the air quality of the Orinoco River Basin. *Atmósfera* 35 (3), 497–520. doi:10.20937/ATM.52979

Ryan, W. F. (2004). *The low level jet in Maryland: Profiler observations and preliminary climatology*. Maryland: Dept. of the Environment Rep, 43.

Salmond, J. A., and McKendry, I. G. (2005). A review of turbulence in the very stable nocturnal boundary layer and its implications for air quality. *Prog. Phys. Geogr.* 29 (2), 171–188. doi:10.1191/0309133305pp442ra

Salmond, J. A. (2004). Wavelet analysis of intermittent turbulence in a very stable nocturnal boundary layer: Implications for the vertical mixing of ozone. *Boundary-Layer Meteorol.* 114 (3), 463–488. doi:10.1007/s10546-004-2422-3

Salmond, J., and McKendry, I. G. (2002). Secondary ozone maxima in a very stable nocturnal boundary layer: Observations from the lower fraser valley, BC. *Atmos. Environ.* 36 (38), 5771–5782. doi:10.1016/s1352-2310(02)00698-2

Samson, P. J. (1978). Nocturnal ozone maxima. *Atmos. Environ.* 12 (4), 951–955. doi:10.1016/0004-6981(78)90035-5

Sánchez, M. P., Pereira de Oliveira, A., Varona, R. P., Tito, J. V., Codato, G., Ynoue, R. Y., et al. (2022). Observational investigation of the low-level jets in the metropolitan region of São Paulo, Brazil. *Earth Space Sci.* 9, e2021EA002190. doi:10.1029/2021ea002190

Sandu, I., Beljaars, A., Bechtold, P., Mauritsen, T., and Balsamo, G. (2013). Why is it so difficult to represent stably stratified conditions in numerical weather prediction (NWP) models? *J. Adv. Model. Earth Syst.* 5, 117–133. doi:10.1002/jame.20013

Schepanski, K., Knippertz, P., Fiedler, S., Timouk, F., and Demarty, J. (2015). The sensitivity of nocturnal low-level jets and near-surface winds over the Sahel to model resolution, initial conditions and boundary-layer set-up. *Q. J. R. Meteorological Soc.* 141 (689), 1442–1456. doi:10.1002/qj.2453

Schepanski, K., Tegen, I., Todd, M., Heinold, B., Bönisch, G., Laurent, B., et al. (2009). Meteorological processes forcing Saharan dust emission inferred from MSG-SEVIRI observations of subdaily dust source activation and numerical models. *J. Geophys. Res.* 114, D10201. doi:10.1029/2008JD010325

Shi, L., Zhang, J., Yao, F., Zhang, D., and Guo, H. (2021). Drivers to dust emissions over dust belt from 1980 to 2018 and their variation in two global warming phases. *Sci. Total Environ.* 767, 144860. doi:10.1016/j.scitotenv.2020.144860

Smith, E. N., Gebauer, J. G., Klein, P. M., Fedorovich, E., and Gibbs, J. A. (2019). The Great Plains low-level jet during PECAN: Observed and simulated characteristics. *Mon. Weather Rev.* 147 (6), 1845–1869. doi:10.1175/mwr-d-18-0293.1

Smith, E. N., Gibbs, J. A., Fedorovich, E., and Klein, P. M. (2018). WRF Model study of the Great Plains low-level jet: Effects of grid spacing and boundary layer parameterization. *J. Appl. Meteorology Climatol.* 57 (10), 2375–2397. doi:10.1175/jamc-d-17-0361.1

Starn, T. K., Shepson, P. B., Bertman, S. B., Riemer, D. D., Zika, R. G., and Olszyna, K. (1998). Nighttime isoprene chemistry at an urban-impacted forest site. *J. Geophys. Res. Atmos.* 103 (17), 22437–22447. doi:10.1029/98jd01201

Stull, R. B. (1988). *An introduction to boundary layer meteorology*. Dordrecht: Kluwer Academic Publishers.

Tindan, J. Z. O., Jin, Q., and Pu, B. (2022). Understanding day-night differences in dust activities over the dust belt of North Africa, the Middle East, and Asia. *Atmos. Chem. Phys. Discuss.*, 1–47. doi:10.5194/acp-2022-490

Todd, M. C., Washington, R., Raghavan, S., Lizcano, G., and Knippertz, P. (2008). Regional model simulations of the bodélé low-level jet of northern Chad during the bodélé dust experiment (BoDEx 2005). *J. Clim.* 21 (5), 995–1012. doi:10.1175/2007JCLI1766.1

Tuononen, M., O'Connor, E. J., Sinclair, V. A., and Vakkari, V. (2017). Low-level jets over Utö, Finland, based on Doppler lidar observations. *J. Appl. Meteorology Climatol.* 56 (9), 2577–2594. doi:10.1175/jamc-d-16-0411.1

Udina, M., Soler, M. R., Olid, M., Jiménez-Esteve, B., and Bech, J. (2020). Pollutant vertical mixing in the nocturnal boundary layer enhanced by density currents and low-level jets: Two representative case studies. *Boundary-Layer Meteorol.* 174 (2), 203–230. doi:10.1007/s10546-019-00483-y

van de Wiel, B. J. H., Moene, A. F., Steeneveld, G. J., Baas, P., Bosveld, F. C., and Holtslag, A. A. M. (2010). A conceptual view on inertial oscillations and nocturnal low-level jets. *J. Atmos. Sci.* 67 (8), 2679–2689. doi:10.1175/2010JAS3289.1

Wainwright, C. E., Stepanian, P. M., and Horton, K. G. (2016). The role of the US Great Plains low-level jet in nocturnal migrant behavior. *Int. J. biometeorology* 60 (10), 1531–1542. doi:10.1007/s00484-016-1144-9

Wang, S. C., Wang, Y., Estes, M., Lei, R., Talbot, R., Zhu, L., et al. (2018). Transport of central American fire emissions to the US Gulf coast: Climatological pathways and impacts on ozone and PM2. 5. *J. Geophys. Res. Atmos.* 123 (15), 8344–8361. doi:10.1029/2018jd028684

Wei, W., Zhang, H., Cai, X., Song, Y., Bian, Y., Xiao, K., et al. (2020). Influence of intermittent turbulence on air pollution and its dispersion in winter 2016/2017 over Beijing, China. *J. Meteorological Res.* 34 (1), 176–188. doi:10.1007/s13351-020-9128-4

Wei, W., Zhang, H. S., Schmitt, F. G., Huang, Y. X., Cai, X. H., Song, Y., et al. (2017). Investigation of turbulence behaviour in the stable boundary layer using arbitrary-order Hilbert spectra. *Boundary-Layer Meteorol.* 163 (2), 311–326. doi:10.1007/s10546-016-0227-9

Wei, W., Zhang, H. S., and Ye, X. X. (2014). Comparison of low-level jets along the north coast of China in summer. *J. Geophys. Res. Atmos.* 119 (16), 9692–9706. doi:10.1002/2014jd021476

Wei, W., Zhang, H., Wu, B., Huang, Y., Cai, X., Song, Y., et al. (2018). Intermittent turbulence contributes to vertical dispersion of PM_{2.5} in the North China plain: Cases from tianjin. *Atmos. Chem. Phys.* 18 (17), 12953–12967. doi:10.5194/acp-18-12953-2018

Wei, Z., Zhang, H., Wei, W., Zhang, X., Cai, X., Song, Y., et al. (2022). Mechanism of the effect of vertically propagating internal gravity waves on turbulence barrier and pollutant diffusion during heavy haze episodes. *Sci. Total Environ.* 845, 157349. doi:10.1016/j.scitotenv.2022.157349

Wexler, H. (1961). A boundary layer interpretation of the low-level jet. *Tellus* 13, 368–378. doi:10.1111/j.2153-3490.1961.tb00098.x

Wiggs, G. F., Baddock, M. C., Thomas, D. S., Washington, R., Nield, J. M., Engelstaedter, S., et al. (2022). Quantifying mechanisms of aeolian dust emission: Field measurements at etosha Pan, Namibia. *J. Geophys. Res. Earth Surf.* 127 (8), e2022JF006675. doi:10.1029/2022jf006675

Wimhurst, J. J., and Greene, J. S. (2019). Oklahoma's future wind energy resources and their relationship with the Central Plains low-level jet. *Renew. Sustain. Energy Rev.* 115, 109374. doi:10.1016/j.rser.2019.109374

Wu, B., Li, Z., Ju, T., and Zhang, H. (2020). Characteristics of Low-level jets during 2015–2016 and the effect on fog in Tianjin. *Atmos. Res.* 245, 105102. doi:10.1016/j.atmosres.2020.105102

Yang, J., Tang, Y., Han, S., Liu, J., Yang, X., and Hao, J. (2021). Evaluation and improvement study of the Planetary Boundary-Layer schemes during a high PM2. 5 episode in a core city of BTH region, China. *Sci. Total Environ.* 765, 142756. doi:10.1016/j.scitotenv.2020.142756

Yang, X., Wu, K., Wang, H., Liu, Y., Gu, S., Lu, Y., et al. (2020). Summertime ozone pollution in Sichuan Basin, China: Meteorological conditions, sources and process analysis. *Atmos. Environ.* 226, 117392. doi:10.1016/j.atmosenv.2020.117392

Zhao, D., Xin, J., Wang, W., Jia, D., Wang, Z., Xiao, H., et al. (2022). Effects of the sea-land breeze on coastal ozone pollution in the Yangtze River Delta, China. *Sci. Total Environ.* 807, 150306. doi:10.1016/j.scitotenv.2021.150306

Zhong, J., Zhang, X., Dong, Y., Wang, Y., Liu, C., Wang, J., et al. (2018). Feedback effects of boundary-layer meteorological factors on cumulative explosive growth of PM_{2.5} during winter heavy pollution episodes in Beijing from 2013 to 2016. *Atmos. Chem. Phys.* 18 (1), 247–258. doi:10.5194/acp-18-247-2018

Zhong, J., Zhang, X., Wang, Y., Sun, J., Zhang, Y., Wang, J., et al. (2017). Relative contributions of boundary-layer meteorological factors to the explosive growth of PM2. 5 during the red-alert heavy pollution episodes in Beijing in December 2016. *J. Meteorological Res.* 31 (5), 809–819. doi:10.1007/s13351-017-7088-0

Zhou, C., Mamtimin, A., Yang, F., Huo, W., Wang, M., Pan, H., et al. (2019). Dust uplift potential in the taklimakan Desert: An analysis based on different wind speed measurement intervals. *Theor. Appl. Climatol.* 137 (1), 1449–1456. doi:10.1007/s00704-018-2678-z

Zhu, X., Ma, Z., Li, Z., Wu, J., Guo, H., Yin, X., et al. (2020). Impacts of meteorological conditions on nocturnal surface ozone enhancement during the summertime in Beijing. *Atmos. Environ.* 225, 117368. doi:10.1016/j.atmosenv.2020.117368

frontiers | Frontiers in Environmental Science

TYPE Original Research
PUBLISHED 04 January 2023
DOI 10.3389/fenvs.2022.1028468

OPEN ACCESS

EDITED BY
Chaoyang Xue,
Laboratoire de physique et chimie de l'environnement et de l'Espace (LPC2E), France

REVIEWED BY
Qifan Liu,
University of Science and Technology of China, China
Li Zhou,
Sichuan University, China

*CORRESPONDENCE
Lingyan Wu,
wuly@cma.gov.cn
Junying Sun,
jysun@cma.gov.cn

SPECIALTY SECTION
This article was submitted to Atmosphere and Climate, a section of the journal Frontiers in Environmental Science

RECEIVED 26 August 2022
ACCEPTED 02 December 2022
PUBLISHED 04 January 2023

CITATION
Wang J, Wu L, Sun J, Zhang S and Zhong J (2023), Characteristics of $PM_{2.5}$ and secondary inorganic pollution formation during the heating season of 2021 in Beijing.
Front. Environ. Sci. 10:1028468.
doi: 10.3389/fenvs.2022.1028468

Characteristics of $PM_{2.5}$ and secondary inorganic pollution formation during the heating season of 2021 in Beijing

Jialing Wang[1], Lingyan Wu[1]*, Junying Sun[1]*, Sinan Zhang[1,2] and Junting Zhong[1]

[1]State Key Laboratory of Severe Weather & Key Laboratory of Atmospheric Chemistry of CMA, Chinese Academy of Meteorological Sciences, Beijing, China, [2]Shaanxi Meteorological Observatory, Xi'an, China

Water-soluble inorganic ions (WSIIs) were measured online in Beijing during the heating season of 2021, during which Beijing 2022 Olympic and Paralympic Winter Games were hosted. The characteristics of $PM_{2.5}$ and water-soluble inorganic ions were investigated in general, as well as during the clean period, polluted period, and Olympic and Paralympic Winter Games periods. It was found that most of the polluted episodes occurred under conditions of low wind speed, temperature inversion, and high relative humidity. The total mass concentration of water-soluble inorganic ions during the polluted period and the clean period accounted for 38.2% and 61.4% of the $PM_{2.5}$ mass concentration, respectively. Both the sulfur oxidation ratio (SOR) and nitrogen oxidation ratio (NOR) showed a strong relationship with relative humidity. During the polluted period, the concentrations of secondary aerosols such as sulfate, nitrate, and ammonium (SNA) increased significantly. Secondary transformation was enhanced compared with that in the clean period. A polluted process after a snowfall event was selected to explore the mechanism of sulfate and nitrate formation under high relative humidity. The results would be beneficial to understanding the causes of pollution and helping the government to formulate effective measures to control air pollution in winter.

KEYWORDS

$PM_{2.5}$, water-soluble inorganic ions, heating season, secondary transformation, sulfur oxidation ratio

1 Introduction

Fine particulate matter ($PM_{2.5}$, particles with an aerodynamic diameter of 2.5 μm or less) has a significant adverse impact on air quality, decreased visibility, global climate, and human health (Geng et al., 2021; Hu et al., 2021; Xu et al., 2022). In January 2013, a series of severe haze pollution episodes occurred in eastern China. The peak of $PM_{2.5}$ hourly average mass concentration in Beijing and its surrounding areas exceeded 500 μg/m^3 (Wang et al., 2013; Liu et al., 2015; Huang et al., 2016; Ren et al., 2021). Since then, the

Chinese government has taken many measures to improve air quality in the Beijing area. For example, stricter emission standards have been issued for coal power plants, industry, and road vehicles since 2013. Although air quality has improved overall and primary pollutants such as SO_2 have decreased significantly, however, $PM_{2.5}$ pollution still occurs frequently, especially in winter (Elser et al., 2016; Wang et al., 2019b; Lachatre et al., 2019; Cao et al., 2021; Huang et al., 2021; Li et al., 2021; Dong et al., 2022).

At present, the formation mechanism of haze pollution dominated by $PM_{2.5}$ is still unclear (Xie et al., 2022), which has become one of the difficulties in air pollution control in Beijing. Many researchers have explored the causes of $PM_{2.5}$ from different perspectives (Zhang et al., 2018b; Ma et al., 2018; Yang et al., 2018; Chen et al., 2019). Some studies have shown that the stagnation of meteorological conditions such as high relative humidity of the atmosphere, low mixed boundary layer height, low wind speed, and rapid chemical reactions leads to frequent pollution (Zhong et al., 2018a; Zhong et al., 2018b). On the other hand, some researchers proposed that the transformation of secondary aerosols promotes the explosive growth of $PM_{2.5}$ (Li et al., 2019; Wu et al., 2020; Dao et al., 2021; Rai et al., 2021; Wu et al., 2022). However, due to the diverse sources of air pollutants, complex chemical composition, and the coupling of various environmental factors, the polluted factors have not been fully quantified, and its chemical reaction mechanism is still controversial.

Water-soluble inorganic ions (WSIIs) are important chemical components in $PM_{2.5}$, accounting for up to 70% of the $PM_{2.5}$ mass concentration (Sun et al., 2019; Su et al., 2021). They exhibit strong hygroscopicity and can directly affect the acidity of atmospheric precipitation (Zhan et al., 2021). Among them, SO_4^{2-}, NO_3^-, and NH_4^+ (SNA) have a great influence on the atmospheric extinction coefficient and are important factors causing urban visibility degradation. Some studies showed that the high concentration of gaseous precursors tends to promote heterogeneous reactions on the $PM_{2.5}$ surface and forms secondary pollutants in haze days (Shao et al., 2019; Wang et al., 2020; Lei et al., 2021). Therefore, it is of great significance to study the concentration characteristics and sources of $PM_{2.5}$ and WSIIs for exploring the cause and control of $PM_{2.5}$.

In order to better understand the formation mechanism of $PM_{2.5}$ in Beijing, we conducted continuous observation of WSIIs in $PM_{2.5}$ during the heating season of 2021 in Beijing. $PM_{2.5}$ pollution is generally the worst during the heating season of a year (Pang et al., 2020; Dao et al., 2022). During this period, a high load of coal particles is generated and released into the atmosphere by the burning of coal for heating (Dao et al., 2022). In addition, low temperatures during the heating season slow down the dispersal of air pollutants, further exacerbating $PM_{2.5}$ pollution. The heating season of 2021 in Beijing lasted for about 5 months, from 28 October 2021 to 23 March 2022. During the heating season, Beijing hosted the XXIV Olympic Winter Games (from 4 February 2022 to 20 February 2022) and the XIII Paralympic Winter Games (from 4 March 2022 to 13 March 2022). Some studies evaluated the air pollution during the 2008 Olympic Games and proposed that atmospheric concentrations of PM_{10}, $PM_{2.5}$, NH_3, NO_2, SO_2, and the particulate ions NH_4^+, NO_3^-, SO_4^{2-}, Ca^{2+}, Mg^{2+}, and K^+ all decreased because of strict emission controls (Shen et al., 2011). While preparing and hosting the Winter Olympics, Beijing, Hebei, and other neighboring cities and provinces have been authorized to temporarily control enterprises and vehicles with heavy pollution, large emissions, and relatively little economic impact to create a favorable environment for hosting the games. Therefore, improved field observation on the Beijing's 2021 heating season can not only measure the impact of heating on $PM_{2.5}$ but also analyze the effects of emission reduction on $PM_{2.5}$. It would be beneficial to understanding the causes of pollution and helping the government to formulate effective measures to control air pollution.

2 Methods and data

2.1 Sampling site

Field measurements were performed on the roof of the building of the Chinese Academy of Meteorological Sciences (CAMS), approximately 53 m above the ground in the yard of the China Meteorological Administration (39°57′N, 116°19′E). The sampling site is located within the northwestern Third Ring Road of Beijing, around 200 m from the main road as shown in Figure 1. It is a typical urban observation station surrounded by traffic and residential emissions without an obvious industrial source nearby.

2.2 Instrument and measurements

From 25 October 2021 to 22 March 2022, major water-soluble inorganic ions (NO_3^-, SO_4^{2-}, Cl^-, NH_4^+, Na^+, K^+, Mg^{2+}, and Ca^{2+}) in $PM_{2.5}$ were continuously measured using an online Ambient Ion Monitor (AIM, model URG-9000D, United States) with 1-h time resolution. The ambient air was pumped through a $PM_{2.5}$ cyclone (at a flow rate of 3 l per minute), parallel plate denuder, steam-jet aerosol collector, aerosol sample collector, and then to two ion chromatographs (model ICS-1000, Dionex, United States) for chemical analysis (Hu et al., 2014). The interfering acidic and basic gases were removed in the parallel plate denuder by ultra-pure water with 0.018% vol H_2O_2. Aerosol particles were grown into liquid droplets inside the steam-jet aerosol collector due to supersaturated water vapor condensation on them. Also, these liquid droplets were collected by the aerosol sample collector until they were injected into ion chromatograph,

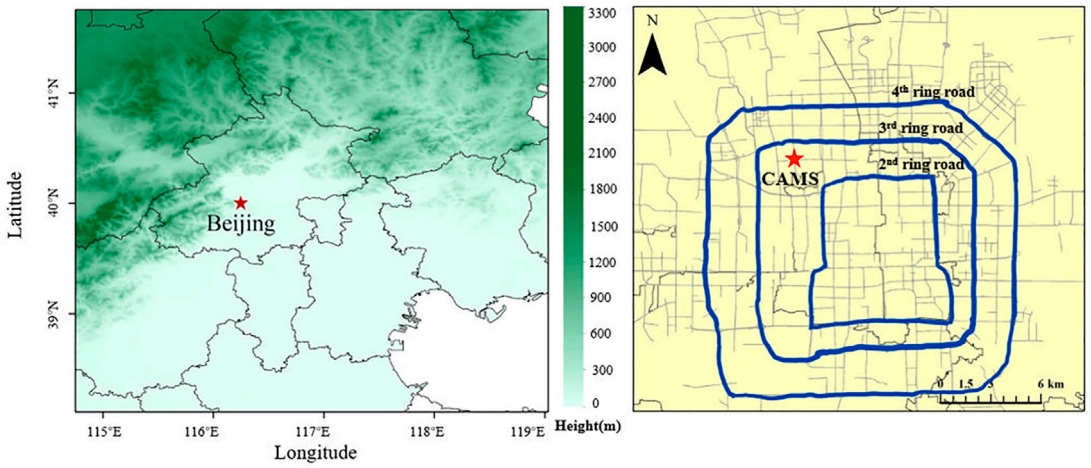

FIGURE 1
Geographical location of the observation site. The blue lines represent Beijing's main ring roads.

where the soluble species were analyzed. The chromatography conditions were as follows: CS12 analytical column, 22 mM MSA eluent, and cation self-regenerating suppressor for cations; AS22 analytical column, 4.5 mM Na_2CO_3/1.4 mM $NaHCO_3$ eluent, and anion self-regenerating suppressor for anions.

To ensure the accuracy of the measurements, the system was calibrated and maintained periodically. The temperature and pressure sensors were calibrated yearly to ensure the accuracy of sample volume. The ion chromatograph was calibrated monthly using standard anionic solutions (NO_3^-, SO_4^{2-}, and Cl^-) and cationic solutions (NH_4^+, Na^+, K^+, Mg^{2+}, and Ca^{2+}). Multi-point calibrations were considered qualified if the linear correlation of the standard curve of each ion was above 0.999. The minimum detection limit (MDL) was estimated by sampling zero air. The MDL for SO_4^{2-}, NO_3^-, and NH_4^+ was 0.0026, 0.047, and 0.013 μg/m^3, respectively. The MDL ranged from 0.002 to 0.307 μg/m^3 for other ions (Cl^-, Na^+, K^+, Mg^{2+}, and Ca^{2+}) (Hu et al., 2014). Membranes in the parallel plate denuder were changed once a month, and the in-line filters, which removed the insoluble particles in the samples, were replaced every 4–7 days.

The mass concentration of $PM_{2.5}$, PM_{10}, and trace gases (SO_2, O_3, and NO_2) used in this study was observed at the Guanyuan Monitoring Station by the China National Environmental Monitoring Center (CNEMC). The Guanyuan Monitoring Station is only 3 km away from our station. Both of them are Beijing urban stations with a similar surrounding environment.

The hourly meteorological data (air pressure, temperature, relative humidity, wind speed, and wind direction) in this study were obtained from the nearest meteorological data station, Haidian Meteorological Observation Station (No. 54399). It is about 5 km northwest to our sampling site, located inside Haidian Park, Beijing. To some extent, the data can represent meteorological conditions at our site.

All data in this study are reported in local time, 8 h ahead of UTC.

3 Results and discussion

3.1 Overview of the air quality during observation

In this study, the days with the daily average air quality index (AQI) greater than 100 were listed as the polluted days, while the days with the average daily AQI less than 50 were defined as the clean period. Time series of the daily mean AQI throughout the 2021 heating season is shown in Figure 2A. There were 17 polluted days (AQI >100) out of 147 days measured, according to the National Standard of the People's Republic of China "Ambient Air Quality Standard" (GB3095-2012). $PM_{2.5}$ was the major air pollutant in these 17 polluted days. Among them, three heavy polluted episodes were characterized by long duration and high daily mean value of AQI. The first heavy polluted episode occurred in the early heating season (from 15: 00 on 3 November 2021 to 03:00 on 6 November 2021) and lasted about 3 days with the hourly maximum AQI of 218. This polluted episode was preceded by a short period of a polluted process. The second polluted episode lasted more than 3 days from 23:00 on 21 January 2022 to 10:00 on 25 January 2022 with AQI rising from 112 to 215, which was about 2 weeks ahead of the start of the XXIV Olympic Winter Games. During the XXIV Olympic Winter Games, air quality was very good, with 10 days being excellent (0 < AQI <50) and 6 days being good (51 < AQI <100).

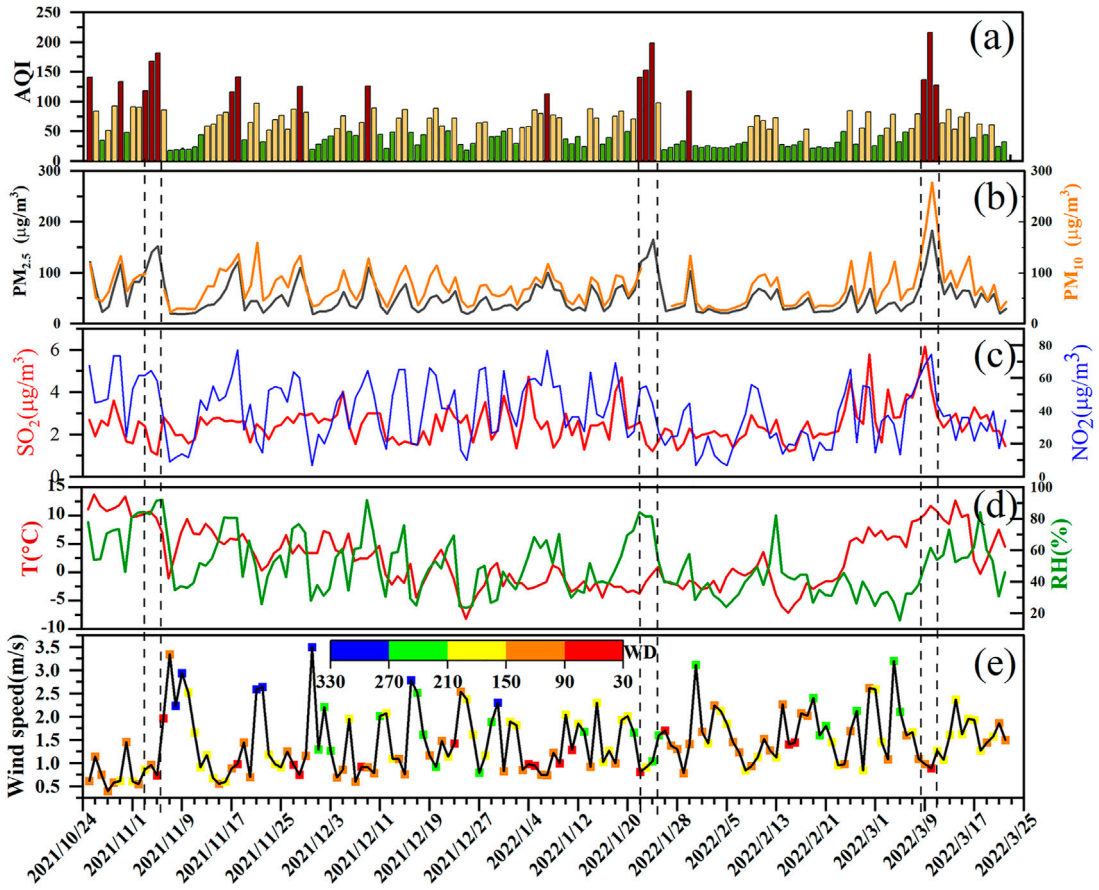

FIGURE 2
Time series of daily **(A)** mean air quality index (AQI); the green, yellow, and brown bars represent excellent day, good day, and polluted day, respectively; **(B)** time series of $PM_{2.5}$ and PM_{10} mass concentration; **(C)** SO_2 and NO_2 mass concentration; **(D)** ambient relative humidity (RH) and temperature (T); and **(E)** wind speed and wind direction (WD); three polluted episodes are highlighted by the black dashed lines.

The air quality during the XIII Paralympic Winter Games was not as good as that during XXIV Olympic Winter Games. There were only 2 days with excellent air quality. In addition, the third heavy polluted episode of the heating season occurred from 03:00 on 10 March 2022 to 03:00 on 11 March. This heavy polluted episode lasted for about 1 day, and the AQI reached its maximum for the entire heating season (hourly AQI reached 234). As shown in Figures 2B,C, the main pollutants in these three pollution episodes were $PM_{2.5}$ with high NO_2 concentrations.

3.2 Meteorological conditions

During the whole heating season of 2021 in Beijing, as shown in Figure 2D, the daily average temperature was low and the temperature span was large. This is shown in the summary of the hourly meteorological data in Table 1, and the mean temperature in the whole heating season was 2.4°C. The highest temperature reached 22.5°C, and the lowest temperature was as low as −10.9°C. The average temperature during the Olympic Winter Games was the lowest (−2.0°C), followed by the clean period (1.2°C) and polluted period (5.1°C). The average temperature during the Paralympic Winter Games was the highest, with a value of 8.5°C. In terms of wind speed, the whole heating season was dominated by light winds. Except for Paralympic Winter Games, the average wind speed was below 2.0 m/s during the clean period, polluted period, and Olympics Winter Games period. Particularly in the polluted period, the wind speed was much lower, and the average wind speed was only 1.0 m/s. As shown in Figure 2E, the polluted period was dominated by south and southwest winds, while the clean period was characterized by north winds, often fluctuating between 0.6 and 4.0 m/s. Winds from the southwest or southeast often bring high concentrations of $PM_{2.5}$, while clean air comes mostly from the northwest, effectively removing air pollution in Beijing (Li et al., 2021; Su et al., 2021).

TABLE 1 Hourly meteorological factors, hourly mass concentration of $PM_{2.5}$ and its water-soluble inorganic ions during the clean period, polluted period, Olympics Winter Games period, and Paralympics Winter Games period.

	Heating season			Clean period			Polluted period			Olympics Winter Games period			Paralympics Winter Games period		
	Min	Max	Mean	Min	Max	Mean	Min	Max	Mean	Min	Max	Mean	Min	Max	Mean
T (°C)	-10.9	22.5	2.4	-10.9	22.5	1.2	-8.5	21.1	5.1	-10.9	10.4	-2.0	-2.9	19.8	8.5
RH (%)	8.0	99.0	50.1	8.0	97.0	36.4	13.0	99.0	74.9	14.0	93.0	41.2	8.0	94.0	42.5
WS (m/s)	0.0	7.7	1.5	0.1	7.7	1.8	0.0	6.5	1.0	0.0	5.9	1.6	0.0	6.5	1.5
$PM_{2.5}$	2.0	201.0	36.9	2.0	48.0	10.8	36.0	201.0	109.8	4.0	97.0	23.3	4.0	195	61.4
NO_3^-	0.01	52.8	6.1	0.01	15.5	1.2	0.3	52.8	22.9	0.1	16.4	3.5	0.01	48.6	13.4
SO_4^{2-}	0.01	17.8	1.7	0.2	4.9	0.8	0.7	17.8	5.2	0.5	7.9	1.8	0.2	7.2	2.0
Cl^-	0.1	3.0	0.7	0.03	2.7	0.5	0.1	3.0	1.3	0.2	2.4	0.7	0.4	2.5	1.0
NH_4^+	0.1	19.2	1.9	0.01	5.5	0.3	0.1	19.2	8.0	0.1	4.3	1.1	0.1	13.0	3.7
Na^+	0.3	4.4	1.5	0.5	4.4	1.6	0.3	3.0	1.3	0.7	1.6	0.9	0.7	1.6	1.0
K^+	0.004	3.0	0.2	0.005	3.0	0.1	0.04	1.1	0.3	0.01	0.2	0.1	0.01	0.3	0.1
Mg^{2+}	0.008	2.4	0.2	0.006	2.4	0.2	0.02	1.0	0.3	0.1	0.6	0.1	0.1	0.6	0.3
Ca^{2+}	0.1	6.4	2.2	0.1	5.6	1.9	0.4	5.3	2.5	1.0	2.0	1.2	1.2	6.4	1.8

The mass concentration unit of $PM_{2.5}$ and water-soluble inorganic ions is $\mu g/m^3$.

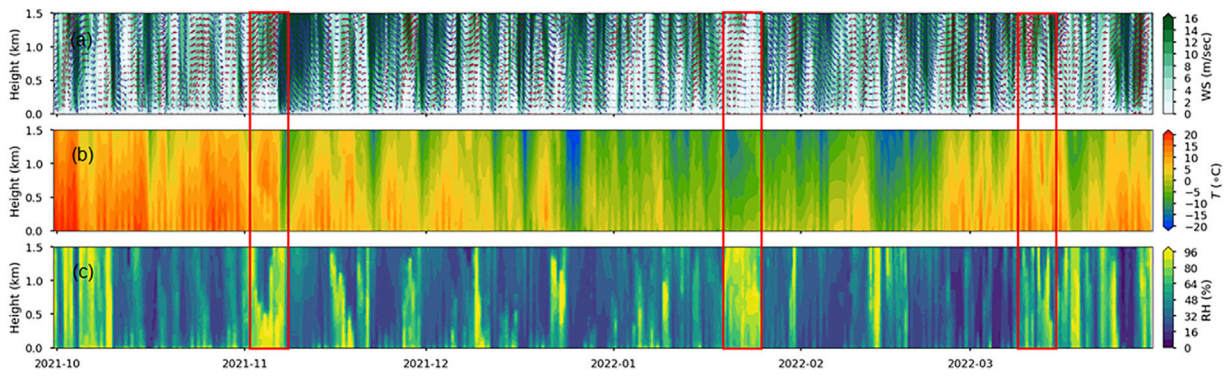

FIGURE 3
Time series of vertical distribution of meteorological factors including **(A)** wind speed; **(B)** temperature (T); and **(C)** relative humidity (RH) from 25 October 2021 to 22 March 2022; the solid red line represents the three polluted episodes.

It can be seen from Figure 2D that heavy pollution usually occurred with relatively high temperature or high humidity in winter. In the early heating season in Beijing (2 November 2021–6 November 2021), the first polluted episode occurred, during which the southwest wind was dominated, the hourly average temperature was 10.4°C, and the average RH was 87%. By the end of this polluted episode (23:00 on 6 November 2021), the wind turned to northwest, with the hourly maximum wind speed of 4.7 m/s, and then the air quality ameliorated. This is due to the fact that strong winds blow away pollutants quickly (Zhao et al., 2019; Han et al., 2020). The second polluted episode occurred after a snowfall on 20 January 2022. This episode lasted for more than 3 days (23:00 on 21 January 2022–10:00 on 25 January 2022), with the hourly average temperature which reached 11.1°C, RH which reached 81.8%, and the wind speed was only 1.1 m/s. Low wind speed was not conducive to the

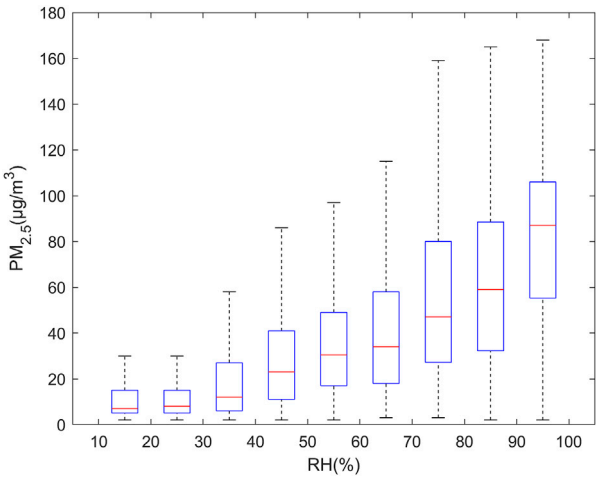

FIGURE 4
Relationship between $PM_{2.5}$ mass concentration and RH in the heating season.

diffusion of pollutants (Wu et al., 2020). The RH in the first and second polluted episodes was high (>80%). In the third polluted episode, the RH was around 60%. It can also be seen from Table 1 that the average RH in the polluted period was 1.5 times larger than the average RH of the whole heating season and 2.1 times larger than that in the clean period.

The vertical distribution of meteorological factors (wind speed, temperature, and relative humidity) from surface up to 1.5 km is shown in Figure 3. As shown in Figure 3A, the wind speed near the ground was low, indicating that it is not conducive to the diffusion of pollutants throughout the whole heating season. It is also worth noting that the air quality would deteriorate once the humidity increased. In Figure 3B, there was a significant temperature inversion in the first and third polluted episodes. As can be seen from Figure 3C, the RH near the ground was above 60% in the three polluted episodes and the early heating season when the pollution occurred frequently. In contrast, the RH in the clean periods was low, which further confirmed that the RH was higher in the polluted periods not only at the surface but also in the upper air.

3.3 $PM_{2.5}$ mass concentration

In this study, the characteristics of $PM_{2.5}$ mass concentration in the 2021 heating season in Beijing were explored. Table 1 shows the statistical results of hourly $PM_{2.5}$ mass concentration during the heating period including the polluted period, the clean period, the XXIV Olympic Winter Games period, and the XIII Paralympic Winter Games period. The hourly mean $PM_{2.5}$ mass concentration during the heating season was 36.9 μg/m^3, which was close to the excellent standard for $PM_{2.5}$ mass concentration (35.0 μg/m^3) in accordance with the Chinese National Ambient Air Quality Standard (GB 3095–2012). During the clean period, the hourly average mass concentration of $PM_{2.5}$ was 10.8 μg/m^3. During the heating period, the highest hourly mass concentration of $PM_{2.5}$ reached 201.0 μg/m^3, which was 5.7 times the national standard (GB3095-2012, 35.0 μg/m^3). While during the Olympic Winter Games, the hourly concentration of $PM_{2.5}$ ranged from 4.0 to 97.0 μg/m^3, with no obvious pollution, and the overall air quality was good, with an average mass concentration of 23.3 μg/m^3. The mass concentration of $PM_{2.5}$ was in the range of 4.0–195.0 μg/m^3 during the Paralympic Winter Games, and the average mass concentration was 61.4 μg/m^3, which was 2.6 times that of the Olympic Winter Games.

RH had a great influence on the formation of pollution; higher RH promoted the growth of the mass concentration of $PM_{2.5}$ (Wu et al., 2022). As displayed in Figure 4, $PM_{2.5}$ mass concentration increased with the increase in RH. When RH was below 40%, $PM_{2.5}$ mass concentration changed slowly with RH. However, when RH was greater than 40%, especially above 60%, $PM_{2.5}$ increased sharply with the increase in RH. Higher relative humidity was believed to increase the content of liquid water on the surface of particles and even cause deliquescence, thus promoting some aqueous-phase reactions on the aerosol surface (Herrmann et al., 2015; Wu et al., 2019). In this case, trace gases such as SO_2 and NO_2 in the atmosphere may be converted into secondary aerosols through aqueous-phase reactions, thus aggravating $PM_{2.5}$ pollution (Sun et al., 2013; Zhong et al., 2017).

3.4 Water-soluble inorganic ions (WSIIs)

$PM_{2.5}$ contains a large number of WSIIs including SO_4^{2-}, NO_3^-, Cl^-, NH_4^+, Na^+, K^+, Mg^{2+}, and Ca^{2+}. The proportions of each ionic component in the clean period and the polluted period are shown in Figure 5. The concentration of WSIIs accounted for 38.2% of $PM_{2.5}$ in the polluted period, while it can be as high as 61.4% during the clean period. The proportion of SNA in $PM_{2.5}$ increased with the increase in pollution (Zhan et al., 2021). SNA accounted for 20%–83% of the total mass WSIIs during the clean period and 22%–96% during the polluted period with the average of 83.1%. Over the whole heating season, the hourly mean mass concentration of sulfate, nitrate, and ammonium was 1.7 μg/m^3, 6.1 μg/m^3, and 1.9 μg/m^3, respectively. Compared with the winter SNA mass concentration of 2013–2017, the SNA concentration of 2021 was reduced (Wang et al., 2019a). The proportions of sulfate, nitrate, and ammonium in $PM_{2.5}$ in the clean period were 7.4%, 11.1%, and 2.5% and in the polluted period were 4.8%, 21%, and 7.3%, respectively. During the XXIV Olympic Winter Games period, the WSII mass concentration accounted for 40.3% of $PM_{2.5}$. SNA contributed to 7.7%, 15%, and 4.7% of the total mass WSIIs, respectively. The WSII mass concentration contributed to 38.0% of $PM_{2.5}$ mass concentration in the Paralympics Winter

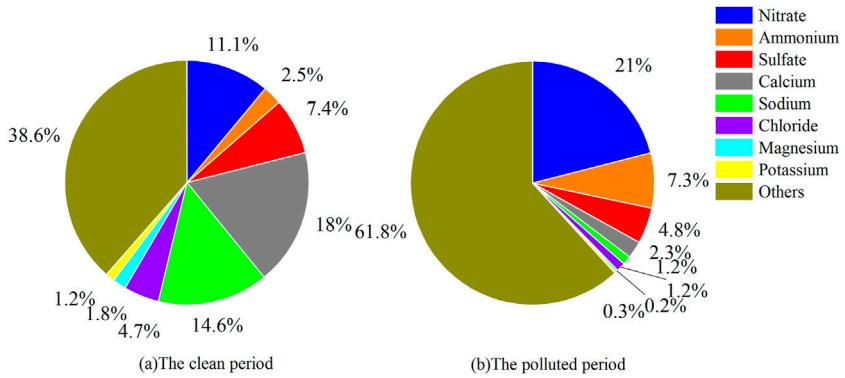

FIGURE 5
Percentage of water-soluble inorganic ions (WSIIs) in $PM_{2.5}$ mass concentration. **(A)** clean period and **(B)** polluted period.

Games period, while SNA accounted for 6.0%, 21.8%, and 3.3%, respectively.

Although the proportion of WSIIs was low in $PM_{2.5}$ during the polluted period compared to the clean period, the overall concentration of WSIIs was higher than that in the clean period. In the clean period, the hourly mean mass concentration of WSIIs was 6.6 μg/m^3, while it was 41.8 μg/m^3 in the polluted period. As shown in Table 1, the hourly average mass concentration of WSIIs in the polluted period was in the following order: NO_3^- > NH_4^+> SO_4^{2-} > Ca^{2+}> Na^+> Cl^- > Mg^{2+}> K^+. During both the clean and polluted periods, the concentration of NO_3^- was the highest among all WSIIs. The hourly average mass concentration of NO_3^- during the polluted period was 22.9 μg/m^3, which was 19.1 times of that in the clean period (1.2 μg/m^3). As for SO_4^{2-}, the mean mass concentration in the polluted period (5.2 μg/m^3) was 6.5 times of that in the clean period (0.8 μg/m^3). NH_4^+ mean mass concentration was 8.0 μg/m^3 and 0.3 μg/m^3 in the polluted and clean periods, respectively. In contrast, the concentrations of Na^+, K^+, Mg^{2+}, Ca^{2+}, and Cl^- in $PM_{2.5}$ were lower. Throughout the heating season, the hourly maximum concentrations of Ca^{2+} and Mg^{2+}, which were mainly from dust, were 6.4 μg/m^3 and 2.4 μg/m^3, respectively. Cl^- mass concentrations fluctuated between 0.1 and 3.0 μg/m^3, while K^+ was usually used as a tracer for biomass burning (Wu et al., 2019), with an hourly average concentration of 0.2 μg/m^3, which was the lowest concentration among WSIIs.

During the Olympics Winter Games period, no polluted episode occurred, and the hourly mean mass concentrations of sulfate, nitrate, and ammonium were 1.8 μg/m^3, 3.5 μg/m^3, and 1.1 μg/m^3, respectively. While the third polluted episode occurred during the Paralympic Winter Games period, a dusty event (9 March 2022–10 March 2022) occurred, and the hourly maximum concentration of Ca^{2+} reached 6.4 μg/m^3. Also, during this episode, the hourly maximum concentration of NO_3^-, SO_4^{2-}, and NH_4^+ reached 48.6 μg/m^3, 7.2 μg/m^3, and 13.0 μg/m^3, respectively. The concentration of sulfate, nitrate, and ammonium during the Paralympic Winter Games period was 1.1, 3.8, and 3.4 times that of the Olympics Winter Games period.

Figure 6 displays time series of major WSII mass concentrations during the filed observation. The variation trend of SNA and $PM_{2.5}$ mass concentration was similar. The peaks and valleys of most SNA and $PM_{2.5}$ basically appeared at the same time. SNA occupied the largest fraction in WSIIs; SNA accounted for 68.1% of the WSIIs during the Olympics Winter Games and 82.0% during the Paralympics Winter Games. This indicates that with the increase in pollution, SNA contributed more, which was roughly similar to the observation of Xu et al. (2019a) during the Asia Pacific Economic Cooperation Summit (APEC). The concentration of WSIIs in the clean period was lower than that in the polluted period. The concentrations of Mg^{2+} and Na^+ in the polluted period were lower and the fluctuation was smaller than those in the clean period. The mass concentrations of Ca^{2+} and Cl^- increased with the increase in pollution.

3.5 Secondary aerosol processes

The secondary transformation process plays an important role in the formation of SNA in $PM_{2.5}$ (Wang et al., 2021). The mass ratio of $PM_{2.5}$/CO is often used to qualitatively evaluate the intensity of secondary transformation of $PM_{2.5}$ to exclude the impact of primary combustion emissions and meteorological conditions (He et al., 2017; Wu et al., 2020). In this study, the hourly ratio of $PM_{2.5}$/CO in Beijing was 0.03 ± 0.01 during the clean period and 0.10 ± 0.03 in the polluted period, which was 3.3 times that of the clean period, indicating that the secondary pollution in the polluted period was aggravated. Figure 7 shows that $PM_{2.5}$/CO increased significantly during the polluted period, especially during the three polluted episodes.

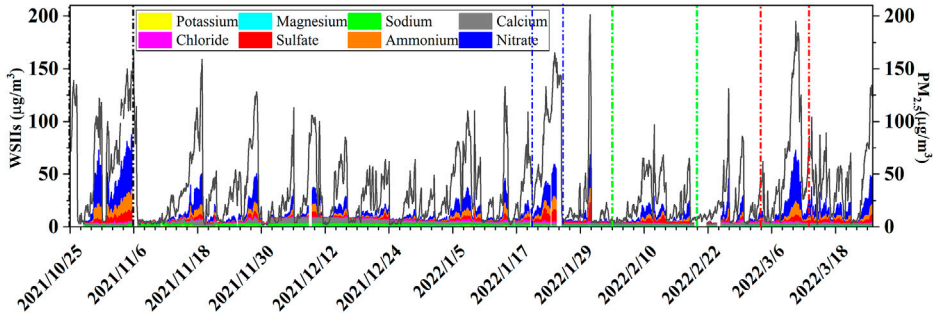

FIGURE 6
Time series of $PM_{2.5}$ and WSIIs mass concentration; the black dotted lines are the test heating time; the blue dotted lines represent snowfall; the green dotted lines represent the Olympic Winter Games period, and the red lines represent the Paralympic Winter Games period.

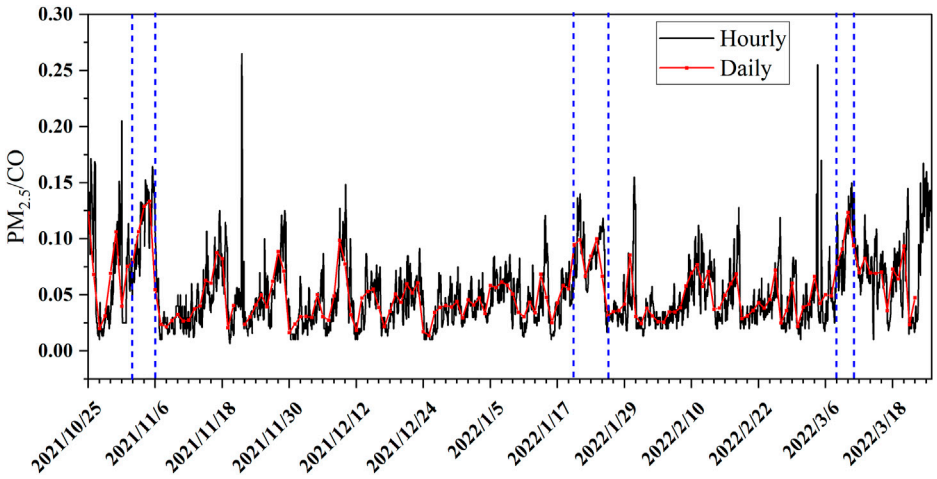

FIGURE 7
Time series of hourly and daily $PM_{2.5}$/CO mass ratios; the three polluted episodes are marked by blue dashed lines.

To further explore the secondary transformation process, the sulfur oxidation ratio (SOR) and nitrogen oxidation ratio (NOR) are usually used to quantitatively study the secondary conversion reactions of SO_2 and NO_2 to form sulfate and nitrate, respectively (Li et al., 2018; Li et al., 2019; Zhao et al., 2019; Yang et al., 2022). They were calculated as follows:

$$\mathrm{SOR} = \frac{\mathrm{n}[\mathrm{SO_4^{2-}}]}{\mathrm{n}[\mathrm{SO_4^{2-}}] + \mathrm{n}[\mathrm{SO_2}]},$$
$$\mathrm{NOR} = \frac{\mathrm{n}[\mathrm{NO_3^{-}}]}{\mathrm{n}[\mathrm{NO_3^{-}}] + \mathrm{n}[\mathrm{NO_2}]}, \quad (1)$$

where n refers to the molar concentration.

The higher SOR and NOR suggested that greater oxidation of gaseous species would occur and secondary aerosols would be formed in the atmosphere (Fu et al., 2008). Generally, when their values were >0.10, secondary transformation processes such as photochemical oxidation and heterogeneous reactions would play an important role in the formation of sulfate and nitrate from gas-phase SO_2 and NOx. Nitrate and sulfate are suggested to be mainly generated from the primary emission sources if NOR and SOR values are less than 0.1 (Xu et al., 2019a).

The SOR in the clean period was 0.22, while the SOR in the polluted period was 0.55. The mean SOR for both clean and polluted periods was greater than 0.1, indicating that the secondary transformation was the primary source of SO_4^{2-} formation. The formation of SO_4^{2-} in the atmosphere proposed by previous studies mainly includes the gas-phase oxidation of SO_2 by OH radicals and the aqueous oxidation of H_2O_2, O_3, and NO_2 to S (VI) and the catalytic oxidation by

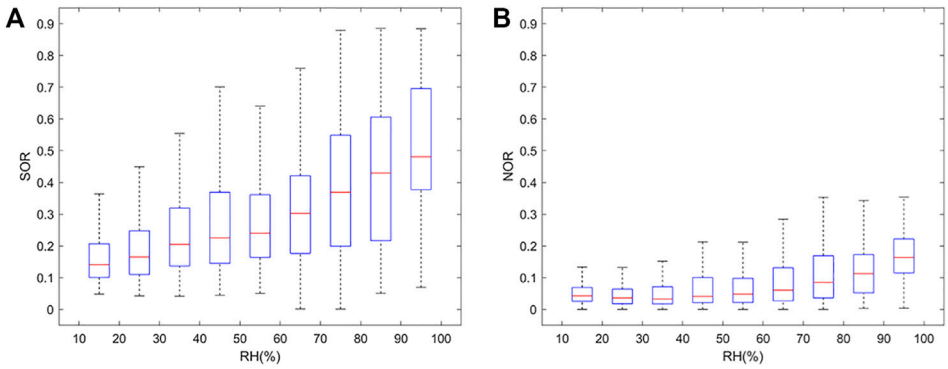

FIGURE 8
Relationship between **(A)** SOR and relative humidity; **(B)**NOR and relative humidity.

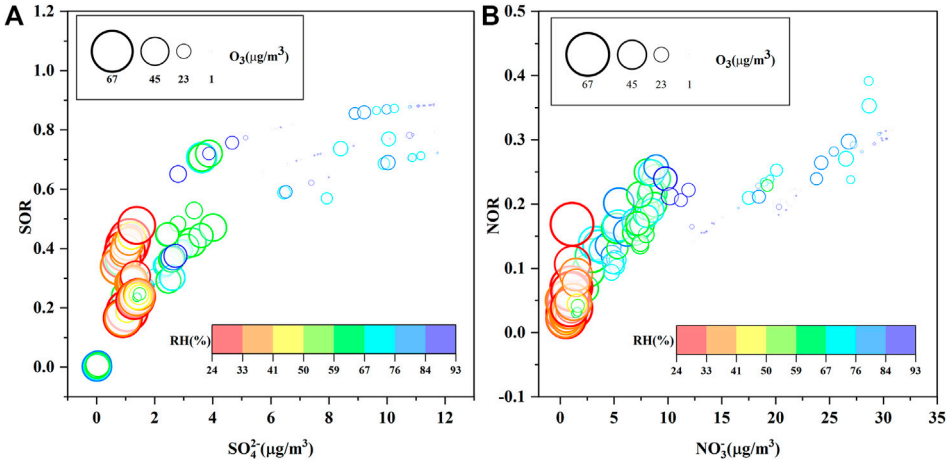

FIGURE 9
(A) Relationship between SOR and SO_4^{2-} colored by RH and **(B)** relationship between NOR and NO_3^- colored by RH; the circle size represents the O_3 mass concentration. The data used in this figure were from January 20 to January 26, 2022 (there were snowfalls during January 20–23).

transition metals such as Fe^{3+} and Mn^{2+} in cloud droplets and aerosols (Dong et al., 2020; Cao et al., 2021). The SOR in this study showed a clearly increasing trend with RH (shown in Figure 8A). When RH > 60%, the SOR increased faster. This possibly suggested that the aqueous oxidation of SO_2 to produce SO_4^{2-} is enhanced under high RH conditions due to high liquid water content in the aerosol (Zhang et al., 2018a; Wu et al., 2022).

In order to further explore the mechanism of sulfate and nitrate formation under high RH, we selected the second polluted episode with a snowfall event (from January 20 to January 26, 2022) as a case for detailed analysis. There were intermittent snowfalls in Beijing from January 20 to 23. After the snowfall stopped, the RH was high and the pollution continued to aggravate. As shown in Figure 6, the $PM_{2.5}$ hourly mass concentration climbed from 73.0 to 165.0 μg/m³ during the second episode. The NO_3^- hourly mass concentration increased rapidly from 12.5 to 30.8 μg/m³, while the sulfate hourly mass concentration rose from 4.6 to 11.9 μg/m³. It was interesting to observe from Figure 9A that the SOR increased with the increase in sulfate mass. When SO_4^{2-} < 2 μg/m³, O_3 promoted the formation of sulfate to some extent, and the SOR increased with O_3 concentration. However, O_3 had little influence on sulfate formation when the sulfate concentration increased. The concentration of O_3 decreased, but the SOR value still grew up. At the same time, it was found that high SOR and sulfate values both appeared at high relative humidity, especially above 60%. O_3 and RH were believed to be two factors in the formation of sulfate (Fang et al., 2019). Previous studies proposed that sulfate formation mechanisms in the atmosphere primarily include gas-phase oxidation of SO_2 by OH radicals and the

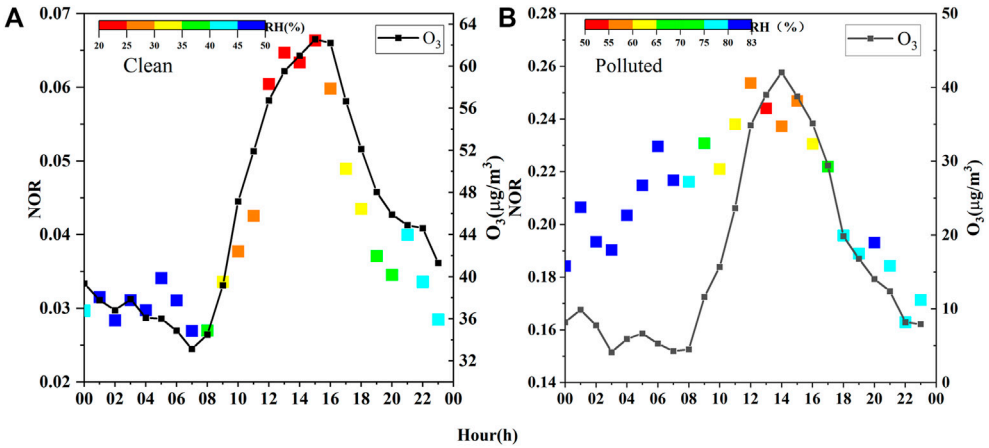

FIGURE 10
Diurnal variation of O_3 and NOR colored by RH **(A)** during the clean period and **(B)** during the polluted period.

aqueous oxidation of S(IV) by H_2O_2, O_3, organic peroxides, and NO_2 and catalytic oxidation by transition metal ions (TMIs), for example, Fe(III) and Mn(II), in cloud/fog water droplets (Li et al., 2020; Wang et al., 2021; Wang et al., 2022b; Wang et al., 2022c; Wang et al., 2022d; Gao et al., 2022; Ye et al., 2022). As sulfate itself exhibit strong hygroscopicity (Kong et al., 2020), with the increase in sulfate and RH, the $PM_{2.5}$ surface water content would increase, which would be more conducive to potential aqueous oxidation of S(IV), resulting in the increase in SOR. This can partly explain the aforementioned fact that RH and O_3 affect the secondary transformation process.

Fu et al. proposed that the NOR was less than 0.1 in the case when nitrate was mainly generated from primary emissions and greater than 0.1 when nitrate was mainly generated through the secondary transformation of NOx oxidation (Fu et al., 2008). The mean NOR value in the clean period was 0.04 and in the polluted period was 0.21, suggesting that nitrate was mainly formed by secondary transformation processes in the polluted period and by primary emission sources in the clean period. RH and O_3 can affect these secondary transformation processes in the polluted period. As shown in Figure 8B, NOR rose with the increase in RH although the effect of RH was less than that of SOR. When the RH was less than 60%, most values of the NOR were less than 0.1. When the RH was more than 60%, the NOR began to rise, and the average values were above 0.1. It indicated that higher RH may promote nitrate formation. The relationship between NOR and NO_3^- with O_3 and RH is shown in Figure 9B. NOR presented an upward trend with the increase in NO_3^-. At high relative humidity, the NOR increased with nitrate concentration and was greater than 0.1 even at low O_3 concentrations. Heterogeneous hydrolysis of N_2O_5 under high humidity conditions may contribute to the formation of HNO_3 at night (Yun et al., 2018; Chen et al., 2020; Yang et al., 2022).

The diurnal variation of O_3 concentration and NOR in the clean and polluted periods is shown in Figures 10A, B, respectively, as well as their relationship with RH. It can be seen from Figure 10A that the diurnal variation of O_3 mass concentration and NOR showed a similar trend during the clean period. They presented an obvious single peak and reached the maximum around 15:00. However, in the polluted period, NOR only maintained a good consistency with O_3 concentration in the afternoon, as shown in Figure 10B. Due to the weakening of the titration effect of NOx, the increase in O_3 concentration leads to the enhancement of atmospheric oxidation capacity, promoting the formation of NOx to HNO_3, and then reacted with NH_3 in the atmosphere to form nitrate (Ren et al., 2021). However, at night, the NOR still rose when O_3 concentration decreased. In addition, it was found that the NOR increased with the increase in RH. According to the studies in previous literatures, heterogeneous hydrolysis of N_2O_5 may contribute to the formation of HNO_3 at night under high humidity conditions (Zhang et al., 2018a; Wang et al., 2022a).

4 Conclusion

Hourly mass concentrations of water-soluble inorganic ions in $PM_{2.5}$ were continuously measured in Beijing during the entire 2021 heating season, which covered not only the 2021 winter but also the periods of XXIV Olympic Winter Games and XIII Paralympic Winter Games. The filed observation lasted for about 5 months from 25 October 2021 to 22 March 2022. This study analyzed the characteristics of $PM_{2.5}$ and WSII mass concentrations during this period and investigated the influence of meteorological conditions on their formation. It was found that meteorological factors played an important role in the $PM_{2.5}$ pollution. Most of the polluted processes occurred

under conditions of low wind speed, temperature inversion, and high RH, which were in favor of local accumulation of pollutants and secondary transformation. The $PM_{2.5}$/CO ratio, an indicator of the contribution of secondary aerosols to $PM_{2.5}$, suggested that the secondary conversion was enhanced in the polluted period.

Total mass concentration of WSIIs accounted for 38.2% and 61.4% in the polluted and clean periods, respectively. Among them, during the polluted period, the average contribution of SNA to WSIIs was 83.1%. The concentration of nitrate was the highest in WSIIs. The SOR and NOR in the polluted period were much higher than those in the clean period, which further confirmed that the secondary transformation process had an important impact on the occurrence of $PM_{2.5}$ pollution. In addition, high RH was conducive to the formation of secondary aerosols such as sulfate, which further aggravated pollution. For secondary aerosols such as nitrate, heterogeneous hydrolysis of N_2O_5 under high humidity conditions may contribute to the formation of nitrate at night in the polluted period, while photochemical reactions were another pathway of nitrate formation during the day.

Data availability statement

All data given in figures are displayed in tables or in digital form. Readers who are interested in the data should contact the corresponding authors.

Author contributions

JW: field investigation, analyzed the observational data and prepared the figures of the manuscript, draft the manuscript. LW: conceptualization, methodology, data analysis, revising—original draft, funding acquisition, and guiding the field investigation. JS: conceptualization, writing—review and editing, supervision, funding acquisition. JW, SZ and LW performed the instrument deployment and operation. SZ: field investigation. JZ: plotting some figures. All co-authors discussed the results and commented on the manuscript.

Funding

This work was supported by the Beijing Natural Science Foundation (No. 8202052), the National Natural Science Foundation of China (Nos. 21777191, 42075082, and 41875147), and the Chinese Academy of Meteorological Sciences (2020KJ001, 2020Z002, and 2022KJ002). It was also supported by the Innovation Team for Haze-fog Observation and Forecasts of the Ministry of Science and Technology of the People's Republic of China and China Meteorological Administration.

Conflict of interest

The authors declare that the research was conducted in the absence of any commercial or financial relationships that could be construed as a potential conflict of interest.

Publisher's note

All claims expressed in this article are solely those of the authors and do not necessarily represent those of their affiliated organizations, or those of the publisher, the editors, and the reviewers. Any product that may be evaluated in this article, or claim that may be made by its manufacturer, is not guaranteed or endorsed by the publisher.

References

Cao, J., Qiu, X., Gao, J., Wang, F., Wang, J., Wu, J., et al. (2021). Significant decrease in SO_2 emission and enhanced atmospheric oxidation trigger changes in sulfate formation pathways in China during 2008–2016. *J. Clean. Prod.* 326, 129396. doi:10.1016/j.jclepro.2021.129396

Chen, X., Wang, H., Lu, K., Li, C., Zhai, T., Tan, Z., et al. (2020). Field determination of nitrate formation pathway in winter beijing. *Environ. Sci. Technol.* 54 (15), 9243–9253. doi:10.1021/acs.est.0c00972

Chen, Z., Chen, D., Wen, W., Zhuang, Y., Kwan, M.-P., Chen, B., et al. (2019). Evaluating the "2+26" regional strategy for air quality improvement during two air pollution alerts in beijing: Variations in $PM_{2.5}$ concentrations, source apportionment, and the relative contribution of local emission and regional transport. *Atmos. Chem. Phys.* 19 (10), 6879–6891. doi:10.5194/acp-19-6879-2019

Dao, X., Di, S. Y., Zhang, X., Gao, P. J., Wang, L., Yan, L. Y., et al. (2022). Composition and sources of particulate matter in the Beijing-Tianjin-Hebei region and its surrounding areas during the heating season. *Chemosphere* 291, 132779. doi:10.1016/j.chemosphere.2021.132779

Dao, X., Di, S., Zhang, X., Gao, P., Wang, L., Yan, L., et al. (2021). Composition and sources of particulate matter in the Beijing-Tianjin-Hebei region and its surrounding areas during the heating season. *Chemosphere* 291, 132779. doi:10.1016/j.chemosphere.2021.132779

Dong, C., Li, J., and Qi, Y. (2022). Decomposing $PM_{2.5}$ air pollution rebounds in Northern China before COVID-19. *Environ. Sci. Pollut. Res.* 29 (19), 28688–28699. doi:10.1007/s11356-021-17889-2

Dong, Z., Su, F., Zhang, Z., and Wang, S. (2020). Observation of chemical components of PM2.5 and secondary inorganic aerosol formation during haze and sandy haze days in Zhengzhou, China. *J. Environ. Sci.* 88, 316–325. doi:10.1016/j.jes.2019.09.016

Elser, M., Huang, R.-J., Wolf, R., Slowik, J. G., Wang, Q., Canonaco, F., et al. (2016). New insights into $PM_{2.5}$ chemical composition and sources in two major cities in China during extreme haze events using aerosol mass spectrometry. *Atmos. Chem. Phys.* 16 (5), 3207–3225. doi:10.5194/acp-16-3207-2016

Fang, Y., Ye, C., Wang, J., Wu, Y., Hu, M., Lin, W., et al. (2019). RH and O_3 concentration as two prerequisites for sulfate formation. *Atmos. Chem. Phys.* 19 (19), 12295–12307. doi:10.5194/acp-19-12295-2019

Fu, Q., Zhuang, G., Wang, J., Xu, C., Huang, K., Li, J., et al. (2008). Mechanism of formation of the heaviest pollution episode ever recorded in the Yangtze River

Delta, China. *Atmos. Environ. X.* 42 (9), 2023–2036. doi:10.1016/j.atmosenv.2007.12.002

Gao, J., Shi, G. L., Zhang, Z. C., Wei, Y. T., Tian, X., Feng, Y. C., et al. (2022). Targeting atmospheric oxidants can better reduce sulfate aerosol in China: H_2O_2 aqueous oxidation pathway dominates sulfate formation in haze. *Environ. Sci. Technol.* 56 (15), 10608–10618. doi:10.1021/acs.est.2c01739

Geng, G., Zheng, Y., Zhang, Q., Xue, T., Zhao, H., Tong, D., et al. (2021). Drivers of PM2.5 air pollution deaths in China 2002–2017. *Nat. Geosci.* 14 (9), 645–650. doi:10.1038/s41561-021-00792-3

Han, X., Guo, Q., Lang, Y., Li, S., Li, Y., Guo, Z., et al. (2020). Seasonal and long-term trends of sulfate, nitrate, and ammonium in $PM_{2.5}$ in beijing: Implication for air pollution control. *Environ. Sci. Pollut. Res.* 27 (19), 23730–23741. doi:10.1007/s11356-020-08697-1

He, J., Gong, S., Yu, Y., Yu, L., Wu, L., Mao, H., et al. (2017). Air pollution characteristics and their relation to meteorological conditions during 2014-2015 in major Chinese cities. *Environ. Pollut.* 223, 484–496. doi:10.1016/j.envpol.2017.01.050

Herrmann, H., Schaefer, T., Tilgner, A., Styler, S. A., Weller, C., Teich, M., et al. (2015). Tropospheric aqueous-phase chemistry: Kinetics, mechanisms, and its coupling to a changing gas phase. *Chem. Rev.* 115 (10), 4259–4334. doi:10.1021/cr500447k

Hu, G., Zhang, Y., Sun, J., Zhang, L., Shen, X., Lin, W., et al. (2014). Variability, formation and acidity of water-soluble ions in $PM_{2.5}$ in Beijing based on the semi-continuous observations. *Atmos. Res.* 145, 1–11. doi:10.1016/j.atmosres.2014.03.014

Hu, S., Zhao, G., Tan, T., Li, C., Zong, T., Xu, N., et al. (2021). Current challenges of improving visibility due to increasing nitrate fraction in $PM_{2.5}$ during the haze days in Beijing, China. *Environ. Pollut.* 290, 118032. doi:10.1016/j.envpol.2021.118032

Huang, X., Liu, Z., Zhang, J., Wen, T., Ji, D., and Wang, Y. (2016). Seasonal variation and secondary formation of size-segregated aerosol water-soluble inorganic ions during pollution episodes in Beijing. *Atmos. Res.* 168, 70–79. doi:10.1016/j.atmosres.2015.08.021

Huang, X., Tang, G., Zhang, J., Liu, B., Liu, C., Zhang, J., et al. (2021). Characteristics of $PM_{2.5}$ pollution in Beijing after the improvement of air quality. *J. Environ. Sci.* 100, 1–10. doi:10.1016/j.jes.2020.06.004

Kong, L., Feng, M., Liu, Y., Zhang, Y., Zhang, C., Li, C., et al. (2020). Elucidating the pollution characteristics of nitrate, sulfate and ammonium in $PM_{2.5}$ in Chengdu, southwest China, based on 3-year measurements. *Atmos. Chem. Phys.* 20 (19), 11181–11199. doi:10.5194/acp-20-11181-2020

Lachatre, M., Fortems-Cheiney, A., Foret, G., Siour, G., Dufour, G., Clarisse, L., et al. (2019). The unintended consequence of SO_2 and NO_2 regulations over China: Increase of ammonia levels and impact on $PM_{2.5}$ concentrations. *Atmos. Chem. Phys.* 19 (10), 6701–6716. doi:10.5194/acp-19-6701-2019

Lei, L., Zhou, W., Chen, C., He, Y., Li, Z., Sun, J., et al. (2021). Long-term characterization of aerosol chemistry in cold season from 2013 to 2020 in Beijing, China. *Environ. Pollut.* 268, 115952. doi:10.1016/j.envpol.2020.115952

Li, J., Gao, W., Cao, L., Xiao, Y., Zhang, Y., Zhao, S., et al. (2021). Significant changes in autumn and winter aerosol composition and sources in Beijing from 2012 to 2018: Effects of clean air actions. *Environ. Pollut.* 268, 115855. doi:10.1016/j.envpol.2020.115855

Li, J., Zhang, Y. L., Cao, F., Zhang, W., Fan, M., Lee, X., et al. (2020). Stable sulfur isotopes revealed a major role of transition-metal ion-catalyzed SO_2 oxidation in haze episodes. *Environ. Sci. Technol.* 54 (5), 2626–2634. doi:10.1021/acs.est.9b07150

Li, W., Liu, X., Zhang, Y., Tan, Q., Feng, M., Song, M., et al. (2019). Insights into the phenomenon of an explosive growth and sharp decline in haze: A case study in beijing. *J. Environ. Sci.* 84, 122–132. doi:10.1016/j.jes.2019.04.015

Li, X., Li, S., Xiong, Q., Yang, X., Qi, M., Zhao, W., et al. (2018). Characteristics of $PM_{2.5}$ chemical compositions and their effect on atmospheric visibility in urban beijing, China during the heating season. *Int. J. Environ. Res. Public Health* 15 (9), 1924. doi:10.3390/ijerph15091924

Liu, X., Sun, K., Qu, Y., Hu, M., Sun, Y., Zhang, F., et al. (2015). Secondary Formation of sulfate and nitrate during a haze episode in megacity beijing, China. *Aerosol Air Qual. Res.* 15 (6), 2246–2257. doi:10.4209/aaqr.2014.12.0321

Ma, J., Chu, B., Liu, J., Liu, Y., Zhang, H., and He, H. (2018). NOx promotion of SO_2 conversion to sulfate: An important mechanism for the occurrence of heavy haze during winter in Beijing. *Environ. Pollut.* 233, 662–669. doi:10.1016/j.envpol.2017.10.103

Pang, N. N., Gao, J., Che, F., Ma, T., Liu, S., Yang, Y., et al. (2020). Cause of $PM_{2.5}$ pollution during the 2016-2017 heating season in beijing, tianjin, and langfang, China. *J. Environ. Sci.* 95, 201–209. doi:10.1016/j.jes.2020.03.024

Rai, P., Furger, M., Slowik, J. G., Zhong, H., Tong, Y., Wang, L., et al. (2021). Characteristics and sources of hourly elements in PM_{10} and $PM_{2.5}$ during wintertime in Beijing. *Environ. Pollut.* 278, 116865. doi:10.1016/j.envpol.2021.116865

Ren, C., Huang, X., Wang, Z., Sun, P., Chi, X., Ma, Y., et al. (2021). Nonlinear response of nitrate to NOx reduction in China during the COVID-19 pandemic. *Atmos. Environ. X.* 264, 118715. doi:10.1016/j.atmosenv.2021.118715

Shao, J., Chen, Q., Wang, Y., Lu, X., He, P., Sun, Y., et al. (2019). Heterogeneous sulfate aerosol formation mechanisms during wintertime Chinese haze events: Air quality model assessment using observations of sulfate oxygen isotopes in beijing. *Atmos. Chem. Phys.* 19 (9), 6107–6123. doi:10.5194/acp-19-6107-2019

Shen, J., Tang, A., Liu, X., Kopsch, J., Fangmeier, A., Goulding, K., et al. (2011). Impacts of pollution controls on air quality in beijing during the 2008 olympic games. *J. Environ. Qual.* 40 (1), 37–45. doi:10.2134/jeq2010.0360

Su, J., Zhao, P., Ding, J., Du, X., and Dou, Y. (2021). Insights into measurements of water-soluble ions in PM2.5 and their gaseous precursors in Beijing. *J. Environ. Sci.* 102, 123–137. doi:10.1016/j.jes.2020.08.031

Sun, J., Liang, M., Shi, Z., Shen, F., Li, J., Huang, L., et al. (2019). Investigating the $PM_{2.5}$ mass concentration growth processes during 2013-2016 in Beijing and Shanghai. *Chemosphere* 221, 452–463. doi:10.1016/j.chemosphere.2018.12.200

Sun, Y., Wang, Z., Fu, P., Jiang, Q., Yang, T., Li, J., et al. (2013). The impact of relative humidity on aerosol composition and evolution processes during wintertime in Beijing, China. *Atmos. Environ. X.* 77, 927–934. doi:10.1016/j.atmosenv.2013.06.019

Wang, H., Lu, K., Tan, Z., Chen, X., Liu, Y., and Zhang, Y. (2022a). Formation mechanism and control strategy for particulate nitrate in China. *J. Environ. Sci.* doi:10.1016/j.jes.2022.09.019

Wang, J., Li, J., Ye, J., Zhao, J., Wu, Y., Hu, J., et al. (2020). Fast sulfate formation from oxidation of SO_2 by NO_2 and HONO observed in Beijing haze. *Nat. Commun.* 11 (1), 2844. doi:10.1038/s41467-020-16683-x

Wang, S., Wang, L., Fan, X., Wang, N., Ma, S., and Zhang, R. (2022b). Formation pathway of secondary inorganic aerosol and its influencing factors in Northern China: Comparison between urban and rural sites. *Sci. Total Environ.* 840, 156404. doi:10.1016/j.scitotenv.2022.156404

Wang, T., Liu, M., Liu, M., Song, Y., Xu, Z., Shang, F., et al. (2022d). Sulfate Formation apportionment during winter haze events in north China. *Environ. Sci. Technol.* 56 (12), 7771–7778. doi:10.1021/acs.est.2c02533

Wang, T., Liu, Y., Cheng, H., Wang, Z., Fu, H., Chen, J., et al. (2022c). Significant formation of sulfate aerosols contributed by the heterogeneous drivers of dust surface. *Atmos. Chem. Phys.* 22 (20), 13467–13493. doi:10.5194/acp-22-13467-2022

Wang, W., Liu, M., Wang, T., Song, Y., Zhou, L., Cao, J., et al. (2021). Sulfate formation is dominated by manganese-catalyzed oxidation of SO_2 on aerosol surfaces during haze events. *Nat. Commun.* 12 (1), 1993. doi:10.1038/s41467-021-22091-6

Wang, X., Wei, W., Cheng, S., Yao, S., Zhang, H., and Zhang, C. (2019a). Characteristics of $PM_{2.5}$ and SNA components and meteorological factors impact on air pollution through 2013–2017 in Beijing, China. *Atmos. Pollut. Res.* 10 (6), 1976–1984. doi:10.1016/j.apr.2019.09.004

Wang, Y., Wang, Q., Ye, J., Yan, M., Qin, Q., Prevot, A. S. H., et al. (2019b). A review of aerosol chemical composition and sources in representative regions of China during wintertime. *Atmosphere* 10 (5), 277. doi:10.3390/atmos10050277

Wang, Y., Yao, L., Wang, L., Liu, Z., Ji, D., Tang, G., et al. (2013). Mechanism for the formation of the January 2013 heavy haze pollution episode over central and eastern China. *Sci. China Earth Sci.* 57 (1), 14–25. doi:10.1007/s11430-013-4773-4

Wu, L., Sun, J., Zhang, X., Zhang, Y., Wang, Y., Zhong, J., et al. (2019). Aqueous-phase reactions occurred in the $PM_{2.5}$ cumulative explosive growth during the heavy pollution episode (HPE) in 2016 Beijing wintertime. *Tellus, Ser. B Chem. Phys. Meteorol.* 71 (1), 1–15. doi:10.1080/16000889.2019.1620079

Wu, L., Wang, Y., Li, L., and Zhang, G. (2020). Acidity and inorganic ion formation in PM2.5 based on continuous online observations in a South China megacity. *Atmos. Pollut. Res.* 11 (8), 1339–1350. doi:10.1016/j.apr.2020.05.003

Wu, L., Zhang, X., Sun, J., Wang, Y., Zhong, J., and Meng, Z. (2022). Intensified wintertime secondary inorganic aerosol formation during heavy haze pollution episodes (HPEs) in Beijing, China. *J. Environ. Sci.* 114, 503–513. doi:10.1016/j.jes.2022.01.008

Xie, X., Hu, J., Qin, M., Guo, S., Hu, M., Wang, H., et al. (2022). Modeling particulate nitrate in China: Current findings and future directions. *Environ. Int.* 166, 107369. doi:10.1016/j.envint.2022.107369

Xu, M., Liu, Z., Hu, B., Yan, G., Zou, J., Zhao, S., et al. (2022). Chemical characterization and source identification of $PM_{2.5}$ in Luoyang after the clean air actions. *J. Environ. Sci.* 115, 265–276. doi:10.1016/j.jes.2021.06.021

Xu, Q., Wang, S., Jiang, J., Bhattarai, N., Li, X., Chang, X., et al. (2019a). Nitrate dominates the chemical composition of $PM_{2.5}$ during haze event in

Beijing, China. *Sci. Total Environ.* 689, 1293–1303. doi:10.1016/j.scitotenv.2019.06.294

Xu, W., Liu, X., Liu, L., Dore, A. J., Tang, A., Lu, L., et al. (2019b). Impact of emission controls on air quality in Beijing during APEC 2014: Implications from water-soluble ions and carbonaceous aerosol in $PM_{2.5}$ and their precursors. *Atmos. Environ. X.* 210, 241–252. doi:10.1016/j.atmosenv.2019.04.050

Yang, J., Wang, S., Zhang, R., and Yin, S. (2022). Elevated particle acidity enhanced the sulfate formation during the COVID-19 pandemic in Zhengzhou, China. *Environ. Pollut.* 296, 118716. doi:10.1016/j.envpol.2021.118716

Yang, S., Ma, Y., Duan, F., He, K., Wang, L., Wei, Z., et al. (2018). Characteristics and formation of typical winter haze in Handan, one of the most polluted cities in China. *Sci. Total Environ.* 613-614, 1367–1375. doi:10.1016/j.scitotenv.2017.08.033

Ye, C., Lu, K., Song, H., Mu, Y., Chen, J., and Zhang, Y. (2022). A critical review of sulfate aerosol formation mechanisms during winter polluted periods. *J. Environ. Sci.* doi:10.1016/j.jes.2022.07.011

Yun, H., Wang, W., Wang, T., Xia, M., Yu, C., Wang, Z., et al. (2018). Nitrate formation from heterogeneous uptake of dinitrogen pentoxide during a severe winter haze in southern China. *Atmos. Chem. Phys.* 18 (23), 17515–17527. doi:10.5194/acp-18-17515-2018

Zhan, Y., Xie, M., Gao, D., Wang, T., Zhang, M., and An, F. (2021). Characterization and source analysis of water-soluble inorganic ionic species in $PM_{2.5}$ during a wintertime particle pollution episode in Nanjing, China. *Atmos. Res.* 262, 105769. doi:10.1016/j.atmosres.2021.105769

Zhang, R., Sun, X. S., Shi, A. J., Huang, Y. H., Yan, J., Nie, T., et al. (2018a). Secondary inorganic aerosols formation during haze episodes at an urban site in Beijing, China. *Atmos. Environ. X.* 177, 275–282. doi:10.1016/j.atmosenv.2017.12.031

Zhang, Y., Li, X., Nie, T., Qi, J., Chen, J., and Wu, Q. (2018b). Source apportionment of $PM_{2.5}$ pollution in the central six districts of Beijing, China. *J. Clean. Prod.* 174, 661–669. doi:10.1016/j.jclepro.2017.10.332

Zhao, L., Wang, L., Tan, J., Duan, J., Ma, X., Zhang, C., et al. (2019). Changes of chemical composition and source apportionment of $PM_{2.5}$ during 2013–2017 in urban Handan, China. *Atmos. Environ. X.* 206, 119–131. doi:10.1016/j.atmosenv.2019.02.034

Zhong, J., Zhang, X., Dong, Y., Wang, Y., Liu, C., Wang, J., et al. (2018a). Feedback effects of boundary-layer meteorological factors on cumulative explosive growth of $PM_{2.5}$ during winter heavy pollution episodes in Beijing from 2013 to 2016. *Atmos. Chem. Phys.* 18 (1), 247–258. doi:10.5194/acp-18-247-2018

Zhong, J., Zhang, X., Wang, Y., Liu, C., and Dong, Y. (2018b). Heavy aerosol pollution episodes in winter Beijing enhanced by radiative cooling effects of aerosols. *Atmos. Res.* 209, 59–64. doi:10.1016/j.atmosres.2018.03.011

Zhong, J., Zhang, X., Wang, Y., Sun, J., Zhang, Y., Wang, J., et al. (2017). Relative contributions of boundary-layer meteorological factors to the explosive growth of $PM_{2.5}$ during the red-alert heavy pollution episodes in Beijing in December 2016. *J. Meteorol. Res.* 31 (5), 809–819. doi:10.1007/s13351-017-7088-0

frontiers | Frontiers in Environmental Science

TYPE Original Research
PUBLISHED 06 January 2023
DOI 10.3389/fenvs.2022.1081453

OPEN ACCESS

EDITED BY
Gen Zhang,
Chinese Academy of Meteorological Sciences, China

REVIEWED BY
Yuanjian Yang,
Nanjing University of Information Science and Technology, China
Haipeng Lin,
Harvard University, United States

*CORRESPONDENCE
Chunmei Geng,
gengcm@craes.org.cn
Xinhua Wang,
wangxh@craes.org.cn

SPECIALTY SECTION
This article was submitted to Atmosphere and Climate, a section of the journal Frontiers in Environmental Science

RECEIVED 27 October 2022
ACCEPTED 14 December 2022
PUBLISHED 06 January 2023

CITATION
Li M, Geng C, Li L, Zheng Z, Xu B, Yang W and Wang X (2023), Meteorological impacts on surface ozone: A case study based on Kolmogorov–Zurbenko filtering and multiple linear regression. *Front. Environ. Sci.* 10:1081453. doi: 10.3389/fenvs.2022.1081453

Meteorological impacts on surface ozone: A case study based on Kolmogorov–Zurbenko filtering and multiple linear regression

Menghui Li[1,2], Chunmei Geng[1]*, Liming Li[1], Zhensen Zheng[1], Bo Xu[3], Wen Yang[1] and Xinhua Wang[1]*

[1]State Key Laboratory of Environmental Criteria and Risk Assessment, Chinese Research Academy of Environmental Sciences, Beijing, China, [2]State Key Laboratory of Organic Geochemistry, Guangzhou Institute of Geochemistry, Chinese Academy of Sciences, Guangzhou, China, [3]Shandong Zibo Eco-Environmental Monitoring Center, Zibo, China

Ozone variation, excluding meteorological effects, is very important to assess the effects of air pollution control policies. In this study, the Kolmogorov-Zurbenko (KZ) filter method and multiple linear stepwise regression are combined to study the impact of meteorological parameters on ozone concentration over the past 5 years (2016–2020) in a petrochemical industrial city in northern China. Monte Carlo simulations were used to evaluate the reliability for the potential quasi quantitative prediction of the baseline component. The average level of the city and the details of five stations in the city were studied. The results show that the short-term, seasonal, and long-term component variances of maximum daily running average 8 h (MDA8) ozone in Zibo city (City) decomposed by the KZ filter account for 32.06%, 61.67% and 1.15% of the total variance, for a specific station, the values were 32.37%–34.90%, 56.64%–62.00%, and .35%–3.14%, respectively. The average long-term component increase rate is 3.19 μg m^{-3} yr^{-1} on average for the city, while it is 1.52–5.95 μg m^{-3} yr^{-1} for a specific station. The overall meteorological impact was not stable and fluctuated between −2.60 μg m^{-3} and +3.77 μg m^{-3}. This difference in trends between the city and specific stations implied that the O_3 precursor's mitigation strategy should be more precise to improve its practical effects.

KEYWORDS

ozone, KZ filter, meteorological conditions, multiple linear regression, Monte Carlo simulation

1 Introduction

Over the past few decades, China's economic development has seen significant advancements, the pace of urbanization and industrialization has also been accelerating. Accordingly, the consumption of fossil fuels, such as coal and petroleum, has increased significantly, leading to severe air pollution. Haze pollution–characterized by a high concentration of inhalable particulate matter (PM_{10}) and fine particulate matter ($PM_{2.5}$)–and photochemical smog pollution–characterized by a high concentration of ozone (O_3)–were severe issues in the past (Huang et al., 2013; Zhang et al., 2015; Wang et al., 2017; Wang et al., 2019). After the implementation of the "Air Pollution Prevention and Control Action Plan" (also referred to as the "Atmospheric Ten Measures"), the concentration of particulate matter in China has been significantly decreasing each year. However, regional photochemical pollution has become increasingly prominent, and the ozone concentration has risen instead of falling in many cities, and threatens human health, which is of significant concern for the scientific community and relevant government departments (Kuerban et al., 2020; Lin et al., 2021). According to the results of monitoring data from 338 cities in China, the 90th percentile of the maximum daily running average 8 h (MDA8) concentration of ozone increased from 134 μg m^{-3} in 2015 to 148 μg m^{-3} in 2019. The proportion of days exceeding the second standard values (160 μg m^{-3}) specified in the National Ambient Air Quality Standards (GB3095–2012), with ozone as the primary pollutant increased from 16.9% in 2015 to 41.7% in 2019, and the proportion of cities exceeding the secondary standard increased from 16% to 30.6% (Ministry of Ecology and Environment of China, 2016, 2019). Research has indicated that the concentration of ozone in 22 of China's 30 provinces increased from 2015 to 2018, and ozone pollution was prominent and concentrated in the Beijing-Tianjin-Hebei (BTH), Yangtze River Delta (YRD), and Pearl River Delta (PRD) regions (Kuerban et al., 2020).

In comparison to other pollutants, ozone is chemically active and susceptible to meteorological (MET) conditions, such as temperature, relative humidity, wind speed, boundary layer (Cheng et al., 2019; Zong et al., 2021; Zong et al., 2022), and atmospheric transmission. The close relationship between the ozone concentration and meteorological conditions may cover up the ozone long-term trend caused by emission change of ozone precursor. Therefore, it is necessary to filter out the meteorological effects to understand the net impact of emission changes (Rao et al., 1997; Yu et al., 2019). Some methods can help separate the influence of meteorological conditions on ozone, such as Fourier transforms and the wavelet transform method (Eskridge et al., 1997). The Kolmogorov-Zurbenko (KZ) filter, combined with the multiple linear regression (MLR) analysis technique proposed by Rao and Zurbenko (1994) can separate the influence of meteorological conditions on ozone concentration. The KZ filter method is a robust statistical model with a simple algorithm that can be used directly in the presence of missing data (Porter et al., 2001), and is widely used to study ozone pollution trends, such as in Tucson (Wise and Comrie, 2005) and Houston in the United States (Botlaguduru et al., 2018); Canoas and Estio in Brazil (Agudelo-Castaneda et al., 2014); Cessa in the Greek Lee Plain (Papanastasiou et al., 2012); Switzerland (Boleti et al., 2018); and major cities in South Korea (Seo et al., 2014), and Australia, and Spain (Anh et al., 1997; Ibarra-Berastegia et al., 2001; Agudelo-Castaneda et al., 2014), and other places (Kang et al., 2013; Luo et al., 2019). Sa et al. (2015) used the KZ filter method to decompose the original time series of atmospheric pollutants O_3, PM_{10}, and NO_2 at different time scales, and then ascertained the influence of meteorological conditions on the components of each pollutant through MLR. Research has shown that the KZ filter method can be used to decompose the air pollutants concentrated in metropolises in China, such as BTH (Ma et al., 2016; Gao et al., 2021) and YRD (Yu et al., 2019). Ma et al. (2016) used KZ filtering to remove meteorological influences and extracted the long-term ozone trend of background stations, finding that meteorological conditions have limited effects on the rapid increases in the ozone concentration in Beijing. Research in Hebei province (Gao et al., 2021) has shown that meteorological factors (temperature, atmospheric pressure, and boundary layer height) account for 64% of long-term ozone changes. Therefore, the influence of meteorological factors varies widely in different cities in different periods. Most previous research has focused on the influence of meteorological parameters on regional ozone pollution. However, for ozone pollution control, emission reduction measures should be implemented in every district in each city. It is imperative to investigate whether the effects are similar in all districts within a city. Thus, it is important to evaluate the effect of emission reduction without the influence of meteorological conditions in specific districts within a city.

In this study, Zibo City was selected as a representative heavily-industrial city. Zibo is an important petrochemical industrial city in the North China Plain (NCP), with significant volatile organic compounds (VOCs) emissions (Luo et al., 2018). The KZ filter method and multiple linear stepwise regression are used to study the impact of meteorological parameters on the O_3 concentration over a 5-year period (1 1 2016–31 12 2020). Pollutant concentrations on different time scales (long-term, seasonal, and short-term) were obtained, and the influence of meteorological conditions was evaluated quantitatively. The details regarding the long-term component and meteorology impact in each division in the city were discussed. This study will help understand the influence of meteorological conditions on O_3 concentration within a city.

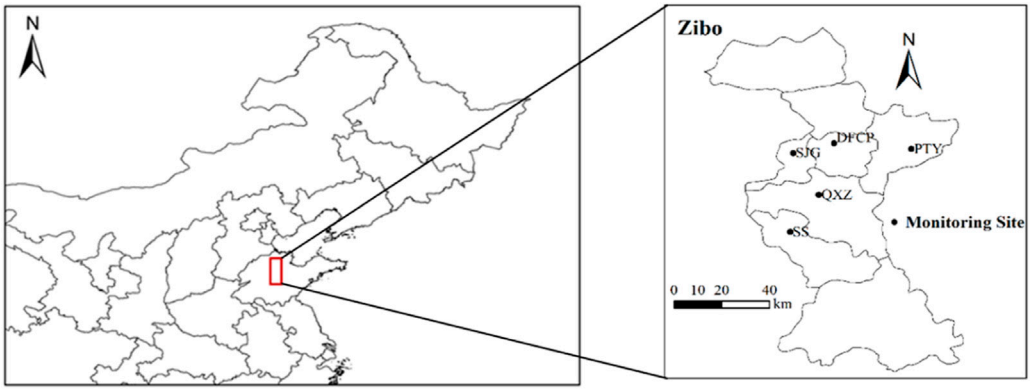

FIGURE 1
Location of the study area and air quality monitoring sites in Zibo City.

2 Materials and methods

2.1 Site description

Zibo is located in the central region of Shandong Province (35°55′20″–37°17′14″N, 117°32′15″–118°31′00″E). It is located in the warm temperate zone, experiencing a semi-humid and semi-arid continental climate; the terrain is high in the south and low in the north, and is surrounded by mountains on three sides—in the east, west, and south. The permanent population was 4.704 million at the end of 2020 (http://www.zibo.gov.cn/).

There are seven national ambient air quality monitoring stations in Zibo. Considering the data integrity of both the O_3 concentrations and meteorological parameters, data from five national environmental monitoring stations are selected to study the characteristics at different sites. The five stations are located in five districts: Dongfeng Chemical Plant (DFCP) in Zhangdian District, Putianyuan (PTY) in Linzi District, Qixiangzhan (QXZ) in Zichuan Dictrict, Sanjin Group in Zhoucun District, and Shuangshan (SS) in Boshan District, as shown in Figure 1. Detailed information on these stations can be found in Supplementary Table S1.

2.2 Data acquisition

The daily concentrations of the maximum daily average 8 h (MDA8) ozone for Zibo city (the average conditions of the city) and the five specific sites were obtained from Zibo Environmental Monitoring Center, and the meteorological data was from China National Meteorological Information Centre (http://data.cma.cn/). The data was obtained from 1 January 2016 to 31 December 2020. The meteorological factors used in this study are the daily average relative humidity (RH), daily average wind speed (WS), and daily average temperature (T).

To facilitate a comparison, the ozone concentration of different cities was found and analysed. The ozone concentration data of Beijing (the average value of 12 sites), Tianjin (the average value of 14 sites) and Shijiazhuang (the average value of 7 sites) are from the national real-time air quality release platform of the China National Environmental Monitoring Centre (https://quotsoft.net/air/), and the ozone data of Shanghai (the average value of 19 sites) were collected from Shanghai Municipal Bureau of Ecology and Environment (https://sthj.sh.gov.cn/). Ozone time series data of Los Angeles, California were collected from Air Data at the US Environment Protection Agency (https://www.epa.gov/outdoor-air-quality-data). Available O_3 time series data in Berlin (the average value of 3 sites), Paris (the average value of 8 sites) and London (the average value of 6 sites) were obtained from https://discomap.eea.europa.eu/map/fme/AirQualityExport.htm.

2.3 KZ filter method

The KZ filter method was used to decompose the time series of ozone and meteorological conditions. According to Rao and Zurbenko (Rao and Zurbenko, 1994), the original time series of pollutants can be expressed as

$$X(t) = e(t) + S(t) + W(t) \quad (1)$$

Where $X(t)$ represents the original time series, $e(t)$ represents the long-term component, $S(t)$ represents the seasonal component, and $W(t)$ represents the short-term component. In terms of the air quality component, the short-term component can be attributed to the weather and the short-term fluctuations of source emissions, the seasonal component can be attributed to the changes in the angle of the sun, for example, solar radiation, monsoon, temperature and rainfall due to solar angle changes

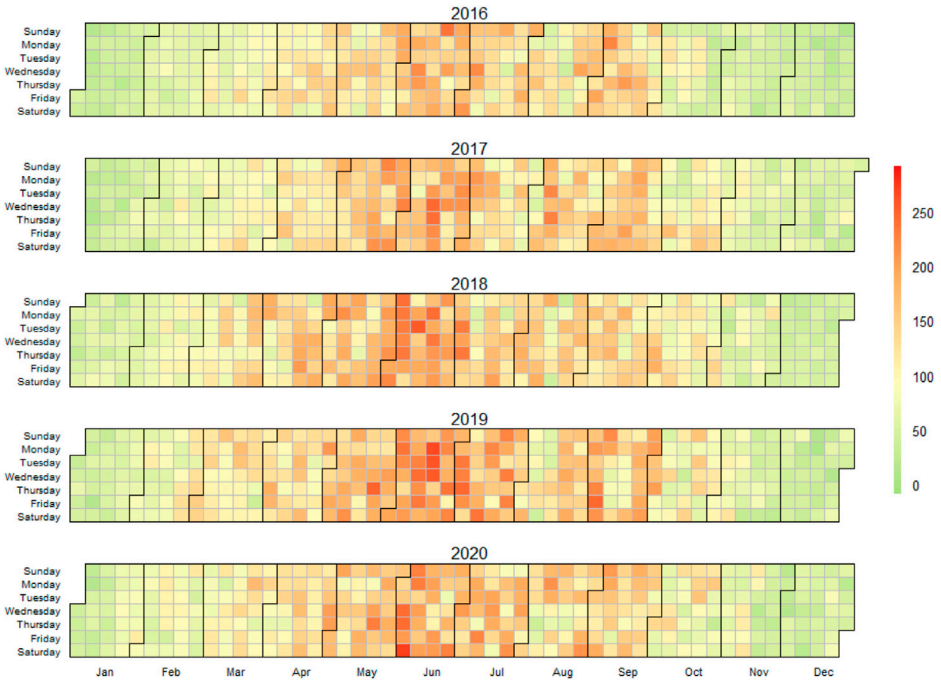

FIGURE 2
Calendar heat map of MDA8 ozone of Zibo city during 2016–2020.

show seasonal variations, and the associated changes in biogenic emissions on a time scale of generally 1a, and the long-term component can be attributed to the changes in source emissions, climate change, policy or economic activities (Rao and Zurbenko, 1994).

The KZ filter method is mainly implemented through the KZA package in R software (Version 4.0.2). It is based on the iterative moving average to eliminate high-frequency changes in the data, which is defined as p applications of a moving average of m points (Rao and Zurbenko, 1994). Its calculation formula is as follows:

$$Y_i = \frac{1}{m}\sum_{j=-k}^{k} X_{i+j} \tag{2}$$

Where Y_i represents the time series after filtering once, and the calculation is performed again using Y_i as the input of the next filter, which iterates p times, and finally yields the filter result $KZ_{(m,\ p)}$. The unit of the filtered result is the same as that of the original time series; m represents the length of the sliding window (m = 2k+1), k represents the length of the sliding window at both ends when X_i is filtered; X represents the original time series; i represents the sequence (the unit of sampling interval in this study is days); j represents the sliding window variable, which represents the time points involved in the sliding. By adjusting the filter parameters m and p, the filtering of different scale processes can be obtained, and the effective filter width satisfies the following formula:

$$m \times p^{½} \le N \tag{3}$$

The above mentioned formula implies that the filter result $KZ_{(m,\ p)}(X)$ removes high-frequency waves with a wavelength less than N. According to formula (Eq. 3), $KZ_{(15,\ 5)}(X)$ (the length of the sliding window is 15, and 5 iterations have been carried out) filters out fluctuations with a period less than 33 d ($15 \times 5^{1/2} \le 33$); the effective filter width is approximately 33 d (Rao et al., 1997).

Apply meteorological weather and air pollutant quality data to the $KZ_{(15,5)}$ filter, and the extracted time series represent the baseline component, which is defined as the sum of the long-term component and the seasonal component:

$$X_b(t) = KZ_{(15,5)} = e(t) + S(t) \tag{4}$$

The long-term component of the data can be obtained by selecting a KZ filter with a larger window length (Eskridge et al., 1997), and by using the $KZ_{(365,\ 3)}$ filter (Rao et al., 1997), the long-term component is extracted in the data, and its effective filter width is 632 d, which is about 1.7a. That is, this component filters out fluctuations in the original sequence whose period is less than 632 d ($365 \times 3^{1/2} \le 632$).

$$e(t) = KZ_{(365,3)} \tag{5}$$

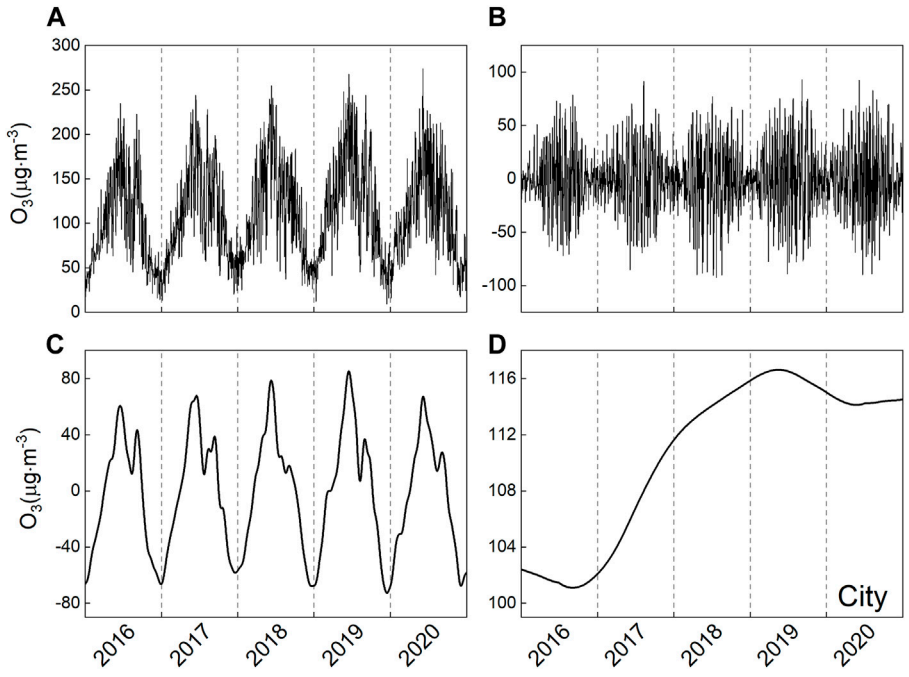

FIGURE 3
Separated time series of MDA8 of the ozone values during 2016–2020. **(A)** the original data; **(B)** the short-term component; **(C)** the seasonal component; **(D)** the long-term component.

From the above mentioned functions, the seasonal and short-term components can be calculated as follows:

$$S(t) = KZ_{(15,5)} - KZ_{(365,3)} \quad (6)$$

$$W(t) = X(t) - KZ_{(15,5)} \quad (7)$$

Ozone is still affected by meteorological conditions after *KZ* filtering. Linear stepwise regression (Version 22.0, SPSS) is used to eliminate these meteorological effects (Flaum et al., 1996). The decomposed baseline component and short-term component, along with the corresponding decomposed meteorological factors, are introduced into stepwise linear regression, and the O_3 statistical model is generated; the corresponding explanatory variance is subsequently given. The robustness of the stepwise linear regression model is tested using 10,000 times Monte Carlo simulation, based on the *t* distribution of the mean squared error of the model (Xiao et al., 2018). The R^2 distribution map is drawn based on this result. It is generally agreed that $R^2 > .64$ indicates that the model has an explanatory degree of 80%. The calculation method for variance explained is as follows (Wise and Comrie, 2005):

$$VE = \left(\frac{\text{var}\, X(t) - \text{var}\, \varepsilon(t)}{\text{var}\, X(t)}\right) \times 100\% \quad (8)$$

Where *VE* is the explained variance, var$X(t)$ is the variance of the original time series of ozone, and var$\varepsilon(t)$ is the variance of the residual series. Generally speaking, the smaller the residual sequence, the larger the interpretation variance, and the greater the explanatory power and influence degree of the meteorological conditions participating in the model construction on the time series of ozone.

O_3 was measured using online commercial gas analyser (Thermo Scientific 49i, United States), and the measurement method was UV photometric. Previous articles have been published using part of these data, for details see Li et al. (2021). In this study, ground observation data in accordance with the Technical Regulation for Ambient Air Quality Assessment (on trial) (HJ 663-2013) in the data statistical validity provisions, that is, the MDA8 within a natural day is specified as at least 14 valid 8-h average concentration values from 08:00 to 24:00 on that day. When the 14 valid data are not met, if the MDA8 concentration exceeds the concentration standard limit, the statistical results are still valid. For the treatment of missing data, KZ is an iterated moving average and can be used with missing values. Please see the introduction of KZA package in R for details.

3 Results and discussion

3.1 General characteristics of meteorology and ozone concentration

Major MET variables in Zibo City in 2016 and 2020 were compared. The monthly variation in (a) temperature, (b)

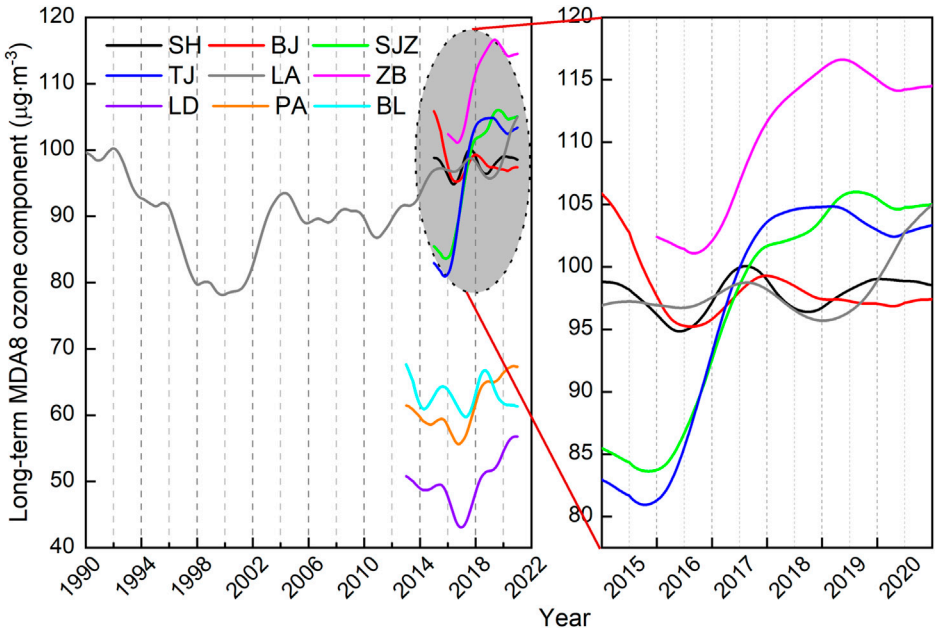

FIGURE 4
Evolution of urban surface MDA8 ozone levels in different cities. SH, Shanghai, BJ, Beijing, SJZ, Shijiazhuang, TJ, Tianjin, LA, Los Angeles, ZB, Zibo, LD, London, PA, Paris, BL, Berlin.

TABLE 1 Contribution of the KZ filter to the total variance of each component in the original MDA8 ozone.

Site	Contribution to the total variance (%)			
	Long-term	Seasonal	Short-term	Sum
DFCP	.67	59.87	34.51	95.06
PTY	.64	62.00	32.31	94.95
QXZ	.35	59.43	34.90	94.68
SJG	.82	61.66	32.27	94.75
SS	3.14	56.64	34.78	94.56
City	1.15	61.67	32.06	94.88

Note: DFCP, Dongfeng chemical plant; PTY, putianyuan; QXZ, Qixiangzhan; SJG, Sanjin Group; SS, Shuangshan.

relative humidity, and (c) wind speed in Zibo City in 2016 and 2020 are illustrated in Supplementary Figure S1. The annual average wind speed and relative humidity decreased (by .25 m/s and .79%, respectively), and the annual average temperature remained basically unchanged (14.3°C in 2016 and 14.2°C in 2020). The changes in the MET conditions will affect the concentration of pollutants. Therefore, it is of great significance to understand the effects of the MET conditions on the concentrations of pollutants to eliminate them.

The 90th percentile of MDA8 of the ozone concentration in Zibo City from 2016 to 2020 is between 184 and 203 μg m^{-3}, exceeding the secondary standard limit (160 μg m^{-3}) by 1.15–1.27 times. The annual ozone concentration reached a maximum in 2019 and a minimum in 2017. Another cumulative index for human health, the annual Sum of Ozone Means Over 35 ppb (SOMO35), was 1.27 × 10^4 ppb d–1.74 × 10^4 ppb d (1.55 × 10^4 ppb d, on average) from 2016 to 2020, which was higher than the highest SOMO35 (6.8 × 10^3 ppb d) reported in the southeastern Unites States in 2000 (Ellingsen

TABLE 2 Stepwise regression model for the baseline and short-term components of MDA8 ozone.

Component	Site	Regression model	VE (%)	N	R^2
$X_b(t)$	DFCP	4.5T-0.903RH+93.83	90.22	1827	.859
	QXZ	4.819T-1.375RH+124.755	86.82	1827	.868
	PTY	4.581T-0.585RH+17.248WS +47.594	87.74	1827	.877
	SJG	4.97T-1.153RH+116.797	90.62	1827	.906
	SS	4.559T-1.432RH-5.895WS+135.759	86.98	1827	.870
	City	4.374T-1.484RH-4.807WS+147.039	89.98	1827	.900
$W(t)$	DFCP	4.75T-0.934RH-8.880WS+0.061	32.78	1745	.326
	QXZ	4.909T-0.863RH-7.992WS-0.063	29.98	1777	.299
	PTY	4.405T-0.720RH-12.565WS+0.016	30.50	1773	.302
	SJG	4.772T-0.854RH-10.794WS-0.019	29.08	1777	.290
	SS	4.938T-0.744RH-3.724WS-0.056	33.59	1777	.335
	City	4.738T-0.881RH-7.703WS-0.101	35.17	1776	.351

Note: VE, explained variance, N, Total number of samples, R^2, square of correlation; DFCP, Dongfeng chemical plant; PTY, putianyuan; QXZ, Qixiangzhan; SJG, Sanjin Group; SS, Shuangshan.

et al., 2008), as well as the observed value (1.5×10^3–6.0×10^3) in France (Sicard et al., 2016).

In terms of monthly variations, as shown in Figure 2, the MDA8 is relatively high from April to September, while the MDA8 is relatively low from December to March of the following year. The highest MDA8 usually appeared in June and July. In terms of daily variations, the concentration of MDA8 ozone varies greatly, ranging from 9 to 274 μg m^{-3}. In terms of the inter-annual variation, an increasing trend can be observed. The overall variations of six percentiles (5%, 25%, 50%, 75%, 95% and 99%) based on the MDA8 ozone statistics were +2.2, +4.0, +4.5, +4.2, and +5.2 μg m^{-3} for the whole city during 2016–2020, indicating increases in all data segments and a relatively faster increase at the upper end of the ozone distribution.

In addition, the time when the MDA8 ozone concentration exceeded the secondary standard limit (160 μg m^{-3}) appeared earlier every year from 2016 to 2019. The first day of MDA8 exceeding 160 μg m^{-3} occurred on 30 April in 2016, on 7 April in 2017, on 25 March in 2018, on 10 March in 2019 and on 23 March in 2020. The MDA8 ozone concentration fluctuated greatly in the summer and remained relatively stable in winter.

3.2 O_3 time series after KZ filtering

3.2.1 Separated time series of MDA8 ozone

KZ filtering was performed on the MDA8 of the ozone sequence of Zibo City (Figure 3) and five sites (Supplementary Figure S2) to obtain the short-term, seasonal and long-term component sequences. It can be seen that, for all cases, there is high-frequency noise in the original time series of MDA8 ozone, which exhibits obvious seasonal characteristics. After removing the short-term component, caused by meso-scale and synoptic-scale meteorological processes (Yu et al., 2019), the seasonal component presents clearer and smoother periodic characteristics, with a trough from December to January of the following year, and with a peak in June. Every site in each year exhibited obvious bimodal peaks. In general, peaks occurred in June and September, and dips occurred in July or August. Owing to the influence of the monsoon climate, the precipitation was mainly concentrated from July to August. For example, the sum of the average precipitation in July to August from 2016 to 2020 was 373.2, 283.9, 422.6, 621.1, and 347.3 mm, respectively, accounting for 52.39%, 56.57%, 45.92%, 78.64% and 48.14% of the total annual average precipitation (Zibo City Statistical Yearbook, 2016, 2017, 2018, 2019, 2020). In additional to the precipitation, the high relative humidity, low temperature, cloudy days, and the clearance of the precursor also weaken the ozone formation (Boleti et al., 2018; Lin et al., 2021).

The long-term component clearly exhibits an upward trend of MDA8 ozone, and this trend is covered in the original time series by high-frequency noise (Yu et al., 2019). The variation shows an obvious increase in the study period for all cases, followed by a smooth or small fluctuation trend. The growth rates of the long-term component of the city is 3.19 μg m^{-3} yr^{-1} from 2016 to 2020. The growth rates of the long-term components of the DFCP, QXZ, PTY, SJG, and SS stations are 1.52, 1.61, 1.97, 1.99, and 5.95 μg m^{-3} yr^{-1}, respectively. The increase rate of the city is higher than the 2.42 μg m^{-3} yr^{-1} rate of the SDZ background station in Beijing (Ma et al., 2016), and is lower than the average value of 3.85 μg m^{-3} yr^{-1} in the YRD region during 2013–2017 (Yu et al., 2019).

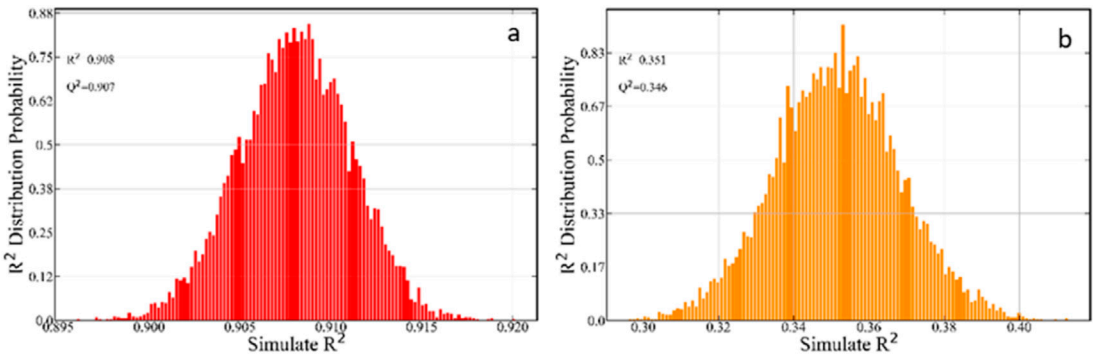

FIGURE 5
The results of 10,000 times Monte Carlo simulation based on the *t* distribution of the mean squared errors of the baseline component **(A)** and short-term component **(B)** regression models in the city.

The long-term component of MDA8 ozone for the city from 2016 to 2020 was compared with the long-term component of MDA8 ozone in Los Angeles from 1990 to 2020, and Beijing, Tianjin, Shijiazhuang, Shanghai, London, Paris, and Berlin in recent years (Figure 4). The trend of the long-term component of MDA8 ozone for compared cities was similar to those found in previous studies (Yu et al., 2020), which proves that our MLR method is reliable. In comparison to London, Paris, and Berlin, the concentration level in the selected cities in China was much higher. Further, there was a large increase from 2017 to 2019 for the long-term component trend of MDA8 ozone in this study, which is similar to that in Shijiazhuang, Tianjin, and Los Angeles in the early 21st century but in different years.

3.2.2 Contribution of each component to the total variance

To identify the contribution of each temporal component to the original ozone data, the variance of each generated time series was calculated and the contribution to the total variance of the original data was determined as shown in Table 1. Ideally, the long-term component, the seasonal component, and the short-term component should be independent of each other, that is, the variance of the original time series should be equal to the sum of the three component variances (Ibarra-Berastegia et al., 2001). The higher the sum of the contribution rate of each component to the variance of the total variance, the better the decomposition effect after filtering. The results from Table 1 show that the sum of the variance of the short-term, seasonal, and long-term components of MDA8 of ozone after KZ filter decomposition contributes 94.56%–95.06% to the variance of the original time series, indicating that the components basically meet the conditions of mutual independence.

The seasonal component contributes the most to the total variance of the original MDA8 ozone sequence (61.67%), followed by the short-term component (32.06%) and the long-term component (1.15%), demonstrating that ground ozone concentrations in the city were mainly affected by the variations in the seasonal and short-term meteorological conditions. These contributions were consistent with these found in previous studies (Ma et al., 2016; Cheng et al., 2019; Yu et al., 2019). For example, Ma (Ma et al., 2016) used KZ filtering to analyse the MDA8 of ozone of Beijing Shangdianzi (SDZ) background station from 2003 to 2015, revealing that the total variance of the seasonal and short-term component accounted for 57.6% and 36.4%, respectively.

It can be seen from Table 1 that the contribution of seasonal and short-term component dominated the variation of ozone for each station, with certain differences. For the SS site, the long-term component (3.14%) is significantly higher than that of the other four sites (.62% on average), while the seasonal component of the SS site (56.64%) is lower than that of the other four sites (average 60.71%). The long-term component represents the combined effects of different factors, such as pollutant emissions, climate change, and socioeconomic development. This site (SS) is located on a hill at an elevation of about 150 m, within 1 km radium, there is a main road on the west sides, and no other obvious sources of contamination. Relative to the other urban sites, the SS site is at higher altitude and may be more influenced by climate and atmospheric circulation in the long term. Therefore, the long-term component contribution of this site is large compared to other sites.

3.3 Quantitative assessment of the long-term impact of meteorological conditions

3.3.1 Multiple linear stepwise regression and robustness test

The time series decomposed by KZ filtering is still affected by some meteorological conditions, and multiple linear stepwise

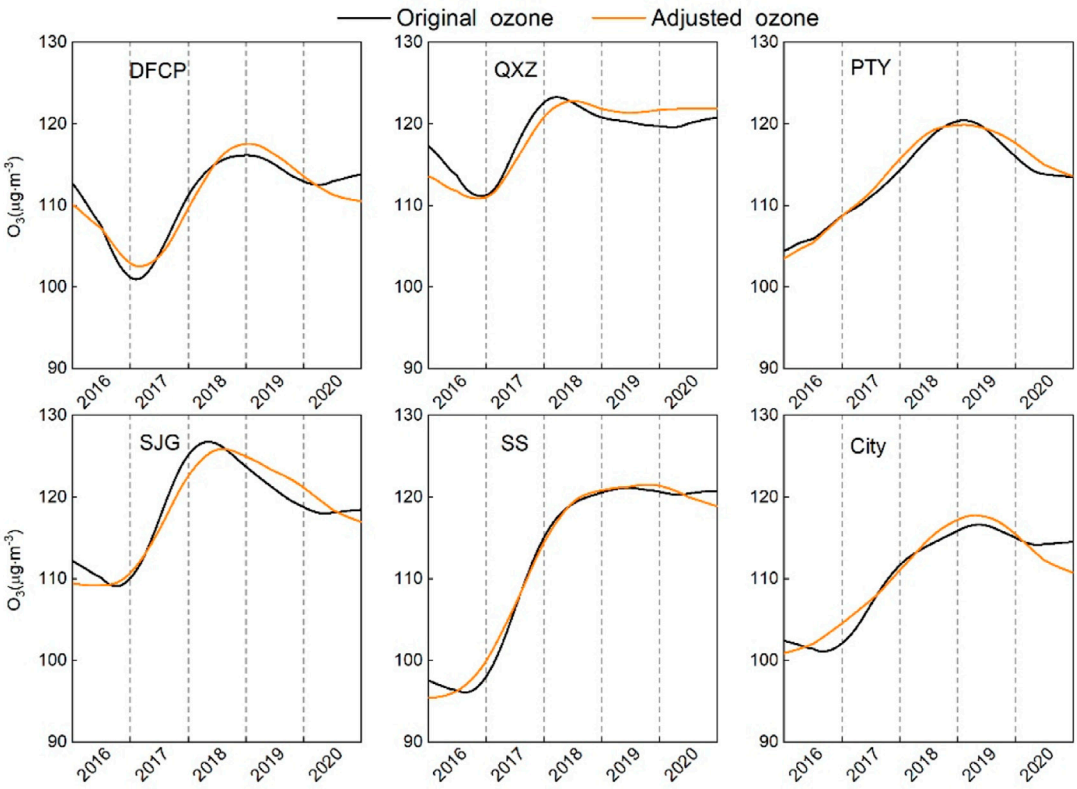

FIGURE 6
Variation in the ozone long-term component before and after meteorological adjustment. DFCP, Dongfeng Chemical Plant site, QXZ, Qixiangzhan, PTY, Putianyuan site, SJG, Sanjin Group site, SS, Shuangshan site and City: Zibo city.

regression is an effective measure to further eliminate meteorological conditions (Flaum et al., 1996). The filtered ozone time series was set as the dependent variable, and the filtered meteorological variable time series was set as the independent variable. By using multiple linear stepwise regression (SPSS 22.0), the model between the ozone and the meteorological conditions was established in terms of the baseline component and the short-term component, and the relationship formula is as follows (Cheng et al., 2019)

$$W(t) = a_0 + \sum a_i w_i(t) + \varepsilon_w(t) \quad (9)$$

$$X_b(t) = b_0 + \sum b_i x_i(t) + \varepsilon_b(t) \quad (10)$$

Where $W(t)$ and $w_i(t)$ are the short-term components of ozone and the ith meteorological conditions respectively. a_0 and a_i are regression coefficients. $\varepsilon_w(t)$ is the regression residual of the short-term component. $X_b(t)$ and $x_i(t)$ are the baseline components of ozone and the ith meteorological conditions, respectively. b_0 and b_i are regression coefficients. $\varepsilon_b(t)$ is the regression residual of the baseline component.

Table 2 shows the statistical model of multiple linear stepwise regression and the corresponding explanatory variance (Gao, et al., 2021). In terms of baseline components, the three meteorological factors explained 89.98% of the total ozone variance in the city, and the value ranged from 86.82% to 90.62% for the five sites. Temperature was positively correlated with MDA8 ozone and relative humidity was negatively correlated with MDA8 ozone. The coefficient of temperature was much higher than that of relative humidity. For wind speed, negative correlations existed for the city, which is consistent with the general finding that a high wind speed facilitates diffusion. However, for specific sites, positive correlations exist between wind speed and MDA8 ozone, which points to significant differences between sites. Monte Carlo simulation (Figure 5A, Supplementary Figure S3) shows that the simulated R^2 surpassed .64 for over 95% of the baseline component, indicating that the model might be reliable for potential quasi-quantitative prediction of the baseline component.

For the short-term component, the relationship between the ozone and the meteorological variables is relatively low, and the explained variance was 29.08%–33.59% (35.17% on average) for all monitoring sites. For this component, wind speed presents the highest explained variance, indicating that wind speed has a great impact on ozone over the short term. Monte Carlo simulation (Figure 5B) shows that the simulated

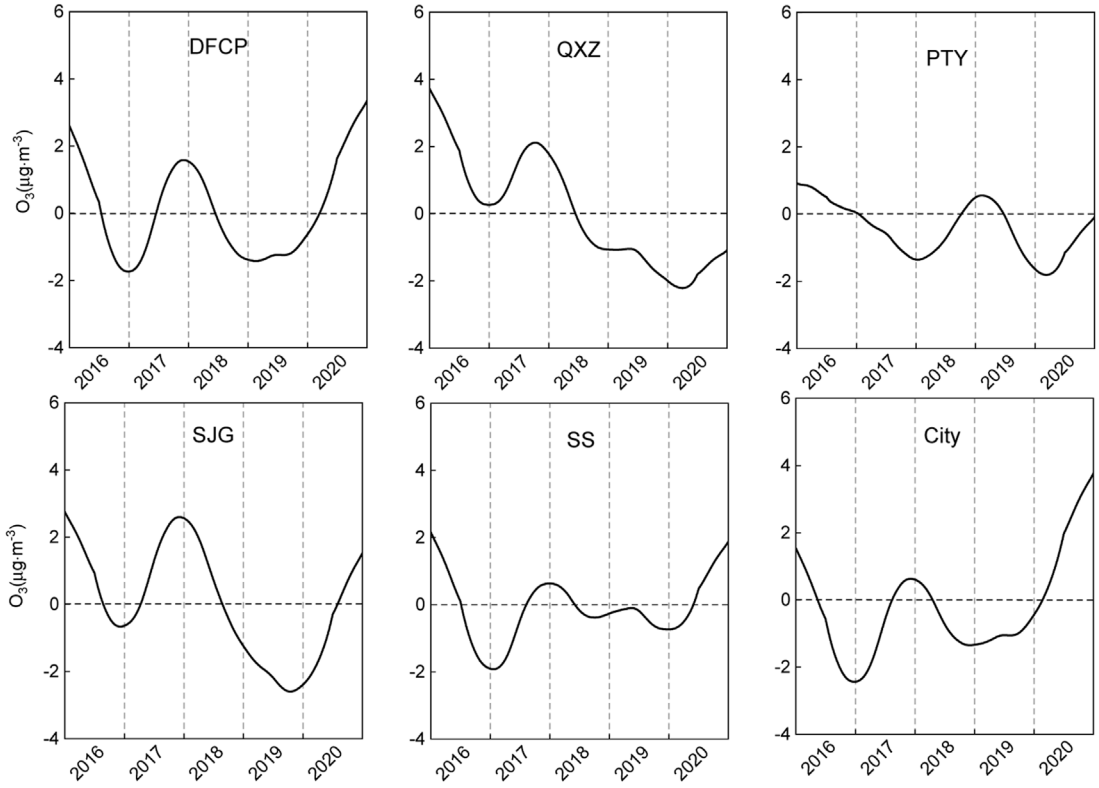

FIGURE 7
Assessment of the influence of weather conditions on the long-term variation of ozone in the city and five districts within the city. DFCP, Dongfeng Chemical Plant site, QXZ, Qixiangzhan, PTY, Putianyuan site, SJG, Sanjin Group site, SS, Shuangshan site and City: Zibo city.

R^2 is widely distributed between 0 and 1, and is smaller than .5 for all cases, indicating that the regression model was less robust (Xiao, et al., 2018).

3.3.2 Reconstruction of long-term ozone component time series

According to Eqs 9, 10, the fitting value of the short-term and the baseline component of ozone can be obtained, and it can be considered that the sum of the short-term and the baseline component primarily reflects the influence of meteorological factors. The residual error between the observed value of ozone and the fitted value is expressed as follows:

$$\varepsilon(t) = \varepsilon_b(t) + \varepsilon_w(t) \tag{11}$$

The residual sequence $\varepsilon(t)$ mainly represents ozone fluctuations caused by the changes in the emissions from the pollution source, but the series still contains the influence of meteorological conditions that are not considered in the regression fitting; further, there are also contributions from modelling errors and monitoring errors of ozone. In view of these factors, KZ $_{(m=365,\ p=3)}$ is used to filter $\varepsilon(t)$ again, and the filter result $\varepsilon_{LT}(t)$ represents the long-term change trend of ozone caused only by changes in the pollution source emissions. Although ε_{LT}(t) is filtered, it is still a residual sequence. To intuitively reflect the long-term component changes of O_3 caused by pollution emissions, $X_{LT}(t)$ is reconstructed (Cheng et al., 2019)

$$X_{LT}(t) = \bar{X}_{LT} + \varepsilon_{LT}(t) \tag{12}$$

Where $\varepsilon_{LT}(t)$ is the result of $\varepsilon(t)$ filtered by KZ $_{(m=365\ p=3)}$, $\bar{X}_{LT}$ is the mean value of the long-term ozone component; $X_{LT}(t)$ is the adjusted and reconstructed long-term ozone component time series, which eliminates the impact of the meteorological conditions, and is only related to pollution source emissions.

Figure 6 shows the variation of the long-term ozone component before and after meteorological adjustment. The red curve represents the long-term change trend of the ozone component after the meteorological influence is eliminated. This series only reflects the variation caused by pollutant emissions. It can be seen that, due to the variation in pollutant emissions, the long-term component of ozone for the city exhibited an overall upward trend in 2016–2018 and a downward trend in 2019–2020. In 2018, the People's Government of Zibo issued the "Three-Year

Implementation Plan for Zibo to Win the Blue Sky Defense War (2018–2020)," which pointed out that the trend of rising O_3 concentration must be significantly curbed by 2020 (http://www.zibo.gov.cn). This indicates that the action plan that began in 2018 has greatly reduced anthropogenic emissions in the city. In terms of the specific districts, the long-term component of ozone in the PTY site exhibited an upward in 2016–2018 and a downward trend in 2019–2020. The QXZ site exhibited a downward trend in 2016, an upward trend in 2017–2018, and no significant variation in 2019–2020. In addition, the SS site does not change much after the meteorological impact is eliminated. This is because the site is a hillside site with a high altitude, relatively good diffusion conditions, relatively large surrounding vegetation coverage, and has less impact from anthropogenic emissions.

The impact of meteorological conditions on the long-term component of ozone can be expressed more directly by calculating the difference between the long-term components before and after adjustment, as shown in Figure 7. If the difference (the ozone concentration before adjustment minus that after) is positive, the meteorological condition does not favour ozone generation. For the city, during the periods from January to May 2016, from July 2017 to April 2018, and from March 2020 to December 2020, the meteorological conditions are not conductive to the improvement of ozone concentrations, increasing the long-term component of ozone by .69, .38, and 2.11 μg m^{-3}, respectively. However, from June 2016 to July 2017 and from May 2018 to February 2020, the meteorological conditions are conducive to the abatement of ozone, reducing the long-term components of ozone by 1.62 and .95 μg m^{-3}, respectively. The overall meteorological impact was not stable and fluctuated between −2.60 and +3.77 μg m^{-3}.

4 Conclusion

KZ filtering is used to decompose the ozone time series into long-term, seasonal, and short-term components in Zibo City and the five stations in this city. Monte Carlo simulation was used to evaluate the reliability of the potential quasi-quantitative prediction of the baseline component. The impact of meteorological parameters on the ozone concentration for the past 5 years (2016–2020) was studied.

The seasonal component contributes the most to the total variance of the original MDA8 ozone sequence (61.67%), followed by the short-term component (32.06%) and the long-term component (1.15%). The growth rate of the long-term component in the city is 3.19 μg m^{-3} yr^{-1} from 2016 to 2020. The growth rates of the long-term component for the DFCP, QXZ, PTY, SJG, and SS stations are 1.52, 1.61, 1.97, 1.99, and 5.95 μg m^{-3} yr^{-1}, respectively. After the meteorological adjustment, the long-term component of ozone for the city exhibited an overall upward trend in 2016–2018 and a downward trend in 2019–2020. This transition time was consistent with the implementation of the Blue Sky Defense Action Plan, which began in 2018. The overall meteorological impact was not stable and fluctuated between −2.60 and +3.77 μg m^{-3}.

In this study, the time period was from 2016 to 2020, as the O_3 monitoring started in 2016 for all cities in China. When more data is available, further evaluations should be conducted. In addition, if more data is available, the influence of solar radiation, the dew-point, the boundary layer height and other pollutants on O_3 concentration could also be analysed using the method in this study.

Data availability statement

The original contributions presented in the study are included in the article/Supplementary Material, further inquiries can be directed to the corresponding authors.

Author contributions

ML, CG, and XW designed the research and led the overall scientific questions. LL, WY, and BX carried out data processing and analysis. ZZ helped with code programming. ML wrote the manuscript and then CG and XW revised the manuscript. All authors read and approved the submitted version.

Funding

This work was supported by Center for Air Pollution Prevention and Control (Nos. DQGG202119 and DQGG202137).

Conflict of interest

The authors declare that the research was conducted in the absence of any commercial or financial relationships that could be construed as a potential conflict of interest.

Publisher's note

Supplementary material

The Supplementary Material for this article can be found online at: https://www.frontiersin.org/articles/10.3389/fenvs.2022.1081453/full#supplementary-material

References

Agudelo-Castaneda, D. M., Teixeira, E. C., and Pereira, F. N. (2014). Time–series analysis of surface ozone and nitrogen oxides concentrations in an urban area at Brazil. *Atmos. Pollut. Res.* 5, 411–420. doi:10.5094/APR.2014.048

Anh, V., Duc, H., and Azzi, M. (1997). Modeling anthropogenic trends in air quality data. *J. Air Waste Manage. Assoc.* 47 (1), 66–71. doi:10.1080/10473289.1997.10464406

Boleti, E., Hueglin, C., and Takahama, S. (2018). Ozone time scale decomposition and trend assessment from surface observations in Switzerland. *Atmos. Environ.* 191, 440–451. doi:10.1016/j.atmosenv.2018.07.039

Botlaguduru, V. S. V., Kommalapati, R. R., and Huque, Z. (2018). Long-term meteorologically independent trend analysis of ozone air quality at an urban site in the greater Houston area. *J. Air Waste Manage. Assoc.* 68, 1051–1064. doi:10.1080/10962247.2018.1466740

Cheng, N. L., Li, R. Y., Xu, C. X., Chen, Z. Y., Chen, D. L., Meng, F., et al. (2019). Ground ozone variations at an urban and a rural station in Beijing from 2006 to 2017: Trend, meteorological influences and formation regimes. *J. Clean. Prod.* 235, 11–20. doi:10.1016/j.jclepro.2019.06.204

Ellingsen, K., Gauss, M., Dingenen, R. V., Dentener, F. J., Emberson, L., Fiore, A. M., et al. (2008). Global ozone and air quality: A multi-model assessment of risks to human health and crops. *Atmos. Chem. Phys. Discuss.* 8, 2163–2223. doi:10.7916/D8M32VD4

Eskridge, R. E., Ku, J. Y., Rao, S. T., Porter, P. S., and Zurbenko, I. G. (1997). Separating different scales of motion in time series of meteorological variables. *Bull. Am. Meteorol. Soc.* 78, 1473–1483. doi:10.1175/1520-0477(1997)078<1473:sdsomi>2.0.co;2

Flaum, J. B., Rao, S. T., and Zurbenko, I. G. (1996). Moderating the influence of meteorological conditions on ambient ozone concentrations. *J. Air Waste Manage. Assoc.* 46, 35–46. doi:10.1080/10473289.1996.10467439

Gao, S., Bai, Z. P., Liang, S., Yu, H., Chen, L., Sun, Y. L., et al. (2021). Simulation of surface ozone over Hebei province, China using Kolmogorov-Zurbenko and artificial neural network (KZ-ANN) combined model. *Atmos. Environ.* 261, 118599. doi:10.1016/j.atmosenv.2021.118599

Huang, J. P., Zhou, C. H., Lee, X. H., Bao, Y. X., Zhao, X. Y., Fung, J., et al. (2013). The effects of rapid urbanization on the levels in tropospheric nitrogen dioxide and ozone over East China. *Atmos. Environ.* 77, 558–567. doi:10.1016/j.atmosenv.2013.05.030

Ibarra-Berastegia, G., Madariagab, I., Elıasb, A., Agirrec, E., and Uria, J. (2001). Long-term changes of ozone and traffic in Bilbao. *Atmos. Environ.* 35, 5581–5592. doi:10.1016/S1352-2310(01)00210-2

Kang, D. W., Hogrefe, C., Foley, K. L., Napelenok, S. L., Mathur, R., and Rao, S. T. (2013). Application of the Kolmogorov–Zurbenko filter and the decoupled direct 3D method for the dynamic evaluation of a regional air quality model. *Atmos. Environ.* 80, 58–69. doi:10.1016/j.atmosenv.2013.04.046

Kuerban, M., Waili, Y., Fan, F., Liu, Y., Qin, W., Dore, A. J., et al. (2020). Spatio-temporal patterns of air pollution in China from 2015 to 2018 and implications for health risks. *Environ. Pollut.* 258, 113659. doi:10.1016/j.envpol.2019.113659

Li, K. W., Wang, X. H., Li, L. M., Wang, J., Liu, Y. Y., Cheng, X., et al. (2021). Large variability of O_3-precursor relationship during severe ozone polluted period in an industry-driven cluster city (Zibo) of North China Plain. *J. Clean. Prod.* 316, 128252. doi:10.1016/j.jclepro.2021.128252

Lin, C. Q., Lau, A. K. H., Fung, J. C. H., Song, Y. S., Li, Y., Tao, M. H., et al. (2021). Removing the effects of meteorological factors on changes in nitrogen dioxide and ozone concentrations in China from 2013 to 2020. *Sci. Total Environ.* 793, 148575. doi:10.1016/j.scitotenv.2021.148575

Luo, H., Astithaa, M., Hogrefe, C., Mathurb, R., and Rao, S. T. (2019). A new method for assessing the efficacy of emission control strategies. *Atmos. Environ.* 199, 233–243. doi:10.1016/j.atmosenv.2018.11.010

Luo, Y. Y., Zhou, X. H., Zhang, J. Z., Xiao, Y., Wang, Z., Zhou, Y., et al. (2018). $PM_{2.5}$ pollution in a petrochemical industry city of northern China: Seasonal variation and source apportionment. *Atmos. Res.* 212, 285–295. doi:10.1016/j.atmosres.2018.05.029

Ma, Z. Q., Xu, J., Quan, W. J., Zhang, Z. Y., Lin, W. L., and Xu, X. B. (2016). Significant increase of surface ozone at a rural site, north of eastern China. *Atmos. Chem. Phys.* 16, 3969–3977. doi:10.5194/acp-16-3969-2016

Papanastasiou, D. K., Melas, D., Bartzanas, T., and Kittas, C. (2012). Estimation of ozone trend in central Greece, based on meteorologically adjusted time series. *Environ. Model Assess.* 17, 353–361. doi:10.1007/s10666-011-9299-6

Porter, P. S., Rao, S. T., Zurbenko, I. G., Dunker, A. M., and Wolff, G. T. (2001). Ozone air quality over north America: Part II—an analysis of trend detection and attribution techniques. *J. Air Waste Manage. Assoc.* 51 (2), 283–306. doi:10.1080/10473289.2001.10464261

Rao, S. T., and Zurbenko, I. G. (1994). Detecting and tracking changes in ozone air quality. *J. Air Waste Manage. Assoc.* 44, 1089–1092. doi:10.1080/10473289.1994.10467303

Rao, S. T., Zurbenko, I. G., Neagu, R., Porter, P. S., Ku, J. Y., and Henry, R. F. (1997). Space and time scales in ambient ozone data. *Bull. Am. Meteorol. Soc.* 78, 2153–2166. doi:10.1175/1520-0477(1997)078<2153:satsia>2.0.co;2

Sa, E., Tchepel, O., Carvalho, A., and Borrego, C. (2015). Meteorological driven changes on air quality over Portugal: A KZ filter application. *Atmos. Pollut. Res.* 6, 979–989. doi:10.1016/j.apr.2015.05.003

Seo, J., Youn, D., Kim, J. Y., and Lee, H. (2014). Extensive spatiotemporal analyses of surface ozone and related meteorological variables in South Korea for the period 1999–2010. *Atmos. Chem. Phys.* 14, 6395–6415. doi:10.5194/acp-14-6395-2014

Sicard, P., Serra, R., and Rossello, P. (2016). Spatiotemporal trends in ground-level ozone concentrations and metrics in France over the time period 1999–2012. *Environ. Res.* 149, 122–144. doi:10.1016/j.envres.2016.05.014

Wang, N., Lyu, X. P., Deng, X. J., Huang, X., Jiang, F., and Ding, A. J. (2019). Aggravating O_3 pollution due to NO_x emission control in eastern China. *Sci. Total Environ.* 677, 732–744. doi:10.1016/j.scitotenv.2019.04.388

Wang, T., Xue, L. K., Brimblecombe, P., Lam, Y. F., Li, L., and Zhang, L. (2017). Ozone pollution in China: A review of concentrations, meteorological influences, chemical precursors, and effects. *Sci. Total Environ.* 575, 1582–1596. doi:10.1016/j.scitotenv.2016.10.081

Wise, E. K., and Comrie, A. C. (2005). Meteorologically adjusted urban air quality trends in the Southwestern United States. *Atmos. Environ.* 39, 2969–2980. doi:10.1016/j.atmosenv.2005.01.024

Xiao, K., Shen, Y. X., Liang, S., Tan, J. H., Wang, X. M., Liang, P., et al. (2018). Characteristic regions of the fluorescence excitation–emission matrix (EEM) to identify hydrophobic/hydrophilic contents of organic matter in membrane bioreactors. *Environ. Sci. Technol.* 52, 11251–11258. doi:10.1021/acs.est.8b02684

Yu, Y. J., Meng, X. Y., Wang, Z., Zhou, W., and Yu, H. X. (2020). Driving factors of the significant increase in surface ozone in the Beijing-Tianjin-Hebei region, China, during 2013-2018. *Environ. Sci.* 41 (1), 106–114. doi:10.13227/j.hjkx.201905222

Yu, Y. J., Wang, Z., He, T., Meng, X. Y., Xie, S. Y., and Yu, H. X. (2019). Driving factors of the significant increase in surface ozone in the Yangtze River Delta, China, during 2013–2017. *Atmos. Pollut. Res.* 10, 1357–1364. doi:10.1016/j.apr.2019.03.010

Zhang, Z. Y., Zhang, X. l., Gong, D. Y., Quan, W. J., Zhao, X. J., Ma, Z. Q., et al. (2015). Evolution of surface O_3 and $PM_{2.5}$ concentrations and their relationships with meteorological conditions over the last decade in Beijing. *Atmos. Environ.* 108, 67–75. doi:10.1016/j.atmosenv.2015.02.071

Zong, L., Yang, Y. J., Gao, M., Wang, H., Wang, P., Zhang, H. L., et al. (2021). Large-scale synoptic drivers of co-occurring summertime ozone and $PM_{2.5}$ pollution in eastern China. *Atmos. Chem. Phys.* 21, 9105–9124. doi:10.5194/acp-21-9105-2021

Zong, L., Yang, Y. J., Xia, H. Y., Gao, M., Sun, Z. B., Zheng, Z. F., et al. (2022). Joint occurrence of heatwaves and ozone pollution and increased health risks in beijing, China: Role of synoptic weather pattern and urbanization. *Atmos. Chem. Phys.* 22, 6523–6538. doi:10.5194/acp-22-6523-2022

frontiers | Frontiers in Environmental Science

TYPE Methods
PUBLISHED 26 April 2023
DOI 10.3389/fenvs.2023.1112874

OPEN ACCESS

EDITED BY
Gen Zhang,
Chinese Academy of Meteorological Sciences, China

REVIEWED BY
Zang Kunpeng,
Zhejiang University of Technology, China
Ning Zong,
Lhasa Ecological Research Station, Chinese Academy of Sciences, Dagze County, Lhasa, Tibet Autonomous Region, China

*CORRESPONDENCE
Mei Huang,
huangm@igsnrr.ac.cn

SPECIALTY SECTION
This article was submitted to Atmosphere and Climate, a section of the journal Frontiers in Environmental Science

RECEIVED 30 November 2022
ACCEPTED 28 March 2023
PUBLISHED 26 April 2023

CITATION
Hu L, Wang Z, Huang M, Sun H and Wang Q (2023), A remote sensing based method for assessing the impact of O_3 on the net primary productivity of terrestrial ecosystems in China.
Front. Environ. Sci. 11:1112874.
doi: 10.3389/fenvs.2023.1112874

A remote sensing based method for assessing the impact of O_3 on the net primary productivity of terrestrial ecosystems in China

Lin Hu[1,2], Zhaosheng Wang[1], Mei Huang[1]*, Hongfu Sun[2] and Qinyi Wang[3]

[1]National Ecosystem Science Data Center, Key Laboratory of Ecosystem Network Observation and Modeling, Institute of Geographic Sciences and Natural Resources Research, Chinese Academy of Sciences, Beijing, China, [2]College of Geoscience and Surveying Engineering, China University of Mining and Technology, Beijing, China, [3]Key Laboratory of Regional Ecology and Environmental Change, School of Geography and Information Engineering, China University of Geosciences, Wuhan, China

O_3 pollution in China has been increasing in recent years, but the process of O_3 impact on net primary productivity of terrestrial ecosystems remains unclear. We attempts to explore a remote sensing-based method to assess the impact of O_3 on NPP of China's terrestrial ecosystems by combining MODIS NPP and the latest ground observation data of O_3 concentration. By comparing the NPP data of MODIS image pixels with the 6-year average AOT40 data of corresponding pixels, we extracted the signal data that highlighted the effects of O_3 on NPP and established the response relationships between AOT40 and NPP. It was found that NPP was significantly negatively correlated with AOT40 in farmland and grassland ecosystems in China (farmland: r = 0.8674, $p < 0.003$, grassland: r = 0.7181, $p < 0.03$). Then the response relationships were adopted to evaluate the effect in China in 2014. The results showed that the estimated percentage of O_3-induced NPP decline was in the range of 5%–35%. Among them, the most significant declines were found in farmland ecosystems, with the vast majority of declines in 10%–35%. The decrease rate of evergreen coniferous forests ranked second, mostly in the range of 15%–20%. The grassland ecosystems declined at a lower rate, almost between 5% and 15%. And the evergreen broad-leaved forests has the lowest decline rate, most distributed in 0%–5%. The highest percentage decreases were mainly found in the Beijing-Tianjin-Hebei region and Shandong Province. And the decline rate of farmland ecosystems was significantly higher than other ecosystem types.

KEYWORDS

ozone pollution, MODIS NPP, AOT40, net primary productivity, China

1 Introduction

Net primary productivity (NPP) is the total amount of organic matter fixed by vegetation per unit time and area, which reflects the capacity of vegetation to absorb carbon dioxide and is an important indicator to evaluate plant growth (Ma et al., 2022). Factors affecting NPP include temperature, precipitation, solar radiation, human activities and regional vegetation types (Tu et al., 2023; Xu et al., 2023). Surface O_3 is mostly a secondary pollutant generated from nitrogen oxides (NOx) and volatile organic compounds (VOCs) as precursors (Feng et al., 2018). When excessive O_3 enters plant cells, it causes damage or death of plant cells,

and affects plant photosynthesis and respiration, thus affecting the NPP of terrestrial ecosystems (Feng et al., 2018). With the rapid economic development of China in recent years, the emission of NOx and VOCs from industries has increased, and O_3 pollution has become increasingly aggravated. Additionally, China has become one of the most serious countries in the world in terms of O_3 pollution (Wang et al., 2008). According to the 2019 China Ecological Environment Bulletin, China's air quality improved greatly during the 13th Five-Year Plan period, with the concentration of the atmospheric pollutant PM2.5 and other indicators decreasing. However, research (Zeng et al., 2019) showed that O_3 concentrations have been on a continuous upward trend from 2013–2017 and have become the primary atmospheric pollutant. It was (Ren and tian., 2007) predicted that 50% of forest ecosystems on land will be exposed to high O_3 concentrations (>60 ppb) by 2,100, and forest productivity will be greatly affected. However, there are fewer domestic studies on the long-term effects of O_3 on ecosystems due to the difficulty of observations and experiments (Ren and tian., 2007). Among foreign studies, Shimzu et al. (2019) selected the Kanto region of Japan as the study area, constructed AOT40-NPP response relationships for different ecosystems, and assessed the effects of O_3 on NPP of vegetation such as evergreen coniferous forests in 2013. However, most domestic studies have focused on the effects of temperature and precipitation on NPP, such as Pan et al. (2015) studied the effects of climate change and extreme climate on global NPP in the first decade of the 21st century. Liu et al. (2018) studied the spatial pattern of grassland NPP and its relationship with hydro-thermal factors in China from 1993 to 2015. Some scholars have also conducted studies on the effects of O_3 on NPP (Ren and tian., 2007), who explored the effects of O_3 on the main processes of photosynthesis, allocation, growth and yield formation of terrestrial ecosystem productivity and its long-term effects on the whole ecosystem. In summary, it is necessary to study the effects of O_3 pollution on terrestrial ecosystem productivity in depth, but there is a lack of quantitative research on the effects of O_3 on NPP and a lack of research on O_3 pollution at the ecosystem level in China (Feng et al., 2019).

The effects of O_3 on plants are usually studied by controlled experiments using Open-Top Chamber (OTC) experiments or Free Air Control Enrichment (FACE) experiments, and the construction of response relationships helps to quantify the effects of O_3 on plants and to assess the effects of O_3 on plants over a large area. Most of the existing studies in China have constructed response relationships based on OTC_S and O_3-FACE mainly for major crop yields in China (Feng et al., 2020; Feng and peng, 2021), including winter wheat (Chen et al., 2011; Feng et al., 2011), rice (Pang et al., 2009; Shi et al., 2009; Luo et al., 2012), soybean (Yang et al., 2010), maize, oilseed rape (Bai et al., 2003; Feng et al., 2006), and spinach (Bai et al., 2004). Methods based on OTC_S and O_3-FACE controlled experiments can study response relationships more precisely, but they can only be based on a limited area, and their observation time is short, which is not conducive to the macroscopic assessments of ecosystems. In addition the quantitative study of the impact of O_3 on terrestrial ecosystems NPP is lacking in China. The studies on O_3 pollution effects were mostly focused on the more serious O_3 pollution regions such as Beijing-Tianjin-Hebei, Yangtze River Delta, and Pearl River Delta (Feng et al., 2020). But the limited number of stations is not conducive to the study at the ecosystem level. In summary, more complete data and new methods are needed to study the effect of O_3 on the NPP of ecosystems.

Remote sensing is a detection technology that emerged in the 1960s, which is based on the theory of electromagnetic waves, applying various sensors to collect, process, and finally image the electromagnetic wave information radiated and reflected by distant targets, so as to detect and identify various scenes on the ground. It has the advantage of efficiently collecting data over a large area. Based on the remote sensing information such as temperature, precipitation, and vegetation obtained from the MODIS sensor carried on the satellite, MOD17A3H NPP data were simulated using a productivity model, which has reliable simulation accuracy and can be inverted to obtain a nationwide NPP. The effects of O_3 on natural ecosystems have been studied mainly by observing O_3 concentrations and O_3 fluxes on terrestrial ecosystems and a series of O_3 concentration and flux assessment indicators, such as the dose response indicator AOT40, have been proposed. By constructing the response relationships between AOT40 and NPP, the impact assessment can be extended to a large regional scale.

Therefore, based on the latest release of ambient air quality site data, we use a new data processing method to produce a ground-based site observation O_3 concentration dataset with increased temporal resolution to hourly and spatial coverage across China. By combining multi-year (2014–2019) MOD17A3H NPP data with the O_3 concentration dataset, we aim to explore a method to establish the AOT40-NPP response relationships for evergreen broad-leaved forests, evergreen coniferous forests, grassland, and farmland ecosystems in China. We also apply this response relationships to assess the impact of O_3 on the NPP of terrestrial ecosystems in China, thus attempting to quantify the impact. The methods used to construct the AOT40-NPP response relationships in this paper include: 1) using the Mann-Kendall mutation test to test for the presence of change mutation points. 2) Based on the idea of Jarvis multiplicative model, we proposed two constraints so as to isolate the signal data that can highlight the influence as the sample data for calculating the response relationships. 3) We selected the corresponding sample data to calculate the AOT40-NPP response relationships and their normalized slopes for evergreen coniferous forests, evergreen broad-leaved forests, farmland, and grassland ecosystems. 4) We apply the established response relationships to 2014 to assess the impact of O_3 on terrestrial ecosystem NPP.

Section 2 introduces the study area, the spatial distribution of the four ecosystem types, small study areas according to climate zones and the spatial distribution of the ground-based observation sites for O_3 concentration. The original data and data processing methods used are also introduced, including: O_3 ground observation site data, MODI7A3H NPP data, and ecosystem classification data. Among them, the data cleaning methods used are described in detail. In addition, the monthly and annual cumulative values of AOT40 in the whole country and different ecosystem types were calculated. Section 3 presents the specific methods and steps to construct the AOT40-NPP response relationships. Section 4 shows the spatial and temporal distribution characteristics and multi-year change rates of the annual average AOT40 and NPP values for the whole country and different ecosystem types from 2014 to 2019, the correlation between the annual average AOT40 and NPP values, the constructed AOT40-NPP response relationships for the four major ecosystems, and the spatial distribution of the percentage of O_3-

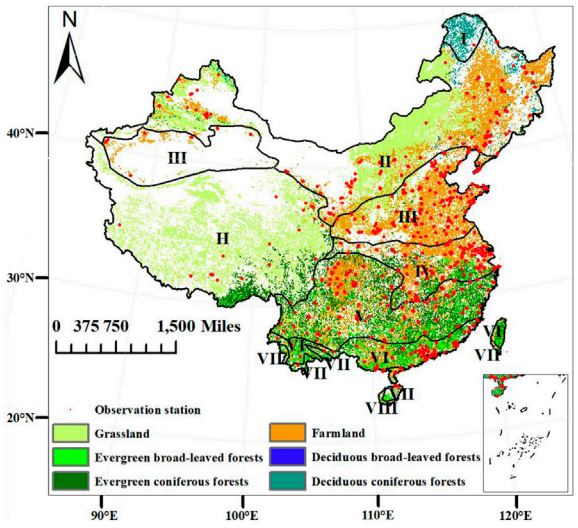

FIGURE 1
Spatial coverage map of six major ecosystem types (from China Cover 2010) and spatial distribution map of O_3 ground observation stations in China, 2010 (from the China Air Quality Real-time Publishing Platform of China Environmental Monitoring Station, http://www.cnemc.cn/sssj/), Climate zoning data (from Resource and Enviroment Science and Data Center, https://www.resdc.cn/Datalist1.aspx?FieldTyepID=4,5).

induced NPP decline. Section 5 discusses the results of this study. Section 6 presents the conclusions.

2 Materials and methods

2.1 Study area

Remote sensing observation has the advantage of collecting large area data efficiently. Therefore, We combines MODIS data to expand the research area to the whole China, and studies the four ecosystems of evergreen coniferous forests, evergreen broad-leaved forests, farmland and grassland. Differences in temperature and precipitation in different regions will affect the NPP differently. In order to reduce the interference of climatic factors in the study, the whole Chinese region was divided into some small study regions based on climatic zones, namely,: I: North Temperate Zone, II: Middle Temperate Zone, III: South Temperate Zone, IV: North Subtropics, V: Middle Subtropics, VI: South Subtropics, VII: North Subtropics, VIII: Middle Tropics, H: Plateau Climate Zone. Figure 1 shows that farmland ecosystems are found mainly in III, parts of the II and the northernmost parts of IV, grassland ecosystems are found mainly in II and H, evergreen coniferous and evergreen broad-leaved forests are found mainly in V, VI, VII, and deciduous coniferous forests are found mainly in I.

2.2 MODIS NPP

The MODIS NPP data used in this paper is derived from the United States Geological Survey (LP DAAC - MOD17A3H (usgs.gov)). The time series is from 2014 to 2019, the spatial resolution is 500 m, the time resolution is 1 year, and the spatial coordinate system is WGS-1984 coordinate system (Liu et al., 2018). Remote sensing technology has the advantage of collecting large area data efficiently, which is suitable for constructing response relationships.

Based on the original data, we carried out the following processing in turn: extracting China's regional data, removing non-vegetation data, adjusting the spatial resolution to 10 km, calculating the true value of NPP and unit conversion. Finally, we get the true value of NPP, whose unit is $gC/m^2/yr$.

2.3 Processing O_3 concentration data

2.3.1 O_3 concentration data

The original O_3 concentration data used in this paper comes from the China Air Quality Real-time Publishing Platform of China Environmental Monitoring Station (http://www.cnemc.cn/sssj/). There are about 1521 O_3 monitoring stations distributed in the whole country. The time series is from 2014 to 2019, the time resolution is 1h, and the unit is ug/m^3. The specific information of the data is shown in Table 1.

The hourly O_3 concentration observation data were recorded at 1,521 stations across the country, and the invalid data included two categories: One is that some stations are invalid due to equipment damage and other reasons, and the observed data at all times are invalid values; the other is that some sites have default values in time series due to instrument damage and other reasons in some time periods, including " _ ", " −99"or " NAN " values.

2.3.2 O_3 concentration data processing

O_3 concentration data are usually derived from ground observation, remote sensing monitoring, model simulation, etc. With the significant increase in the number of ambient air quality sites in recent years, the new O_3 concentration data provides data support for research work. Therefore, based on the newly released O_3 ground observation station data, we obtains a data set closer to the real O_3 concentration on the surface. It has a spatial resolution of 10 km and a temporal resolution of 1h, and covers the whole China region spatially with a time series of 2014–2019. The data processing method is mainly divided into two parts: O_3 concentration data cleaning and China regional spatial interpolation.

The main purpose of data cleaning is to replace the default values. Due to the obvious monthly and daily variation of O_3 concentration, O_3 pollution is mainly concentrated in June and July in summer, spring and autumn come in second place, and basically no pollution in winter (Zhang et al., 2022). In the diurnal variation, the O_3 concentration usually reaches a low value at 6 : 00–7 : 00, then the concentration rises rapidly, the concentration reaches a peak around 14 : 00–15 : 00, and then begins to decline until the next morning. The O_3 concentration remained at a low value at night (Wang et al., 2017; Lin et al., 2022; Zhang et al., 2022). Therefore, spatial coordinate matching is first performed on the original input data. Secondly, the original data is cleaned, as shown in Figure 2. The O_3 concentration data of each hour are judged as normal value or default value, and the original observation data are retained when judged as normal value; when it is judged to be the

TABLE 1 O_3 concentration data of ground observation stations.

Data year	Effective number of ground stations/total number of stations (n)	Temporal resolution	Unit	Data size
2014	942/1,521	hourly	Ug/m³	365 days*24 h*n
2015	Jan-Feb:1,494/1,521	hourly	Ug/m³	365 days*24 h*n
	Mar: 1,495/1,521			
	Apr: 1,496/1,521			
	May-Jun: 1,497/1,521			
	Jul: 1,498/1,521			
	Aug-Dec:1,519/1,521			
2016	1,492/1,521	hourly	Ug/m³	365 days*24 h*n
2017	1,521/1,521	hourly	Ug/m³	365 days*24 h*n
2018	1,521/1,521	hourly	Ug/m³	365 days*24 h*n
2019	1,521/1,521	hourly	Ug/m³	365 days*24 h*n

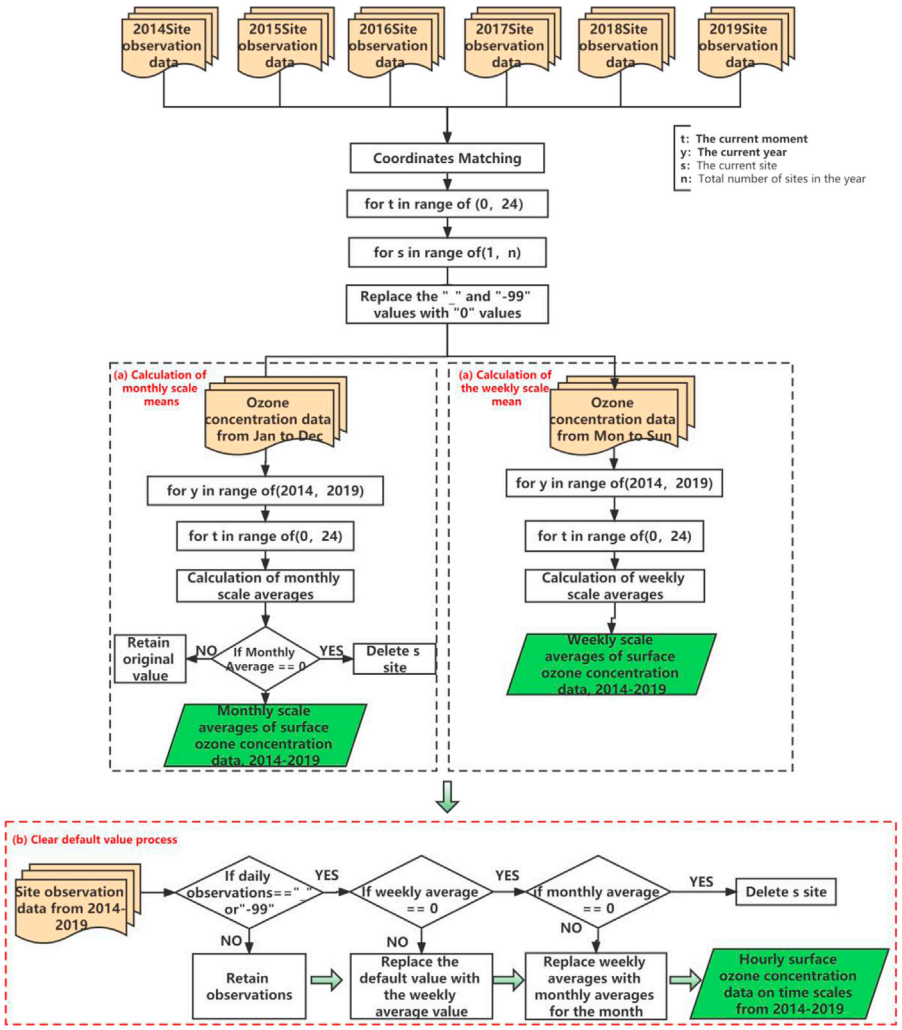

FIGURE 2
Process of surface observation O_3 concentration data cleaning algorithm.

default value, the O_3 concentration at the site and time of the default value is estimated and replaced. The estimation of the default data is achieved by calculating the monthly scale mean and the weekly scale mean for each hour. The monthly scale mean refers to the arithmetic mean of the daily evaluation concentration in a calendar month, and the weekly scale mean refers to the arithmetic mean of the daily evaluation concentration in a calendar week. If the monthly scale mean is 0, representing that the current site has no valid data in this month's measurement, the current invalid site is deleted directly. If the monthly mean is not 0, the weekly mean continues to be calculated. Finally, the monthly and weekly mean values of surface O_3 concentration data from 2014 to 2019 were obtained. For the replacement process of the default value, the first step is to determine whether the observation value at the current time of the current site is valid data. If it is a default value, it is replaced in order of priority according to the weekly mean and monthly mean.

ArcGIS 10.6 software was used for spatial interpolation. The inverse distance interpolation method was selected, in which the number of adjacent points was 20 and the power was 2, so as to obtain the hourly O_3 concentration data set with full coverage in China.

2.4 Annual AOT40 calculation

A series of evaluation indicators of O_3 concentration and flux are proposed (Feng et al., 2020). Including evaluation indicators based on O_3 concentration, O_3 dose and O_3 flux. The dose refers to the accumulation of O_3 concentration in a plant growth period, which is calculated by assigning different weights to O_3 concentration per hour, such as SUM06, W126, AOT40 (Feng and Peng, 2021). Such indicators take into account O_3 concentration, exposure time and plant tolerance to O_3 concentration, and are relatively simple to calculate. The AOT40 index is widely used, which is the accumulation of the difference between the hourly concentration of O_3 above 40 nL L^{-1} and 40 nL L^{-1}. In this paper, the effect of O_3 on NPP of terrestrial ecosystems was studied by AOT40 index. The calculation formula is as follows:

$$AOT40 = \sum_{i=1}^{n} ([O_3] - 40) \times \Delta t \quad (1)$$

where Δt is the cumulative time period for calculating O_3 evaluation index. Since the time resolution of MOD17A3H NPP data used in this paper is 1 year, AOT40 is adjusted to annual AOT40 value in order to maintain the unity of time resolution. Data from 8: 00 a.m. to 8: 00 p.m. daily were extracted from 2014–2019 O_3 concentration data, and the monthly and annual cumulative AOT40 values were calculated using the model builder of ArcGIS 10.6. The annual AOT40 values of evergreen coniferous forests, evergreen broad-leaved forests, farmland and grassland ecosystems from 2014 to 2019 were extracted respectively.

2.5 Ecosystem classification data

The original data of ecological system classification used comes from China Cover 2010 data (https://kns.cnki.net/kcms2/article/abstract?v=3uoqIhG8C44YLTlOAiTRKibYlV5Vjs7ir5D84hng_y4D11vwp0rrta3RDv2Tx3hkXc19TbqMxdjxDMZ09MZGlf8qtkDSEgjR&uniplatform=NZKPT), The spatial resolution was adjusted to 10 km to keep consistent with the annual AOT40, and then the data of evergreen coniferous forests, evergreen broad-leaved forests, farmland and grassland ecosystems were extracted.

3 Methods and steps

3.1 Establishment of AOT40-NPP response relationships

In previous studies, the relationship between the factors affecting NPP and the response of NPP was usually assumed to have a linear influence (Peng et al., 2022; Wang et al., 2020; Shimizu et al., 2019). This paper attempts to establish linear response relationships between AOT40 and NPP. The formula is as follows:

$$y = a \cdot x + b \quad (2)$$

where y is the estimated NPP, x is the annual average AOT40 value, a is the slope of the response relationships between AOT40 and NPP, b is the NPP value of the ecosystem before the effect of O_3 is highlighted. The b values of different ecosystem types are different. In order to standardize the slope of the response relationships of different ecosystems, the regression equation is transformed by dividing the left and right of Eq. 2 by intercept b. The formula is as follows:

$$y' = a \cdot \frac{x}{b} + 1 \quad (3)$$

where y' is the ratio of NPP to NPP before the effect of O_3 (AOT40) is highlighted. Therefore, determining the a and b values is the key to establishing a response relationships. The determination of a value is calculated by separating the scatter plot signal, and the determination of b value is estimated by combining the NPP background values of different ecosystem types.

Jarvis (Jarvis et al., 1976) estimated the leaf - level water vapor stomatal conductance using a multiplicative model. Yo Shimizu et al. applied this method of determining the limit function in the Jarvis model to estimate the AOT40-induced NPP decline. They believe that the top point of the scatter plot with annual AOT40 as the X-axis and annual NPP as the Y-axis represents the optimal regional data for all environments such as temperature, humidity, solar light intensity, and soil moisture at the corresponding AOT40 level. Therefore, the change of the top point reflects the relationship between NPP change and AOT40 increase to some extent (Shimizu et al., 2019).

The traditional AOT40 is calculated over a six-month period, which covers the period from April to September when most plants grow. In order to unify with the time resolution of MODIS NPP, we calculated the annual AOT40 value. The scatter plot of AOT40-NPP was drawn for each ecosystem type, where the X-axis is the annual AOT40 value and the Y-axis is the annual NPP value. In order to reduce the impact of interannual variation of O_3 pollution, the X-axis was adjusted to the 6-year AOT40 average.

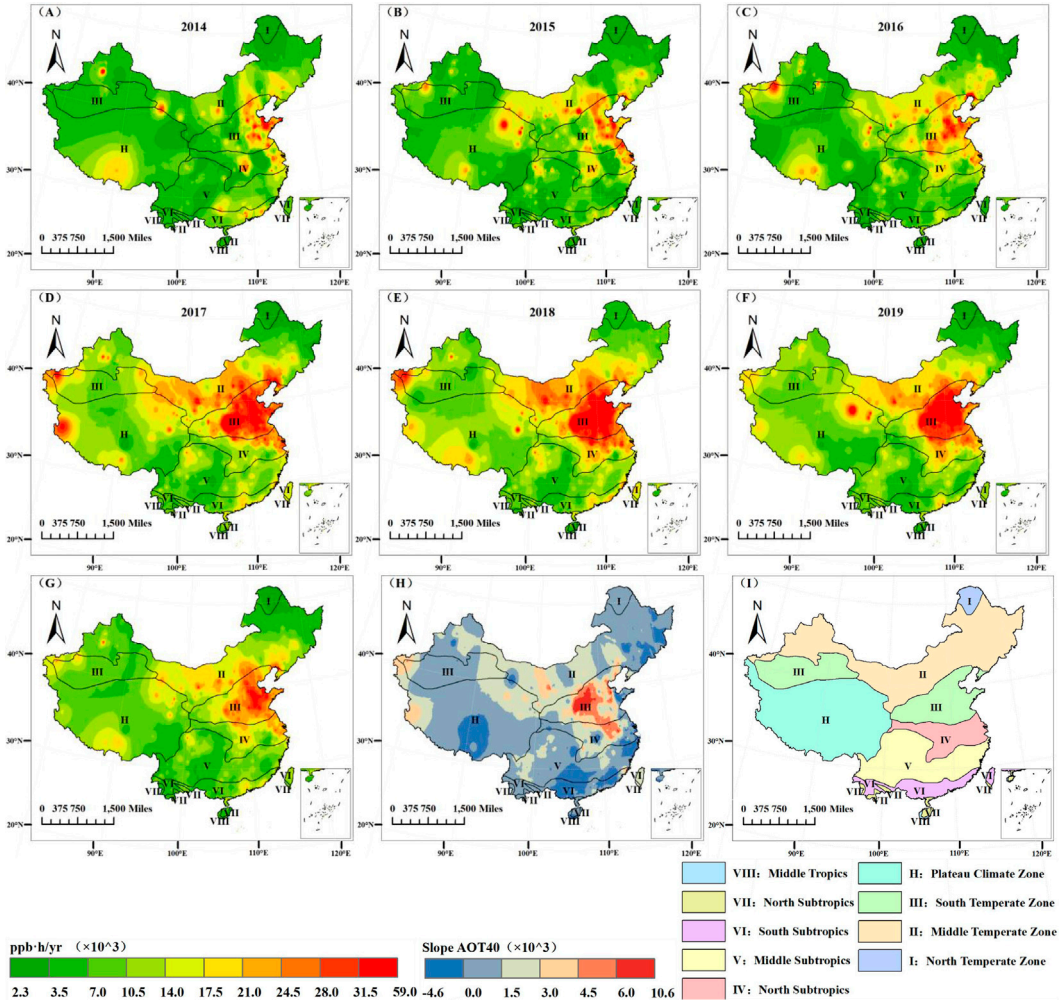

FIGURE 3
Spatial distribution of annual AOT40 **(A–G)**, annual change rate of AOT40 **(H)** and Climate zone map **(I)**, 2014 to 2019. A slope greater than 0 indicates an upward trend in annual AOT40 values in **(H)**.

It can be clearly seen from the scatter diagram, whether it is from the overall trend of 6-year data or the trend of every 1-year data, when the AOT40 value of the year increases to a certain extent, the annual NPP value of the top point tends to decrease continuously and stably with the increase of the annual AOT40 value. It is considered that "continuous and stable downward trend " indicates that the effect of AOT40 on NPP begins to highlight at this time. We attempts to separate the signal data showing "continuous and stable downward trend" by a certain method, and establish response relationships to quantify the relationship between AOT40 and NPP. The AOT40 value corresponding to the onset of a "continuous and stable downward trend" is called the annual AOT40 threshold.

Due to the need to extract the signal data after the annual AOT40 threshold, it is necessary to first obtain the annual AOT40 threshold of different ecosystems. Firstly, all pixel points of evergreen coniferous forests were extracted. Secondly, the scatter points (top points) with NPP value above 80% quantile were extracted as sample data A. For the sample data A, the scatter plot is drawn, the Y-axis is set as the annual NPP value, and the X-axis is adjusted to the annual average of AOT40 of 6 years to reduce the influence of AOT40 interannual variation, and the average is divided into 10 intervals. The average value of the annual NPP value in each interval is calculated to represent the overall data characteristics of the top point NPP in the AOT40 interval, and the midpoint value of the AOT40 interval is taken as the X value to draw 10 scatter points. Mann-Kendall mutation test method was used to test the signal mutation point. This method has no requirement for the distribution of samples and is less disturbed by a few outliers, so the results are reliable. In this paper, the Mann-Kendall mutation test is implemented by Python programming. The calculation formula is as follows:

$$S_k = \sum_{i=1}^{k} r_i \tag{4}$$

where,

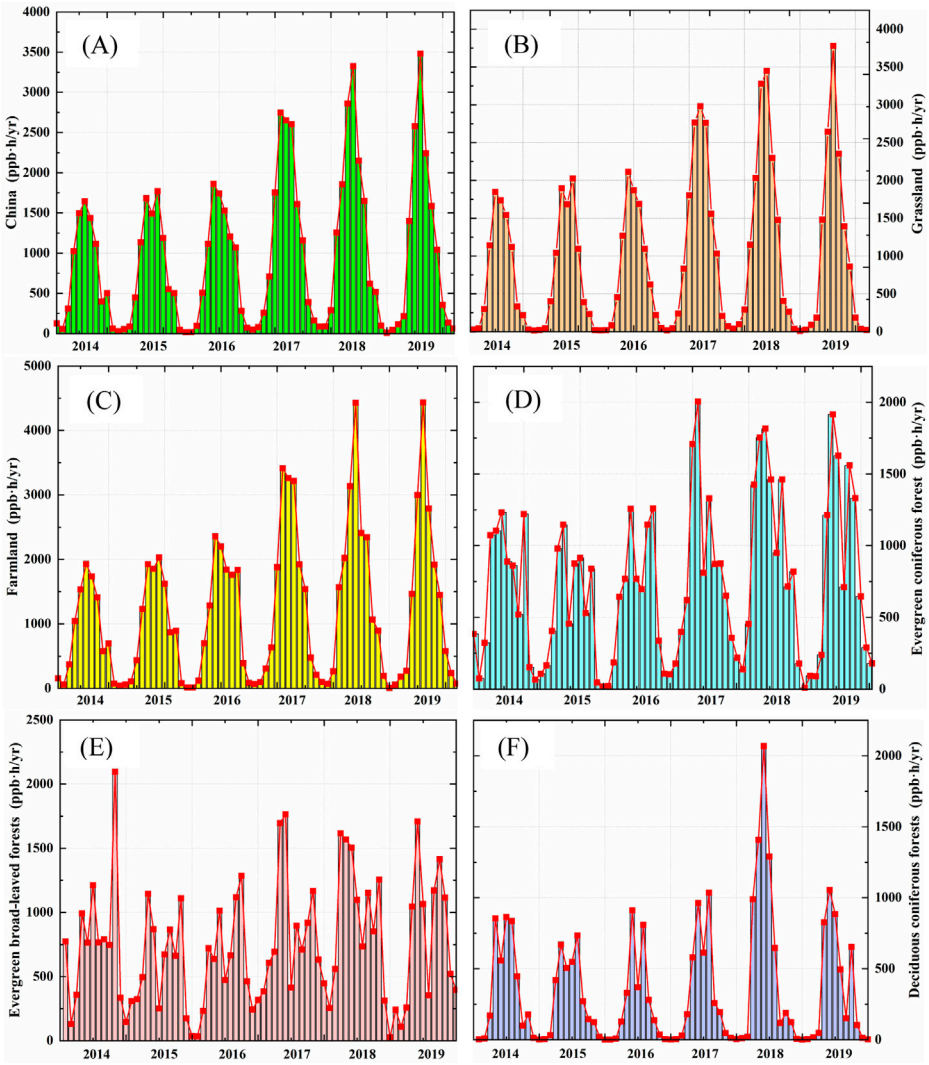

FIGURE 4
Monthly AOT40 spatial distribution, 2014–2019, **(A–F)** are China, Grassland, Farmland, Evergreen coniferous forests, Evergreen broad-leaved forests, Deciduous coniferous forests.

$$r_i = \begin{cases} 1, & x_i > x_j \\ 0, & x_i \le x_j \end{cases}, j = 1, 2, \ldots, i$$

$$UF_k = \frac{S_k - E(S_k)}{\sqrt{Var(S_k)}} \quad (5)$$

Specifies $UF1 = 0$, and:

$$\boldsymbol{E}(S_k) = \frac{n \times (n-l)}{4} \quad (6)$$

$$Var(S_k) = \frac{n \times (n-l) \times (2n+5)}{72} \quad (7)$$

$$UB_k = -UF_k r$$

After determining the signal mutation point, this paper proposes two constraints to separate the signal data that can reflect the response relationships between AOT40 and NPP, which are.

1) the annual AOT40 value needs to exceed the annual AOT40 threshold of the corresponding ecosystem type;
2) Scatter from 1) for NPP values greater than 80% of the quantile points.

Firstly, the regional scatter points of annual AOT40 exceeding annual AOT40 threshold are extracted as sample data B, and then the scatter points of NPP value exceeding 80% quantile points in sample data B are extracted as sample data C to solve the slope of response relationship. The scatter plot is drawn for the extracted sample data C, and the *X*-axis is divided into 10 intervals on average. The average NPP value of each interval is calculated as the y value, and the midpoint value of the AOT40 interval is taken as the x value to obtain 10 scatter points. Then a linear regression fitting is performed to obtain the fitting line slope *a*.

The *b* value represents the NPP background value when the corresponding ecosystem type has just reached the annual

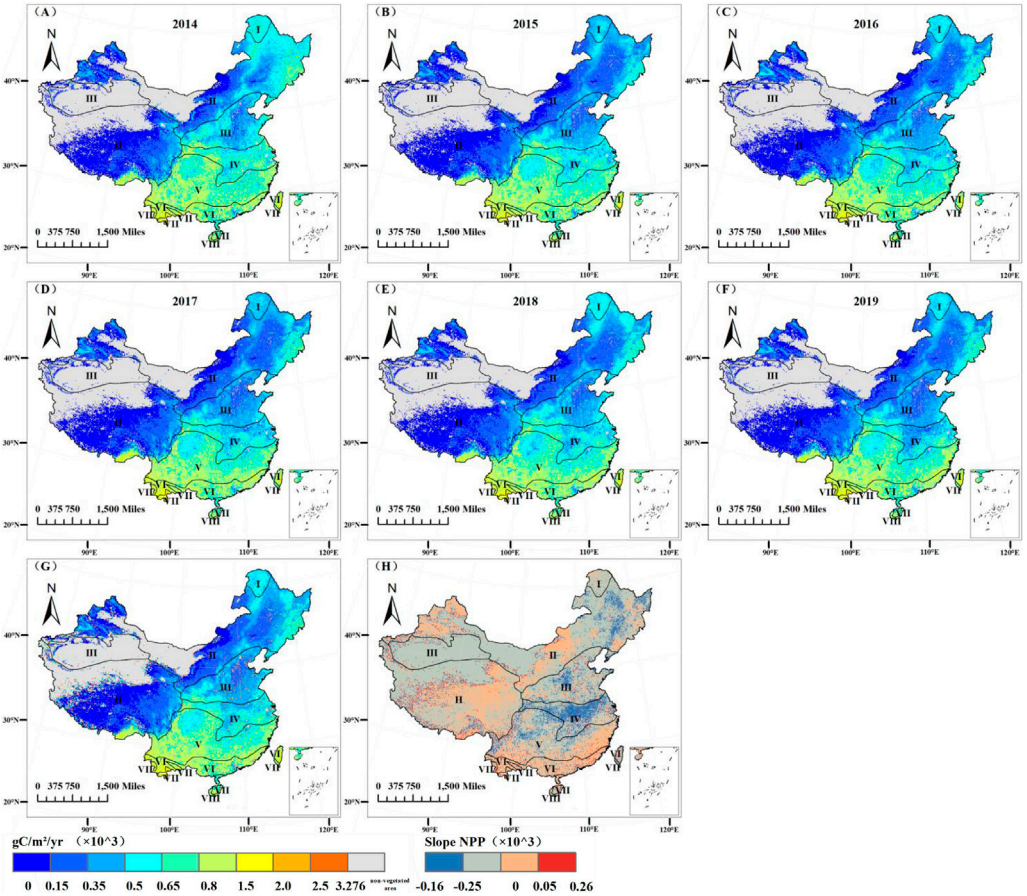

FIGURE 5
Spatial distribution of annual average NPP **(A–G)** and annual change rate of NPP **(H)** in China from 2014 to 2019.

AOT40 threshold and has not been significantly affected by O_3, rather than the intercept in the mathematical sense of the fitted regression line. Therefore, for each ecosystem type, the average of its top point near the AOT40 threshold is calculated as the b value.

3.2 Calculation of O_3-induced NPP decline percentage

For each type of ecosystem, the area where the annual AOT40 value reaches the corresponding ecosystem annual AOT40 threshold is selected as the evaluation area. Based on the established response relationships, the percentage of O_3-induced NPP decline in this part of the region was calculated. The formula is as follows:

$$I_{ozone} = \frac{a \cdot x}{b} \tag{8}$$

The response relationship was then applied to the 2014 annual AOT40 image to obtain the NPP reduction percentage of each ecosystem type, as shown in Figure 7.

3.3 Annual trends of AOT40 and NPP from 2014 to 2019

In this paper, the trend analysis method is used to analyze the trend of annual AOT40 mean and annual NPP mean in China from 2014 to 2019, so as to obtain the change rate of AOT40 and NPP. The calculation formula is as follows:

$$Slope = \frac{n\sum_{i=1}^{n}(i \times AOT40_i) - \sum_{i=1}^{n} i \times \sum_{i=1}^{n} AOT40_i}{n\sum_{i=1}^{n} i^2 - \left(\sum_{i=1}^{n} i\right)^2} \tag{9}$$

where $Slope$ is the slope of the pixel regression equation, $AOT40i$ is the average value of AOT40 in year i, n is the length of time studied, $n = 6$ in this paper. When Slope >0, it means that the pixel $AOT40$ is an increasing trend; when $Slope = 0$, it means that the pixel $AOT40$ is basically unchanged; when Slope <0, it indicates that the pixel $AOT40$ is a decreasing trend. The change rate of NPP from 2014 to 2019 was calculated by the same method.

TABLE 2 Correlation between AOT40 and NPP for each ecosystem, 2014–2019.

Ecosystem types	r-value	*p*-value
China Region	−0.460	0.359
Evergreen coniferous forests	−0.071	0.894
Evergreen broad-leaved forests	0.629	0.181
Farmland	−0.653	0.159
Grassland	−0.484	0.331

4 Results

4.1 Spatial-temporal characteristics and annual change rate of AOT40

The O_3 concentration dataset obtained by data cleaning and spatial interpolation in this paper has a spatial resolution of 10 km and a temporal resolution including 1 h, 1 day, 1 month and 1 year. The spatial coverage is the China region and the time series is 2014–2019. This dataset removes and replaces default values to improve data availability and extends point data only located at observation locations to regional data at the Chinese scale. Figure 3 shows the spatial distribution of annual AOT40 (A-G), annual AOT40 trends H) and the climatic zoning map I) within the Chinese region from 2014–2019. As shown in Figure 3, the highest value of national annual AOT40 mainly occurs in Beijing, Tianjin and Hebei, Shanxi, Shandong, Henan and the northern regions of Jiangsu and Anhui in the Southern Temperate Zone, where the annual AOT40 values are higher than 20,000 ppbh/yr. The second highest annual AOT40 values are found in the Inner Mongolian Plateau in the Middle Temperate Zone and in the southern regions of Jiangsu and Anhui in the Southern Temperate Zone, with annual AOT40 values above 14,000 ppbh/yr. The annual AOT40 values in all other regions are relatively low, below 17,500 ppbh/yr.

The annual AOT40 values during 2017–2019 were generally higher relative to those during 2014–2016, indicating that the O_3 pollution became more serious. During 2014–2015, AOT40 in the Inner Mongolia Plateau region had significantly increased. During 2016–2017, AOT40 in the Inner Mongolia Plateau region, the Middle Temperate Zone region, Jiangsu and the southern part of Anhui Province had significantly increased, indicating a significant deterioration of O_3 pollution.

From (H), it can be seen that the annual AOT40 value has been on an increasing trend for six years. Among them, the most significant increase was observed in the Southern Temperate Zone, including the south-central Shanxi province (annual growth rate >6,000), southern Hebei, northern Henan, and some parts of Anhui (annual growth rate >3,000). The second most pronounced increase is found in the Middle Temperate Zone, including the Inner Mongolia Autonomous Region, Gansu and a few other areas of the North China Plain, and the Guangxi Zhuang Autonomous Region (annual growth rate >1,500). However, a few areas in Guangdong, Fujian and the Tibet Autonomous Region located in the subtropics show a decreasing trend (slope <0).

The above results indicate that O_3 pollution is most serious in the Southern Temperate Zone and the Inner Mongolia Plateau region located in the Middle Temperate Zone nationwide during 2014–2019, and their O_3 pollution intensification is most pronounced.

Figure 4 shows the temporal variation of monthly AOT40 for different ecosystems from 2014 to 2019. Farmland and Grassland ecosystems are located in areas with the highest monthly AOT40, largely remaining around 2,000 ppbh/yr. Evergreen coniferous and Evergreen broad-leaved forests have the second highest monthly AOT40, remaining around 1,000–2,000 ppbh/yr. Deciduous coniferous forests had the lowest monthly AOT40, remaining below 1,000 ppbh/yr most of the time. The appeal results indicate that O_3 pollution is most severe in areas of Grassland and Farmland ecosystems. Areas where Evergreen coniferous and Evergreen broad-leaved forests are located have the second worst O_3 pollution. Areas where deciduous coniferous forests are located have no serious O_3 pollution. The inter-month variation in China's AOT40 values from 2014 to 2019 is very consistent with the inter-month variation in the regions where Farmland and Grassland ecosystems are located. Moreover, O_3 pollution has a clear seasonal effect, being most severe in summer and autumn, but less severe in spring and winter. Seasonal effects are most pronounced in Grassland and Farmland, second most pronounced in Evergreen coniferous and Deciduous coniferous forests, and less pronounced in Evergreen broad-leaved forests.

4.2 Spatial-temporal characteristics and annual change rate of NPP

From Figure 5, we can see that China's annual NPP values are higher in the east and south than in the west and north. Among them, Evergreen coniferous and Evergreen broad-leaved forests in subtropical regions have the highest annual NPP values, which range from 350–1,500 $gC/m^2/yr$; Farmland, Grassland and Deciduous coniferous forests have lower annual NPP values, which range from 350–700 $gC/m^2/yr$. The annual NPP values of Farmland and Deciduous coniferous forests located in the Southern

TABLE 3 AOT40 thresholds, a, b and normalized slopes for each ecosystem.

Ecosystem types	AOT40 threshold (ppb·h/yr)	a	b	Normalized slope
Evergreen coniferous forests	13,411	- 0.0104	966.51333	1.076×10^{-5}
Evergreen broad-leaved forests	13,485	- 0.003487	1,387.91875	0.2512×10^{-5}
Farmland	11,741	- 0.00457	628.91117	0.7267×10^{-5}
Grassland	15,877	- 0.00224	479.50508	0.4671×10^{-5}

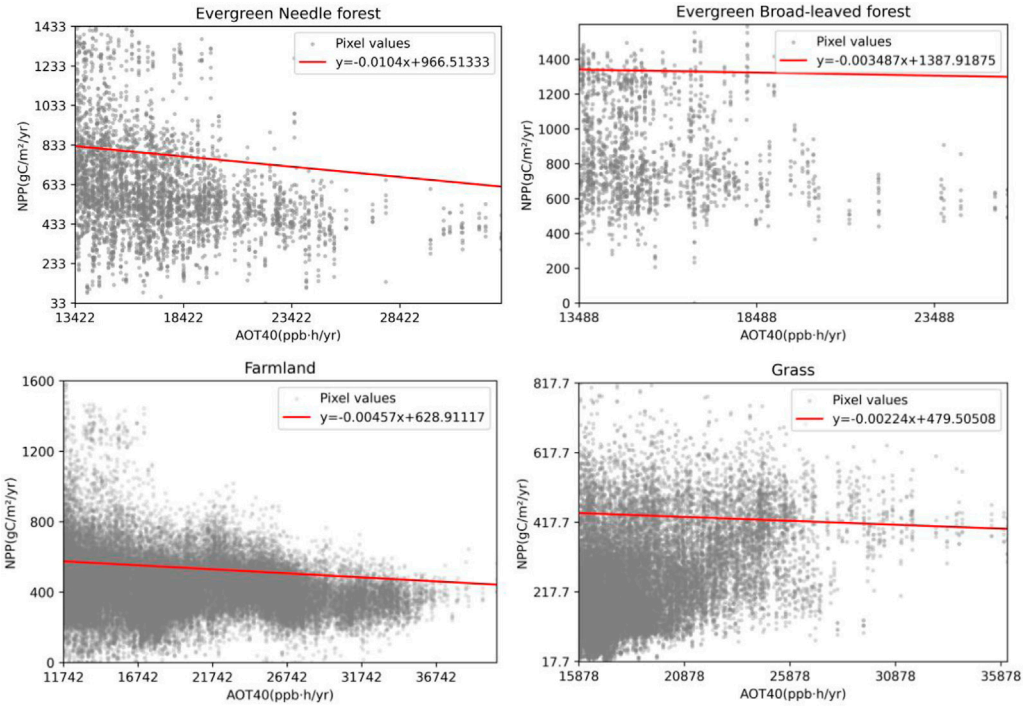

FIGURE 6
6-year scatter plot and response relationships fitted line of annual NPP and annual AOT40 of four ecosystems.

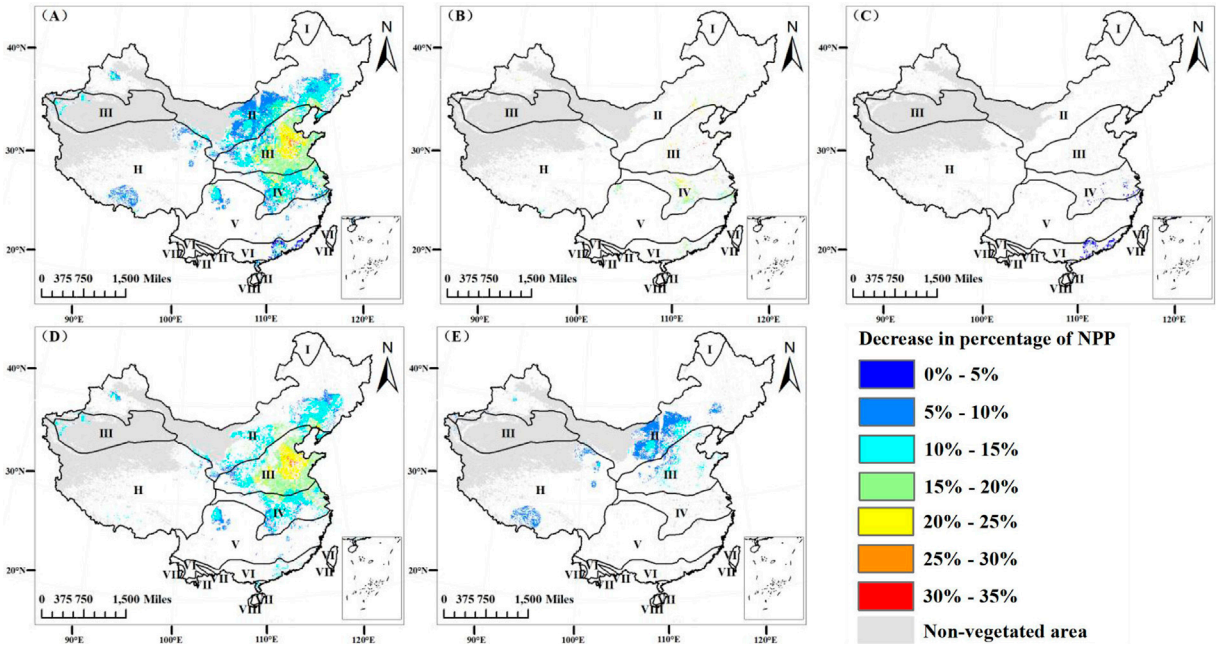

FIGURE 7
Spatial distribution of the percentage of NPP decline induced by O_3 in the four major terrestrial ecosystems in China, **(A)** reflects the overall situation of the percentage of NPP decline induced by O_3 in the four major ecosystems, **(B–E)** reflects the effects of O_3 on the NPP of Evergreen coniferous forest, Evergreen broad-leaved forest, Farmland and Grassland.

Temperate Zone showed a clear downward trend during 2014–2015. The annual NPP values of Farmland located in the Subtropical Zone showed a clear downward trend during 2015–2016 and 2018–2019. The annual NPP values of other ecosystems did not change significantly. From H), it can be seen that annual NPP values in some areas of farmland, Deciduous coniferous forests and Grassland show a decreasing trend. The annual NPP of Evergreen coniferous and Evergreen broad-leaved forests showed an increasing trend in most regions and a decreasing trend in a few regions.

The above results indicate that there is a significant downward trend in the annual NPP values of Farmland, Deciduous coniferous forests and some areas of Grassland. However, there is no significant downward trend in either Evergreen coniferous or Evergreen broad-leaved forests during the period 2014–2019.

4.3 Relationship between AOT40 and NPP

For the different ecosystem types, correlation coefficients and *p*-value between AOT40 and NPP were calculated for 2014–2019 using all scatter points within that ecosystem region, as shown in Table 2. The 2014–2019 annual average AOT40 and annual average NPP from the national scale and for each ecosystem other than Evergreen broad-leaved forests showed a non-significant negative correlation. Therefore, we needed to select the signal data to establish the response relationships.

4.4 The year AOT40 threshold and response relationships

AOT40 thresholds were obtained for Evergreen coniferous forests, Evergreen broad-leaved forests, Farmland and Grassland ecosystems based on the Mann-Kendall mutation point detection method. As shown in Table 3, the signal data were then extracted according to the constraints and we obtained the a-values, b-values and normalised slopes of the regression lines for each of the four ecosystems. When a<0, it means that NPP is negatively correlated with AOT40.

The scatter plots of the signal data separated from the four types of ecosystems are shown in Figure 6, and the response relationships are as follows:

$$y = -0.0104x + 966.51333\mathrm{r}\,(r = 0.5164,\ p = 0.1546),$$
$$y = -0.003487x + 1387.91875\,(r = 0.1959,\ p = 0.6134),$$
$$y = -0.00457x + 628.91117\,(r = 0.8674,\ p < 0.003),$$
$$y = -0.00224x + 479.50508\,(r = 0.781,\ p < 0.03).$$

4.5 O_3-induced NPP decrease percentage

Figure 7 shows the spatial distribution of NPP decline induced by O_3 in 2014. In China, the estimated O_3-induced NPP decline ranged from 5% to 35%. Among them, the decline rate of Farmland ecosystem was the most significant (in range of 5%–35%), and most of the decline rate was 10%–25%. The decline rate of Evergreen coniferous forests was the second (in range of 10%–25%), mostly between 15% and 20%. The decline rate of Grassland ecosystem is low (in range of 5%–20%), most of which is between 5% and 15%. The Evergreen broad-leaved forests have the lowest decline rate (in range of 0%–10%), mostly between 0% and 5%. The regions with the highest percentage of NPP decline induced by O_3 in various ecosystem types are mainly Beijing-Tianjin-Hebei and Shandong. The decline rate of Farmland ecosystem in the study area was significantly higher than other ecosystem types.

5 Discussion

Remote sensing is a detection technique that emerged in the 1960s and has the advantage of obtaining data with wide coverage and a long time span, which also facilitates the expansion of the spatial and temporal span of O_3 impacts on vegetation, thus facilitating the quantification of O_3 impacts on vegetation at the ecosystem level. Remote sensing also allows for fast and efficient acquisition of images and corresponding data, thus providing data to support studies at smaller time scales, such as hourly.

The MODIS NPP data used in this paper is derived from the NASA Earth Observing System and is simulated by the Light Energy Utilisation Model. The NDVI data obtained from MODIS for the inversion of NPP is affected by the sensitivity of the satellite sensors, cloud cover, satellite orbit, etc. Therefore, the MODIS data needs to be denoised at first. Although this process can improve the quality of the data, there are inevitable limitations in the denoising algorithm, which affects the accuracy of the inverse NPP data. Secondly, we, like previous researchers, assumed the AOT40-NPP correlation to be a linear response relationship, and thus fitted their response relationship a linear relationship. However, the AOT40-NPP correlation may be better described by a non-linear correlation, which is one of the directions to be further investigated. Finally, the spatial interpolation method used in this paper is ArcGIS's distance interpolation method, which inevitably has its own corresponding errors.

6 Conclusion and prospect

Based on the idea of Jarvis multiplication model, this paper proposes a method of constructing AOT40-NPP response relationships based on remote sensing technology combined with MOD17A3H NPP data, and applies the response relationship to evaluate the impact rate of O_3 on NPP in 2014. The results show that the established response relationship between Farmland and Grassland ecosystems has the highest correlation coefficients and strong significance, so the results are statistically significant. The percentage of NPP reduction induced by O_3 in 2014 was in the range of 5%–35%. Among them, the decline rate of Farmland ecosystem is the most significant, mostly between 10% and 35%. The decline rate of evergreen coniferous forest is the second, mostly between 15% and 20%. The decline rate of Grassland ecosystem is low, mostly between 5% and 15%. The decline rate of Evergreen broad-leaved forests is the lowest, mostly between 0% and 5%. In addition, we have produced the O_3 concentrations dataset of ground-based observations over the Chinese region.

The prospects of the research work are as follows: 1) The limitation of the spatial resolution (10 km) of the O_3 concentration dataset used in this paper leads to the possibility of mixing other types of vegetation within the same image element. Therefore, in the subsequent study, the spatial resolution of AOT40 spatially interpolated images and remote sensing images can be improved to analyze the effect of O_3 on NPP of specific species more precisely. 2) Since NPP is greatly influenced by environmental factors such as temperature and precipitation, in the subsequent study, the same ecosystem can be further divided into different regions according to the different climate zones they are located in, and the AOT40-NPP response relationships can be constructed separately for different climate zones to obtain more accurate assessment results.

Data availability statement

The original contributions presented in the study are included in the article/supplementary material, further inquiries can be directed to the corresponding author.

Author contributions

ZW and MH conceptualized this study. LH and ZW performed the analysis and wrote the paper. MH, HS, and QW contributed to reviewing and polishing the manuscript. All co-authors commented on and reviewed this manuscript. MH raised funds to support this study.

Funding

This research was supported by the National Natural Science Foundation of China (grant 41971135 and 41801082), and the Research program on the flora of Yunnan Province, the Sustainable Utilization of Vegetation Resources in Yunnan.

Acknowledgments

We thank the reviewers and the senior editor for their comments and suggestions, which helped improve the manuscript.

Conflict of interest

The authors declare that the research was conducted in the absence of any commercial or financial relationships that could be construed as a potential conflict of interest.

Publisher's note

All claims expressed in this article are solely those of the authors and do not necessarily represent those of their affiliated organizations, or those of the publisher, the editors and the reviewers. Any product that may be evaluated in this article, or claim that may be made by its manufacturer, is not guaranteed or endorsed by the publisher.

References

Bai, Y. M., Wang, C., Guo, J. P., and Wen, M. (2003). Experimental study on Rapeseed yield response to ozone stress. *J. Agro-Environment Sci.* 3, 279–282.

Bai, Y. M., Wang, C. Y., Wen, M., and Guo, J. P. (2004). Influences of different ozone concentrations and fumigation days on spinach growth and yield. *Sci. Agric. Sin.* 12, 1971–1975.

Chen, J., Zeng, Q., Zhu, J. G., Liu, G., Cao, J. L., Xie, Z. B., et al. (2011). Nitrogen supply mitigates the effects of elevated [O_3] on photosynthesis and yield in wheat. *Chin. J. Plant Ecol.* 35 (05), 523–530. doi:10.3724/sp.j.1258.2011.00523

Feng, Z., De Marco, A., Anav, A., Gualtieri, M., Sicard, P., Tian, H., et al. (2019). Economic losses due to ozone impacts on human health, forest productivity and crop yield across China. *Environ. Int.* 131, 104966. doi:10.1016/j.envint.2019.104966

Feng, Z., Pang, J., Kobayashi, K., Zhu, J., and Ort, D. R. (2011). Differential responses in two varieties of winter wheat to elevated ozone concentration under fully open-air field conditions. *Glob. Change Biol.* 17 (1), 580–591. doi:10.1111/j.1365-2486.2010.02184.x

Feng, Z., and Peng, J. (2021). Relationship between relative crop yield/woody plant biomass and groundlevel ozone pollution in China. *Environ. Sci.*, 42(6): 3084–3090. doi:10.13227/j.hjkx.202009226

Feng, Z., Yuan, X., Li, P., Shang, B., Ping, Q., Hu, Y., et al. (2020). Progress in the effects of elevated ground-level ozone on terrestrial ecosystems. *Chin. J. Plant Ecol.* 05, 526–542. doi:10.17521/cjpe.2019.0144

Feng, Z. Z., Li, P., Yuan, X. Y., Gao, F., Jiang, L., and Dai, L. (2018). Progress in ecological and environmental effects of ground-level O_3 in China. *Acta Ecol. Sin.* 38 (5), 1530–1541. doi:10.5846/stxb201704100618

Feng, Z. Z., Wang, X. K., Zheng, Q. W., Feng, Z. W., Xie, J. Q., and Chen, Z. (2006). Response of gas exchange of rape to ozone concentration and exposure regime. *Acta Ecol. Sin.* 26 (03), 823–829. doi:10.1016/s1872-2032(06)60014-0

Jarvis, P. G. (1976). The interpretation of the variations in leaf water potential and stomatal conductance found in canopies in the fieldPhil. *Trans. R. Soc. Lond.*, B273593–610. doi:10.1098/rstb.1976.0035

Lin, W., and Guo, X. (2022). Analysis of the spatial and temporal distribution of ozone in urban clusters in China[J]. *China Environ. Sci.* 42 (06), 2481–2494. doi:10.19674/j.cnki.issn1000-6923.20220207.002

Liu, X., Zhao, J., Du, Z., and Zhang, H. (2018). Net primary productivity pattern of grassland in China and its relationship with hydrothermal factors during 1993-2015. *Bull. Soil Water Conservation* 01, 299–305+329. doi:10.13961/j.cnki.stbctb.2018.01.052

Luo, K., Zhu, J., Liu, G., Tang, H., Li, C., and Zeng, Q. (2012). Effects of elevated ozone on leaf photosynthesis of rice (Oryza sativa L.) and mitigation with high nitrogen supply. *Ecol. Environ. Sci.* 03, 481–488. doi:10.16258/j.cnki.1674-5906.2012.03.021

Ma, Z. X., Cui, H. J., and Ge, Q., S. (2022). Prediction of net primary productivity change pattern in China based on vegetation dynamic models. *J. Geogr.* 77 (07), 1821–1836. doi:10.11821/dlxb202207017

Pan, S., Tian, H., Dangal, S. R., Ouyang, Z., Lu, C., Yang, J., et al. (2015). Impacts of climate variability and extremes on global net primary production in the first decade of the 21st century. *J. Geogr. Sci.* 25 (9), 1027–1044. doi:10.1007/s11442-015-1217-4

Pang, J., Kobayashi, K., and Zhu, J. (2009). Yield and photosynthetic characteristics of flag leaves in Chinese rice (Oryza sativa L.) varieties subjected to free-air release of ozone. *Agric. Ecosyst. Environ.* 132 (3-4), 203–211. doi:10.1016/j.agee.2009.03.012

Ren, W., and Tian, H. Q. (2007). Ozone pollution and terrestrial ecosystem productivity. *Chin. J. Plant Ecol.* 31 (02), 219–230. doi:10.17521/cjpe.2007.0026

Shi, G., Yang, L., Wang, Y., Kobayashi, K., Zhu, J., et al. (2009). Impact of elevated ozone concentration on yield of four Chinese rice cultivars under fully open-air field conditions. *Agric. Ecosyst. Environ.* 131 (3-4), 178–184. doi:10.1016/j.agee.2009.01.009

Shimizu, Y., Lu, Y., Aono, M., and Omasa, K. (2019). A novel remote sensing-based method of ozone damage assessment effect on Net Primary Productivity of various vegetation types. *Atmos. Environ.* 217, 116947. doi:10.1016/j.atmosenv.2019.116947

Tu, H. Y., Jiapaer, G., Yu, T. X., and Chen, B. J. (2023). Analysis ofspatio-temporal variation characteristics and influencing factors of net primary productivity in terrestrial ecosystems of China. *Acta Ecol. Sin.* 43, 1. doi:10.5846/stxb202201230216

Wang, Q., Huang, M., Wang, Z., Wang, S., and Li, Y. (2008). Impact of ozone pollution on productivity and biomass of subtropical forests: A case study in dinghushan. *Acta Ecol. Sin*.

Wang, X. L., Zhao, W. J., Li, L. J., Yang, X. C., Jiang, J. F., and Sun, S. (2020). Characteristics of spatiotemporal distribution of O_3 in China and impact analysis of socio-economic factors. *Earth Environ.* 1, 66–75. doi:10.14050/j.cnki.1672-9250.2020.48.006

Wang, Y. H., Shi, X. Z., Wang, M. Y., and Zhao, Y. C. (2017). Spatio-temporal variation of NPP in cropland ecosystem of China during the years from 2001 to 2010. *Acta Pedol. Sin.* 2, 319–330. doi:10.11766/trxb201604220153

Xu, Y., Huang, W. T., Zheng, Z. W., Dai, Q. Y., and Li, X. Y. (2023). Detecting influencing factor of vegetation NPP in southwest China based on spatial scale effect. *Environ. Sci.* 44, 900. doi:10.13227/j.hjkx.202203254

Yang, L., Wang, Y., Zhao, Y., Zhu, J., Sun, Y., and Wang, Y. (2010). Responses of soybean to free-air ozone concentration enrichment: A research review. *Acta Ecol. Sin.* 23, 6635–6645.

Zhang, X., Tao, S., Dong, S., and Xiao, X. (2022). Study on the characteristics and influencing factors of ozone pollution[J]. *Environ. Sci. Manag.* 47 (02), 47–50+66.

Zeng, Y., Cao, Y., Qiao, X., Seyler, B. C., and Tang, Y. (2019). Air pollution reduction in China: Recent success but great challenge for the future. *Sci. Total Environ.* 663 (1), 329–337. doi:10.1016/j.scitotenv.2019.01.262

Frontiers in Environmental Science

Explores the anthropogenic impact on our natural world

An innovative journal that advances knowledge of the natural world and its intersections with human society. It supports the formulation of policies that lead to a more inhabitable and sustainable world.

Discover the latest Research Topics

See more →

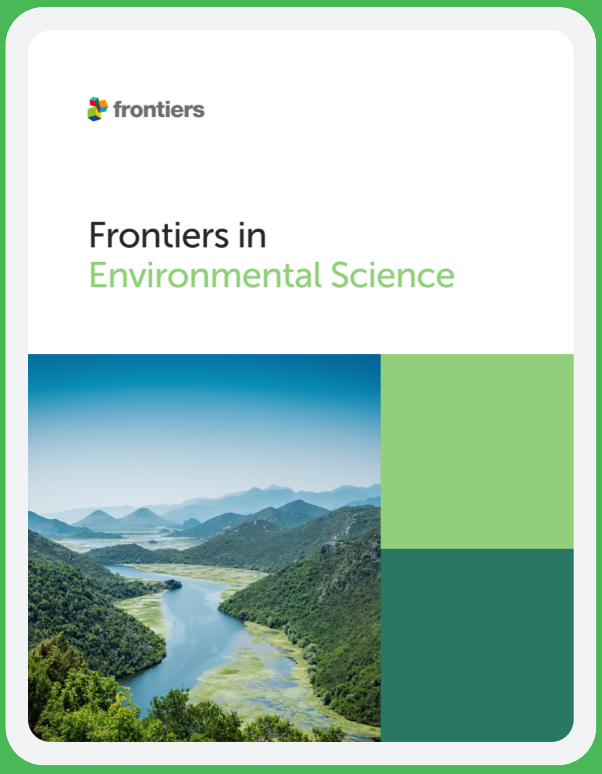

Frontiers

Avenue du Tribunal-Fédéral 34
1005 Lausanne, Switzerland
frontiersin.org

Contact us

+41 (0)21 510 17 00
frontiersin.org/about/contact